AN INVESTIGATION OF THE PHYSICAL AND ELECTRICAL PROPERTIES OF INDIUM ARSENIDE FILMS

A Thesis Submitted To

THE UNIVERSITY OF SOUTHAMPTON

For The Degree Of Doctor Of Philosophy

by

NORMAN GODINHO

December 1969

ABSTRACT

FACULTY OF SCIENCE

ELECTRONICS

Doctor Of Philosophy

AN INVESTIGATION OF THE PHYSICAL AND ELECTRICAL PROPERTIES OF INDIUM ARSENIDE FILMS

by Norman Godinho

Indium Arsenide films have been prepared from the elements by a modified 'three temperature' method, in a conventional vacuum system. The films have been examined by X-ray and electron diffraction and the electrical properties evaluated by Hall effect and conductivity measurements down to liquid nitrogen temperatues.

Initially, polycrystalline films were deposited on amorphous substrates and the conditions established to give a compound with good electrical properties. Epitaxial layers were then deposited on {100}, {110} and {111}As faces of semi-insulating GaAs. Deposition rates of 0.1μm/min. in an Arsenic pressure of 10^{-4}torr and substrate temperatures of 600-650°C, resulted in films with mirror smooth surfaces and sharp interfaces. Laue back reflection and reflection electron diffraction indicate that the films are single crystal.

Room temperature mobilities of 23,000cm^2/V-sec and electron concentrations of 1-2x$10^{16}/cm^3$ have been obtained with epitaxial films thicker than 4μm, increasing to 45,000cm^2/V-sec at 100°K. A

reduction in thickness results in a fall in mobility to about $1000cm^2/V\text{-}sec$ with 300Å films and a rapid decrease in mobility with temperature at this thickness. It has not been possible to explain this on the basis of impurity scattering, since it appears that very little auto-doping by the substrate is taking place. A conventional Boltzmann surface scattering theory has been used to explain some of the results.

A photomechanical process has been used to fabricate 12x12 arrays of insulated gate field effect structures on the very thin epitaxial films, using evaporated contacts and gate insulator. Source-drain spacings of 10, 25, 40, and 110μm were incorporated, with Hall probes in the 110μm gaps. These are essentially accumulation and depletion mode devices and the saturation characteristics are not good. Hall mobility measurements with low drift fields, well below pinch-off, indicate a reduction in mobility with increasing gate field and a surface transport theory is presented which may explain this. However, because of the large electron wavelength in InAs, it is believed that quantization of the conduction band levels could affect the transport properties in these films considerably.

ACKNOWLEDGEMENTS

I would like to thank my supervisor, Dr. A. Brunnschweiler, for his help and guidance during the project, and all those in the Electronics Department, too numerous to be mentioned individually, who have helped me considerably. I am very grateful to Derek Hurne for the electron diffraction work and to Colin Driscoll and Drs. A.F.W. Willoughby and R. Farrar, of the Materials Laboratory, for their help and advice. I am extremely grateful to Professor G.D. Sims for providing me with facilities in the Electronics Department to carry out this work, and to Professor R.L. Bell for facilities in the Materials Laboratory. Finally, I would like to thank the Science Research Council for providing an equipment grant and to the Association of Commonwealth Universities for supporting me financially.

Page

List Of Figures

Page

Page

Page

Page

List Of Figures In Appendices

List Of Tables

LIST OF SYMBOLS - CHAPTERS 2 and 3

Symbol	Represents	Unit
a	Lattice constant	cm
a_o	Adatom jump distance	cm
A_o	Effective evaporation area	cm^2
C_l	Coefficient of elasticity	
D	Spacing of hetero-junction misfit dislocations	cm
$f_1(\theta)$	Geometrical function for critical nucleus	
$f_L(\theta)$	Geometrical function for nucleation at surface steps	
g	Fraction of surface sites occupied by steps	
ΔG^*	Free energy of formation of a critical nucleus	ergs
ΔG_v	Free energy change per unit volume associated with the transformation of adatoms to the crystalline state	$ergs/cm^3$
ΔG_{des}	Free energy of activation for desorption of adatoms	ergs
ΔG_{diff}	Free energy of activation for surface diffusion of adatoms	ergs
ΔG_q	Statistical mechanical correction to free energy of formation of critical nucleus	ergs
h	Plancks constant	erg-sec
ΔH_v	Enthalpy associated with the vapour to solid transformation	$ergs/cm^3$

Symbol	Represents	Units
i^*	Number of monomers in critical nucleus	
J	Nucleation rate	$cm^{-2}sec^{-1}$
J_L	Nucleation rate at surface steps (ledges)	$cm^{-2}sec^{-1}$
k	Boltzmanns constant	$ergs/^oK$
m	Number of dangling bonds associated with unit mesh	
M_i	Atomic (molecular) weight of component i	
n_o	Number of surface sites on substrate/unit area	cm^{-2}
n_s	surface concentration of adatoms	cm^{-2}
n_{AB}	Rate of collision of A adatoms with B adatoms	$cm^{-2}sec^{-1}$
n^*	Number of critical nuclei/unit area	cm^{-2}
N_{s1}, N_{s2}	Densities of dangling bonds presented by each surface of heterojunctions	cm^{-2}
$\pm \Delta N_s = N_{s1} - N_{s2}$	Net density of dangling bonds at heterojunction interface	cm^{-2}
p_i	Vapour pressure of component i above source	$dynes/cm^2$
p_{ei}	Equilibrium vapour pressure of i at substrate temp. T	$dynes/cm^2$
p	Vapour pressure at substrate due to impinging flux	$dynes/cm^2$

Symbol	Represents	Units
q_1, q_2	Unit mesh vectors	cm
r_o	Source-substrate spacing	cm
r^*	Radius of critical nucleus	cm
R_{+i}	Impingement rate of component i	$cm^{-2}sec^{-1}$
R_{-i}	Desorption rate of component i	$cm^{-2}sec^{-1}$
t	Exposure time of substrate to impinging flux	sec
T	Substrate temperature	^oK
T_i	Temperature of source i	^oK
T_p	Equilibrium temperature of transformation at pressure, p	^oK
v	Atomic (molecular) volume	cm^{-3}
x	Lattice parameter of nucleus interface plane	cm
Z	Zeldovich non-equilibrium factor	
α	$= -\frac{4\pi\alpha_o n_o \sigma_{c-v}}{(2\pi MkT_p)^{\frac{1}{2}}} \cdot \frac{P}{\Delta G_v} \cdot \exp\{\frac{\Delta G_{des} - \Delta G_{diff}}{kT}\}$	$cm^{-2}sec^{-1}$
α_1	$= \alpha/J$	
β	$= \frac{16\pi\sigma_{c-v}^3}{3kT\Delta G_v^2}$	
γ	Number of sites covered in unit time by adatom	sec^{-1}
Γ	Loathe-Pound correction factor	

Symbol	Represents	Units
δ	Lattice disregistry	
ϵ	Strain in nucleus due to lattice misfit	
η	Constant of proportionality	$ergs/cm^2$
θ	Contact angle of critical nucleus	degrees
λ_1, λ_2	Interatomic spacing along particular crystallographic directions	cm
$\pm \Delta\lambda$	$= \lambda_1 - \lambda_2$, lattice misfit	cm
ν	Lattice vibration frequency	sec^{-1}
σ_{c-s}	Condensate-substrate interfacial free energy	$ergs/cm^2$
σ_{s-v}	Substrate-vapour interfacial free energy	$ergs/cm^2$
σ_{c-v}	Condensate-vapour interfacial free energy	$ergs/cm^2$
τ_s	Adatom residence time	sec
τ_{cB}	Mean lifetime of B adatom before collision with A adatom	sec
ω	Frequency factor for the addition of monomers to the critical nucleus	sec^{-1}

LIST OF SYMBOLS - CHAPTERS 5 and 6

Note: Although the expressions are in the m.K.s. system, the units are expressed in c.g.s.

Symbol	Respresents	Units
a, a_x, a_y, a_z	Acceleration of carriers and components in appropriate directions	cm^2/sec
a_o	Impact parameter for coulomb scattering	cm
$\bar{a}$	Average crystallite size	cm
$b = \mu_1/\mu_2$	Mobility ratio in two band system	
B_z	Magnetic field in z direction	gauss
C_{ox}	Gate oxide capacitance/unit area	$Farads/cm^2$
2d	Semiconductor film thickness	cm
d_{ox}	Gate oxide thickness	cm
E, E_x, E_y, E_z	Electric field	V/cm
E_s	Surface electric field	V/cm
f	Non-equilibrium distribution function	
f_o	Equilibrium distribution function	
$f_1 = f-f_o$	Pertubation in distribution function	
$f_{11} = qE_x v_x \tau_b f_o/kT$	Pertubation in distribution function in the bulk with an applied field E_x	
$F(\psi, \psi_d, \lambda)$	Normalized field function $2d << L_B$	
$F(u, u_b)$	Normalized field function $2d >> L_B$	
g_m	Small signal transconductance	ma/V
$g(v)$	Surface scattering functions given by equations B4 and B5	

Symbol	Represents	Units
G_{DS}	D.C. source-drain conductance	mhos
$G(\psi,\psi_d,\lambda)$	Excess carrier function $2d \ll L_B$	
$G(u,u_b)$	Excess carrier function $2d \gg L_B$	
$\hbar = h/2\pi$	Plancks constant/2π = 1.054×10^{-27}	erg-sec
$H(v)$	Function in equation 6.46	
I_D	Drain current	mA
I_{nx}	Current per unit width	mA/cm
k	Boltzmanns constant = 1.38×10^{-16}	ergs/^oK
k,k_x,k_y,k_z	Electron wavevector	cm^{-1}
$K(v_z,v_{zs})$	Integral given by equation 6.47	
L	Source-drain length	cm
$L_B = (\varepsilon'_o\varepsilon_s kT/2q^2n_b)^{\frac{1}{2}}$	Extrinsic Debye length	cm
$L_D = (\varepsilon'_o\varepsilon_s kT/2q^2n_i)^{\frac{1}{2}}$	Intrinsic Debye length	cm
m	Free electron mass	gm
m*	Electron effective mass	gm
n,n_1,n_2	Electron concentration	cm^{-3}
n_b	Bulk electron concentration	cm^{-3}
n_i	Intrinsic electron concentration	cm^{-3}
n_s	Electron concentration per unit area	cm^{-2}
Δn_s	Surface excess electron concentration	cm^{-2}
N_A	Acceptor concentration	cm^{-3}
N_D	Donor concentration	cm^{-3}
N(v)	Density of states in velocity space	cm^{-6}-s^3

Symbol	Represents	Units
N_{ss}	Density of charged surface states	cm^{-3}
N_l	Number of barriers per unit length in polycrystalline films	cm^{-1}
Δp_s	Surface excess hole concentration	cm^{-2}
q	Electronic charge	Coulombs
$r = \mu_H/\mu_\sigma$	Hall coefficient factor for bulk scattering mechanisms	
$r_s(\beta)$	Hall coefficient factor for surface scattering	
R_H	Hall coefficient	cm^3/Coulomb
T	Absolute temperature	^oK
u	Normalized potential in kT/q units	
u_s	Normalized surface potential in kT/q units	
$u_b = (\epsilon_f - \epsilon_i)/kT$	Normalized bulk Fermi potential	
v, v_x, v_y, v_z	Carrier velocity and components in appropriate directions	cm/sec
v_{zs}	v_z at surface z = 0	cm/sec
v_{zd}	v_z at surface z = 2d	cm/sec
V_D	Source-drain voltage	volts
V_H	Hall voltage	volts
V_G	Gate voltage	volts
W	Source-drain width	cm
x,y,z	Direction co-ordinates	cm
Zq	Surface state charge	Coulombs

Symbol	Represents	Units
α	Index of energy dependence of relaxation time	
$\beta = d/\lambda_n$	Film thickness normalized to $2\lambda_n$	
γ	Fuchs reflectivity parameter at surface z = 0	
$\gamma_o = \{ \frac{1+\lambda^{-2}}{2L_B^2} \}^{\frac{1}{2}}$		cm^{-1}
$\Gamma_1(\beta),\Gamma_2(\beta),\Gamma_3(\beta)$	Functions of β given by integrals in equations 6.37-6.39	
δ	Perturbation in distribution function due to surface scattering with band bending	
$\Delta\epsilon_{N,N+1}$	Energy separation of two quantized levels	eV
ϵ	Energy	eV
ϵ_f	Fermi level	eV
ϵ_i	Intrinsic Fermi level	eV
ϵ_{ox}	Relative permittivity of gate oxide	
ϵ_s	Relative permittivity of semiconductor	
ϵ'_o	Permittivity of vacuum = $8\pi x10^{-12}$	F/m
η	Ratio of mean free path to extrinsic Debye length	
θ	Scattering angle	
$\lambda = n_b/n_i$	Normalized bulk doping density	
$\lambda_n = \tau_b(\frac{kT}{2\pi m^*})^{\frac{1}{2}}$	Mean free path associated with surface scattering	cm
μ_b	Bulk electron mobility	cm^2/V-sec
μ_B	Intercrystalline barrier mobility	cm^2/V-sec

Symbol	Represents	Units
μ_F	Flat band surface scattering electron mobility	$cm^2/V\text{-}sec$
μ_{FE}	Field effect mobility	$cm^2/V\text{-}sec$
μ_H	Hall mobility	$cm^2/V\text{-}sec$
μ_I	Mobility due to ionized impurity scattering	$cm^2/V\text{-}sec$
μ_o	Mobility due to interaction with optical lattice vibrations	$cm^2/V\text{-}sec$
μ_s	Surface scattering electron mobility with band bending	$cm^2/V\text{-}sec$
μ_{ss}	Charged surface state scattering mobility	$cm^2/V\text{-}sec$
μ_σ	Conductivity mobility	$cm^2/V\text{-}sec$
$\nu = \frac{m^* v_z^2}{2kT} + \psi$	Normalized electron energy associated with its motion in the z-direction	
$\rho(\psi)$	Charge density	$Coulombs/cm^3$
ρ_o	Resistivity in zero magnetic field	$\Omega\text{-}cm$
$\Delta\rho/\rho_o$	Magnetoresistance ratio	
σ	Conductivity	$(\Omega\text{-}cm)^{-1}$
$\sigma(\theta)$	Differential 'cross-section' for scattering in two dimensions	cm
τ_b	Bulk relaxation time	sec
τ_{ss}	Relaxation time due to scattering by charged surface states	sec
ϕ_B	Intercrystalline barrier height	eV
ψ_s	Surface band bending normalized to kT/q	

Symbol	Represents	Units
ψ_d	Band bending at substrate-film interface, z = 2d, when 2d << L_B, normalized to kT/q	
ω	Fuchs reflectivity parameter at surface z = 2d	
Ω	Solid angle	

1. INTRODUCTION

1.1. Introduction

Since Welker[1.1] first reported the semiconducting properties of the group III - V compounds in the early fifties, there has been considerable technological interest in these materials, because of their high electron mobility. Later it was realised that these compounds offer unique properties which cannot be observed in the elemental semiconductors, Silicon and Germanium. This results in such devices as the Gunn effect oscillator and the semiconductor laser, the operation of which depend on the band structure of the material. Although much of the effort has been concentrated on GaAs, the electrical properties of melt grown material is poor, probably due to non-stoichiometry and other defects. However, the recent advance in epitaxy has led to the growth of GaAs films with far superior properties to pulled crystals, and which are now used for the majority of Gunn effect devices. Thus, epitaxial films are not only useful from a device point of view, but also because higher quality material may be produced, permitting a better understanding of the physics of these compounds.

Indium Arsenide, the material studied in this project, has a sphalerite (zincblende)lattice, in common with other III - V compounds, which is similiar to the FCC Diamond lattice, except that the nearest neighbour atoms are occupied by different elements. The first Brillouin zone of these compounds is a truncated octahedron, as with Silicon and Germanium. The conduction band minimum in InAs is at the

centre of the Brillouin zone and so are the valence band maxima, i.e., a direct bandgap. Very little is known about the higher sub-bands, but it is believed that there are minima in the [100] and [111] directions, which are predicted[1.2] to be 1.1 and 1.2eV above the lowest conduction band minimum, although the exact positions of these are not known. Apparently, the valence band is similiar to that of Germanium and Silicon, with light and heavy hole bands[1.3]. Fig.1.1 shows the suggested band structure of InAs. A summary of the other relevant properties of InAs is given in Appendix F.

This project was begun* with the intention of depositing Indium Arsenide films and using them to fabricate insulted gate field effect devices. InAs was chosen because it has a high bulk mobility at room temperature which should make it suitable for device operation in the gigahertz region, while at the same time the bandgap is not too small so that the room temperature intrinsic concentration is below $10^{15}cm^{-3}$. The feasibility of such a device depends on several factors, but the most important is the need for a low surface state density. By choosing a suitable semiconductor-insulator combination together with appropriate annealing procedures, it should be possible to reduce this to an acceptable level. This, of course, involves a considerable amount of technology, and so in this project we have attempted only to demonstrate the possibility of fabricating such a device. The devices

---

* See Appendix G.1.

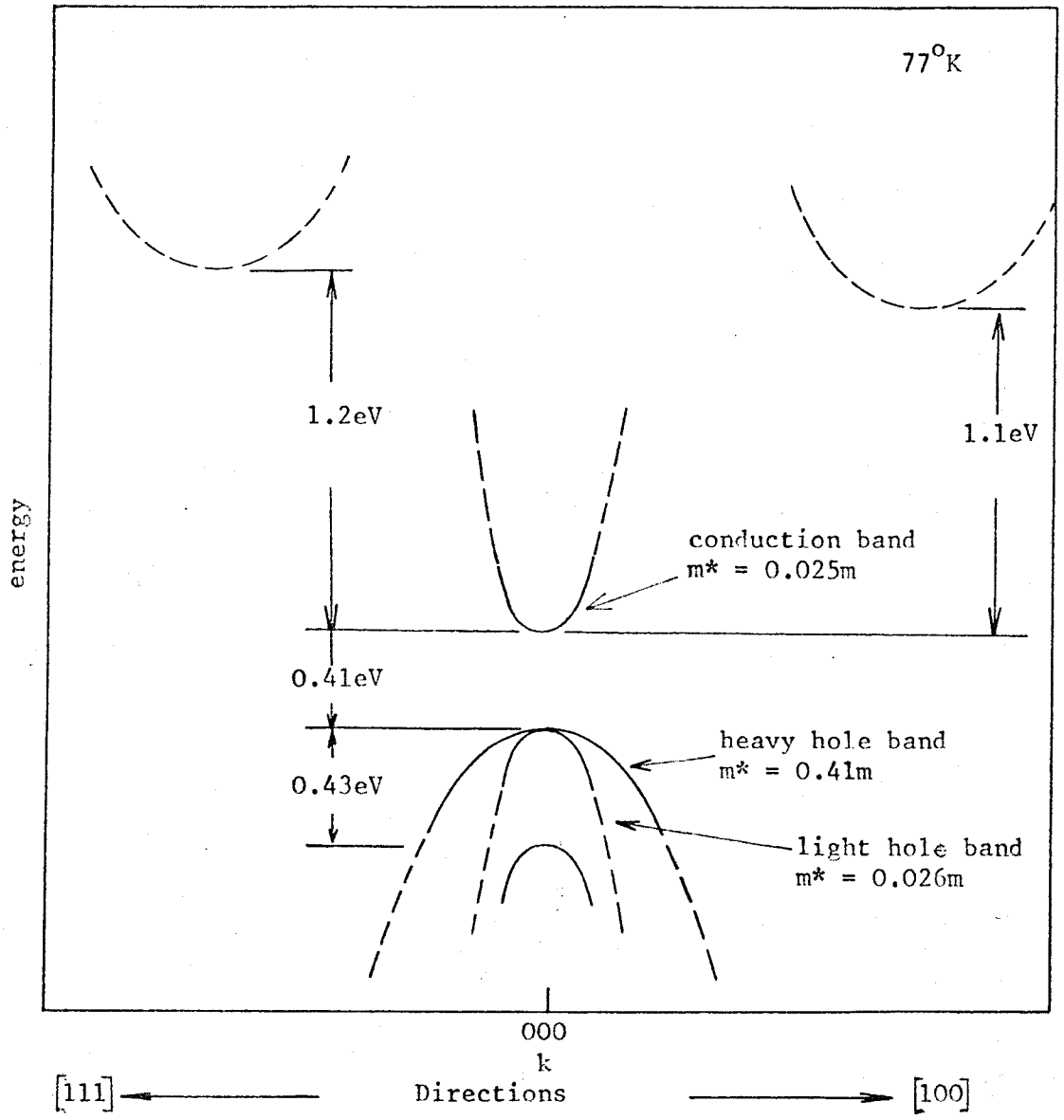

Fig.1.1

Suggested Band Structure Of Indium Arsenide

fabricated are similiar to Weimer's[1.4] thin film transistor but employ different fabrication procedures. These devices operate in the accumulation and depletion mode and do not require p-n junctions with their inherent capacitances, which degrade high frequency performance. Thus, with a particular mobility it should be possible to operate a thin film transistor at a higher frequency, than an inversion layer device using diffused source and drain contacts. The results of De Graff[1.5] using CdSe transistors appears to confirm this, since he obtained cut-off frequencies of 150Mc/s with channel mobilities of 50-100cm^2/V-s and a source-drain length of 10μm. However, it is essential to have good saturation characteristics for such operation.

Brody and Kunig[1.6] and Kunig[1.7] were the first to report the successful operation of a thin film transistor using polycrystalline InAs films. However, their devices were rather crude since they used metallic out of contact masks, but this permitted all depositions to be carried out in one pump-down, which is both rapid and less likely to cause contamination. These devices had cut-off frequencies of about 8Mc/s and they did expect operation in the gigarhertz region with a reduction in size, but this was not realised[1.8]. Page[1.9] has suggested that heat dissipation problems with glass substrates, which have a low thermal conductivity, can degrade the high frequency performance. However, the smaller source-drain spacing used by Kunig[1.7] resulted in poor saturation, which was probably the cause of the degradation. The

transistors we have fabricated on epitaxial InAs also do not saturate properly, but this could be improved by a reduction of the impurity concentration in the InAs film, and of source drain parasitic resistances.

Initially, we encountered considerable difficulties in depositing stoichiometric InAs films, hence the electrical properties of the early films were very poor. III - V compounds generally tend to dissociate when evaporated, therefore special techniques have to be employed to deposit the films. We have used the 'three temperature' method, developed by Gunther[1.10], which employs two independently controlled sources, one for each of the elements, and a suitable substrate temperature. It appears that only polycrystalline InAs has been deposited by Gunther[1.10,1.11] and other workers, using this method. We have deposited epitaxial InAs[1.12] on semi-insulating GaAs comparable to melt grown and epitaxial InAs deposited by chemical vapour deposition. All the films were n-type, no attempts being made to deposit p-type material.

Although chemical deposition methods are attractive for industrial applications, they usually require high temperatures with consequent auto-doping of the epitaxial layers, and the interfaces are often not very sharp. These are important factors when studying very thin films for use in field effect structures or in the study of hetero-junctions, which has received much attention recently. Evaporation also permits easy control of film thickness when very thin films are required. There is also a distinct possibility of extending the multi-

source method to deposit pseudo-binary alloys of the form, $(In_xGa_{1-x})As$, by employing three independently controlled sources. The variation of bandgap with composition is almost linear in such alloys, which should be useful for infra-red detectors.

III - V compounds, particularly InAs, in single crystal bulk form, are used extensively in such applications as Hall effect analogue multipliers and gaussmeters[1.13]. In order to get the required sample geometry, the single crystals must be ultra-sonically cut or sand blasted which is a time consuming process and not always successful. However, a photomechanical process can be used with thin films, followed by chemical etching, a method which is rapid and can give precise geometries. Also, for a given current, the Hall voltage in a thin film is much larger than that in a thick single crystal.

1.2. The Use Of Thin Films In Physical Investigations

Apart from the technological applications of thin films, they are an ideal tool for many physical investigations. The effect of the surface on the transport properties of the carriers can be studied by depositing films of various thickness, provided that auto-doping by the substrate is negligible. Most of the early studies have been on polycrystalline metal films, where it was found that the surface was a diffuse scatterer. However, more recent investigations with epitaxial Gold indicate that it has a specular surface[1.14,1.15]. Since the electron effective mass in most of the III - V compounds is small, the mean free path is large (in InAs $m^* = 0.025m$ and $\lambda = 3000\text{Å}$),

therefore the surface dominates the electron mobility even with a film thickness of the order of a micron or less. The small effective mass also implies a large electron wavelength, which should make the electron scattering insensitive to microscopic surface roughness, and may result in specular reflection. However, our results indicate a rapid fall in mobility with a reduction in thickness below a few microns in both epitaxial and polycrystalline InAs.

When the film thickness is of the order of the electron wavelength, quantization of the energy levels into sub-bands is believed to occur, due to quantization of the electron motion perpendicular to the surface. Blatt[1.16] has indicated that a spherical constant energy surface will be split into discs, as shown in Fig.1.2, the separation of which is inversely proportional to the number of inter-atomic spacings occupied by the film thickness. If this separation is large compared to the electron energy, the transport properties of the latter could be affected considerably.

Accumulation or inversion layers at the surface, induced by the field effect, will also give rise to this quantization because the carriers are confined in an even narrower potential well. The recent observations by Fowler et. al[1.17] of Shubnikov-de Hass oscillations in Silicon inversion layers, demonstrated for the first time the two dimensional nature of the electron transport. From the period of the conductance oscillations with gate field, they were able to calculate the electron effective mass, which fitted well with the bulk value.

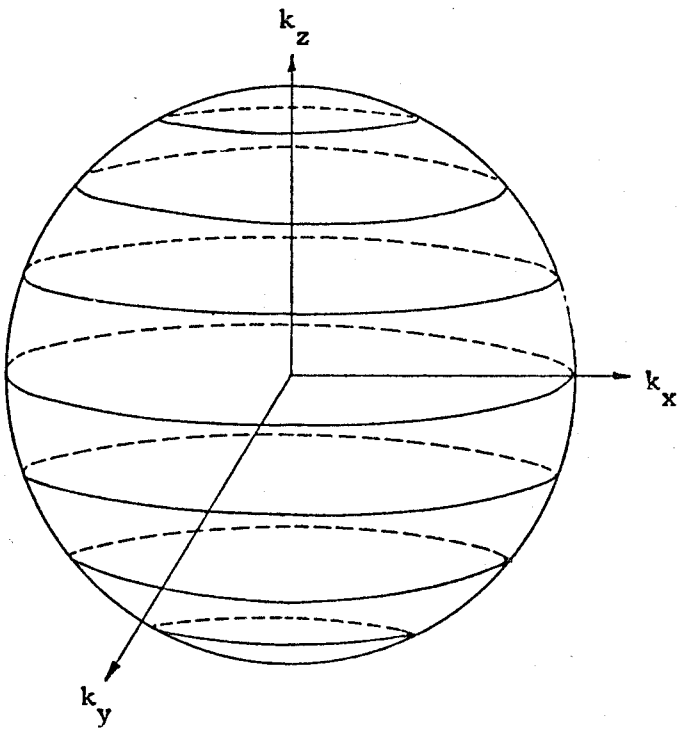

Fig.1.2

Quantization of energy states in a thin film with spherical constant energy surfaces

Murphy[1.18] has suggested that, since the low effective mass in III - V compounds indicates a low density of conduction band states, splitting of the energy levels into sub-bands could result in conduction electrons higher up the band, which may permit a study of the band structure of the material and may even result in a controlled Gunn effect type oscillator.

2.1. DEPOSITION METHODS

2.1.1. Introduction

Attempts to deposit III - V semiconducting compounds by evaporating the compound directly, result in layered films which are completely non-stoichiometric and, therefore, possess very poor electrical properties[2.1]. This is because there is a wide disparity in the vapour pressures of the two components of the compound at any particular temperature, so when the compound is heated the more volatile group V element evaporates preferentially and deposits on the substrate. As the temperature is raised further, the group III element then begins to evaporate and deposits on top of the volatile component. Flash evaporation and the "three temperature" method are two techniques which have been used to overcome this problem. These methods have been used to deposit both polycrystalline and epitaxial films, whereas the chemical transport methods to be described have been used to deposit epitaxial layers. In chapter 5, a comparison will be presented of the electrical properties of InAs films deposited by the various methods.

2.1.2. Chemical Vapour Deposition

The various continuous flow open tube systems used to deposit epitaxial GaAs can also be used for epitaxial InAs. The more common methods employ (i) Hydrogen Chloride, (ii) Water Vapour, as transport agents.

The first method has been used by Cronin et. al[2.2] and McCarthy[2.3, 2.4] to deposit epitaxial InAs. Fig. 2.1. is a schematic diagram of the HCl

system used by McCarthy. Pure hydrogen is bubbled through Arsenious Chloride which is then fed to one end of the tube in a three zone furnace. The reaction taking place in zone 1 is:

$$4AsCl_3+6H_2 \rightleftarrows As_4+12HCl$$

A boat containing Indium or InAs is placed in zone 2. If an Indium source is used, it must be saturated with Arsenic before transport of the latter can take place to zone 3. McCarthy found that this could take a considerable length of time during which the Indium source was depleted, so he used InAs, instead, as the source (Cronin et. al overcame this problem by using a separate Arsenic source). Apparently the reaction taking place in zone 2 is:

$$4InAs+4HCl \rightleftarrows 4InCl+As_4+2H_2$$

Finally, the reaction in zone 3 where the substrate is placed is probably given by:

$$6InCl+As_4 \rightleftarrows 4InAs+2InCl_3$$

$InCl_3$ is deposited on the tube walls beyond zone 3, which can be a separate (dump) tube to facilitate cleaning. Doping of the layers can be achieved by using an appropriately doped InAs source.

The furnace zone temperatures shown in Fig. 1 are those used by McCarthy[2.4]. In order to obtain good epitaxial layers he found it essential to etch the substrate by raising its temperature above the source temperature for about ten minutes before the deposition; transition to growth conditions had to be made at a maximum cooling rate of $2^{\circ}C$/min.

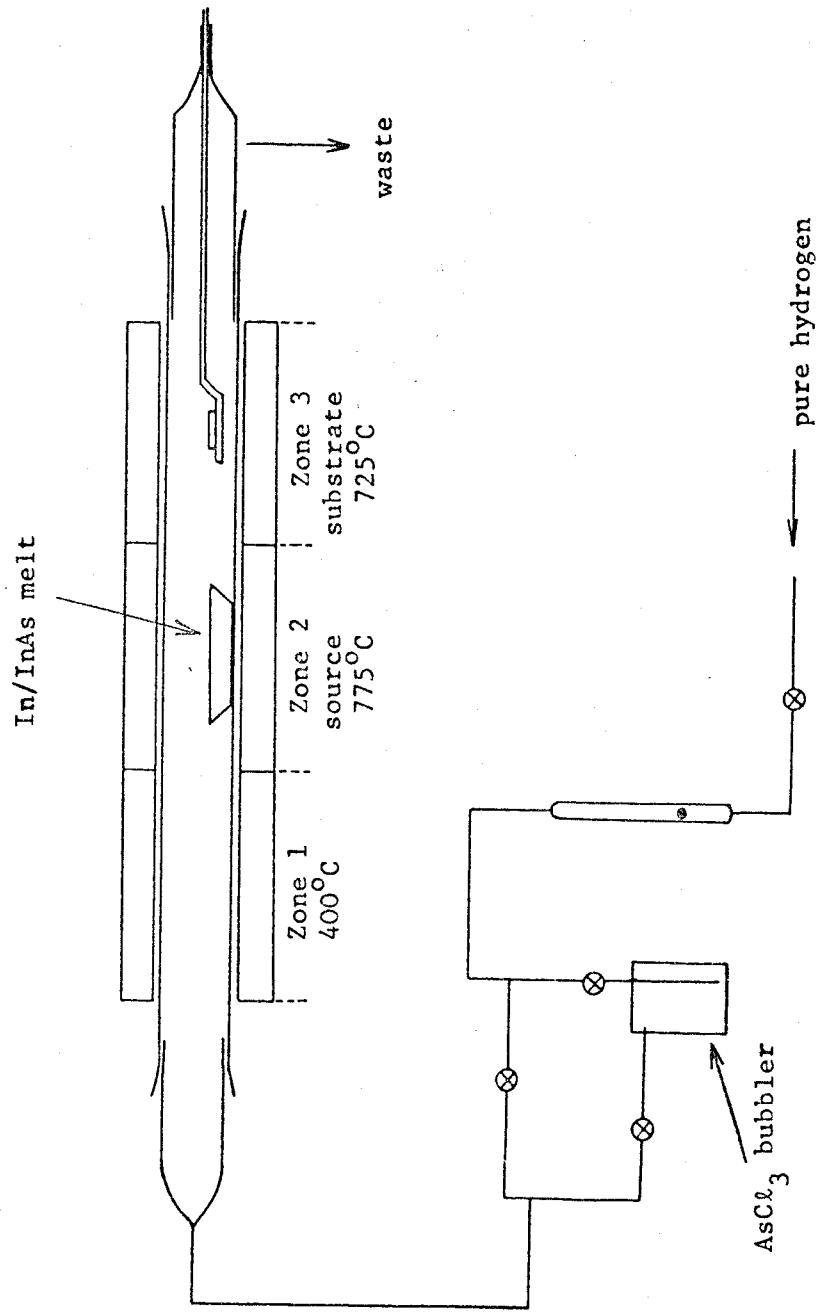

Fig.2.1.

Schematic Diagram Of Chemical Vapour Deposition System

Cronin et. al used {100}, {111}A and {111}B ± $\frac{1}{2}^{o}$ semi-insulating GaAs substrates and found the {100} orientations gave the best crystalline structure and highest growth rate, in the region of 0.5μm/min. McCarthy found no difference in the properties of films on {100} and {110} orientations of GaAs.

A closed spaced technique using water vapour as the transporting agent has been used by Robinson[2.5] to deposit GaAs. The reaction appears to proceed as follows:

$$2GaAs+H_2O \rightleftarrows Ga_2O+H_2+As_2$$

Robinson also mentions that he has used this method to deposit epitaxial InAs and InP but gave no details of the quality of these layers.

2.1.3. Liquid Epitaxy

Liquid epitaxy[2.6] of InAs on an InAs substrate has been employed by Brown and Porteous[2.7] to fabricate laser diodes. A melt of pure Indium with about 3% by weight of InAs is placed in a silica boat together with the InAs substrate. The boat is placed in a furnace which is tilted at a small angle from the horizontal so that the melt is at one end, and the substrate at the other end. With the furnace at approximately 470°C, the melt is tilted onto the substrate and the temperature lowered to 300°C at about 4°C/min, thus promoting the InAs growth. When the desired layer thickness is reached the melt is tipped off the substrate. Doping of the epitaxial layers can be achieved by adding an appropriate amount of dopant to the melt.

Brown and Porteous have given no details of the electrical properties of their epitaxial layers, except that the layers were doped to give 10^{19} carrier/cc, which was required for laser operation. Apparently, epitaxial GaAs grown by this method usually has inferior electrical properties[2.8] and the layer surfaces are usually rough, containing an excess of Gallium. The advantage of this method is its simplicity and the high growth rates that can be achieved. Recently, however, Harris and Snyder[2.41] claim that they have obtained high quality epitaxial GaAs by this method, having mirror smooth surfaces and very uniform doping, for use in Gunn devices.

2.1.4. Flash Evaporation

This method was originally devised by Harris and Siegel[2.9] to deposit alloy films and more recently used by Richards et. al[2.10] to deposit III - V compounds.

A powder of the compound, or a mixture of the components in the correct proportions, is allowed to fall grain by grain onto a hot boat, which vapourises all the constituents of the powder rapidly. A grain following on the boat will result in the volatile group V element evaporating first, followed by the group III component. If the powder delivery is rapid, there will be several grains in the boat at any particular instant which are at different stages of decomposition. Providing the powder feed is at a continuous and uniform rate and no material accumulates in the boat then the vapour which impinges on the substrate has the same composition as the powder, resulting in

a stoichiometric film. Small fluctuations in grain delivery may result in inhomogeneties, but this can be overcome by adding an excess of the group V element to the powder. This will provide an excess of the volatile component at the substrate so that no unreacted group III element deposits, and providing the substrate is heated to a suitable temperature, no free group V material will condense on it. Doped films can be deposited by inserting the appropriate amount of dopant in the powder. Richards et. al[2.10] and Richards[2.11] have used this method to deposit various III - V compounds, particularly InSb and GaAs, epitaxially, but have given very few details of their electrical properties. Juhasz and Anderson[2.12] have used this method to deposit InSb on mica, but it appears they did not obtain epitaxy. Recently, Vlasov and Semiletov[2.13] have deposited InAs and InSb by flash Evaporation. Apparently, their films usually had an excess of Indium on the surface, giving it a rough appearance.

It appears that the disadvantage of the flash evaporation method is the poor control of evaporation rate. Presumably, this is achieved by varying the rate of grain delivery together with an appropriate change in boat temperature, so that the number of grains in the boat remains constant.

2.1.5. Three Temperature Method

This method was originally developed by Günther[2.14,2.15,2.16,2.17] to deposit various III - V compounds.

Basically, two independently controlled sources are used, one for each component of the compound. The temperatures of these

sources are maintained such that there is an excess of the volatile group V element over the group III element at the substrate surface. Providing the substrate temperature is sufficiently high the group V material will deposit only if it forms a stoichiometric compound with the group III material, any excess material re-evaporating. However, there is an upper limit on the substrate temperature, above which the volatile component begins to evaporate preferentially, leaving an excess of the non-volatile component. The process of film formation is aided by the self-stoichiometry of III - V compounds.

Following Günther[2.18], we calculate the upper and lower limits of substrate temperature, at a particular deposition rate, that will result in a stoichoimetric compound.

The number of atoms (molecules), R+i, impinging on a substrate which is at a distance r_o from a point source is:

$$R_{+i} = P_i(2\pi M_i kT_i)^{-\frac{1}{2}} A_o/\pi r_o^2 \text{ cm}^{-2}\text{sec}^{-1} \quad \ldots(2.1)$$

where the subscript represents the component, i, of the compound and,

P_i vapour pressure above the source

M_i atomic (molecular) weight

T_i temperature of source

A_o effective evaporation surface

The angle dependency of the source is neglected, since it is assumed that the angle subtended at the substrate is small.

The film growth rate will be controlled by the impingement rate of the less volatile component. Therefore, for a certain film

growth rate, the impingement rate of the group III element is fixed. Knowing the vapour pressure-temperature relationship for the particular element[2.19], it is then possible to calculate P_{III} and T_{III}. The impingement rate for the group V element is given an excess by a factor of about ten and P_V and T_V can then be calculated similarly.

Now, the rate of desorption from the substrate is:

$$R_{-i} = P_{ei}(2\pi M_i kT)^{-\frac{1}{2}} \text{ cm}^{-2}\text{sec}^{-1} \quad \ldots(2.2)$$

where P_{ei} is the equilibrium vapour pressure of component i, at the substrate temperature T.

If the group V element is not to deposit on its own, then $R_{-V} = R_{+V}$, using (2.1) and (2.2), this gives:

$$P_{eV} = \frac{A_o P_V}{\pi r_o^2}\left\{\frac{T}{T_V}\right\}^{\frac{1}{2}} \quad \ldots(2.3)$$

Since P_V, T_V and r_o are known, it is possible to plot P_{eV} vs T. The intersection of this with the equilibrium vapour pressure-temperature curve of this element will give the substrate temperature, T_{min} above which free group V material will not deposit.

The upper temperature limit is set by the dissociation pressure of the group V element above the compound (such curves have been published by Goldfinger and Jeunehomme[2.20] and Renner[2.21] for III - V compounds). The intersection of equation 2.3 with the appropriate dissociation pressure curve will give T_{max} the temperature above which the volatile component will evaporate preferentially, resulting in an excess of the non-volatile component. A detailed calculation

for the case of InAs will be given in chapter 3, which shows that there is a wide region of substrate temperature at which stoichiometry can be achieved. However, in practice it is necessary to use the highest possible temperature to obtain good quality films.

Some of the advantages of the "three temperature" method are:

1. Temperature control of the two sources is not critical.
2. Film growth occurs under quasi-equilibrium conditions, thus enhancing epitaxy.
3. Stoichiometry can be achieved with substrate temperatures higher than that permitted with flash evaporation, which is important if epitaxy is to be attempted.

It should be possible to deposit doped layers by using the appropriate depant in a separate reservoir source, similar to the method used by Ito et. al[2.22] to deposit doped epitaxial silicon.

Deposition of pseudo-binary alloys of the form $In_xGa_{1-x}As$ should be possible using three independently controlled sources, the composition being controlled by the In/Ga ratio. It appears all the III - V compound films deposited by Günther and other workers[2.23, 2.24], using this method, have been on amorphous substrates, which result in polycrystalline films. Johnson[2.24] used Sapphire substrates, but apparently did not obtain epitaxy. Noteworthy, is the work of Deklerk and Kelly[2.25], who used this method to deposit CdS films on glass with the c axis perpendicular to the substrate plane.

The only published work on the use of the "three temperature" method to deposit epitaxial layers is by Davey and Pankey[2.26], who deposited GaAs on Ge substrates, and Steinberg and Scruggs[2.27] who

deposited GaAs on NaCℓ, in a conventional high vacuum plant. Davey and Pankey employed a system similar to that of Gunther's, in which the vacuum chamber is a silica tube with the two evaporation sources connected to the side walls of the tube and the temperatures monitored by thermocouples. In order to eliminate contamination from glass sealing operations, they used metal flanges and viton gaskets to seal the entrance port. An elaborate process of cleaning, ion bombardment and annealing of the substrates was employed to remove contamination and damage. Extremely low deposition rates, less than 100 A^{o}/min, were used in order to avoid condensation of free gallium. Their electron diffraction patterns indicate considerable twinning in their films. Similarly the electron diffraction results of Steinberg and Scruggs[2.27] indicate their GaAs films to be highly defective. No details of electrical properties were given by either of these workers.

2.2. NUCLEATION, GROWTH AND EPITAXY

2.2.1. Introduction

The sequence of growth of a thin film on a substrate may be summarised as follows:

1. The formation of a surface distribution of small three dimensional nuclei. These critical nuclei may consist of only a few atoms (molecules) or more, depending on the particular interface.
2. The growth in size of these nuclei, without any increase in their numbers, by the addition of monomers through surface diffusion.
3. Further increase in the size of these nuclei or islands, accompanied by the coalescence of neighbouring islands and, hence, a gradual decrease in their numbers.
4. The formation of a connected network of deposits, which develops rapidly into a channelled structure.
5. A continuous deposit film free of holes.

The contribution of nucleation to epitaxy is very important, and so in this section we attempt to find, qualitatively, the conditions necessary for epitaxial nucleus formation. No attempt will be made to calculate the specific values of the deposition parameters, since this would require a knowledge of the various interfacial energies and surface diffusion and desorption energies, for our particular system.

We assume we are dealing with a uniary vapour, in order to simplify the analysis. This is justifiable for our system, since it is most probable that in the case of a compound the process of surface diffusion

and addition to the nuclei occurs by compound molecules, rather than the separate components. This is because the interaction rate of the impinging atoms of the two elements is much more rapid (and greater), than the nucleation rate. Later, we attempt to obtain, again qualitatively, the conditions necessary for compound formation.

2.2.2. The Role Of Nucleation In Epitaxy

Experimental evidence indicates that coherent nucleation is not essential, in order to obtain epitaxy. According to Bassett et. al[2.28] and Pashley[2.29], epitaxy may also result from, either semi-coherent or incoherent nucleation. (A coherent interface has perfect one-to-one matching between the substrate and deposit and usually occurs with low index planes. An interface is said to be semi-coherent if there is one-to-one matching over most of the contact area, but which has some interface dislocations.) The critical requirement for epitaxy is that a particular orientation has (i) a lower free energy of formation, ΔG^*, and therefore has a much higher nucleation rate than any other modification, (ii) is characterised by a state of binding and of position on the surface conducive to a high rate of growth.

Coalesing nuclei with small mis-orientations (less than a degree) have been observed to undergo a process of rotation by which they orient themselves exactly with each other[2.29]. However, if the nuclei have large mis-orientations this will result in permanent defects, particularly dislocations and grain boundaries. Thus the need for single orientation nuclei, if good epitaxy is to be achieved.

2.2.3. Heterogeneous Nucleation Theory

The two approaches to nucleation theory are based on (i) a capillarity model (ii) an atomistic model. The first assumes a cap-shaped nucleus, which is part of a sphere, with bulk thermodynamic properties. This model is satisfactory for experimental conditions in which the critical nucleus is large, i.e. greater than 50 - 100 atoms. In some systems, the critical nucleus can contain only a few atoms, and is it is desirable to use the atomistic model[2.31,2.32], which does not depend on macroscopic parameters. However, this theory is still at an early stage, and has not yet been employed to obtain quantitative information, so the capillarity model will be used here.

The mechanism of nuclei formation is as follows. Atoms from the vapour phase strike the surface and either immediately rebound, or are thermally equilibrated and are adsorbed, provided the vapour is super-saturated with respect to the bulk solid phase. These adsorbed atoms (adatoms) diffuse at random over the surface and form small clusters, which grow and decay by the addition or loss of single atoms. Energitically formation of a cluster is unfavourable until it exceeds a certain size, afterwhich growth proceeds rapidly.

The nucleation rate, J, is the rate at which monomers are added to the critical nuclei, and is given by[2.30]

$$J = \omega n^{*} Z \Gamma \qquad \ldots(2.4)$$

where ω is a frequency factor for the addition of monomers to the critical size nucleus,

n^{*} is the number of critical nuclei/unit area,

Z is the Zeldovich non-equilibrium factor,

Γ is the Lothe-Pound correction factor.

The frequency with which single atoms join a critical nucleus to promote it to a stable growing nucleus may occur either by direct addition from the vapour, or by surface diffusion of an adatom, as mentioned earlier. Apparently the latter process is more rapid by a factor $\exp\{\frac{\Delta G_{des}-\Delta G_{diff}}{kT}\}$ where ΔG_{des} and ΔG_{diff} are the free energies of activation for desorption and surface diffusion, respectively, of adatoms. We may assume $\Delta G_{des} >> \Delta G_{diff}$ for our system, hence addition by surface diffusion is the dominant mechanism. Now the probability that an adatom is adjacent to a critical nucleus is given by, $n_s 2\pi r^* a_o \sin\theta$, where n_s is the surface concentration of adatoms, r^* is the radius of the critical nucleus, a_o is the jump distance, and θ is the angle of wetting of the cap shaped nucleus (see Appendix A, Fig. A2). The frequency at which an adjacent adatom will jump to join the nucleus is $\nu\exp(-\Delta G_{diff}/kT)$, ν being the lattice vibration frequency.

ω is then given by:

$$\omega = n_s 2\pi r^* a_o \nu \sin\theta \exp\{-\Delta G_{diff}/kT\} \qquad ...(2.5)$$

The concentration of critical nuclei is:

$$n^* = n_s \exp(-\Delta G^*/kT) \qquad ...(2.6)$$

where ΔG^*, the Gibbs free energy of formation of a critical nucleus derived in Appendix A, is:

$$\Delta G^* = \left[16\pi\sigma_{c-v}^3 / 3\Delta G_v^2\right] f_1(\theta) \qquad ...(2.7)$$

σ_{c-v} is the condensate-vapour interfacial free energy/unit area, which is assumed to be isotropic, hence a spherical cap. The driving force for the phase transformation is ΔG_v, Gibbs free energy change/unit volume, associated with the transformation of the adsorbed atoms to the crystalline embryo. In terms of super-saturations, it is given by:

$$\Delta G_v = -\left(\frac{kT}{v}\right)\ln(P/P_e) \qquad \ldots(2.8)$$

P is the super-saturated vapour, P_e the equilibrium vapour pressure and v the atomic (molecular) volume.

$f_1(\theta)$ is the geometrical function given by (Appendix A):

$$f_1(\theta) = \frac{2-3\cos\theta+\cos^3\theta}{4} \qquad \ldots(2.9)$$

The Zeldovich non-equilibrium factor, Z, takes into account the loss of critical nuclei, both by promotion to super-critical size and by decomposition to become sub-critical embryos and is given by[2.33]:

$$Z = \left\{\frac{\Delta G^*}{3\pi kTi^{*2}}\right\}^{\frac{1}{2}} \qquad \ldots(2.10)$$

where i^* is the number of monomers in the critical nucleus. In the usual experimental case, this correction factor is not large, and so in order to simplify the analysis, we neglect it.

The Lothe-Pound factor, Γ, is a statistical mechanical correction to the free energy of formation of the critical nucleus. It takes into account the number of complexions that arise from the distribution of adsorbed atoms, n_s, among the n_o sites on a solid substrate lattice. In the normal experimental case $n_o >> n_s$, so the contribution to the

free energy of formation of the critical nucleus can be approximated[2.30] to:

$$\Delta G_q = -kTIn(n_o/n_s) \qquad \ldots(2.11)$$

and

$$\Gamma = e^{-\frac{\Delta G_q}{kT}} = \frac{n_o}{n_s} \qquad \ldots(2.12)$$

The surface concentration of monomers can be expressed as:

$$n_s = R\tau_s\left[1-\exp(-t/\tau_s)\right] \qquad \ldots(2.13)$$

t is the time of exposure, the impingement rate is given by:

$$R = \frac{P}{(2\pi MkT_p)^{\frac{1}{2}}} \qquad \ldots(2.14)$$

where T_p is the equilibrium temperature of transformation at the pressure of interest, and τ_s, the residence time is:

$$\tau_s = \frac{1}{\nu}\exp\left(\frac{\Delta G_{des}}{kT}\right) \qquad \ldots(2.15)$$

ΔG_{des} is the free energy of activation for desorption of adsorbed atoms.

Experimentally $t >> \tau_s$ so n_s is given by:

$$n_s = \frac{P}{(2\pi MkT_p)^{1/2}\nu}\exp\left(\frac{\Delta G_{des}}{kT}\right) \qquad \ldots(2.16)$$

Substituting equations 2.5, 2.6, 2.7, 2.12, 2.16 in equation 2.4, the nucleation rate can be expressed as follows:

$$J = \frac{-4\pi a_o n_o \sigma_{e-v}}{(2\pi MkT_p)^{\frac{1}{2}}} \cdot \frac{P}{\Delta G_v} \cdot \sin\theta\exp\left[\frac{\Delta G_{des}-\Delta G_{diff}}{kT}\right] \times \exp\left[\frac{-16\pi\sigma_{e-v}^{3}}{3kT\Delta G_v^{2}} f_1(\theta)\right] \qquad \ldots(2.17)$$

Following Moazed[2.50], we can express this in the form:

$$J = \alpha \sin\theta \exp\{-\beta f_1(\theta)\} \qquad \ldots(2.17)$$

where

$$\alpha = -\frac{4\pi a_o n_o \sigma_{c-v}}{(2\pi M k T_p)^{\frac{1}{2}}} \cdot \frac{P}{\Delta G_v} \cdot \exp\left[\frac{\Delta G_{des} - \Delta G_{diff}}{kT}\right] \qquad \ldots(2.18)$$

$$\beta = \frac{16\pi \sigma_{c-v}^{3}}{3kT\Delta G_v^{2}} \qquad \ldots(2.19)$$

Equation 2.17 is the general nucleation rate equation. For a particular substrate-vapour system, the nucleation rate is a function of the substrate temperature, T, and the vapour pressure, P, of the impinging atoms and, therefore, also on ΔG_v and the contact angle θ.

2.2.4. Heterogeneous Nucleation Theory Applied To Epitaxy

In order to achieve epitaxy, the majority of growing nuclei must be aligned in one orientation and have a high growth rate. In the following two sections the nucleation rate equation will be used to understand basically, the effects of super-saturation and substrate temperature variations in the epitaxial nucleus formation.

Following Moazed[2.50], we can express equation 2.17 as follows:

$$\ln\alpha/J = \ln\alpha_1 = \beta f_1(\theta) - \ln\sin\theta \qquad \ldots(2.20)$$

J is set to a constant, which is just measurable, the value depending on the method of measurement. By differentiating the R.H.S. of equation 2.20 with respect to θ and equating to zero, we obtain the value of θ at the minimum of equation 2.20. For a particular value of β this is:

$$\beta_{\theta min} = \frac{4\cos\theta}{3\sin^4\theta} \qquad \ldots(2.21)$$

This indicates that with β decreasing, the minimum occurs at a higher θ value. The R.H.S. of equation 2.20 is plotted in Fig. 2.2 as a function of θ for various β values.

2.2.5. Effect Of Super-Saturation Changes On Epitaxy

The ratio (P/P_e) is a good representation of the super-saturation, since P is the pressure due to the impingement flux and P_e is the equilibrium pressure at the substrate temperature T, which we set to a constant value.

We can express α and β in terms of P/P_e using equation 2.8 for ΔG_v:

$$\alpha_1 = \frac{\alpha}{J} = \frac{4\pi a_o n_o \sigma_{c-v} v}{(2\pi M k T_p)^{\frac{1}{2}} J k T} \cdot \frac{P}{\ln(P/P_e)} \cdot \exp\{\frac{\Delta G_{des} - \Delta G_{diff}}{kT}\}$$

$$= K_1 \cdot \frac{P}{\ln(P/P_e)} \qquad \ldots(2.22)$$

$$\beta = \frac{16\pi v^2 \sigma_{c-v}^3}{3k^3T^3\{\ln(P/P_e)\}^2} = \frac{K_2}{\{\ln(P/P_e)\}^2} \qquad \ldots(2.23)$$

where K_1 and K_2 are constants at a particular substrate temperature.

Any increase in P above P_e will increase α_1, therefore $\ln\alpha_1$, which can be represented by a straight line in Fig. 2.2, will rise from a low value. At the same time β decreases, but since β is large and α_1 small, the $\ln\alpha_1$ line will not intersect the appropriate β curve and no measurable nucleation will take place. As P/P_e is increased further there will be a point when the α_1 line just intersects the

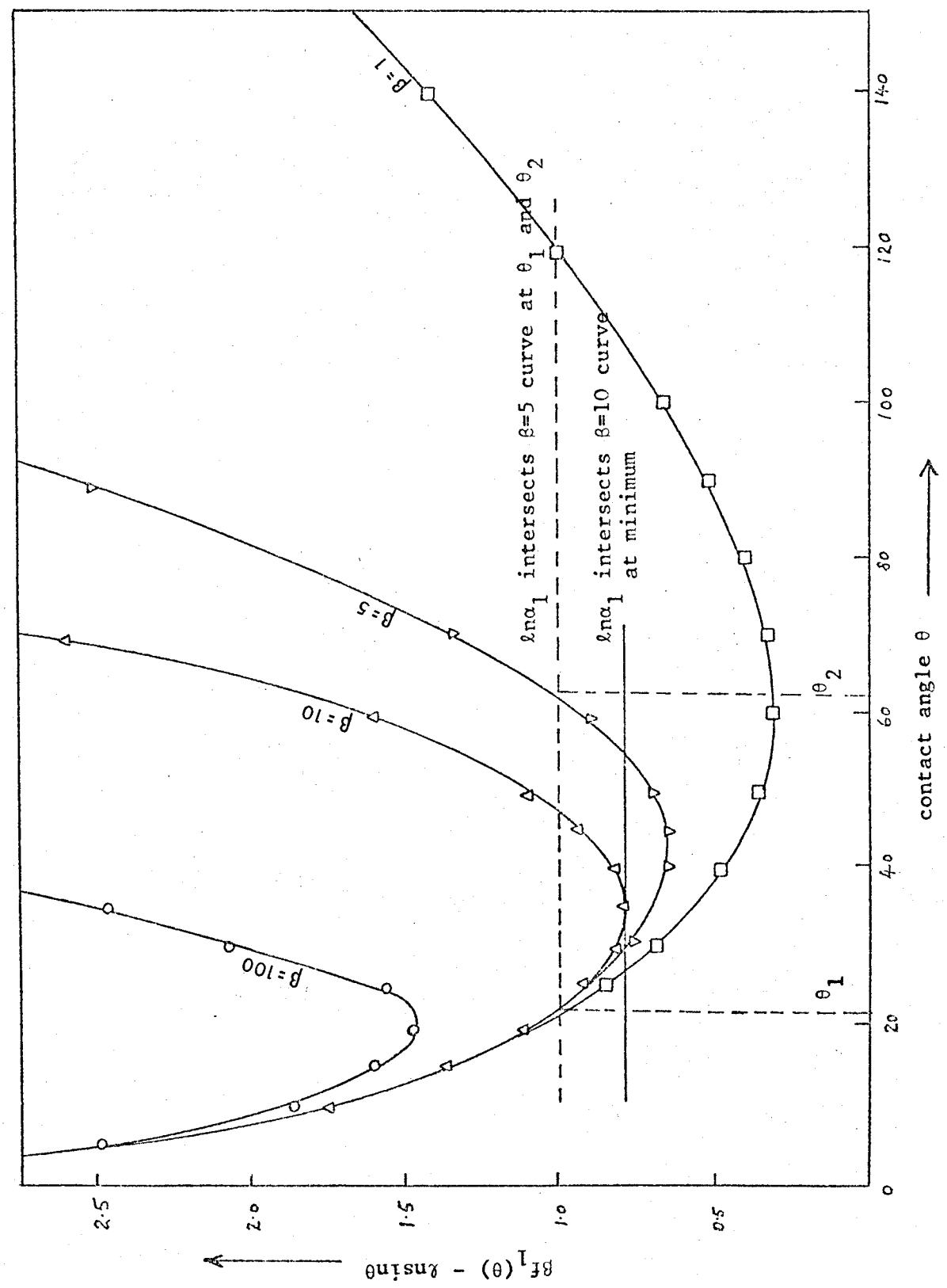

Fig.2.2.

$\beta f_1(\theta) - \ln\sin\theta$ as a Function Of θ

appropriate β curve and the nucleation rate will rise rapidly. This is the critical super-saturation, $(P/P_e)_{crit}$, and the critical nucleus will have a single θ value. This value of (P/P_e) will be the critical value only if the substrate surface has sites which, energetically, correspond to the θ values at the point of tangency.

Some substrates may have none or very few such sites, and so the super-saturation would have to be increased to give a reasonable nucleation rate. This would cause the $\ln\alpha_1$ line to intersect the appropriate curve at two different θ values, θ_1 and θ_2, as shown by the broken line in Fig. 2.2, making all sites on the surface corresponding energetically to θ values between these two points, potential nucleation sites.

Now, from equation A.5, $\cos\theta = (\sigma_{s-v}-\sigma_{c-s})/\sigma_{c-v}$. Assuming σ_{s-v} and σ_{c-v}, the interfacial energies of the substrate-vapour and condensate-vapour, respectively, are constant, then θ is a minimum when σ_{c-s} is a minimum, which is the case when the nucleus is in the epitaxial orientation. Therefore, at low super-saturations, ideally a P/P_e value corresponding to a single θ value, the nuclei should all be oriented correctly, resulting in epitaxy. However, at high super-saturations random nucleation, corresponding to a range of θ values, destroys the epitaxy.

2.2.6. Effect of Substrate Temperature On Epitaxy

We now maintain the impingement flux constant and vary the substrate temperature. ΔG_v can be expressed in terms of substrate temperature as follows:[2.50]

$$\Delta G_v = \Delta H_v\left\{\frac{T_p - T}{T_p}\right\} \qquad \ldots(2.24)$$

ΔH_v is the enthalpy associated with the vapour to solid transformation at the pressue of interest, and T_p is the equilibrium temperature of transformation at the pressure of interest.

Using equation 2.24 we can expess β as follows:

$$\beta = \frac{16\pi\sigma_{c-v}^3 T_p^2}{3kT\Delta H_v (T_p - T)^2} = \frac{K_3 T_p^2}{T(T_p - T)^2} \qquad \ldots(2.25)$$

K_3 is a constant at a particular pressure P. This expression is plotted in Fig. 2.3 (a).

At a particular evaporation rate, and therefore, pressure P at the substrate surface, lowering the substrate temperature will increase the super-saturation. Now, in the last section we concluded that low super-saturations are required for epitaxy. Therefore we must work with substrate temperature well above the minimum of β in Fig. 2.3a. Also, since the super-saturation ratio must be greater than unity, the branch of the curve we are interested in is below T_p. (The super-saturation is unity at $T = T_p$). Therefore, in this region of temperatures, marked X in Fig. 2.3, a decrease in substrate temperature will cause a decrease in β.

Again using equation 2.24, α_1 can be expressed:

$$\alpha_1 = \frac{K_4 P}{J\Delta H_v} \cdot \frac{T_p}{T_p^{\frac{1}{2}}(T_p - T)} \cdot \exp\left\{\frac{\Delta G_{des} - \Delta G_{diff}}{kT}\right\} \qquad \ldots(2.26)$$

where K_4 is a constant for a particular system.

One would expect that in the case of a crystalline substrate ΔG_{des} is large and the residence time is long. The evidence also indicates

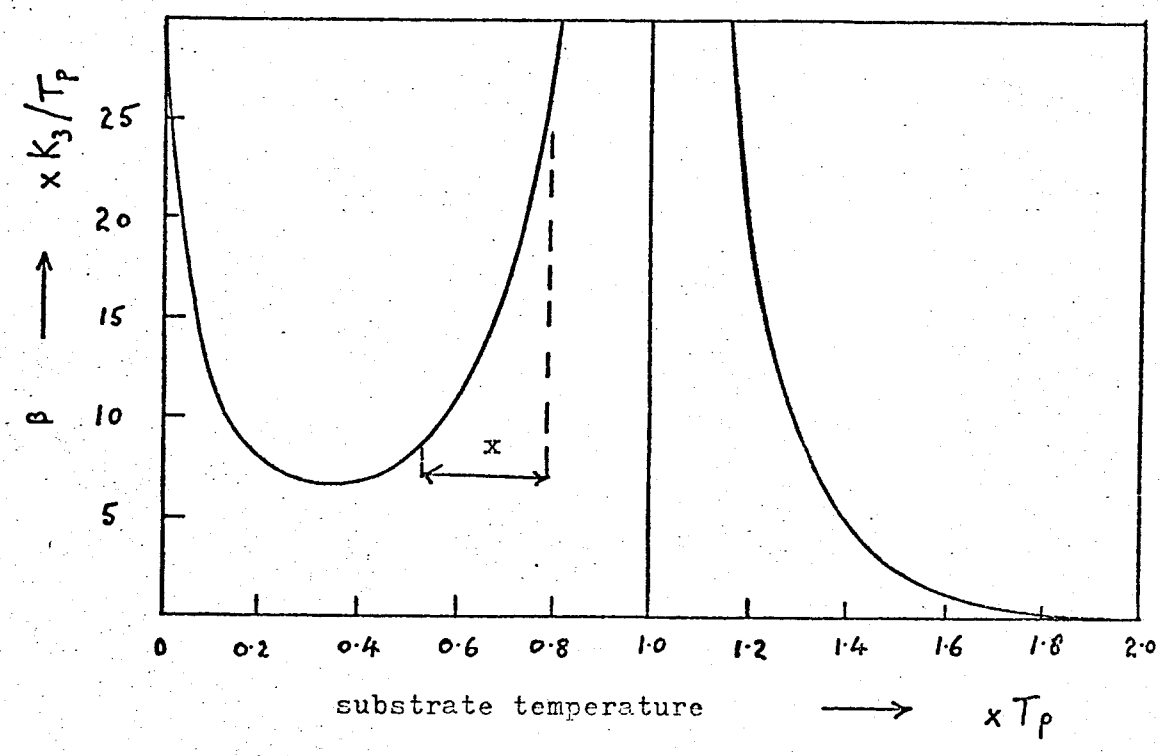

(a) Variation of β with substrate temperature at a constant impingement flux

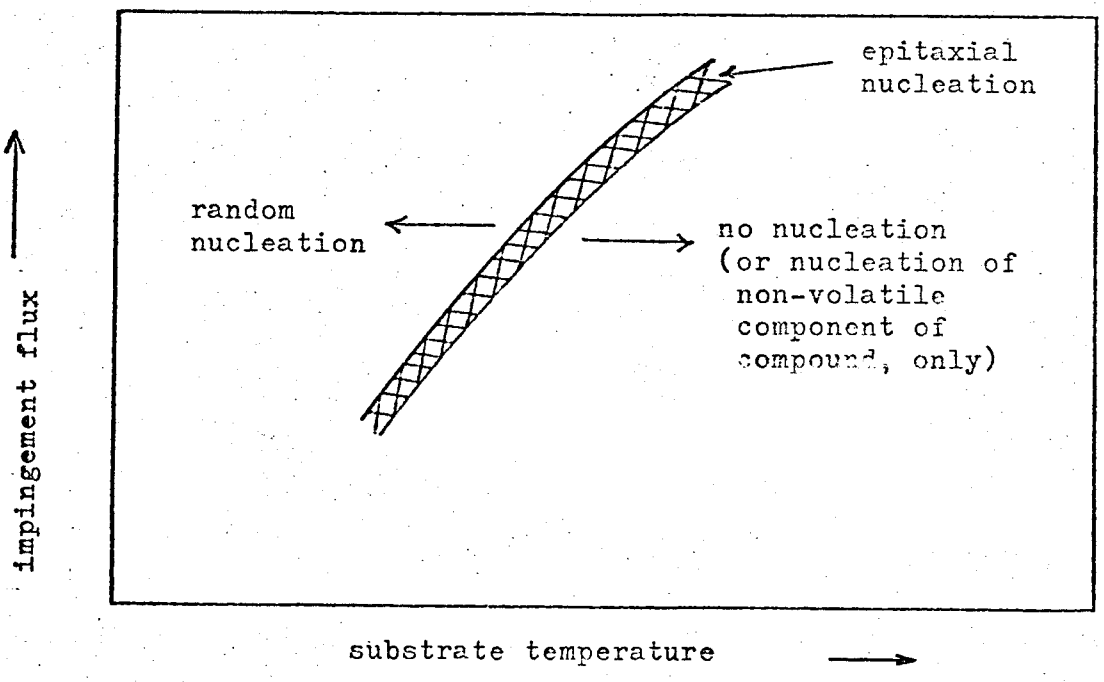

(b) Predicted relationship between impingement flux and substrate temperature, defining epitaxial region

Fig.2.3

that the adatoms are highly mobile, hence a low surface diffusion energy. Thus $(\Delta G_{des} - \Delta G_{diff})$ is positive, and therefore, a decrease in substrate temperature will increase the exponential term in equation 2.26. The pre-exponential will decrease with a decrease in substrate temperature in the region of interest. However, the exponential term should dominate causing α_1 to increase.

Now assume the impingement flux and substrate temperature are set so that the $\ln\alpha$ line intersects the appropriate β curve in Fig.2.2, at or near the minimum, thus favouring epitaxy. A decrease in temperature will raise the $\ln\alpha_1$ line, which will intersect a lower value β curve at two widely separated points. Following the earlier arguments, this would destroy the epitaxy. Since α_1 and β are moving in opposite directions, it would appear that the change from epitaxial to random nucleation can occur very rapidly, i.e. with a very small decrease in substrate temperature.

It should be mentioned here that there may be small differences in the values of the interfacial energies, and in a_o and n_o, of the various low index orientations of a particular material. This could result in small changes in the substrate temperature and/or super-saturations required for epitaxy on the various orientations.

Since the impingement flux and the substrate temperature both affect the super-saturation ratio, it may appear that varying either of these two parameters has the same effect on nucleation and epitaxy. However, it must be remembered that the substrate temperature also affects drastically the surface diffusion of adatoms.

We may conclude that, at a particular impingement flux epitaxy will be encouraged with substrate temperatures at or near the highest temperature at which nucleation just takes place. The above theory also predicts that to maintain epitaxy any increase in impingement flux must be accompanied by an increase in substrate temperature in order to keep the super-saturation ratio constant, but this is valid only within a limited range of temperatures. Graphically, this can be represented by plotting the impingement flux as a function of substrate temperature over which epitaxy occurs, as shown in Fig.2.3(b). The reason for the band of temperatures, is that epitaxy may still be obtained below the 'epitaxial temperature' provided $\theta_1 - \theta_2$ is small, since re-orientation of the nuclei can occur at the coalescence stage. Temperatures below the lower limit will result in increasing random nucleation and above the upper limit in no nucleation. However, with a III - V compound, for example, temperatures above the upper limit correspond to nucleation of the non-volatile component only, since the residence time of the volatile component is very short.

Recently, Kenty and Hirth[2.42] have used the capillarity model to calculate the conditions for the epitaxy of silver. However, they approached the problem by calculating the ratio of epitaxial to random nucleation, assuming as we have done above, that the inter-facial energy is a minimum when the nuclei are orientated correctly for epitaxy. Qualitatively, both these approaches come to the same conclusions regarding epitaxy.

2.2.7. Lattice Misfit, Strain and Pseudomorphism

The disregistry δ, between two lattices is defined in terms of lattice misfit $\Delta\lambda$, as:

$$\delta = \left| \frac{\Delta\lambda}{\lambda_1} \right| \qquad \ldots(2.27)$$

where $\pm\Delta\lambda = \lambda_1 - \lambda_2$, λ_1 is the lattice parameter of the substrate interface plane and λ_2 that of the deposit material with the same interface plane.

The strain in the nucleus is given by:

$$\varepsilon = \left| \frac{x-\lambda_2}{\lambda_2} \right| \qquad \ldots(2.28)$$

where x is the lattice parameter of the nucleus interface plane.

It has been postulated[2.34] that the interfacial energy between two phases is a minimum when they are in perfect registry across their boundary. This implies that any misfit between the lattices must be taken up by strain in the condensing lattice, i.e. $\varepsilon = \delta$. However, if $\varepsilon < \delta$, the actual disregistry is equal to $(\delta - \varepsilon)$. The interfacial energy may then be represented by[2.30]:

$$\sigma'_{c-s} = \sigma^{o}_{c-s} + \eta(\delta-\varepsilon) \qquad \ldots(2.29)$$

where η is a constant and σ^{o}_{c-s} is the term due to bond type.

The strain energy is given by $C_1\varepsilon^2$, where C_1 is the appropriate co-efficient of elasticity. This must be added to ΔG_v to give for the free energy of formation of the critical cluster:

$$\Delta G^* = \frac{16\pi\sigma_{c-v}^{3} f_1(\theta')}{3(\Delta G_v + C_1\varepsilon^2)^2} \qquad \ldots(2.30)$$

where θ' is the contact angle of the critical nucleus with $\sigma_{c-s} = \sigma'_{c-s}$ in equation A.5.

Now δ is the upper limit on ε. Therefore if $|\Delta G_v|_{crit} >> C_1\delta^2$, the nucleus will form coherently such that $\varepsilon \sim \delta$ and $\sigma'_{c-s} = \sigma^o_{c-s}$. On the otherhand, if $C_1\delta^2 >> |\Delta G_v|_{crit}$ the nucleus will be incoherent, with $\varepsilon \sim o$ and $\sigma'_{c-s} = \sigma^o_{c-s} + \eta\delta$.

According to Bassett et. al[2.28] and Pashley[2.29], electron and X-ray diffraction fail to reveal coherency lattice strains in the 3-dimensional nucleiof a growing epitaxial layer, therefore they conclude that coherency is not essential to produce epitaxy. Generally, lattice constant measurements of thin deposits indicate that the spacings of the initial deposit is characteristic of the deposit material and is not modified to match the substrate lattice spacing, except in a few systems, where pseudomorphisin has been observed with films less than 100 A^o thick[2.49].

Experimental evidence[2.29,2.35] indicates that nucleation usually occurs at monatomic ledges or near imperfections such as grain boundaries or dislocations. Therefore, under these circumstances, it appears that whatever the misfit, it is unlikely that any degree of coherency exists between the nuclei and substrate.

2.2.8. Nucleation At Macroscopic Ledges

Chakraverty and Pound[2.36] have examined the effect of a macroscopic ledge on the nucleation rate. They obtained an expression for the free energy of formation of the critical nucleus similar to equation 2.9 but with $f_1(\theta)$ replaced by $f_L(\theta)$, the latter being a complicated function of θ. The ratio of the nucleation rate at a ledge, J_L, to that

on a flat surface, J, is then given by:

$$\ln(J_L/J) = \ln g + \left(\frac{16\pi\sigma_{c-v}^3}{3\Delta G_v^2 kT}\right)\left\{f_1(\theta) - f_L(\theta)\right\} \quad \ldots(2.31)$$

where g is the fraction of surface sites occupied by steps.

$f_L(\theta) < f_1(\theta)$ at any θ.

By plotting $\ln(J_L/J)$ vs. θ for typical values of g and $\frac{\sigma_{c-v}^3}{kT\Delta G_v^2}$ they have shown that with contact angles between 50^o and 100^o, nucleation will occur predominantly at these ledges. This has been verified, for example, by the decoration of cleavage steps of rock salt by gold[2.35].

It would appear from Chakraverty and Pound's theory that the critical super-saturation for nucleation on a surface with a large density of steps would be lower, thus encouraging epitaxy, by providing preferential sites for nuclei possessing a particular structural feature.

2.2.9. Effect Of Impurities On Nucleation and Epitaxy

A residual gas pressure of 10^{-5} torr is equivalent to an impingement rate of approximately one monolayer per sec. The impurities adsorbed on the substrate surface can affect the nucleation rate in several ways, e.g. ΔG_{des} can be reduced, thus reducing J. Adsorption of gas molecules on the substrate and on the cap nucleus can also modify the interfacial energies, reducing the nucleation rate in general, according to Hirth and Pound[2.30].

The effect of impurity adsorption on epitaxy is still not understood properly. Mathews and Grünbaum[2.51] found that gold films deposited on air cleaved rock salt at 10^{-7}-10^{-8} torr had lower dislocation densities than those deposited at 10^{-9} torr, probably because the bake-out at the

lower pressure removed some of the contaminants on the rock salt.

2.2.10. Orientation Changes And Re-Crystallisation

The importance of re-orientation and re-crystallisation during the coalescence stage has been demonstrated by many in-situ electron microscope studies of the growing nuclei[2.37,2.38], using Moiré fringe patterns[2.39] to identify the relative orientations of the crystallites. Crystallites which are slightly misaligned have been observed to re-orient themselves perfectly during the coalescence stage, by rotation in the plane of the substrate. However, it appears that this occurs only at an early stage of growth, when the coalescing islands are not too large. At a later stage of growth, when larger islands coalesce and during filling in of channels, apparently very little re-orientation takes place. It is at this stage that dislocations become permanently incorporated in the film.

Often the islands have gross mis-alignments such as double positioning where there is a 180^{o} mis-orientation in the substrate plane. According to Jabobs et. al[2.38], when two such islands coalesce the fault at the junction moves out of the compound island by a process of re-crystallisation, rather than by island rotation. This occurs simultaneously with the liquid like coalescence of the two nuclei. Apparently, a similiar process occurs with polycrystalline deposits, particularly those nucleated at a very high density.

2.2.11. Condensation Of Multicomponent Vapours

In section 2.1.5. we considered the condensation of binary vapours and estimated the substrate temperatures necessary for the formation of a stoichiometric compound, on the basis of vapour pressure data. We now examine the processes occuring in terms of surface diffusion and desorption energies and try to obtain the general conditions to be satisfied for stoichiometric condensation of binary vapours. The processes to be described will be limited to the period after nucleation and formation of a continuous film, so the various activation energies are characteristic of the elements on a substrate of the compound. We also assume that the incident atoms reach thermal equilibrium with the substrate surface in a short time, compared with that spent mobile on the surface.

Atoms incident on the surface move about between surface states, corresponding to a minima in their potential energy, until they finally condense by forming a molecular bond with neighbouring unlike atoms. Therefore, it is essential that the number of collisions between atoms of the two elements is large.

The number of sites covered in unit time, by surface diffusion of an adatom is given by:

$$\gamma = \nu \exp\left[-\frac{\Delta G_{diff}}{kT}\right] \qquad \ldots(2.32)$$

The number of sites covered in unit time by atoms of elements A (group III) and B (group V) is:

$$\gamma_{A+B} = \nu\left[\exp\left\{-\frac{\Delta G_{diffA}}{kT}\right\} + \exp\left\{-\frac{\Delta G_{diffB}}{kT}\right\}\right] \qquad \ldots(2.33)$$

and the time to cover one site is:

$$\tau_1 = 1/\gamma_{A+B} \qquad \ldots(2.34)$$

The mean lifetime of an atom of the volatile element B before collision with an atom of element A, is given by[2.40]:

$$\tau_{c_B} = \frac{n_o \tau_1}{n_{s\,A}} = \frac{n_o}{\nu n_{s\,A}} \left[\exp-\left\{\frac{\Delta G_{diffA}}{kT}\right\} + \exp-\left\{\frac{\Delta G_{diffB}}{kT}\right\} \right]^{-1} \qquad \ldots(2.35)$$

where $n_{s\,A}$ is the number of surface sites occupied by atoms of element A, i.e. the surface population of A.

The rate of collision of B with A adatoms is:

$$n_{AB} = n_{sB}/\tau_{cB} \qquad \ldots(2.36)$$

Using equation 2.13 for the surface population of adatoms (with $t >> \tau_s$), we have for the rate of collision of A with B:

$$n_{AB} = R_A R_B / n_o \nu \exp\left\{\frac{\Delta G_{desA} + \Delta G_{desB}}{kT}\right\} \left[\exp -\left\{\frac{\Delta G_{diffA}}{kT}\right\} + \exp -\left\{\frac{\Delta G_{diffB}}{kT}\right\} \right] \qquad \ldots(2.37)$$

R_A and R_B are the respective impingement rates. Equation 2.37 is also roughly the rate of formation of the compound, providing the activation energy for this process is low.

There are two conditions to be satisfied for stoichiometric compound formation. The first requires the residence time τ_{sB} to be much greater than the mean collision time τ_{cB}, otherwise compound formation will not occur, i.e.

$$\tau_{s\,B} = \nu^{-1} \exp\left\{\frac{\Delta G_{desB}}{kT}\right\} >> \left\{\frac{n_o \tau_1}{n_{sA}}\right\} \qquad \ldots(2.38)$$

The second condition[2.40] requires the surface population of the volatile element to be much less than the number of surface sites. If the impingement rate of this element is too high, all the surface sites may be occupied and a situation may arise where elemental material may be trapped. Thus:

$$R_B \tau_s \ll n_o \qquad \ldots(2.39)$$

By substituting for τ_s, τ_1 and n_{sA} in equations 2.38 and 2.39 and re-arranging, we have:

$$R_A \gg \frac{n_o \nu \left[\exp - \left\{\frac{\Delta G_{diffA}}{kT}\right\} + \exp - \left\{\frac{\Delta G_{diffB}}{kT}\right\}\right]^{-1}}{\left[\exp\left(\Delta G_{desA}/kT + \Delta G_{desB}/kT\right)\right]} \qquad \ldots 2.40$$

$$R_B << n_o \nu \exp - \left\{\frac{\Delta G_{desB}}{kT}\right\} \qquad \ldots(2.41)$$

(since $\nu = \frac{kT}{h}$, $n_o \nu$ is of the order of 10^{27}-10^{28} $cm^{-2}sec^{-1}$ for the range of substrate temperatures in use.)

We also know that R_B must be greater than R_A. Thus, for experimentally permissible impingement rates (in the region of 10^{14}-10^{18} $cm^{-2}sec^{-1}$), equation 2.40 requires the desorption energies to be high and the surface diffusion energies to be low. This also implies a high rate of formation of the compound, according to equation 2.37.

However, in order to satisfy equation 2.41, ΔG_{desB} must be low coupled with a high substrate temperature. Therefore, to satisfy the two conditions above it is necessary that $\Delta G_{desA} >> \Delta G_{desB}$. Using equations 2.40 and 2.41, and from a knowledge of the desorption and surface diffusion energies of the two components of the compound, it is then possible to decide if satisfactory deposition of the compound is possible with the two source method.

Using the above equations together with the nucleation theory given earlier, it should be possible to calculate the optimum impingement rates and substrate temperatures necessary for nucleation and growth of an epitaxial film. However, with some systems it may not be possible to satisfy both these requirements with one set of deposition parameters, in which case epitaxial nucleation must be initiated and the conditions then changed to optimise compound formation.

2.3. Defects In Epitaxial Films Of Sphalerite Structure Compounds

A brief outline of some common defects in sphalerite structures will be presented in this section.

2.3.1. Point And Line Defects

Point Defects

The number of possible point defects in binary compound semiconductors is double that in the elemental semiconductors, germanium and silicon. Thus, both cation and anion vacancies or interstitials may occur. However, to preserve overall stoichiometry vacancies of opposite type (Schottky defects) or vacancy-interstitial pairs (Frenkel defects), for example, are necessary. Point defects in III - V compound semiconductors can affect the electrical properties considerably, since a group III vacancy will probably behave like an acceptor, while a group V vacancy as a donor, as well as recombination and trapping centres. There do not appear to be any studies of point defects and non-stoichiometry in InAs, but X-ray lattice parameter[2.43] and other measurements[2.44] on bulk GaAs, indicate a very large density of such defects, of the order of 2-5 x $10^{19} cm^{-2}$.

Line Defects

In the Diamond structure the {111} planes are the slip planes with the slip along the <110> directions. This results in dislocations with a 60° Burgers vector. The corresponding defects in the sphalerite structure are the $\alpha 60^{\circ}$ and $\beta 60^{\circ}$ dislocations, depending on whether they consist of group III or V atoms, as shown in Fig.2.4(a). Apparently, these give rise to the triangular etch pits often observed on {111} surfaces, (see section 4.3.2.).

2.3.2. Stacking Sequences, Faults And Twining

The normal stacking sequence in an FCC structure is abcabc ... and in the sphalerite structure these are the double atom planes aαbβcγ ... shown in Fig.2.4(a). A stacking diagram is plotted in Fig.2.4(b), demonstrating that the sphalerite stacking is represented by a straight line. Also shown is the stacking sequence of the hexagonal wurtzite structure, in which some compound semiconductors cyrstallize, and some longer, regular repeat sequences called polytypes. Polytypism often occurs in II - VI compounds, but there appears to be little evidence to suggest that it occurs in III - V compounds.

Intrinsic stacking faults, due to aggregation of pairs of vacancies to remove double atom layers of {111} planes, and extrinsic faults, due to the introduction of out of sequence extra double atom layers, both occur in sphalerite structures. The dissociation of a 60^{o} dislocation can result in four types of stacking faults[2.44], (i) intrinsic and extrinsic upright faults (no wrong bonds up or down from the fault), (ii) intrinsic and extrinsic inverted faults, (wrong bonds up and down from the fault). Energetically, however, upright faults would be expected to predominate. Successive stacking faults of the form abcbac ... (omitting the Greek letter planes), result in twining, with the <111> directions as the twin axes. (In an FCC structure a rotation twin about a <111> is also a reflection twin, and because of the high symmetry it is equivalent to a 60^{o} rotation about this axis). There is a tendency for multiple twinning to occur about <111> axes in epitaxial films of sphalerite compounds when the deposition temperature is too low. This reduces to simple twinning as the temperature

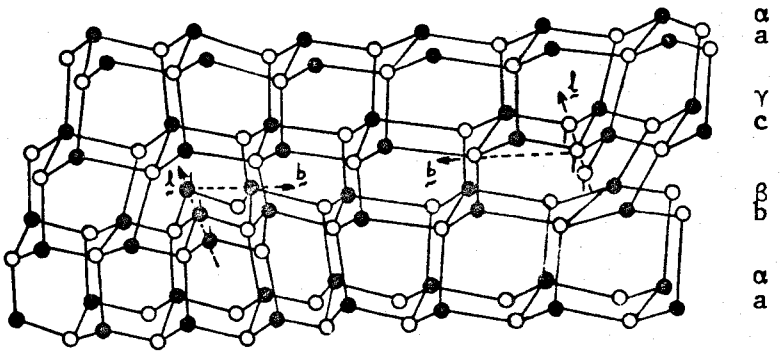

(a) 60° dislocation in sphalerite structure, with {111} slip planes. The Burgers vectors and dislocation lines are in <110> directions

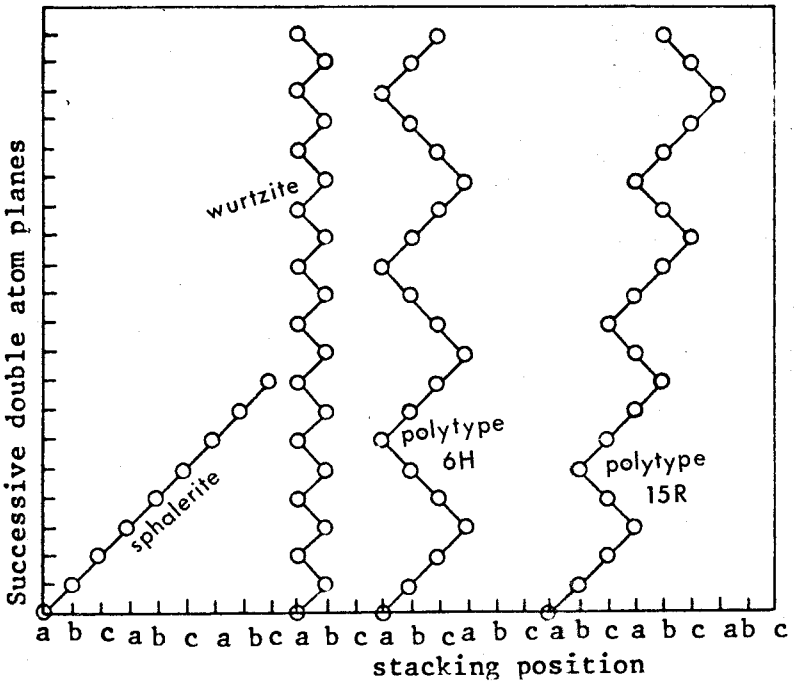

(b) Stacking sequence diagram for sphalerite and wurtzite structures, and some polytypes (after Holt, ref.2.44). The Greek letter planes have been omitted to simplify the diagram.

FIG.2.4

is increased and finally to untwinned epitaxy, but in some cases it persists up to the highest permissible deposition temperatures[2.45].

2.3.3. Heterojunction Misfit Dislocations

It was mentioned in section 2.27 that there is little evidence to suggest that epitaxial layers are pseudomorphic except with very thin films (<100Å), of some systems. Therefore, if we assume the change in lattice parameter is abrupt across the heterojunction interface, this will result in dislocation lines in two or three directions along the interface plane[2.46], which consist of atoms of the material with the smaller lattice constant. This is illustrated in Fig.2.5(a) for a (111) interface seen on a $(1\bar{1}0)$ plane. These are pure edge type dislocation lines which are perpendicular to the plane of the drawing, with the Brugers vector in this plane. The spacings of these dislocations depend on the substrate and deposit lattice parameters and the orientation of the interface plane[2.47], forming a right angle cross grid in {100} and {110} interfaces and a 60° grid in {111} interfaces, as shown in Fig.2.5(b). If λ_1 and λ_2 are the atomic repeat distances perpendicular to the dislocation lines and along the interface plane of the materials with the smaller and larger lattice constant, respectively, then there will be an interger N for which $N\lambda_2 = (N+1)\lambda_1 = D$, the spacing of the dislocation lines. Therefore,

$$D = \frac{\lambda_1\lambda_2}{\lambda_2-\lambda_1} \qquad \ldots(2.42)$$

The spacings for the three low index planes of a GaAs/InAs heterojunction are given in table 2.1.

The number of dangling bonds ΔN_s at the interface is the difference between the dangling bonds presented at the appropriate surface by the two materials, i.e. $\Delta N_s = N_{s_1} - N_{s_2}$, and N_s is given by:

$$N_s = \frac{m}{q_1 x q_2} \qquad \ldots(2.43)$$

where $q_1 x q_2$ is the unit mesh of the crystallographic plane and m is the number of dangling bonds associated with this area. For the case of a (100) surface, shown in Fig.2.5(a), $q_1 = a/2[0\bar{1}\bar{1}]$ and $q_2 = a/2[0\bar{1}1]$, hence $q_1 x q_2 = a^2/2$. There are two dangling bonds per atom, which are shared by four meshes, hence 2/4 = 1/2 dangling bond per corner atom. Therefore, m = 4 x ½ = 2, and $N_s\{100\} = 4/a^2$. The density of dangling bonds for the various GaAs/InAs interfaces is presented in table 2.1.

TABLE 2.1

Density of dangling bonds and misfit dislocation spacing in a GaAs/InAs heterojunction

GaAs a=5.6535Å InAs a=6.0583Å Misfit 7.14% Plane	N_{s_1} GaAs cm^{-2}	N_{s_2} InAs cm^{-2}	Density of dangling bonds at hetero-junction ΔN_s cm^{-2}	Misfit dislocation Space D Å
{100}	1.25×10^{15}	1.09×10^{15}	1.6×10^{14}	59.83
{110}	8.85×10^{14}	7.71×10^{14}	1.14×10^{14}	D_1=59.83 D_2^1=84.61
{111}	7.22×10^{14}	6.29×10^{14}	9.3×10^{13}	59.83

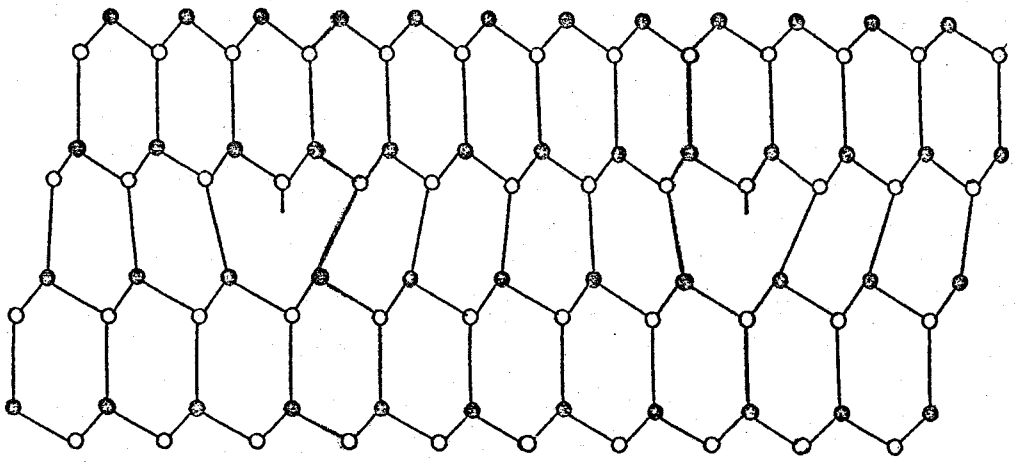

(a) Heterojunction misfit dislocations in a (111) interface seen on a (1$\bar{1}$0) plane, for a lattice misfit of 20%

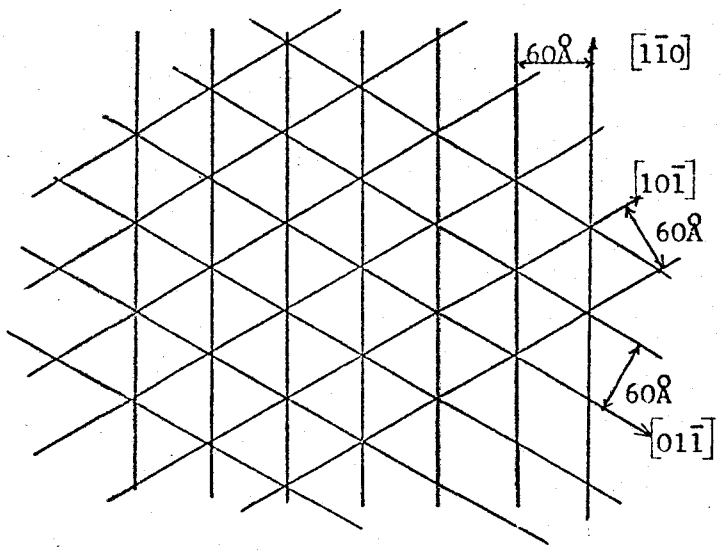

(b) Cross-grid of misfit dislocations in a (111) interface, for an InAs/GaAs heterojunction

Fig.2.5

Since the misfit dislocations in an abrupt heterojunction are confined to the interface plane, according to the above model, they should not affect the electrical properties of an epitaxial layer on an insulating substrate. However, thay are of considerable importance in the study of heterojunctions[2.48].

Recently, Abrahams et. al.[2.52] have put forward a model in which the misfit dislocations in both abrupt and graded heterojunctions are not only confined to the interface plane, but also give rise to inclined dislocations that propagate through the growing layer. Since epitaxy occurs by a process of heterogenous nucleation and island growth, the misfit dislocations may be expected to be segmented, as illustrated in Fig.2.6(b). Apparently, since dislocations cannot end within a crystal, the segmented misfit dislocations must bend upwards and propagate through the growing crystal. Abraham et. al. suggest that the inclined dislocations can bend in and out of any subsequently formed misfit plane to relieve the strain, and their density will remain constant with increasing thickness. Studying GaAs/$GaAs_{1-x}P_x$ heterojunctions by transmission electron microscopy, they have obtained conclusive evidence to support this model. These inclined dislocations can have a high density and one may assume they would affect the conduction properties of the epitaxial layer.

The [111] direction is not equivalent to the $[\bar{1}\bar{1}\bar{1}]$ direction in sphalerite compounds which is a consequence of the non-centrosymmetric structure. Hence the <111> directions are referred to as the polar

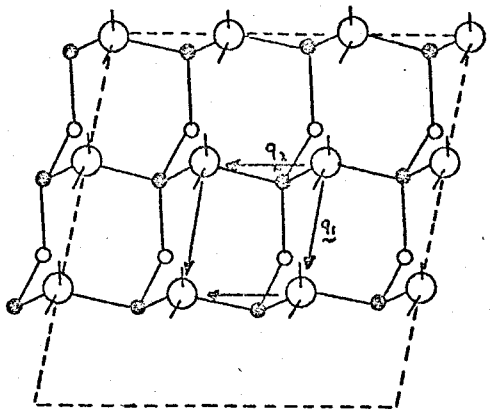

(a) {100} surface of sphalerite structure showing unit mesh vectors. Shaded atoms are of one component of the compound and open atoms of the other. (After Holt, ref.2.47).

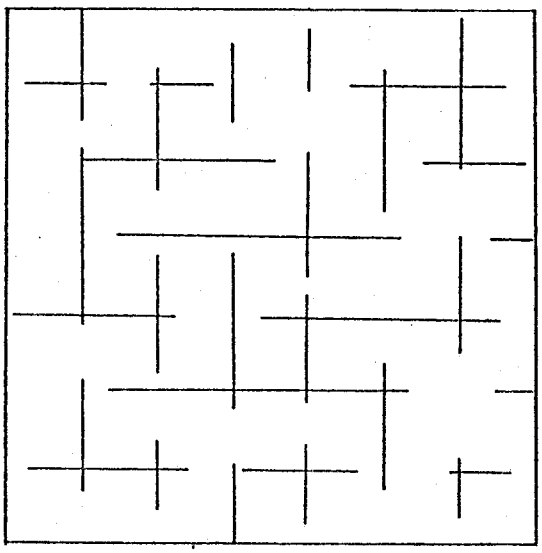

(b) Schematic diagram of segmented misfit dislocations in {100} interface

Fig.2.6

axes. This results in one face of a slice containing a surface layer of group III atoms and the other face group V atoms, since the surface atoms which are triply bonded to the underlying layer are more stable than the single bonded atoms (see section 3.1.3).

A heterojunction between two sphalerite compounds should result in the epitaxial layer continuing the polarity of the substrate. According to Holt[2.47], however, in a compound/element heterojunction there would be a tendency for deposition of the compound to occur with the polarity so oriented that alternation of lower and higher electronegativity atom planes is obtained across the interface.

3. EXPERIMENTAL

3.1.1. Calculation Of Deposition Parameters

In section 2.1.5 we outlined the method of calculating the limits of substrate temperatures, for particular impingement fluxes, which should result in stoichiometric film formation. We now illustrate this with a calculation for the case of Indium Arsenide.

Fig.3.1 is a plot of equation 2.1 for the impingement rates of Indium and Arsenic, assuming an effective evaporation area of 0.31 sq.cm. and source-substrate spacings of 5, 7 and 10 cm. Suppose we require a deposition rate of 10 Å/sec, which corresponds to an Indium impingement flux of $1.8\text{x}10^{15}\text{cm}^{-2}\text{sec}^{-1}$, assuming the Indium flux controls the film growth rate. We let the Arsenic flux have an excess by a factor of about ten, i.e. $R_{+B} = 2\text{x}10^{16}\text{cm}^{-2}\text{sec}^{-1}$. With a source-substrate spacing of 10 cm, the source temperatures required, from Fig.3.1, are:

$$T_A = 982^{\circ}\text{C}, \qquad 1255^{\circ}\text{K}$$

$$T_B = 308^{\circ}\text{C}, \qquad 581^{\circ}\text{K}$$

From the vapour pressure graphs of the elements, Fig.3.2, the above temperatures result in the following vapour pressures above the sources:

$$P_{1A} = 2\text{x}10^{-2} \text{ torr}$$

$$P_{1B} = 7\text{x}10^{-2} \text{ torr}$$

Hence, the vapour pressures at the substrate are:

$$P_{2A} = 2\text{x}10^{-5} \text{ torr}$$

$$P_{2B} = 7\text{x}10^{-5} \text{ torr}$$

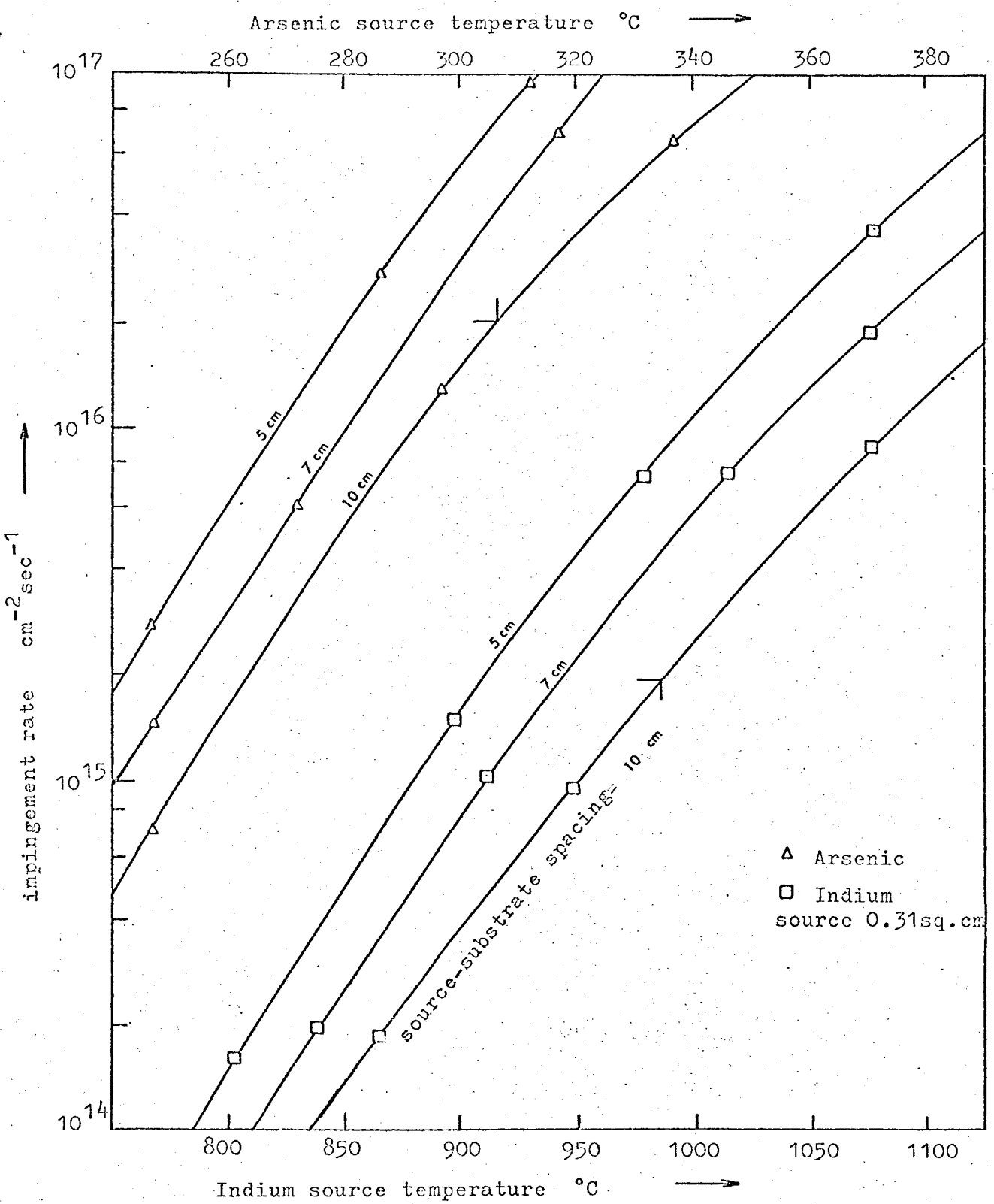

Fig.3.1
Indium and Arsenic impingement rate as a function of source temperature

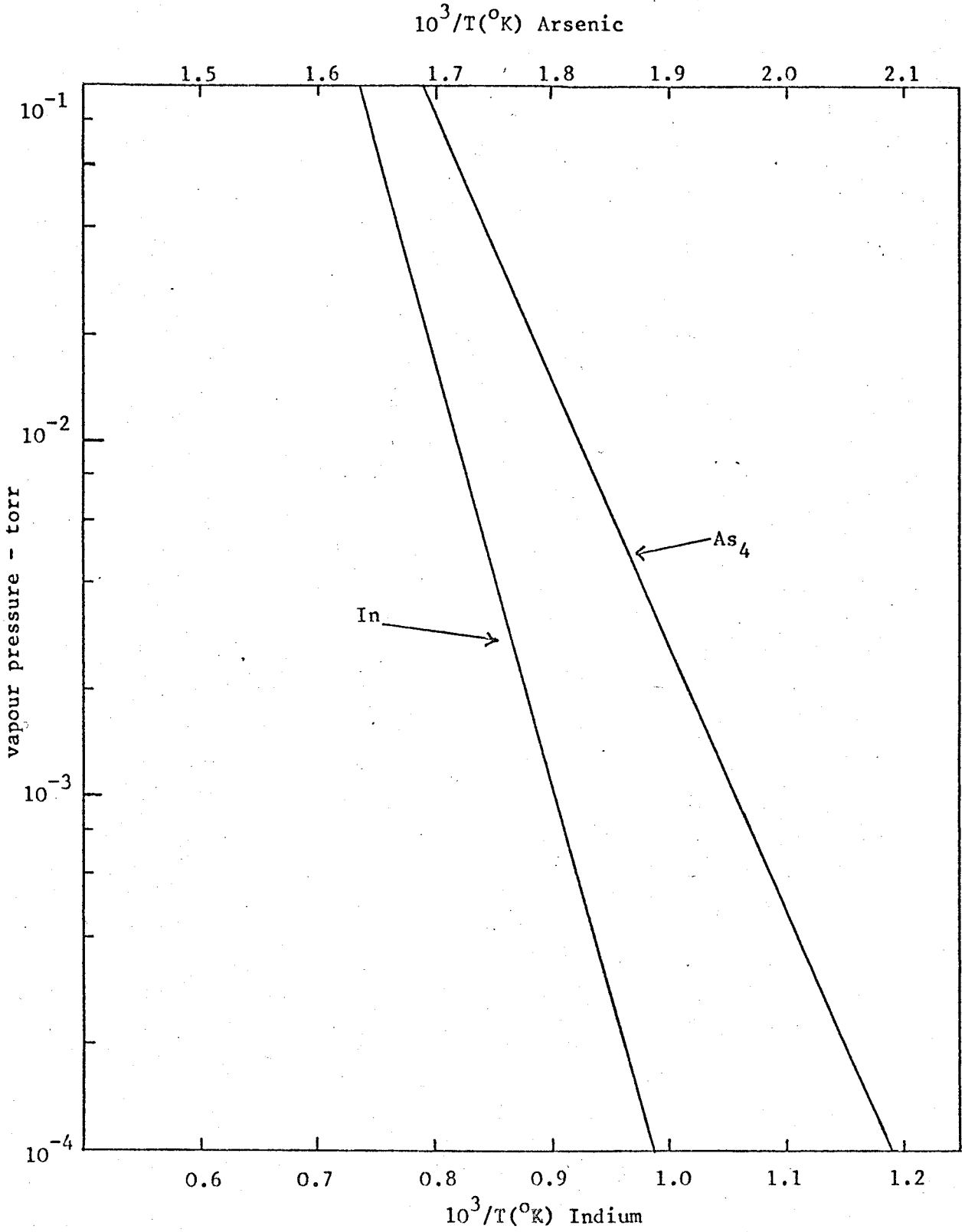

Fig.3.2

Vapour Pressures Of Indium And Arsenic

where the suffixes 1 and 2 represent the source and substrate, respectively.

From equation 2.3 we then have:

$$P_{eB} = 7\times10^{-5}(T/581)^{1/2} \text{ torr} \qquad ...(3.1)$$

Fig.3.3 is a plot of the vapour pressure of As_4 above Arsenic and of As_2+As_4 above InAs. The intersection of equation 3.1 with these two curves gives the minimum and maximum substrate temperatures required for stoichiometry. For the particular case above:

$$T_{min} = 198^{o}C, \quad 471^{o}K$$

$$T_{max} = 692^{o}C, \quad 965^{o}K$$

Also plotted are two similar curves for $P_{2B} = 2\times10^{-4}$ and 2×10^{-5} torr.

Temperatures above T_{max} will result in an excess of Indium and below T_{min} in an excess of Arsenic. This is illustrated in Fig.3.4 for the three Arsenic pressures considered, which shows the 'stoichiometric interval', and the shift to higher temperatures of this inverval with increasing Arsenic pressure. It must be emphasized that although stoichiometry should be achieved over this wide temperature range, the substrate temperature required to obtain large grains or for epitaxy is usually near the upper limit.

If annealing is to be performed after the deposition, this must be done in an Arsenic pressure greater than its partial pressure above the compound, at the particular annealing temperature (see Fig.3.3), otherwise a loss of Arsenic from the deposited film may result.

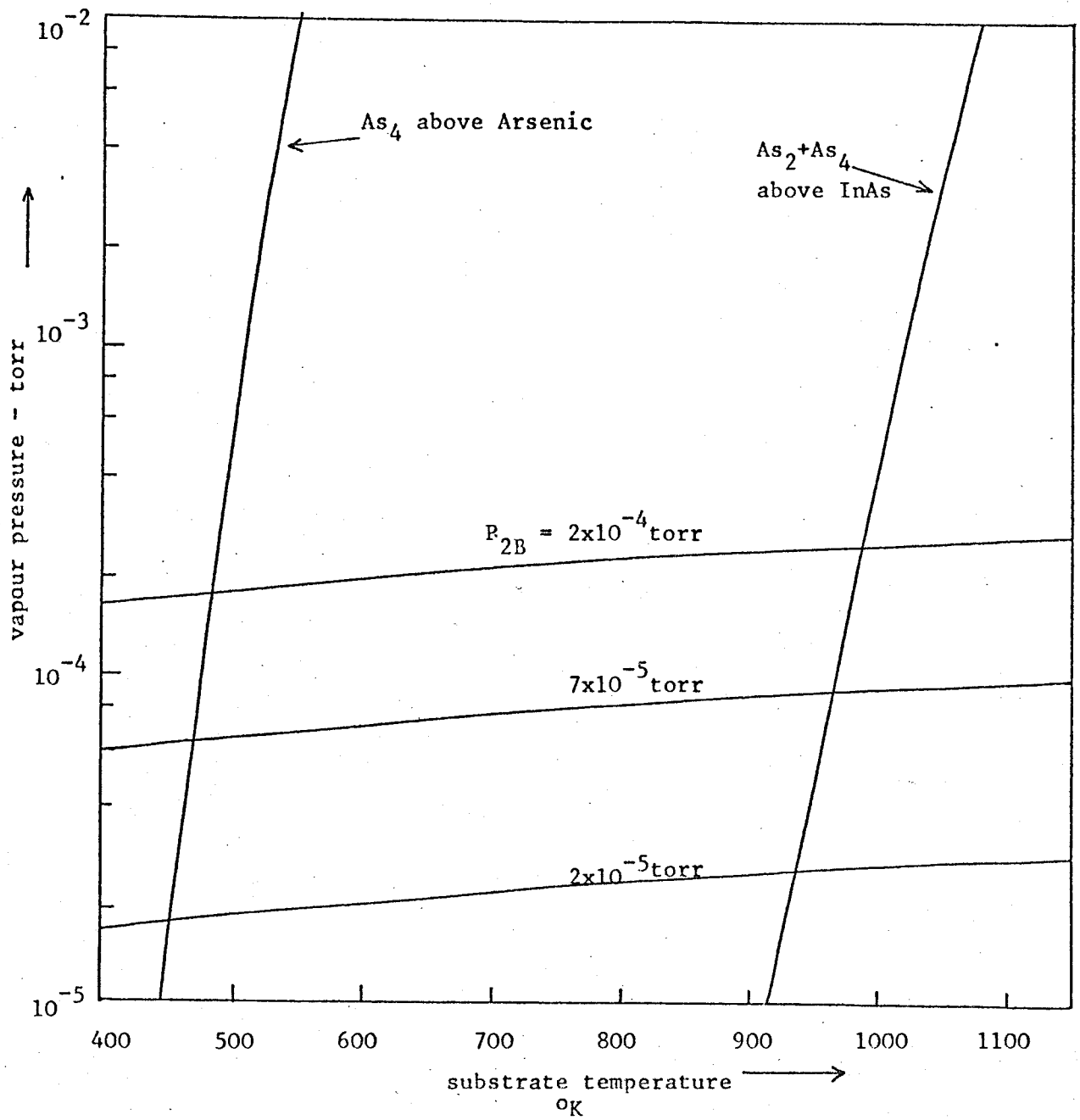

Fig.3.3

Intersection Of Equation 3.1 With As_4 Vapour Pressure Above Arsenic And Arsenic Partial Pressure Above InAs

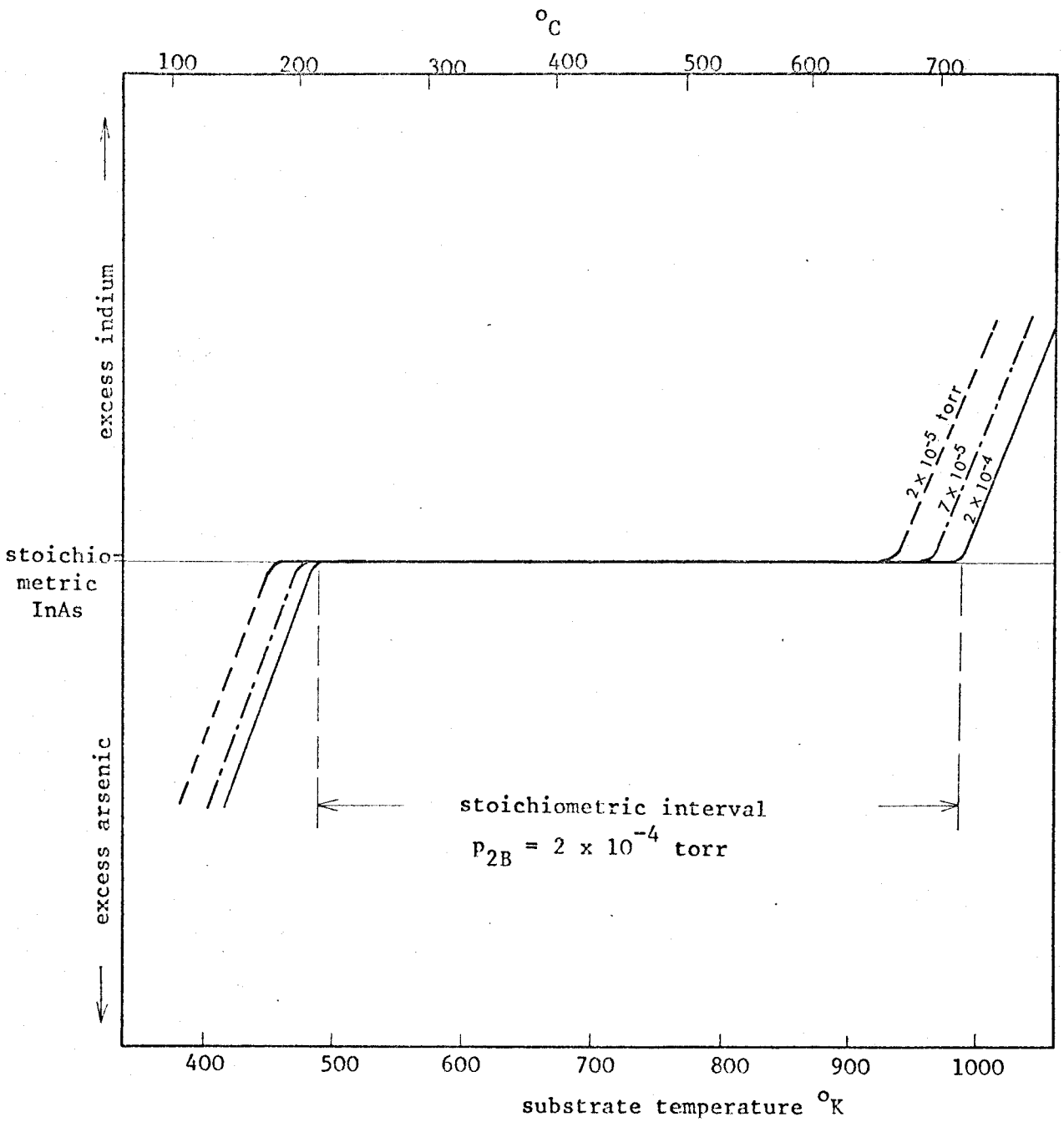

FIG.3.4

Composition of condensed InAs as a function of substrate temperature

3.1.2. Deposition System

The vacuum system employed is a conventional 18" bell jar high vacuum plant, consisting of a 360 litre/min rotary pump, a 6" oil diffusion pump and a liquid nitrogen trap. The vacuum that could be achieved normally was about 5×10^{-6} torr, and under optimum conditions, 10^{-6} torr.

Most of the components in the vacuum chamber were made of stainless steel. However, the substrate base plate, holder and heater were made of Molybdenum, since it was found that stainless steel was not suitable at temperatures above 600°C.

Initially, the evaporation sources were cylindrical Alumina crucibles with Tungsten spiral heaters, which were cemented to the crucibles with Alumina cement. Pt./Pt.+10% Rhodium thermocouples were cemented to the bottom or sides of the crucibles, in order to monitor the temperatures. However, the purity of the Alumina cement was suspect, so Molybdenum boats were used instead, with thermocouples spot-welded to the sides of the boats. With both types of sources it was found that the true temperatures of the evaporating sources were not being monitored, and therefore the impingement fluxes were incorrect. Even if a calibration was made for a particular source geometry and source-substrate spacing, it would be difficult to get a reproducible impingement rate, since this would also be a function of the amount of material in the source.

Therefore, it was decided to use an Edwards oscillating Quartz crystal thin film monitor; which can monitor both the rate of deposition

and the film thickness. The monitor operates on the principle that material deposited on the Quartz crystal results in a shift in the resonant frequency, which is monitored by heterodyne action. This method is suitable to monitor the Indium evaporation, since it has a condensation coefficient near unity at, say 200°C, which is probably the maximum temperature the crystal would be at during the deposition, without using a special cooling system. However, Arsenic will not deposit on a surface at this temperature, and attempts to cool the crystal resulted in condensation on the cooling coils only, which appeared to attract the Arsenic away from the crystal, probably because the coils were much colder than the Quartz crystal.

Finally, a nude ionization gauge head placed near the substrate was employed to monitor the Arsenic pressure, instead, giving satisfactory results. The Indium rate, hence the film growth rate and thickness, were monitored by the crystal monitor. Figure 3.5 is a schematic diagram of the vacuum chamber and a photograph of the chamber is shown in Fig.3.6.

The substrate heater consists of a 1mm diameter Tungsten wire spiral with a Molybdenum heat shield. In order to achieve rapid temperature changes, the substrate holder has a small thermal mass, but this, of course, does not allow for good temperature stability. The temperature was monitored with a Pt./Pt+13%Rh thermocouple, spot welded to a Molybdenum sheet, which was placed on the substrate holder. It is probable that the thermocouple indication was higher than the true temperature of the condensation surface.

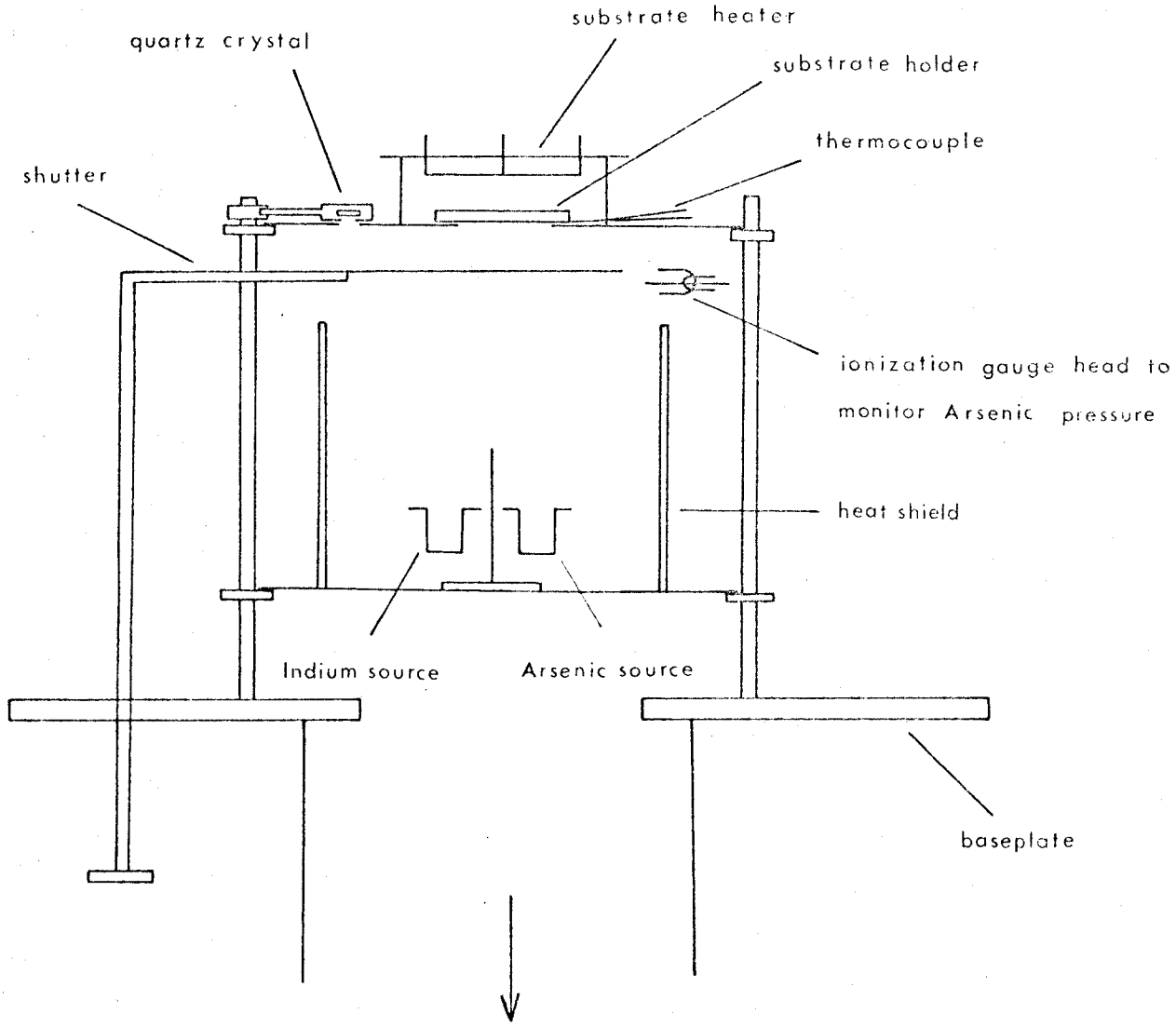

Fig.3.5

Schematic diagram of the vacuum chamber

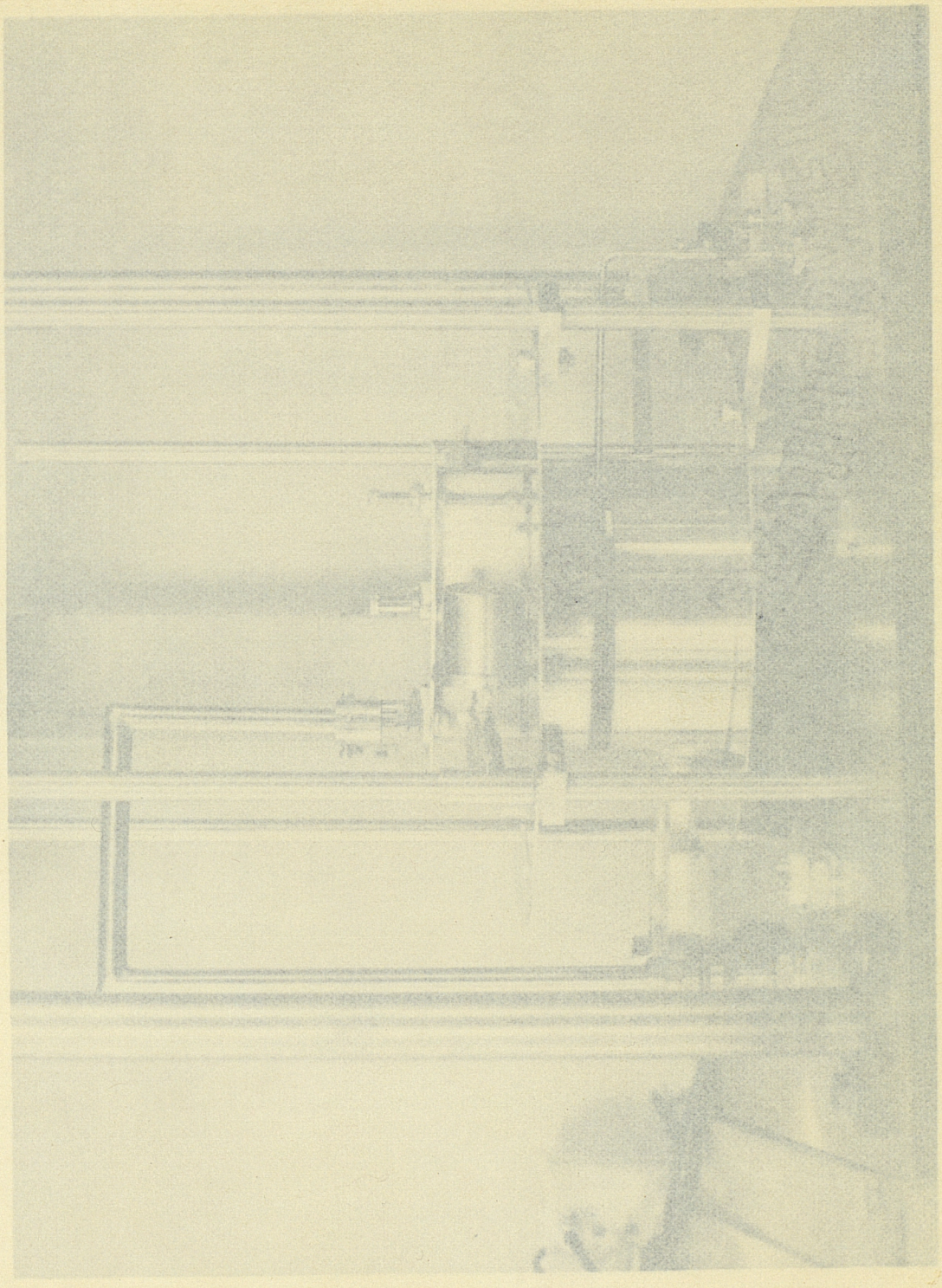

Fig.3.6

A photograph of the vacuum chamber

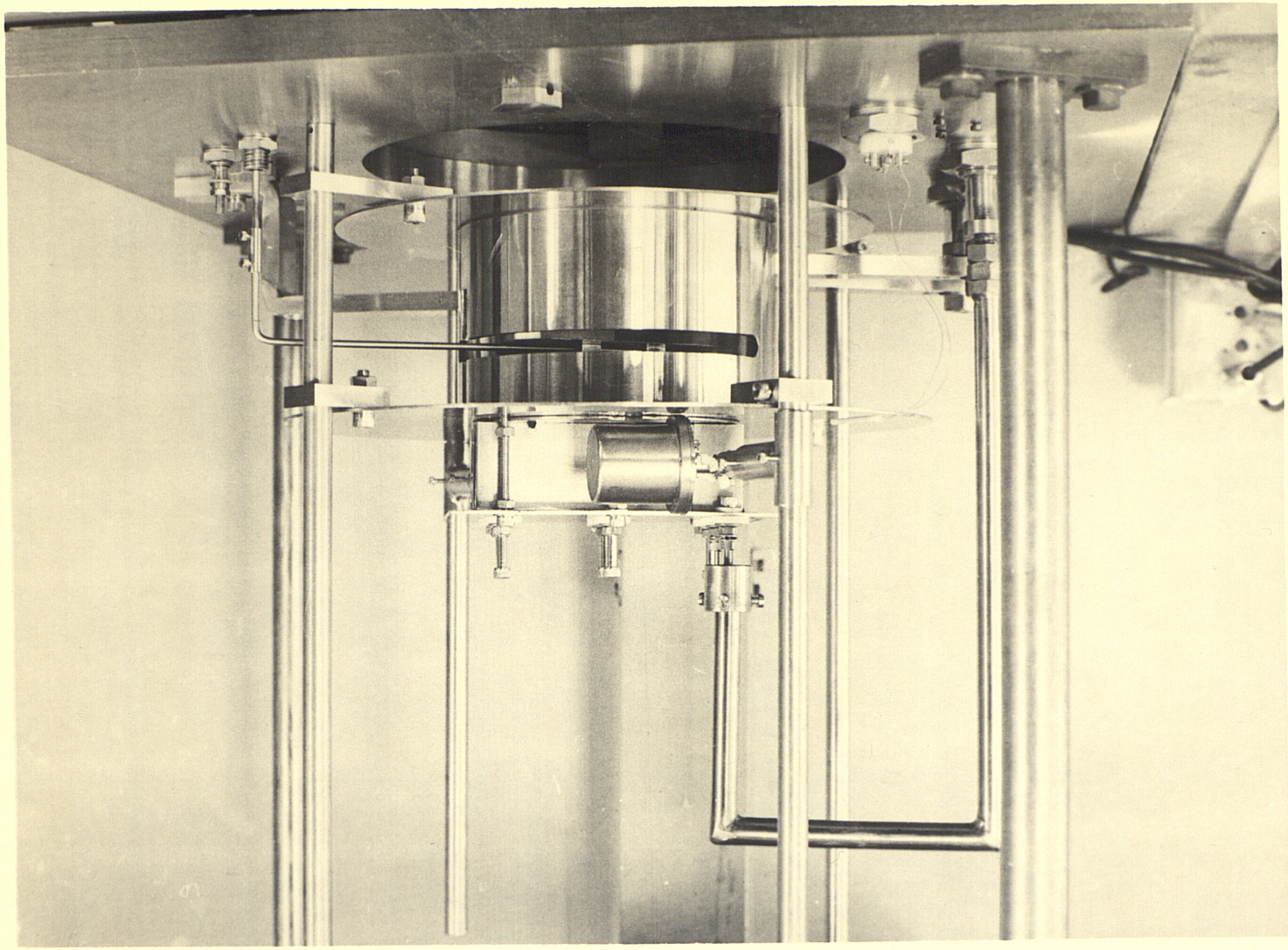

3.1.3. Substrate And Source Materials

Substrates

The polycyrstalline films were deposited on the following types of substrates:

(1) Corning 7059 glass

(2) Fused Quartz

(3) Alumina

The majority of these films were deposited on Corning glass, since the use of fused Quartz and Alumina did not result in any improvement in film quality.

The following procedure was employed to clean the substrates*:

(1) Rinse in de-ionized water

(2) Ultrasonically agitate in de-ionized water for 5 minutes

(3) Ultrasonically agitate in iso-propyl alcohol for 5 minutes

(4) Blow dry with Nitrogen gas

After this cleaning procedure the substrates were placed immediately in the vacuum chamber.

The epitaxial films were deposited on semi-insulating GaAs ($\rho > 10^7 \Omega$-cm), having the following orientations:

(1) {100} 2° OFF singular orientation

(2) {110} 2° OFF singular orientation

(3) {111} 2° OFF singular orientation

(4) {111} 1/2° OFF singular orientation

These substrates were obtained from the Royal Radar Establishment, Malvern, cut to the required orientation, but not polished. Mechanical

* See Appendix G.2.

lapping and polishing was carried out as follows:

(1) Lap with 600 grade Silicon Carbide

(2) Polish successively with 6, 1 and 1/4 micron Diamond paste on Hyprocel Pellon pad.

Between each of these stages the substrates and mounts were ultrasonically agitated in water to remove the grit left from the previous stage.

Before deposition, the GaAs substrates were prepared as follows:

(1) Ultrasonically agitate in hot isopropyl alcohol for five minutes

(2) Etch for ten minutes in: $3H_2SO_4:1H_2O_2:1H_2O$ at approximately $50^{o}C$

(3) Flood with de-ionized water and rinse thoroughly

(4) Repeat step 1

(5) Dry in Nitrogen gas or on a hot plate

The substrates were then placed immediately in the vacuum chamber.

A common method of polishing GaAs is due to Reisman and Rohr[3.1]. This is a wet pad method which involved squirting a solution of Sodium Hypochlorite onto a rotating pad at intervals of a few minutes, with the substrates held against the pad. Apparently, the surfaces obtained do not have the familiar 'orange peel' effect often observed after chemically polishing a lapped surface. Since the wet pad method is a lengthy process and requires specialized equipment, it was decided to use the method outlined above, which results in extremely smooth surfaces.

As mentioned in chapter 2, the <111> directions in sphalerite compounds are the polar axes, i.e. in one direction the A atoms are triply bonded to the underlying layer and the B atoms are singly bonded, and vice versa. This is illustrated in Fig.3.7. The singly bonded layers are unstable, thus the two (111) faces contain the triply bonded atoms; one face consisting of A atoms and the other of B atoms.

The etch given above will only polish the Arsenic face. Therefore, before mechanically polishing the {111} substrates the correct face was determined by etching for a short period in this etch. Attempts to find a suitable polishing etch for the Gallium face have been unsuccessful.

Source Materials

+99.999% pure source materials were used, which were obtained from Koch-Light Laboratories and from New Metals and Chemicals. A small amount of 6N pure materials, also obtained from Koch-Light was used in two evaporations. Unfortunately, these evaporations were unsuccessful, resulting in polycrystalline films, so no comparison could be made regarding the effect of material purity on electrical properties.

3.1.4. Experimental Deposition Conditions

Polycrystalline InAs

The source-substrate spacing was 10 cm for most evaporations. Before deposition, the substrates were outgassed for about an hour at 550 - 600^{o}C, and the sources outgassed during this period at increasing temperatures in steps, up to the evaporation temperature. This process

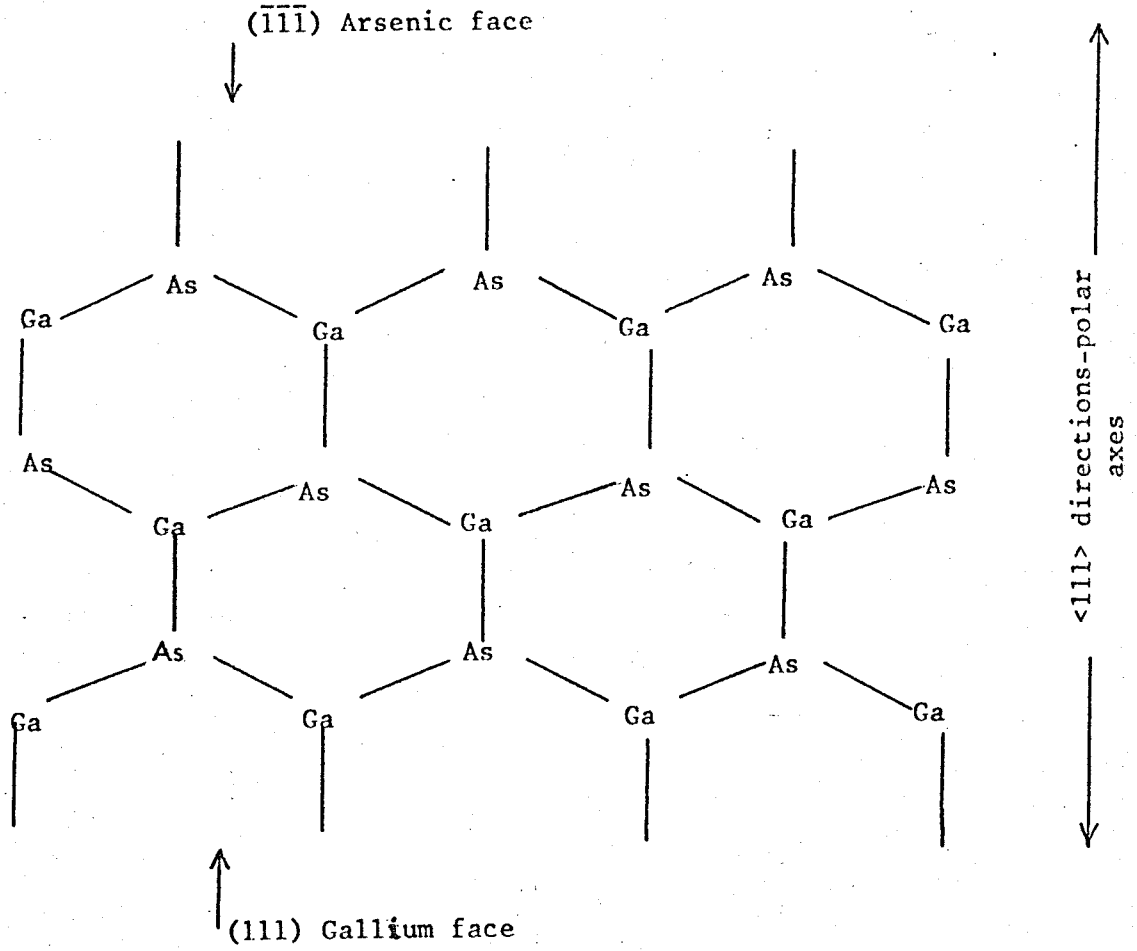

Fig.3.7

Schematic representation of structure of GaAs showing <111> polar axes

may also result in the preferential evaporation of volatile impurities in the source materials.

The Indium impingement rate was set to the required value by moving the shutter vertically upwards so that the Quartz crystal was exposed to the Indium flux but the substrates were still covered. When the required rate was obtained the shutter was moved sideways to expose the substrates. During the evaporation the Arsenic pressure was maintained at approximately 10^{-4}torr. Deposition was usually carried out at substrate temperatures in the region of 450 - 500°C. Nucleation of the compound would not occur if the temperature was above 550°C. However, in order to obtain a large grain size, it was found necessary to anneal the films after deposition at temperatures up to 620°C in an Arsenic atmosphere. Alternatively, the temperature could be raised as soon as a continuous film was deposited, with the re-crystallization occuring during the deposition. During deposition or annealing, any excess Arsenic above $5x10^{-5}$torr appeared to have no effect on the electrical properties of the films.

The effect of various deposition parameters, such as annealing temperature, time and impingement rate on the electrical properties has been investigated. These results will be presented in chapter 5. It was found that the best films, i.e. having high mobilities and low carrier concentrations, were obtained with a deposition temperature between 330 and 500°C and annealing at approximately 620°C for 15 minutes or longer in an Arsenic pressure of 10^{-4}torr. Above

630°C, Arsenic re-evaporation occured, the transition being very rapid. According to the calculations of section 3.1.1. the transition should occur at 715°C. The discrepancy could be due to errors in temperature and pressure measurements and in the Arsenic partial pressure data.

Epitaxial InAs

Outgassing of the substrates was carried out in steps up to a maximum of 700°C, for a period of one to two hours. The sources were also outgassed during this period and maintained at the evaporation temperature for 10 to 20 minutes before the deposition.

The deposition parameters for the growth of single crystal films have been found to be extremely critical compared to the polycrystalline films. It was found that epitaxy occured at different substrate temperatures with the three orientations used. With an Indium rate of 10 - 15Å/sec and an Arsenic pressure of 10^{-4}torr, the limits of substrate temperatures required for epitaxy were approximately:

orientation	T_{min} °C	T_{max} °C
{110}	595	620
{100}	605	640
{111}B	630	665

Temperatures above the maximum resulted in Indium rich films. This was confirmed by dipping the sample in concentrated HCl, which reacts with the free Indium to give off Hydrogen. If the compound

is stoichiometric InAs there is no reaction. Temperatures well below the minimum resulted in films which were highly twinned or polycrystalline as indicated by electron diffraction. These films usually had rough matt surfaces, whereas the good epitaxial layers have optically smooth surfaces with some growth features. However, below 450°C the twinned and polycrystalline films also have mirror smooth surfaces, due to the small grain size, but no growth features are observed under the optical microscope.

Epitaxy on {111} surfaces could still be achieved with rates of 20 Å/sec, but attempts at 50 Å/sec resulted in polycrystalline deposits. A proper investigation of the epitaxial relation between impingement rate and substrate temperature would require a large number of substrates of one orientation.

3.1.5. Insulator Film Deposition

Silicon Oxide was used as the gate insulator for the field effect devices fabricated. It was vacuum evaporated at a rate of 40 Å/sec onto a substrate maintained at 200°C. A separate vacuum system was used, which was capable of pressures down to 5×10^{-6} torr.

Apparently, vacuum evaporated films of Silicon Oxide may contain a mixture of the Monoxide and the Dioxide, the composition depending on the Oxygen pressure of the system during the deposition*. It is also possible that changes in composition occur with time, thus making it a poor gate insulator. However, it was chosen as an interim measure, since it is easy to deposit and is one of the few evaporated

* See Appendix G.3.

insulators that has been studied extensively.

The possibility of using reactively sputtered Tantalum Oxide for the gate insulator has also been considered, since it has a high dielectric constant. However, preliminary results[3.2] indicate that the surface state density at the interface of InAs and Ta_2O_5 is very high, thus giving very poor conductivity modulation.

3.2.1. Measurement Of Film Thickness

Since the substrates were placed on a holder for the deposition, usually there was an edge where the film thickness could be measured directly by interference methods. Thickness measurements of the films on glass substrates were often carried out after depositing a thin film of Aluminium. A Zeiss multiple reflection interference microscrope with a Thallium source ($\lambda/2$= 2675 Å) was used. The accuracy of the measurements were probably not better than ± 10%, particularly with the very thin films. This method is suitable if the film surface is optically reflecting, and in the thickness range 0.03 to 1.0μm. However, the thick epitaxial layers were either angle lapped and measured in the interference microscope, or stained cleavage sections were photographed under high magnification (x2800). The latter method is only suitable with orientations which cleave easily perpendicular to the surface. There is a slight colour difference between the epitaxial InAs and the GaAs substrate, which can be distinguished under the microscope. However, this difference can be enhanced by staining the GaAs in Sodium Hypochlorite for about 10 secs.

3.2.2. Preparation Of Films For Electrical Measurements

Initially, the films were deposited through out of contact Molybdenum masks to obtain the required geometry for Hall effect and conductivity measurements. A disadvantage of using metal masks is that at high temperatures there can be a large gradient across the exposed and unexposed areas of the substrate. Therefore, the films were deposited over the whole substrate and a photo-mechanical process used to define the pattern. PMD 'superline' positive resist was found satisfactory, since it dissolves very easily in acetone. A six arm bridge geometry was used for these measurements. The Aluminium contact pattern was evaporated through a Molybdenum mask. This geometry was chosen in conjunction with R. Hawkins, who has made low frequency noise measurements on these films.

The InAs films were etched in one of the following:

1. $3HNO_3$: $1H_2O$
2. $3H_2SO_4$: $1H_2O_2$: $1H_2O$
3. $1HNO_3$: $1HCl$

} at approximately 30-40°C

Contact to the pads was made using Johnson & Mathey Silver preparation FSP51, which was found satisfactory in the temperature range 65 - 450°C. With a sufficiently high input impedance meter, it is not essential to have ohmic contacts if a bridge specimen is

employed. The resistance between any two probes of the very thin films measured was less than 10^5 ohms, whereas the electrometer used has an input impedance greater than 10^{14} ohms.

3.2.3. Field Effect Device Fabrication

Fig.3.8 is a cross sectional view of the thin film field effect structures fabricated. Evaporated source-drain contacts were used and isolation is achieved with the semi-insulating substrate. The fabrication method to be described is applicable to both polycrystalline and epitaxial InAs.

The photographic masks required to fabricate these devices were produced with a Watson mark 3 step and repeat camera, which has a reduction of 10 : 1. The total reduction from the master was 250.

Figs.3.9 (a) - (c) show the basic geometries of the various masks, magnified about twenty times. (a) defines the semiconductor, (b) the source-drain contacts, and (c) the field plate etc. The gate insulator was evaporated through a metal mask consisting of strips, as shown in Fig.3.9 (d). The basic pattern incorporates four transistor structures with source-drain spacings of 10, 25, 110 and 40μm. The 40μm gap is not shown in (b), but occurs in the step and repeat pattern. There are two Hall probes in the 110μm gap for channel mobility measurements. Also included is an MOS capacitor, the small circular pattern, and a plain capacitor, the large circular pattern. This basic

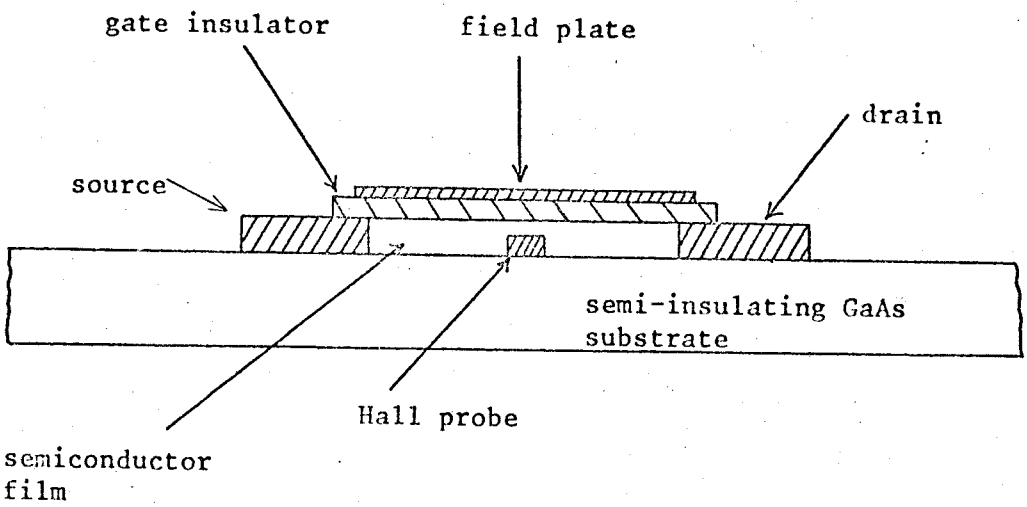

Fig.3.8

Cross-sectional view of a thin film field effect structure (schematic)

Fig.3.9
Masks for field effect device fabrication

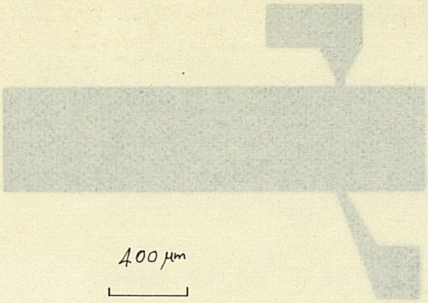

(a) Semiconductor geometry

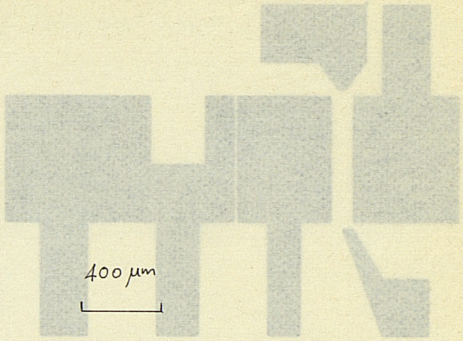

(b) Source-drain contacts

(c) Field plates, capacitors and Hall contacts

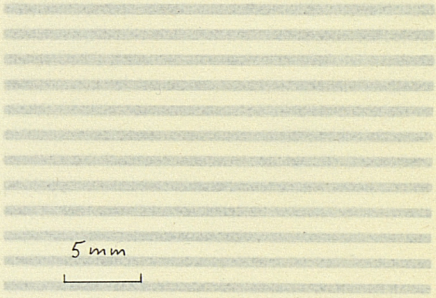

(d) Gate insulator-complete mask, x2 actual size

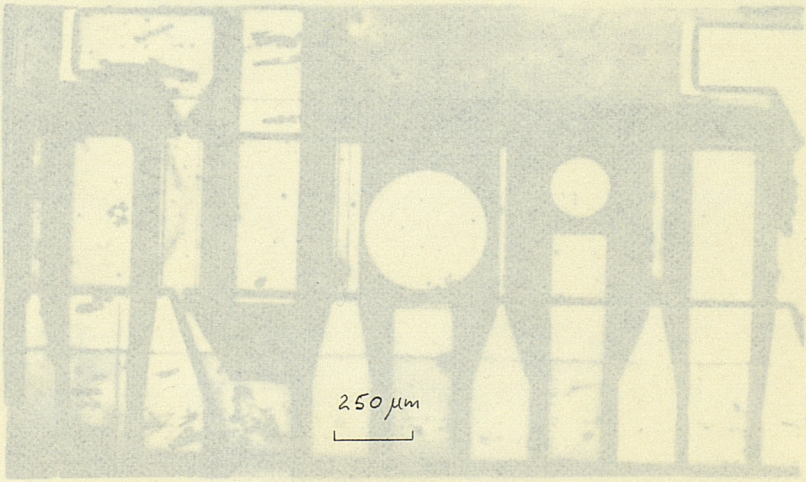

(e) Completed devices

set is repeated in a 12x12 array. All the devices have a channel width of 500μm.

The device fabrication procedure is as follows:-

1. Spin PMD 'superline' positive resist on epitaxial layer and bake at 80°K for 20 minutes,
2. Expose resist with mask of Fig.3.9 (a) to define semiconductor pattern. Etch in $3H_2SO_4:1H_2O_2:1H_2O$. Remove resist with acetone,
3. Deposit 2000Å thick Aluminium film,
4. Spin resist and expose with mask of Fig.3.9 (b) to define source-drain contacts, etc. Etch in Orthophosphoric acid. Remove resist,
5. Deposit Silicon Oxide through metal mask shown in Fig.3.9 (d),
6. Deposit 1000Å Aluminium film,
7. Spin resist and expose with mask of Fig.3.9 (c) to define field plate, etc. Etch in Orthophosphoric acid. Remove resist.

Ocassionally it was found that in step 4 the Orthophosphoric acid attacked the epitaxial InAs, so an alternative procedure in place of steps 3 and 4 is as follows:-

3. Spin positive resist and expose with a double reversal negative mask of Fig.3.9 (b), thus removing resist in Aluminium contact areas,
4. Evaporate Aluminium (2000Å). Remove resist and excess Aluminium by ultrasonic agitation in acetone.

A photograph of devices fabricated on epitaxial InAs is shown in Fig.3.9(e). Only a few slices have been processed in order to demonstrate the feasibility of making such devices, and the measurements have been of a limited nature. It was decided that the effort should be concentrated instead on improving and characterising the epitaxial layers. A contributing factor was the lack of a suitable gate insulator.

3.2.4. Electrical Measuring Apparatus

The measurement set-up employed was arranged so that measurements could be made on the films or on the field effect devices. A Keithley 610B electrometer, with an input impedance greater than 10^{14} ohms, was used to measure the D.C. voltages. The Hall effect and magnetoresistance measurements were carried out either with a 1.5" or a 4" Newport magnet, the latter capable of fields of up to 10,000 gauss with a 3cm gap.

In order to make measurements down to liquid Nitrogen temperatures a vacuum cryostat was constructed in stainless steel. Temperature control was achieved with a Nichrome wire heater on a copper sleeve, and measured with a copper/constantan thermocouple. A vacuum better than 10^{-1} torr was obtained using a mechanical pump. Temperatures down to 65^{o}K were achieved by pumping on the liquid Nitrogen.

4. PHYSICAL INVESTIGATIONS

4.1. X-Ray Diffraction

4.1.1. Diffractometer Studies

X-ray diffractometry was used to study the texture of the polycrystalline films and to obtain lattice constant measurements of both, the polycrystalline and epitaxial layers.

A schematic diagram of the Siemens Kristalflex diffractometer table is shown in Fig. 4.1. The target is copper and the output of the monochromator and slit system is Cu kα, which has a weighted average wavelength $\lambda = 1.54178\text{Å}$ ($k\alpha_1$ is given twice the weight of $k\alpha_2$). The specimen is rotated at ϕ rads/sec and the detector at 2ϕ rads/sec, thus satisfying the Bragg conditions $n\lambda = 2d\sin\theta$, at the appropriate angle θ, for crystal planes parallel to the substrate. The output of the detector is fed to a pulse-height analyser and then to a counter and chart recorder, which is synchronised to the detector rotation.

In order to obtain an accurate value of the lattice constant, the step scan arrangement was employed. By using an appropriate reduction ratio, the table is rotated in steps of 0.005° or 0.05° at intervals of 0.1, 1.0, and 10 minutes, depending on the accuracy required. At the end of each interval the number of counts is printed on a console, and the table is stepped to the next position.

The step scan is usually carried out at a high angle peak since, for a given error in θ, the error in $\sin\theta$ is smaller as θ approaches $\pi/2$ radians. However since the higher angle peaks of these polycrystalline

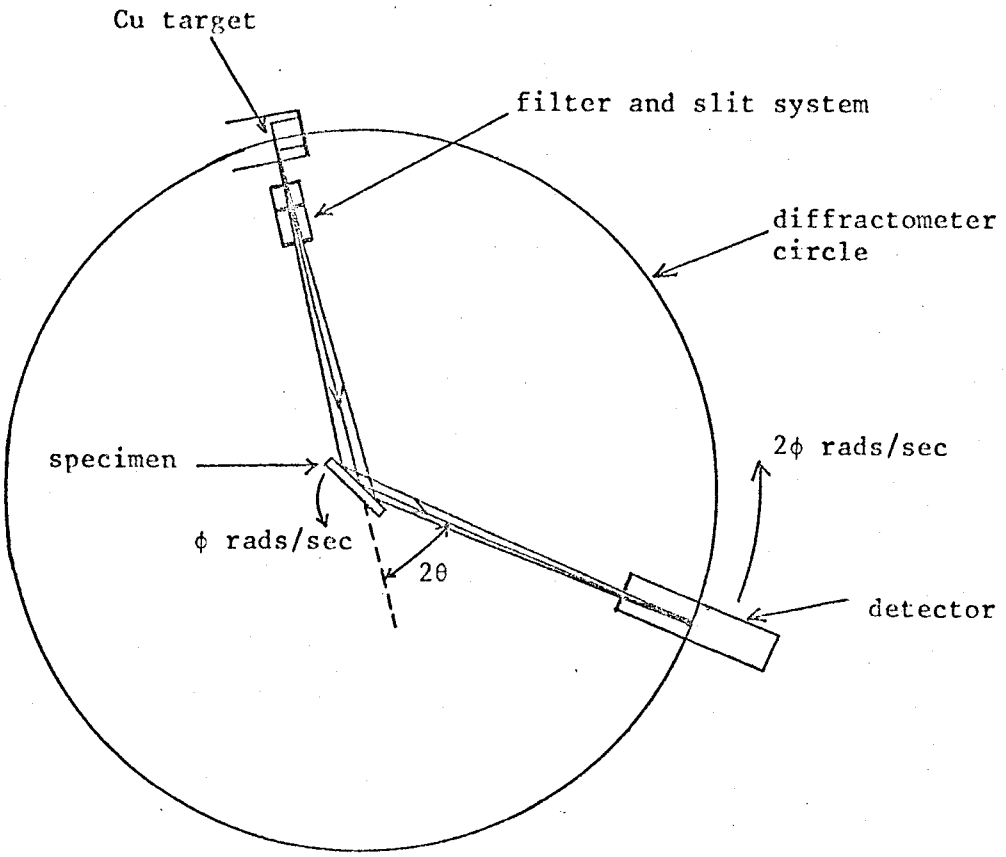

(a) Schematic diagram of diffractometer table

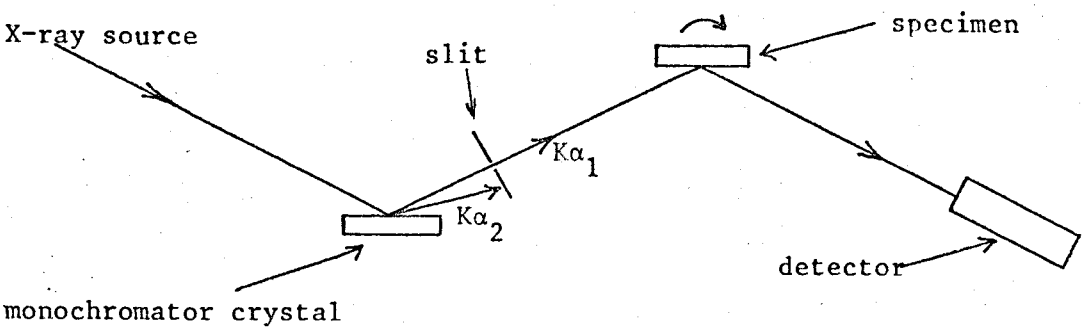

(b) Double crystal diffractometer to obtain rocking curves

Fig.4.1

films were usually broader and of lower intensity, the (111) peak was used. In order to eliminate errors due to mechanical backlash, the stepping was carried out in both directions through the peak. This was repeated at an angle of $-\theta$ degrees to compensate for zero off-set, because the incident X-rays and the detector may not be parallel when θ is zero. The average of these four peaks was then used to calculate the lattice constant.

Although transmission electron microscopy, coupled with diffraction is an extremely powerful method to study the defect structure of crystals, it is essential to use thin samples, less than a few thousand angstroms thick. With epitaxial films, such as InAs on GaAs, this requires jet etching from the back of the substrate until the required thickness is achieved, which is a delicate and time consuming process.

A very useful technique for studying the perfection of epitaxial layers, which does not require thinning, is by X-ray rocking curves obtained with a double crystal diffractometer. The first crystal is the monochromator, which should be good quality resulting in a source of highly collimated X-rays. The second is the specimen to be examined. Ideally, the two crystals are of the same orientation, resulting in the parallel arrangement shown in Fig.4.1.(b). However, this may not always be possible when examining different epitaxial orientations, unless the appropriate monochromating crystal orientations are available. A perfect crystal combination results in a peak width

of the order of a few seconds to a few tens of seconds of arc[4.1,4.2]. If the specimen has low angle grain boundaries, a considerable increase in the peak width will then be observed. Apparently, with a peak width of about 25" low angle grain boundaries with tilts down to 5 - 10" can be detected[4.1]. The peak width and the total integrated intensity, i.e. the area under the peak, are therefore very sensitive to crystal perfection. However, since facilities to obtain rocking curves were not readily available, we have not been able to make such measurements.

4.1.2. Texture Of Polycrystalline InAs Films

Fig.4.2 is part of a typical chart record of a 5000Å polycrystalline film, which shows a strong (111) peak. In order to obtain a comparison, table 4.1 gives the relative intensities of an InAs powder pattern from the ASTM Powder Data File, together with the relative intensities of sample C168, for all reflections of the F.C.C. structure upto the (440) peak. The intensities are given relative to the (111) peak, which is arbitrarily set to 100. This indicates clearly a strong (111) texture in these films, i.e. the crystallites are orientated with their <111> axes perpendicular to the substrate surface plane.

The intensity of the (111) peak relative to the (220) peak was found to increase considerably with higher annealing temperatures. The results in table 4.2 are the relative intensities, I(111)/I(220), for several films, the higher values corresponding, in general, to higher anneal temperatures.

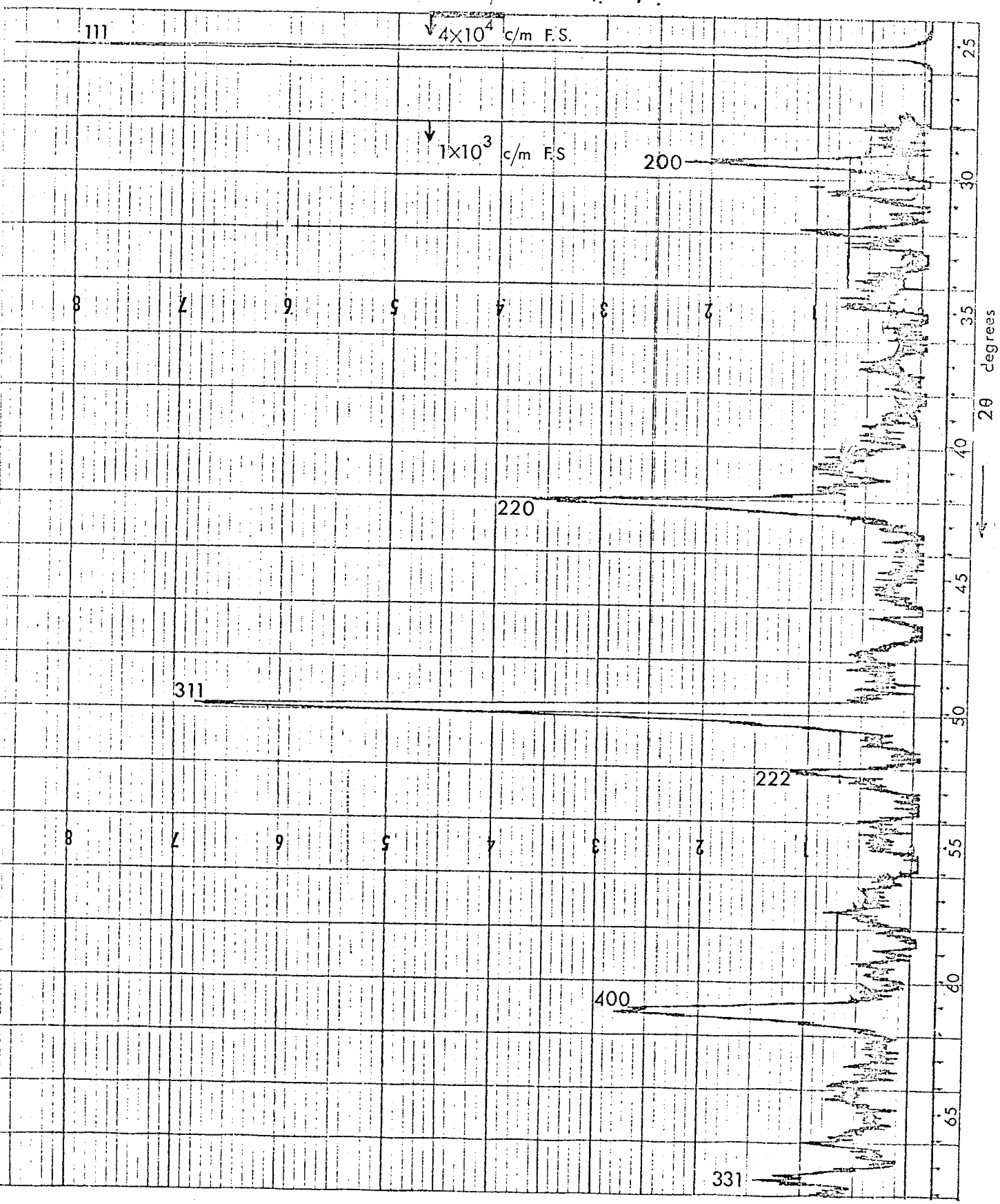

Fig.4.2 Typical diffractometer chart record of a polycrystalline InAs film on glass. Deposited at 500 °C. Annealed at 520 °C

2θ (approx.)	Reflecting Plane	Peak Intensity I counts/min.	I/I(111)x100 intensity relative to (111) peak	I/I(111)x100 from ASTM Powder Data File InAs card 15-869
25.4	111	8.0×10^4	100	100
29.5	200	1.5×10^2	0.188	8
42.3	220	3.6×10^2	0.450	60
50.0	311	4.9×10^2	0.612	40
52.3	222	2.8×10^2	0.350	2
61.3	400	1.0×10^2	0.125	10
67.5	331	2.0×10^2	0.250	14
77.25	422	3.0×10^2	0.375	16
82.75	511 333	3.3×10^2	0.412	10
92.2	440	~ 0.0		8

Table 4.1

Comparison of relative intensities with ASTM Powder Data File.Sample C168.

Since the crystallite size of the thick films is usually large, it was not possible to obtain an estimate of the size from the line broadening, since the machine broadening is of the same order or greater. This method is suitable only with a crystallite size of about 1000Å or less[4.3].

Sample	I(111)/I(220) relative intensity	I(111)/I(220) from ASTM Powder Data File
C168	222	1.67
C231	8	1.67
C299	26	1.67
C307	173	1.67
C317	92.2	1.67

Table 4.2

Intensity of (111) peak relative to (220) peak of several polycrystalline samples.

4.1.3. Lattice Constant Measurements

Polycrystalline InAs Films

A plot of the step scan data indicated that there was a very small error, of the order of 0.01°, between the forward and reverse scan peaks,

at one position. However, there was a difference of approximately 0.20° between the average of the peaks on each side of θ = 0, due to the zero offset, (see Fig.4.3). Apparently the accuracy of the system, without any temperature control, is of the order of ± 0.0002Å. Also, the variation of lattice constant with temperature is about 0.0001Å/°C. It is unlikely that the sample temperature varies by more than about ± 1°C after the system has been running for a few hours. Hence the results should be accurate to the third decimal place.

Taking the average of the four peaks, the lattice constants of several polycrystalline samples have been calculated to five digits and the results are presented in table 4.3.

Substrate	Sample	Average θ (111) peak	Lattice Constant a Å
Corning 7059	C168	12.700°	6.0672
Corning 7059	C231	12.712°	6.0690
Corning 7059	C299	12.720°	6.0639
Corning 7059	C307	12.672°	6.0854
Corning 7059	C317	12.695°	6.0756

Table 4.3

Results of lattice constant measurements on polycrystalline InAs Films

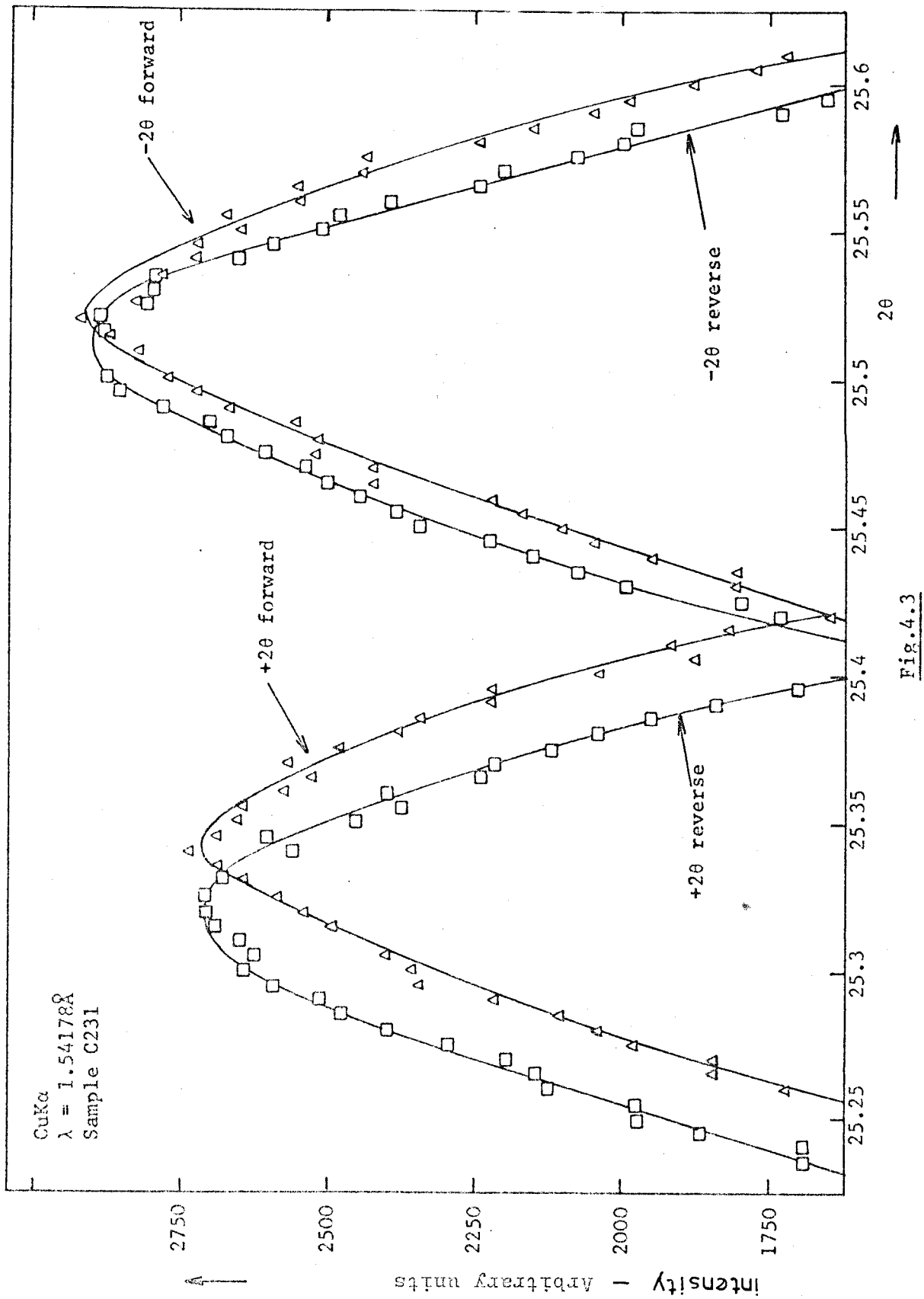

Fig.4.3

Plot Of X-ray Step-Scan Diffractometer Data For A Polycrystalline Film

The lattice constant of melt grown InAs, given in the literature[4.4], is 6.05838 ± 0.00005Å at 25°C, which indicates a large difference with the results in table 4.3. Johnson[4.5] has measured a value of 6.063Å in polycrystalline InAs deposited on corning glass by the same method.

The larger value measured could be explained by differences in thermal expansion coefficients of the substrate and deposit. The average expansion coefficient of corning 7059 glass is $4.6 \times 10^{-6}/^{\circ}C$ and that of InAs is $6.67 \times 10^{-6}/^{\circ}C$. When the sample is cooled from about 600°C after deposition, the substrate contracts less then the film material, thus causing a strain in the film. If we assume this difference in contraction is taken up entirely by strain in the film, and the strain is uniform across the film thickness, then a simple calculation shows that the lattice constant at 25°C should be 6.0658Å. Although this figure compares favourably with some of the results in table 4.3, it is difficult to believe that the strain is uniform across the film thickness.

Epitaxial InAs

The usual method for lattice constant measurements of a single crystal is to use a powder of the specimen in the diffractometer. However, since this is a destructive method and because our films are thin, we have obtained a diffractometer step scan by mounting directly, the GaAs substrate with the epitaxial layer, on a glass plate which fits into the specimen holder of the diffractometer.

Chart records of epitaxial layers on (111) GaAs gave a very strong (111) peak and no other InAs peaks. However, probably due to some penetration of the substrate, a weak (111) GaAs peak was observed.

Since the goniometer in the diffractometer did not have an arrangement to tilt the specimen about a horizontal axis parallel to the film surface it was not possible to align the specimen accurately. Therefore, the lattice constant measurements were inaccurate. For example, values of 6.05Å and 6.12Å were obtained for samples G339 and G334 respectively. Clearly, these have very large measurement errors. Since these films are several microns thick, it is unlikely that the lattice mismatch has any effect on the deposit.

4.1.4. Laue Back Reflection To Determine Orientation Of Epitaxial Layers

Several thick epitaxial InAs films and some GaAs substrates have been examined by Laue back reflection, in order to determine the orientation of the layers. The X-ray source was unfiltered radiation from a copper target. The photographic film and sample surface were set parallel and 3cm apart, with the X-ray beam perpendicular to this plane. All the crystallographic planes of one zone will give rise to a set of spots on the film which lie on a straight line or hyperbola[4.3]. Using a Greininger chart and a Wulff nett, it is then possible to construct a sterographic projection for a particular sample and the orientation of the surface plane obtained.

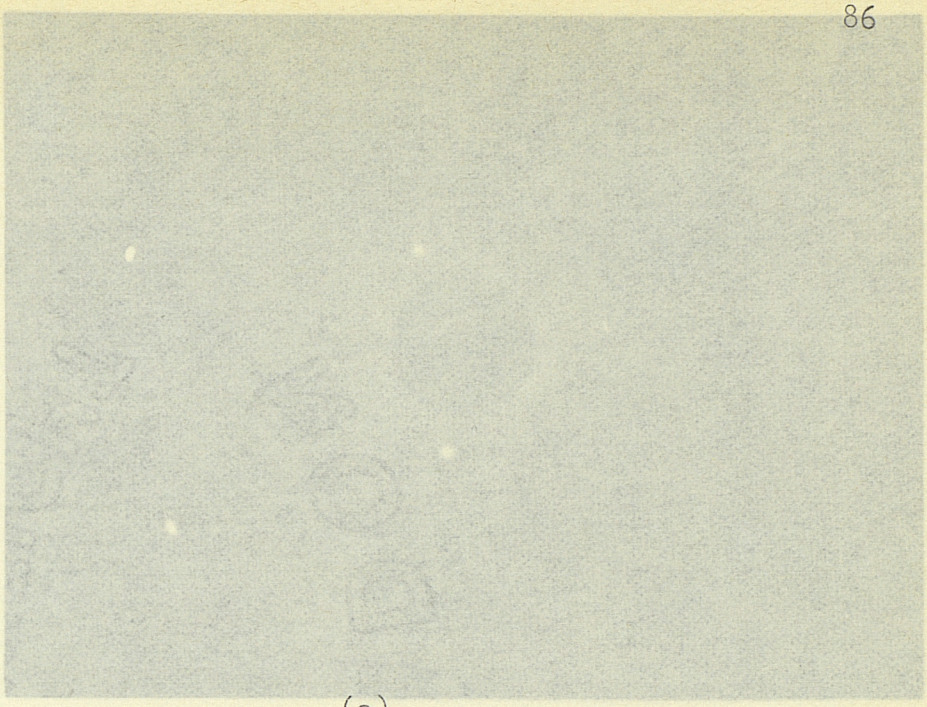

(a)

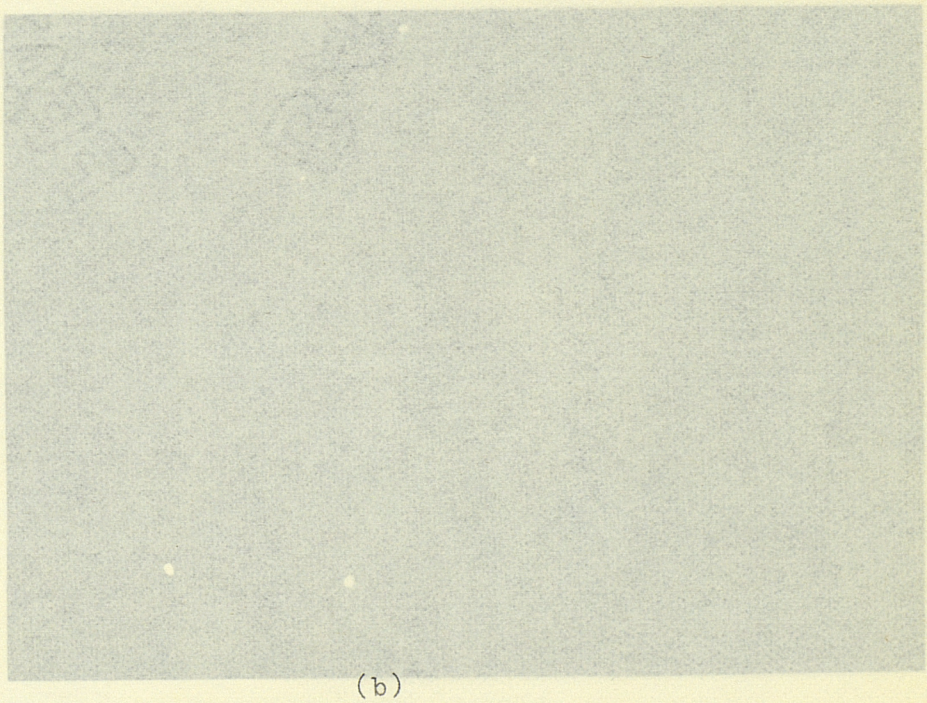

(b)

Fig.4.4
Laue back reflection photographs of epitaxial InAs,
(a) (100), (b) (111) orientation

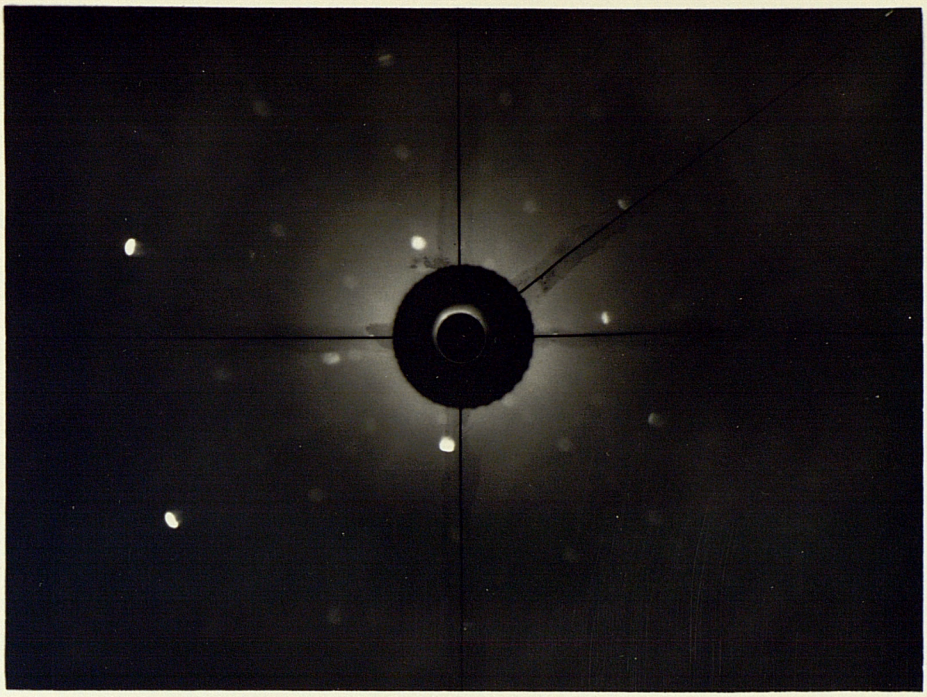

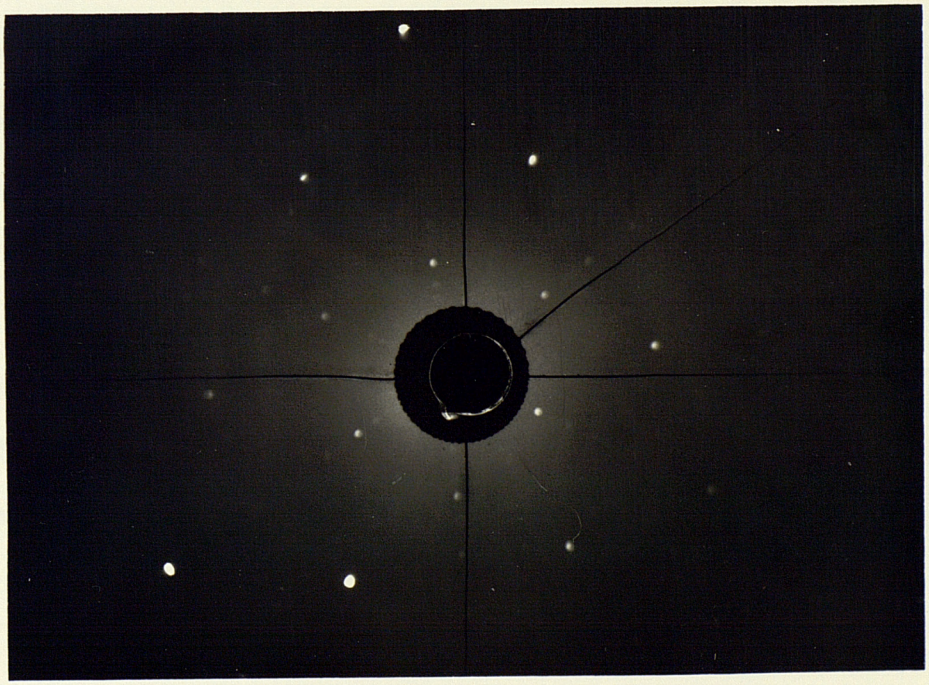

Fig.4.4 shows typical Laue photographs of (100) and (111) epitaxial InAs which indicate the layers are single crystal. By plotting stereographic projections they were found to be of the order of 2^{o} OFF singular orientation, which is the same as the substrate misorientation.

4.2. Electron Microscopy

4.2.1. Transmission Electron Microscopy and Diffraction

Several polycrystalline films, less than 3000Å thick, were examined by transmission electron microscopy and diffraction in an AEI EM6G microscope. The films were stripped from the glass substrates by dipping them in dilute Hydrofluoric acid, ($3H_2O$:1HF at R.T. for approximately 10 minutes), which attacks the glass but does not appear to etch the InAs. Sections of the film which floated off were rinsed in distilled water and placed on a microscope grid.

Figs.4.5 and 4.6 show bright field micrographs of two polycrystalline samples, together with their diffraction patterns. Fig.4.7 illustrates the ring pattern to be expected for InAs, with a camera constant $\lambda L = 1.366$ cmÅ (100 KV electrons). The diffraction patterns indicate that the films have condensed in the cubic phase with perhaps a (111) preferred orientation, since these are the most intense rings. However, the intensity of the various rings is also a function of the structure and multiplicity factors.

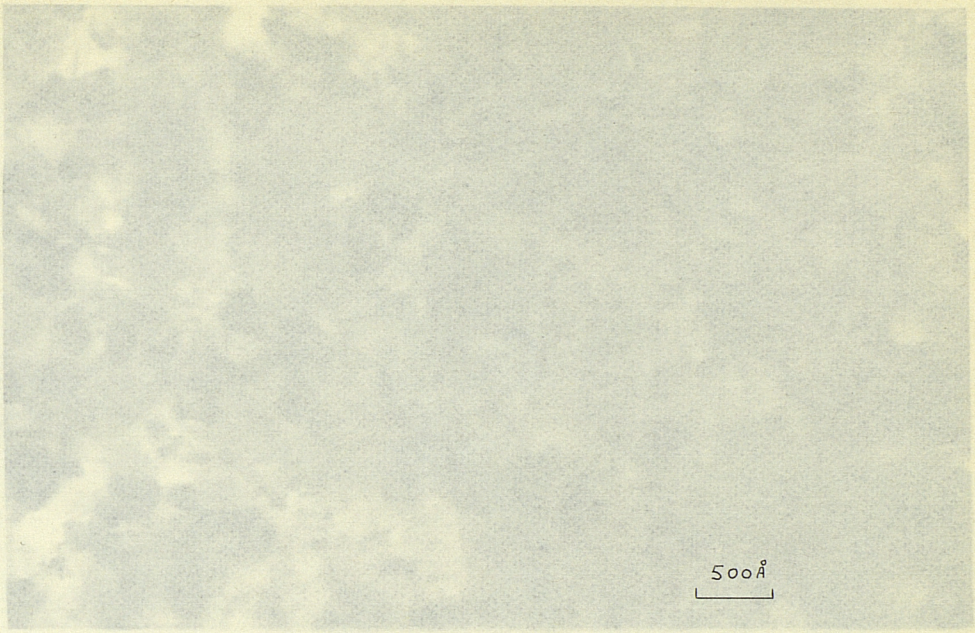

(a) Bright field transmission electron micrograph of a thin polycrystalline InAs film on glass, sample C259-500Å. Deposited at 400 °C, no anneal

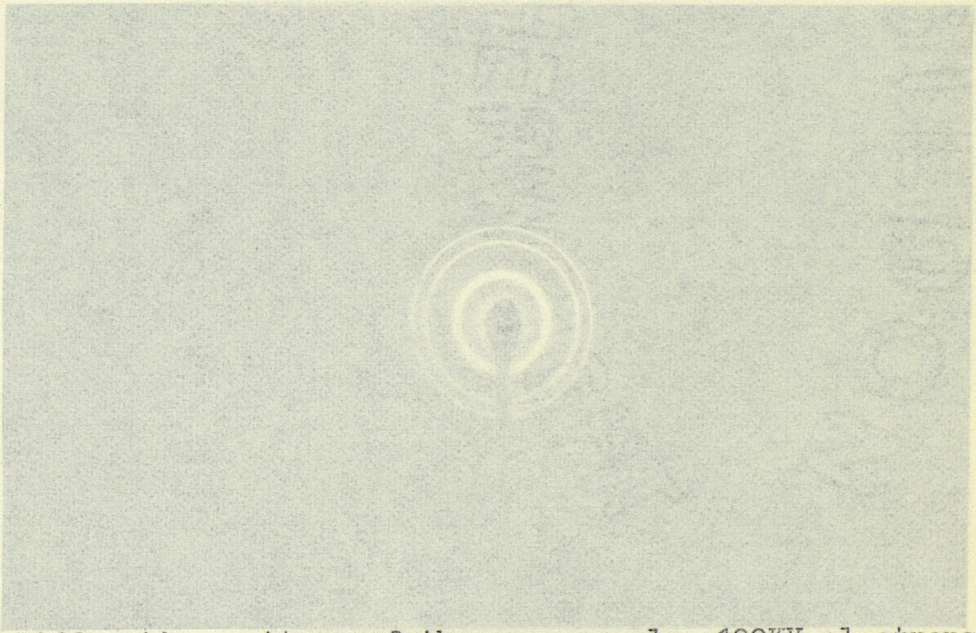

(b) Diffraction pattern of the same sample. 100KV electrons

Fig.4.5

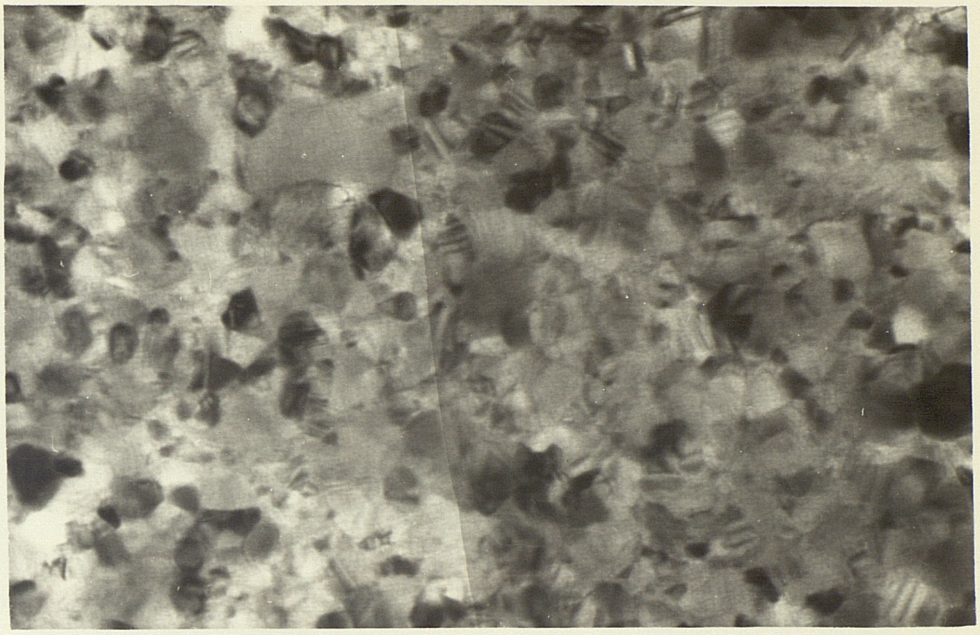

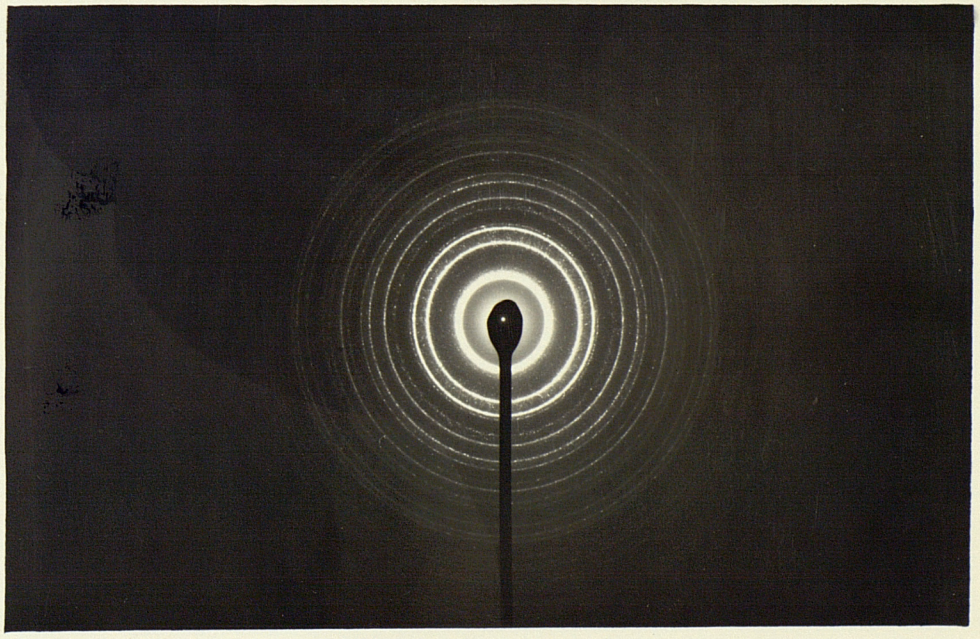

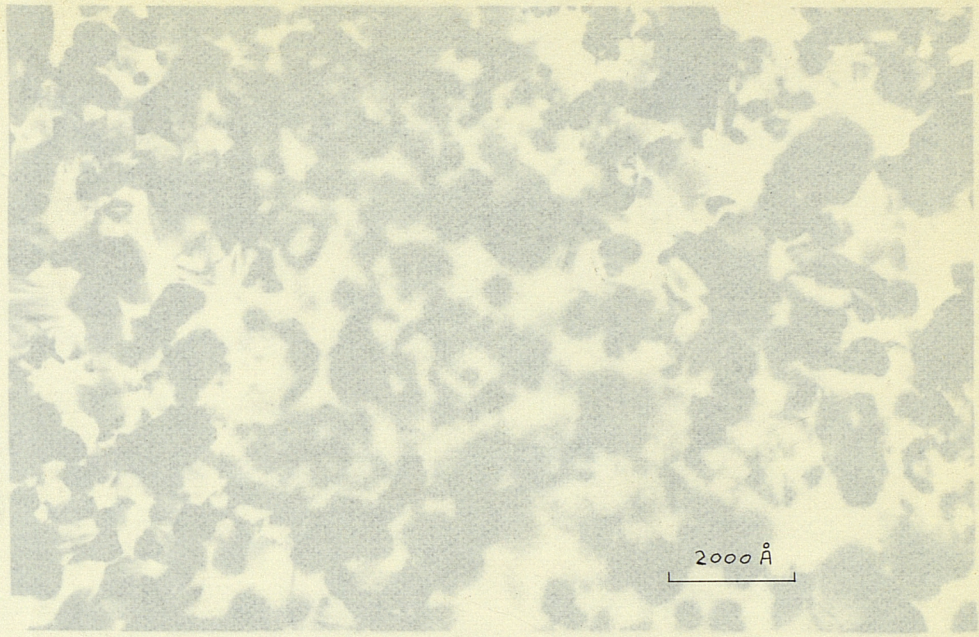

(a) Bright field transmission electron micrograph of a 500Å polycrystalline InAs film, deposited at 525 °C and annealed at 595 °C for 10 minutes. Sample C228

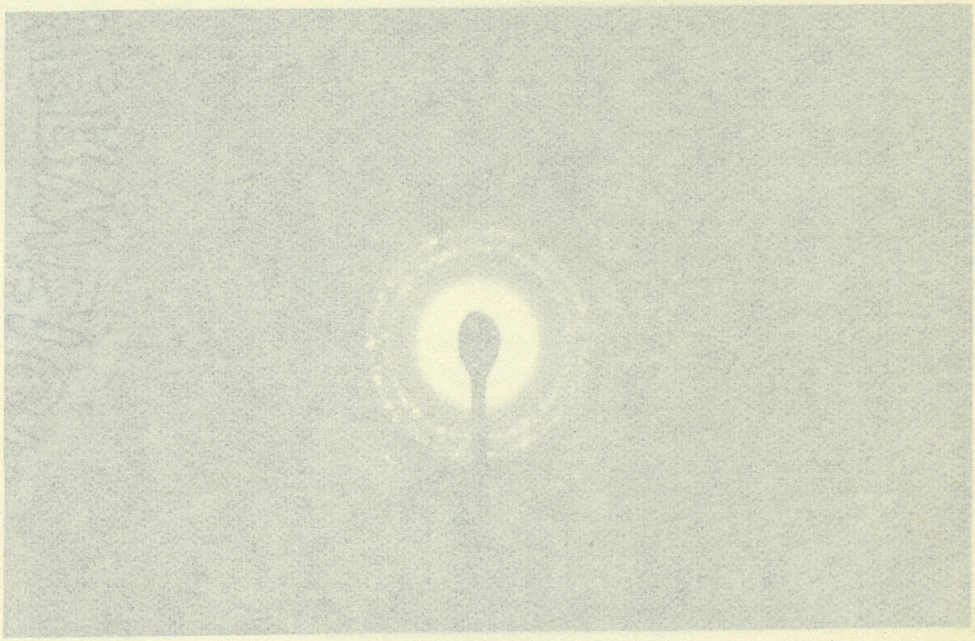

(b) Diffraction pattern of the same sample. 80 KV electrons

Fig.4.6

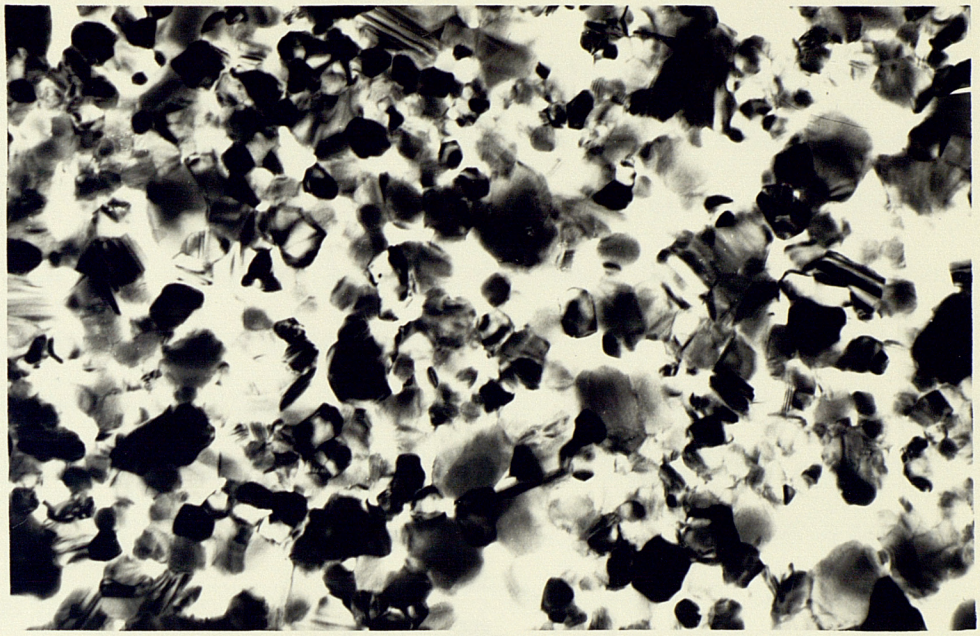

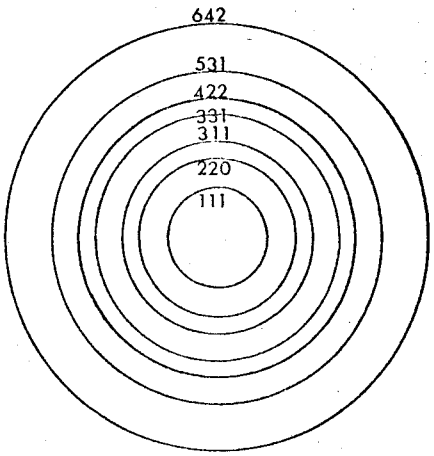

Fig.4.7

Indexed ring pattern of Fig.4.5(b), showing some high intensity FCC refelctions. 100 KV electrons. Diffraction constant - 1.365 cm-Å. Magnified x1.64

By obtaining an average of the measured crystallite sizes from the electron micrographs of the thin films and the optical micrographs of the thicker layers, it has been established that the crystallite size is of the same order as the fimm thickness, when the films are annealed at the highest temperature possible without dissociation taking place. Fig.4.8 shows the variation of the average grain size with film thickness. It appears these films exhibit "growth orientation", i.e. the grain size is of the same order as the film thickness. If the films are deposited at a low substrate temperature, the grain size may be very small, but annealing at a higher temperature increases the size to the point where it is limited by the film thickness.

4.2.2. Reflection Electron Diffraction Of Epitaxial InAs

Although Laue back reflection can give an indication of single crystallinity, it is only suitable if the epitaxial layer is more than 5-10μm thick, otherwise the X-ray beam penetrates the substrate. Also, Laue photographs provide very little information on crystal defects. Therefore, most of the epitaxial layers were examined by glancing angle high energy reflection electron diffraction, which also permits viewing the specimen at different azimuths. Initially, the EM6G microscope was used, but it did not have a proper reflection stage. Hence, a crude specimen holder, with no facilities for tilting, had to be used. More recently, many samples were examined in a Hitachi H.U.11 microscope, which has a proper reflection stage with facilities to

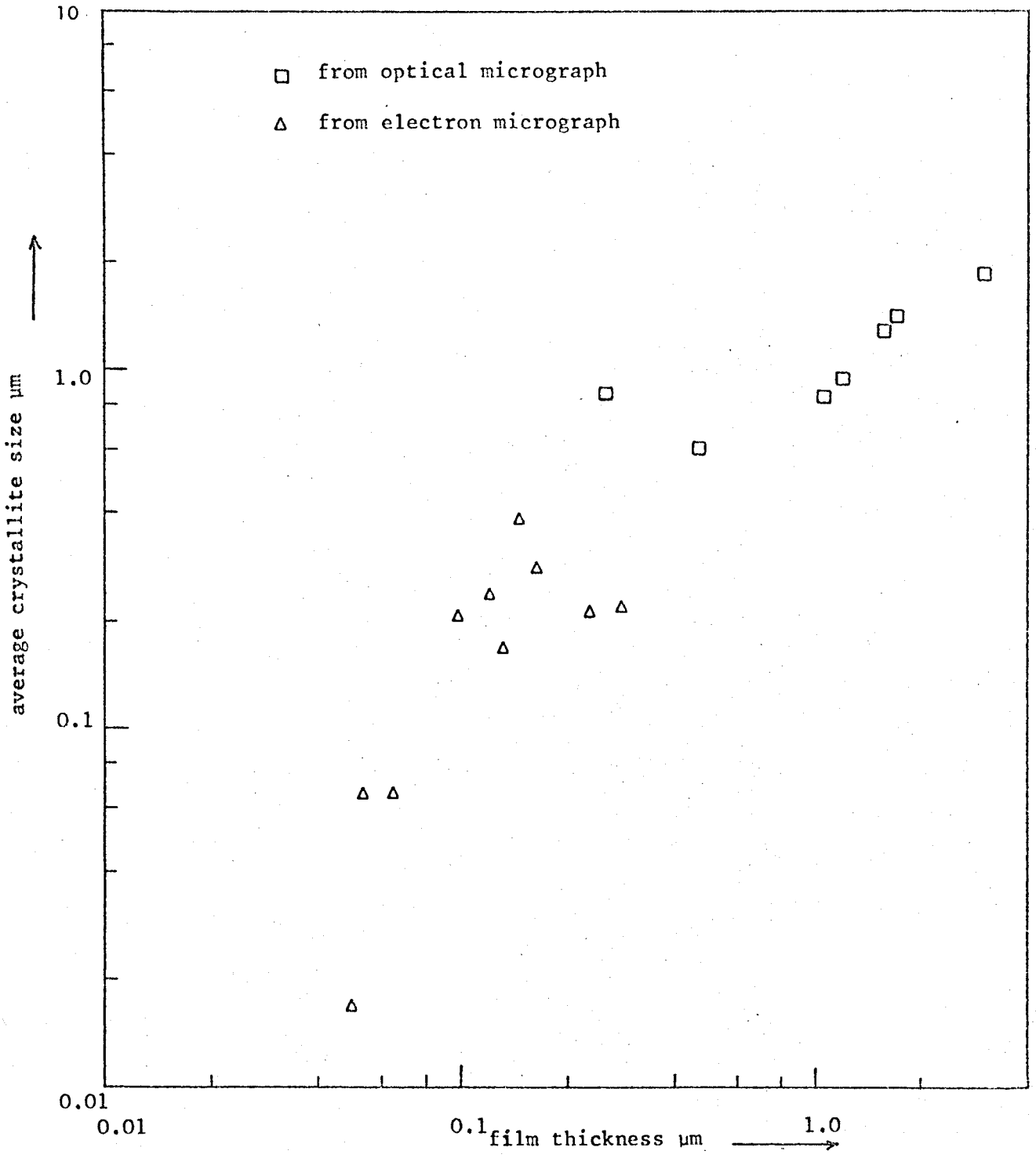

Fig.4.8

Average Crystallite size As A Function Of Film Thickness, Of Polycrystalline InAs On Glass

insert a Gold standard for calibration without removing the specimen being examined. The diffraction patterns were taken at 75kV, giving a diffraction constant $\lambda L = 1.97 cm\mathring{A}$.

Fig.4.9 shows diffraction patterns of InAs films on {111} and {110} GaAs deposited at 260°C and 400°C respectively. The first clearly indicates the film is a highly orientated polycrystalline sample, while the second shows a large number of extra spots, probably due to multiple twinning.

Films deposited at higher temperatures, but still below the optimum value, result in layers which are epitaxial, but with considerable twinning. Fig.4.10(a) is a pattern of an InAs film on (100) GaAs, sample G350, viewed at $[\bar{1}01]$ azimuth, i.e. the electron beam is along this crystallographic direction. The many satellite spots occuring at one third the distance between the main matrix spots are due to twinning[4.6]. The twin axes in FCC sphalerite structure materials are usually along <111> directions. Since the diffraction pattern represents the intersection of the Ewald sphere with the reciprocal lattice[4.7], directions along the diffraction pattern represent particular crystallographic directions. Now, rotation of a twin by 180° about the twin axis should bring it in coincidence with the matrix orientation. Therefore, if this is performed on the diffraction pattern, the twin spots should coincide with the matrix spots as shown in Fig.4.11(a). Hence, all the satellite spots in Fig.4.10(a) can be identified due to simple twinning. It should be noted that the above case occurs

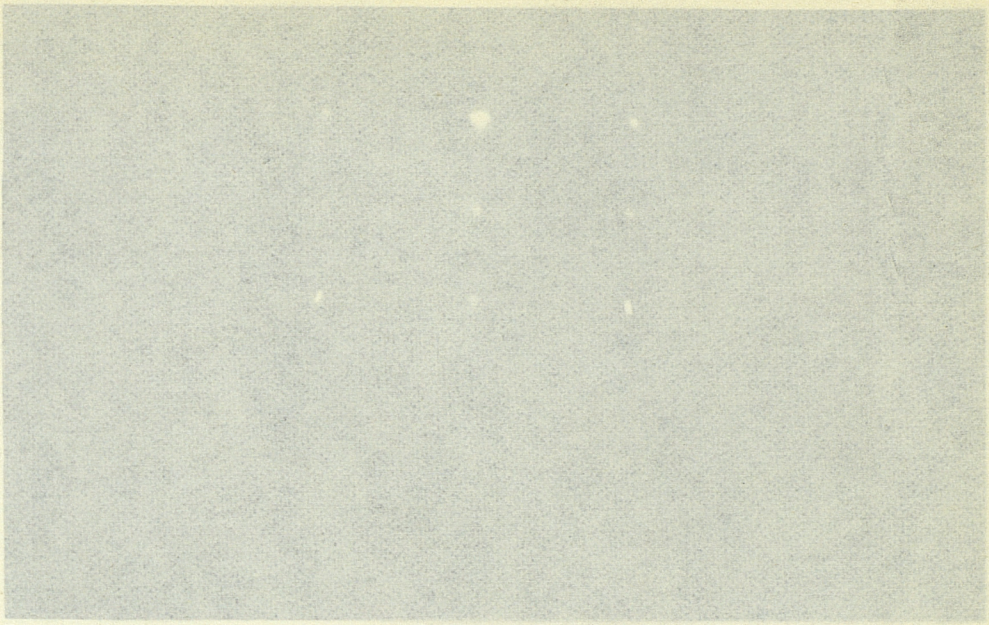

(a) Reflection electron diffraction of an InAs film on {111} orientation GaAs, deposited at 260 °C

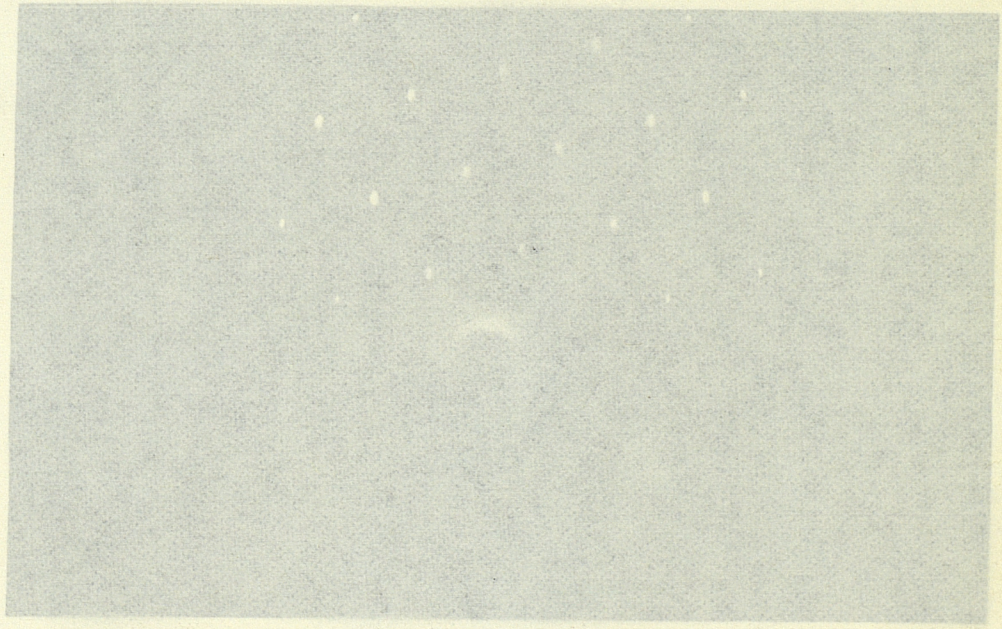

(b) RED, InAs on {110} GaAs, deposited at 400 °C

Fig.4.9

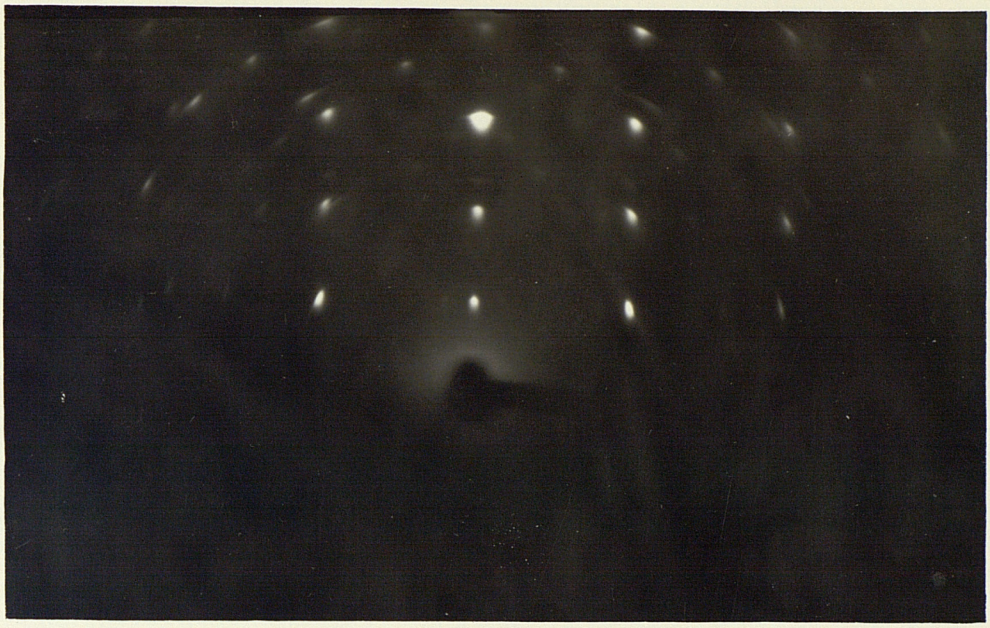

(a) Electron diffraction of a highly twinned InAs film on (100) GaAs, sample G350 deposited at 540 °C. Seen at $[\bar{1}01]$ azimuth.

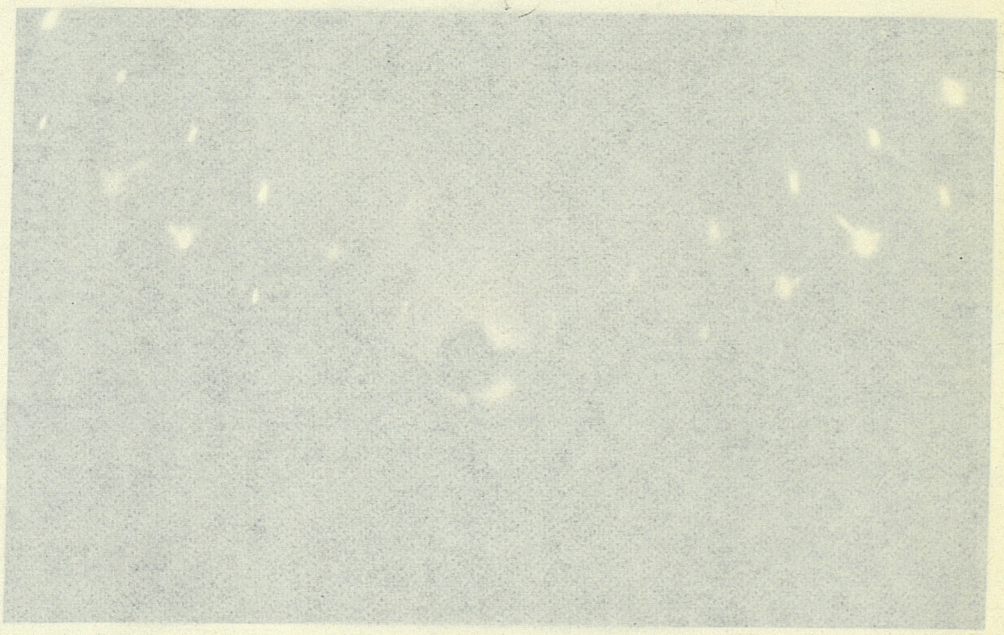

(b) Same as above but viewed at $[10\bar{1}]$ azimuth.

Fig.4.10

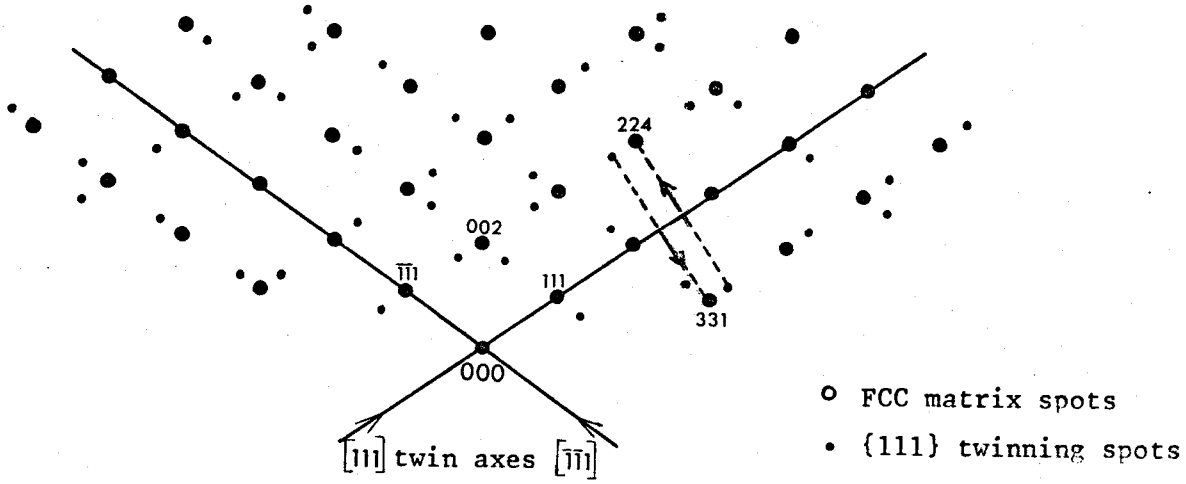

(a) Diffraction pattern of Fig.4.10(a) indicating twinning spots and axes

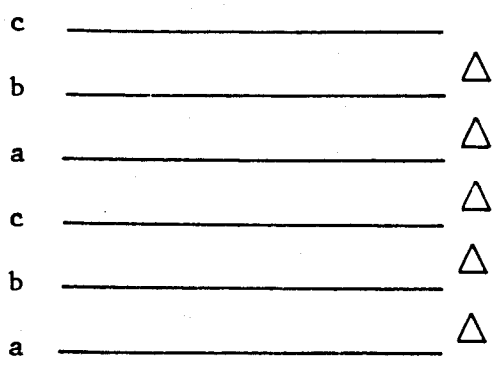

(b) Normal FCC stacking sequence along <111> directions

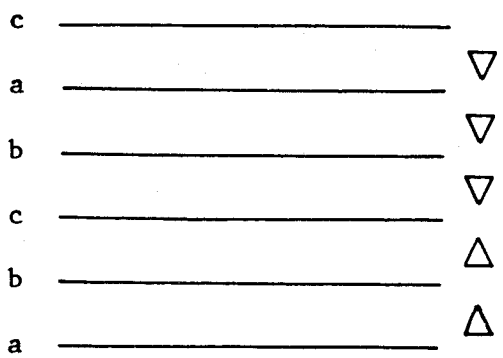

(c) Successive stacking faults which results in twinning

FIG.4.11

only when the beam direction is perpendicular to a twin axis. The indices of the twin spots can be obtained easily in this case, once the matrix spots have been indexed. Thus, if (hkl) is a matrix reciprocal lattice point, twinning about (pqr) transforms it to the point (h'k'l') given by[4.6]:

$$h' = \frac{p(ph + 2qk + 2rl) - h(q^2 + r^2)}{p^2 + q^2 + r^2} \quad \ldots(4.1)$$

$$k' = \frac{q(2ph + qk + 2rl) - k(p^2 + r^2)}{p^2 + q^2 + r^2} \quad \ldots(4.2)$$

$$l' = \frac{r(2ph + 2qk + rl) - l(p^2 + q^2)}{p^2 + q^2 + r^2} \quad \ldots(4.3)$$

For example, the matrix spot (331) in Fig.4.11(a) gives rise to the twin spot 1/3(5,5,11) due to twinning about (111), by putting hkl = 331 and pqr = 111 in equations 4.1 to 4.3. When the same sample, G350, was viewed at 180° from that in Fig.4.10(a) streaking occured as shown in Fig.4.10(b). The difference in these two patterns is, perhaps because the (100) surface plane is not perpendicular to the specimen rotation axis. Apparently, a high density of stacking faults can result in a relaxation of the Bragg condition due to a limitation of the extent of the diffraction grating[4.8]. If this limitation is strongly orientation dependent, the reciprocal lattice points are extended in some directions, and in extreme cases become an assemblage of intersecting rods. This results in streaking under certain conditions and the

streaks run along <111> axes, i.e. the directions of the stacking faults. The normal stacking sequence along these directions, in an FCC structure is abcabc ..., as shown in Fig.4.11(b). A succession of stacking faults could result in a stacking sequence, abcbac ....., shown in Fig.4.11(c). This is in fact a reflection twin with C the twin plane, and the twin axis perpendicular to this plane. (In an FCC structure a reflection twin is also a rotation twin and due to the high symmetry in cubic structures, a 60^{o}C rotation is equivalent to a 180^{o} rotation of the twin).

Since $p^2 = q^2 = r^2 = 1$, the reciprocal lattice twin point (h'k'1') given by equations 4.1 to 4.3 reduces to:

$$\left(\frac{1}{3p}(-ph+2qk+2rl), \frac{1}{3q}(2ph-qk+2rl), \frac{1}{3r}(2ph+2qk-rl)\right) \quad ...(4.4)$$

As shown above, the reciprocal lattice point (331) gives rise to the twin spot $\frac{1}{3}(5, 5, 11)$, which can be written:

$$(331) \rightarrow \frac{1}{3}(5,5,11) \rightarrow (224) - \frac{1}{3}(111)$$

i.e. the twin of (331) is displaced from the matrix point (224) by $-\frac{1}{3}(111)$. Thus it can be seen that the twin points divide the distance between matrix points in threes, i.e. the twin points are given by:

$$(u \pm \frac{1}{3}p, \; v \pm \frac{1}{3}q, \; w \pm \frac{1}{3}r) \quad ...(4.5)$$

where (uvw) is a matrix reciprocal lattice point. However, not all such points are permissible. Pashley and Stowell[4.14] have shown that the two conditions to be satisfied are:

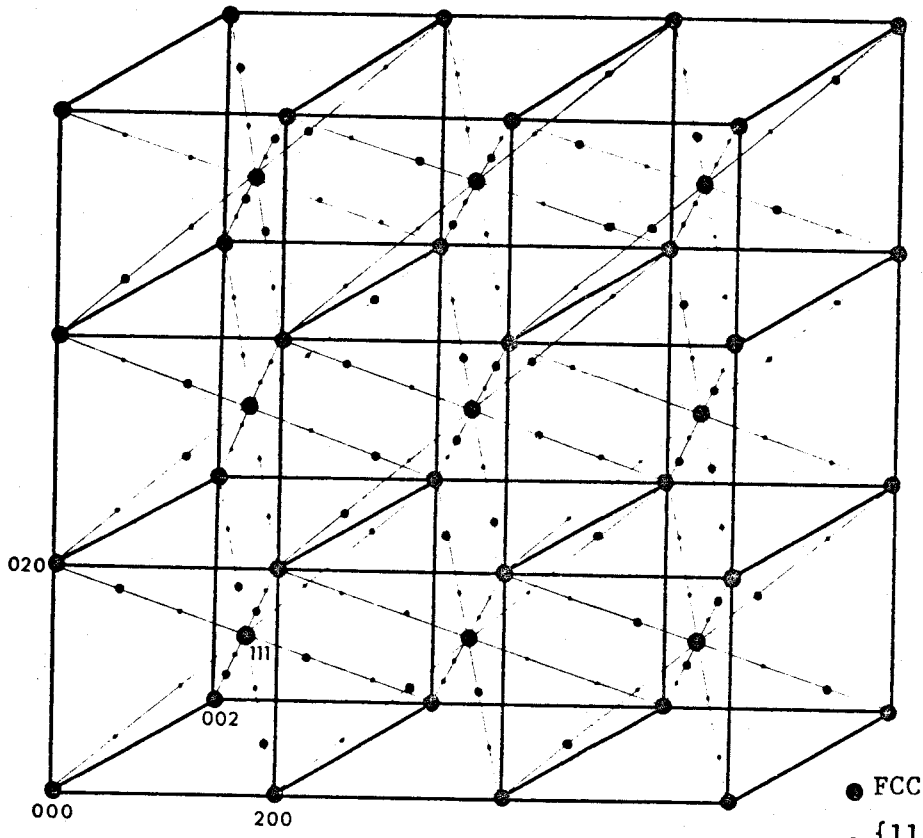

(d) Reciprocal lattice for an FCC crystal including points due to twinning. The extra spots are due to double diffraction (after Pashley and Stowell, ref.4.14)

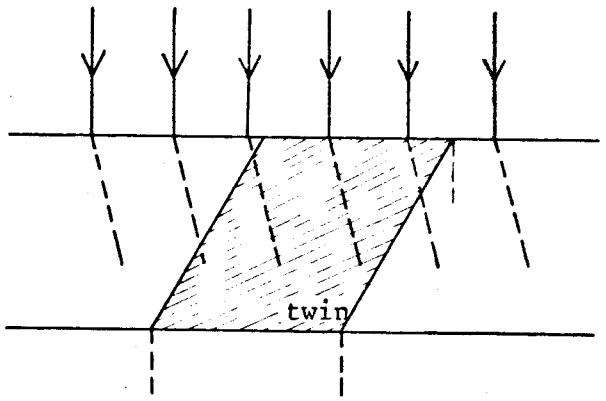

(e) Schematic diagram to illustrate matrix-twin double diffraction

FIG.4.11

1. $pu + qv + rw = \pm (3N+1)$ ...(4.6)

   where N is an integer, either positive or negative.

2. The distance of an allowed twin reciprocal lattice point from the origin must be equal to that of an allowed matrix reciprocal lattice vector. For example, if (uvw) = (220), then the left hand side of equation 4.5 gives 4, 0, 0, -4, for the twin planes (111), $(\bar{1}11)$, $(1\bar{1}1)$, and $(\bar{1}\bar{1}1)$. Only the first and last values are acceptable, with N = +1. The second condition above will allow only the postive sign in 4.5 for twinning about (111) and the negative sign for twinning about $(\bar{1}\bar{1}1)$, i.e. the twin points are

$$(220)+\frac{1}{3}(111) \quad \text{and} \quad (220)-\frac{1}{3}(\bar{1}\bar{1}1)$$

   By this method all the twin points can be deduced, and this is shown in Fig.4.11(d), which is a reciprocal lattice for an F.C.C. crystal. Since, by rotating, or tilting, the specimen in diffraction one can explore the whole of the reciprocal lattice, the above method permits an easy deduction of the twin spots.

Thus, when sample G350 was viewed slightly off an [001] azimuth the diffraction pattern shown in Fig.4.12(a) was obtained, in which some of the matrix points were surrounded by up to four satellite spots. One or two of the satellite spots around each main point are primary twin spots and the rest are due to double diffraction. Apparently, it is geometrically favourable for electrons diffracted

(a) RED of epitaxial InAs on (100) GaAs, sample G350, viewed at a small angle off an [001] direction.

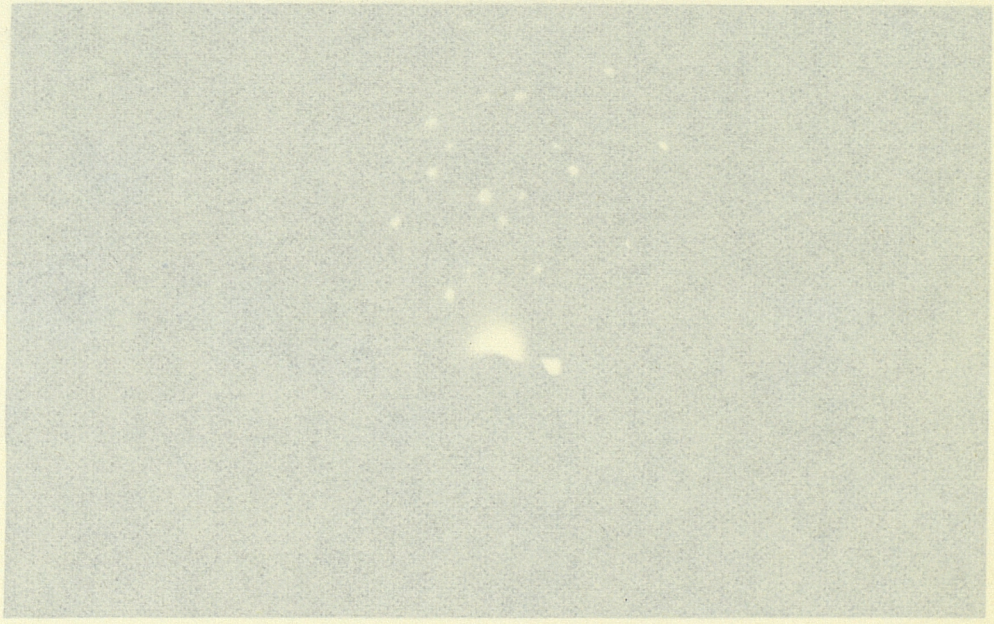

(b) RED of epitaxial InAs on {110} GaAs, deposited at 595 °C. [101] azimuth. Note the high intensity twin spots.

Fig.4.12

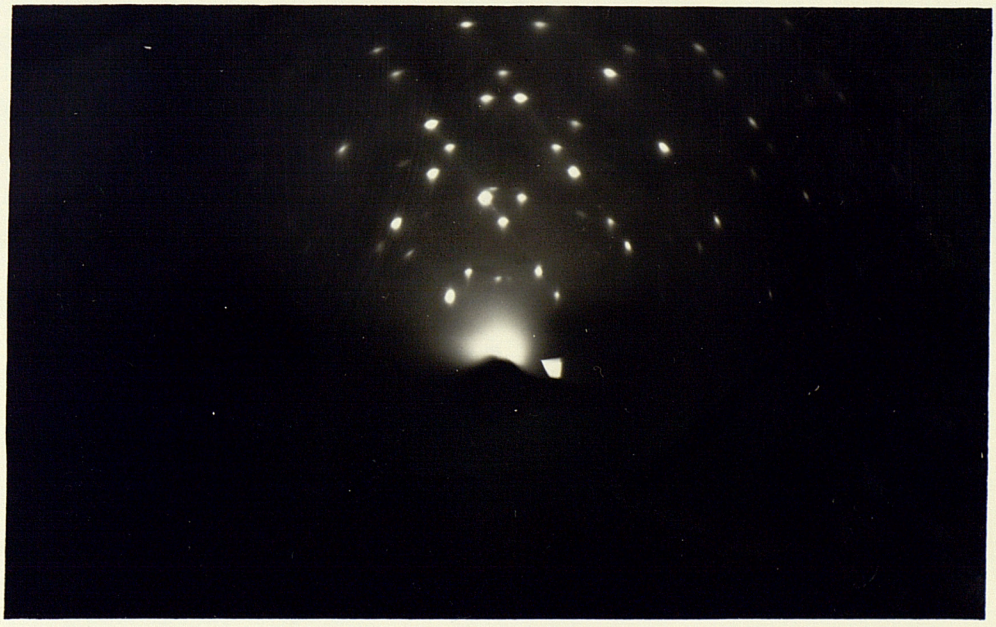

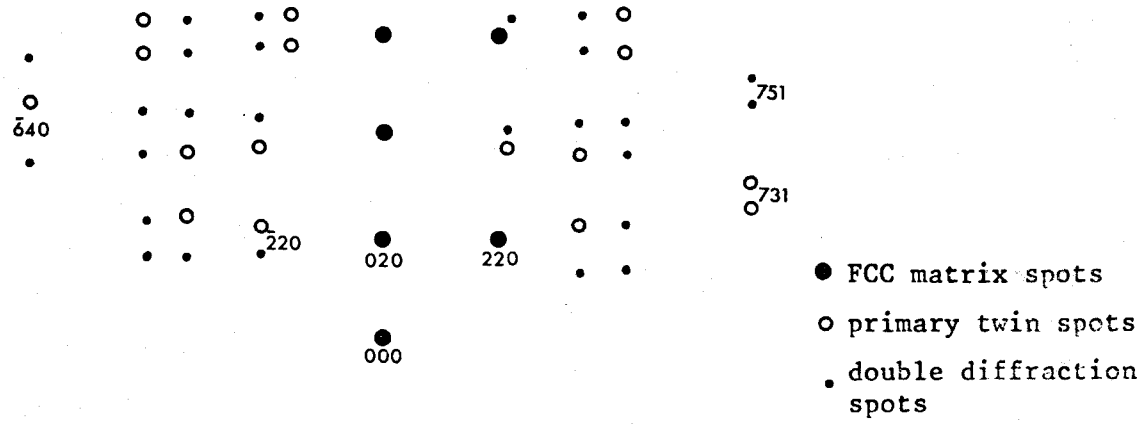

(c) Indexed pattern of Fig.4.12(a) showing primary twin and double diffraction spots

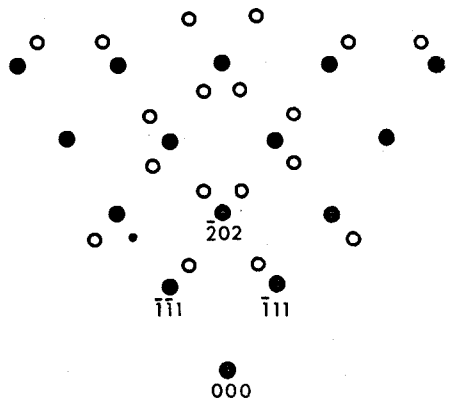

(d) Diffraction pattern of Fig.4.12(b), sample G345, showing primary twin spots and one double diffraction spot

Fig.4.12

in the matrix in the vicinity of a twin boundary, as shown in Fig.4.11(e), to pass into the twin, or vice-versa, giving rise to double diffraction[4.6]. Knowing the matrix and primary twin spots, it is possible to deduce the double diffraction spots by treating a primary diffracted beam as a new source for diffraction in a twin.* All the extra spots in Fig.4.12(a) can then be accounted for in this manner, as shown in Fig.4.12(c). The double diffraction spots could, of course, be deduced directly from the reciprocal lattice in Fig.4.11(d), since the rest of the points at one third the distance from the main matrix points are due to double diffraction. Note that the diffraction pattern of Fig.4.12(a) is slightly off the (001) reciprocal lattice plane passing through the origin, so that further away from the origin towards the right the twin spots observed change from those around even index spots such as (420), to those around odd index spots such as (731), (751) etc.

Since some of the double diffraction spots are quite intense, it appears that a substantial fraction of the electrons are crossing twin boundaries, therefore these must be closely spaced, i.e. micro-twins. This sample was deposited at 540°C.

A further example of twinning is shown in Fig.4.12(b), which is a (101) pattern of a sample G345 deposited at 595°C. The twin points are deduced from Fig.4.11(d) and shown in Fig.4.12(d). Since the twin spots are very intense and there are only one or two double diffraction spots it indicates that the twins are large. However, the absence of double diffraction spots in this pattern

---

* In a recent paper Holt[4.15] has given a similar interpretation in the case of epitaxial ZnTe.

and in Fig.4.11(a) could be because it is not geometrically favourable in <110> azimuths. When sample G345 was viewed at [001] no double diffraction spots were observed, confirming that the twins are large. Films, resulting in diffraction patterns of the type shown in Fig.4.11 and Fig.4.12 had matt surfaces and were not normally considered suitable for electrical evaluation. However, room temperature measurements made on some such samples indicated the electron mobilities were up to 40% lower than that in the untwinned samples.

Epitaxial InAs layers deposited at substrate temperatures between 600-650°C (the temperature limits for each of the three orientations used are given in section 3.1.4), and having mirror smooth surfaces resulted in single crystal diffraction patterns. Examples are given in Fig.4.13 of a thick InAs film on (111) GaAs seen at $[1\bar{1}0]$ and $[\bar{2}11]$ directions. These patterns are indexed in Fig.4.14. Such samples when viewed at various azimuths, generally gave good diffraction patterns which were easily indexed, and without satellite spots.

Diffraction patterns of good quality InAs on (100) and (110) GaAs are shown in Fig.4.15. The (100) film is 2.7μm and the (110) film is about 1.0μm thick. Kikuchi lines and bands have been observed often, particularly when examining the thick epitaxial specimens. They arise when electrons are inelastically scattered, with a small energy loss, and are subsequently elastically scattered[4.6]. As the specimen is

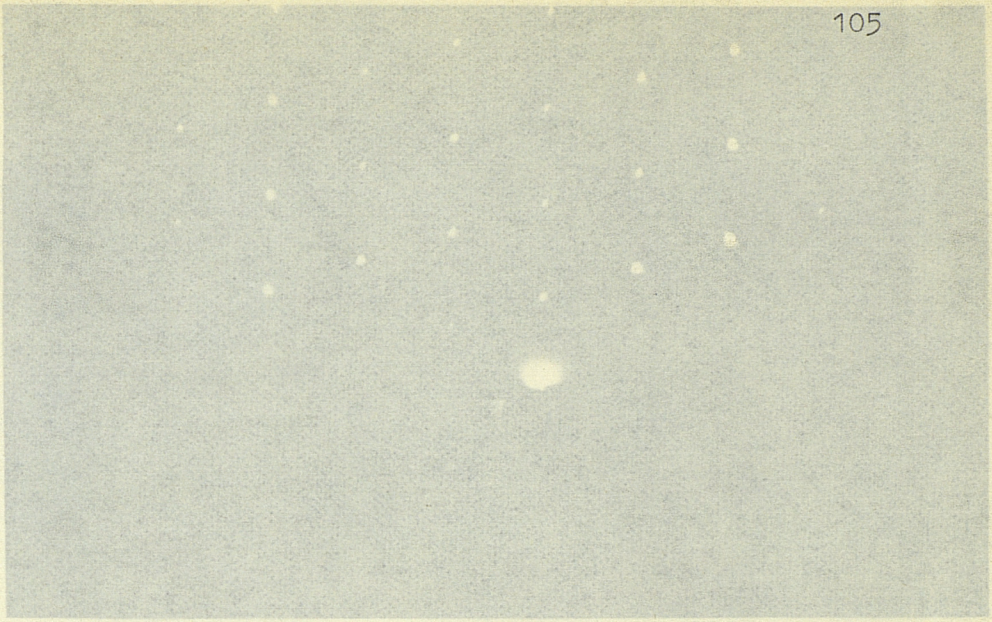

(a)

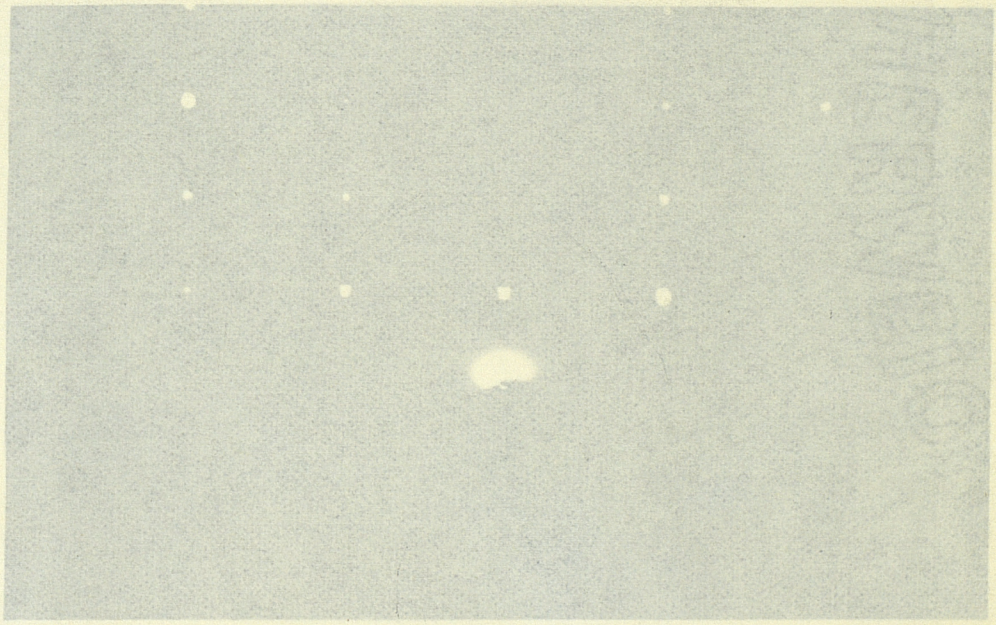

(b)

Fig.4.13
Electron diffraction of an untwinned eoitaxial InAs film on (111) GaAs, deposited at 640 °C. (a) $[1\bar{1}0]$, (b) $[\bar{2}11]$ azimuth. 6.7 μm thick layer

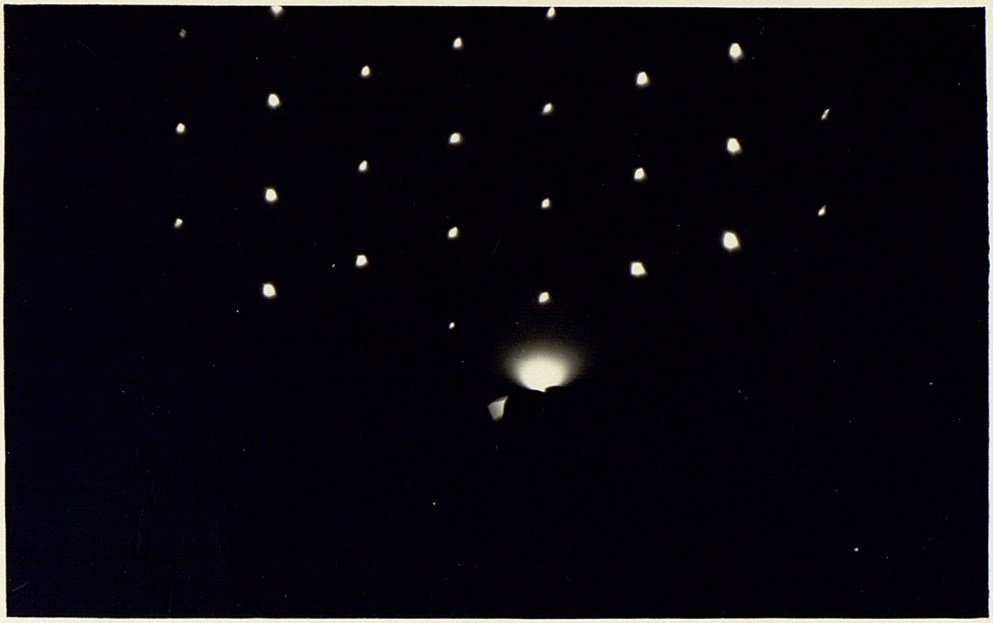

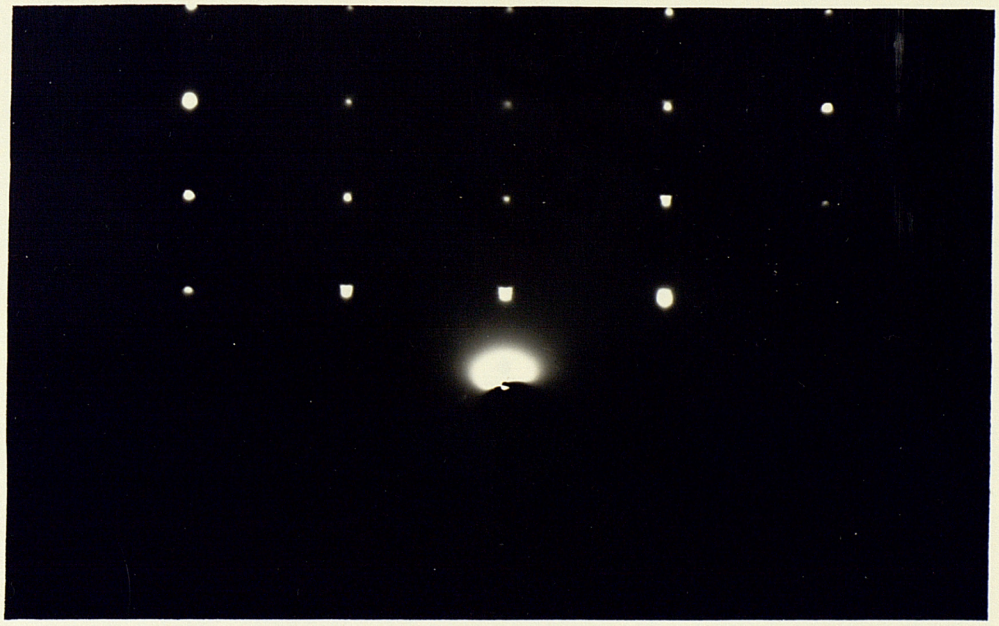

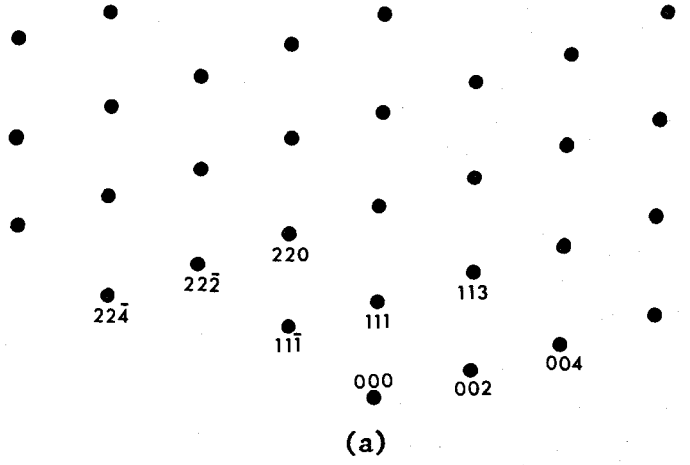

(a)

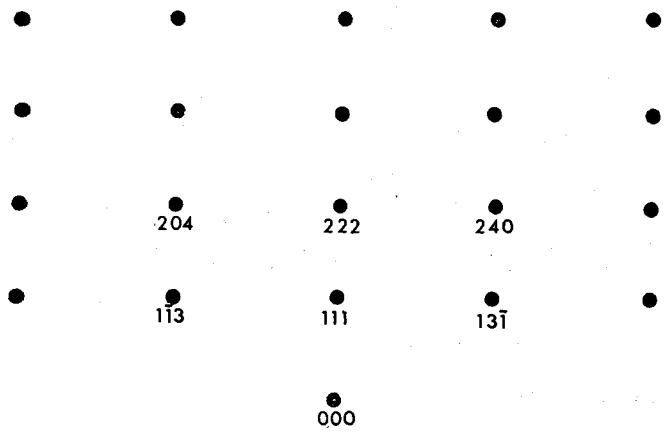

Indexed Diffraction Patterns Of Fig.4.13, Sample G339. All The Spots Can Be Indexed As Those Of An Untwinned FCC Structure

Fig.4.14

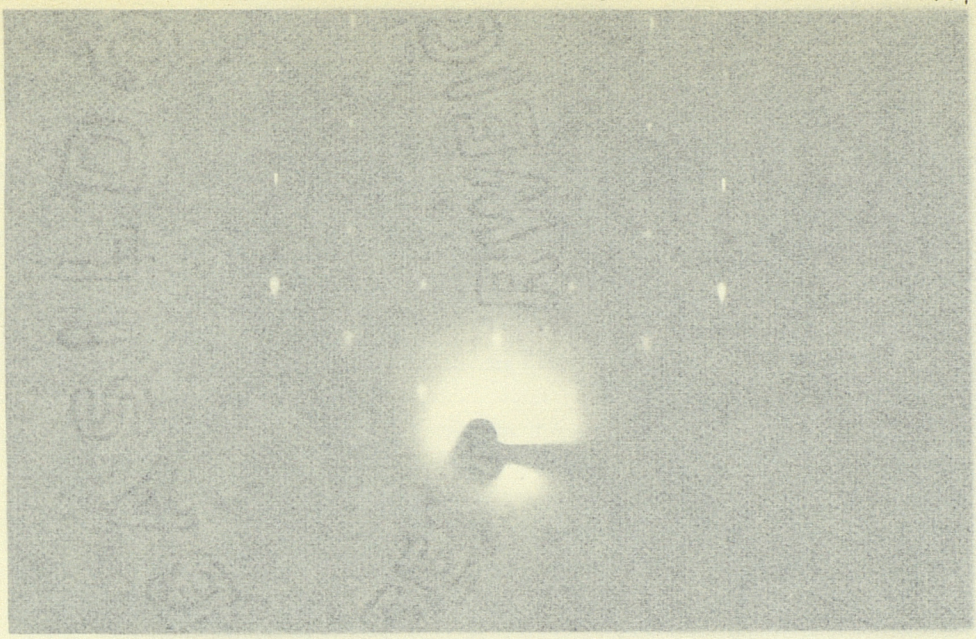

(a) Epitaxial InAs on {100} GaAs, deposited at 655 °C. Seen at ⟨110⟩ azimuth.

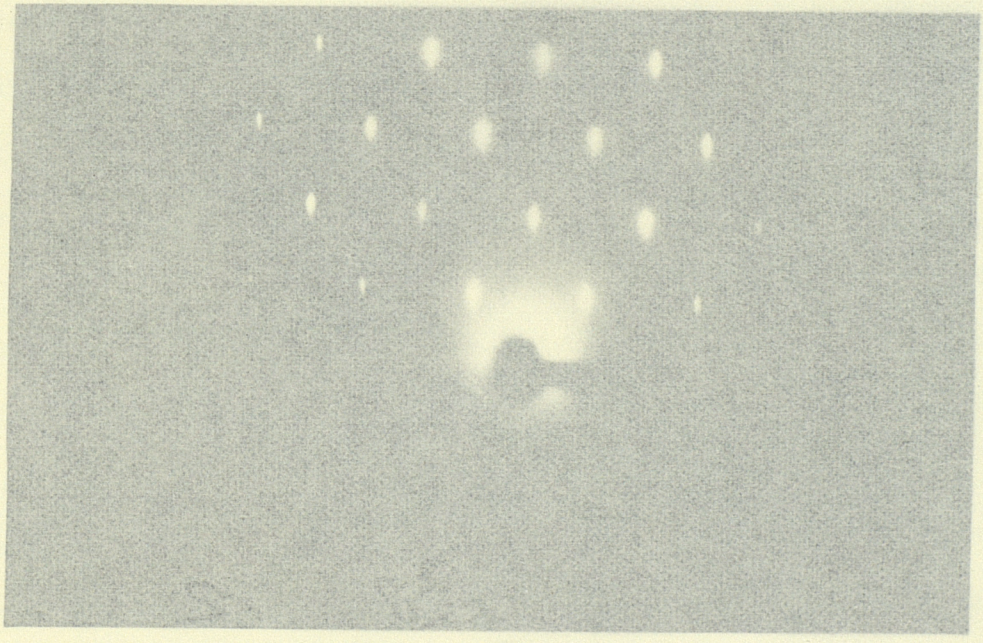

(b) Epitaxial InAs on {110} GaAs, seen at ⟨110⟩ azimuth.

Fig.4.15

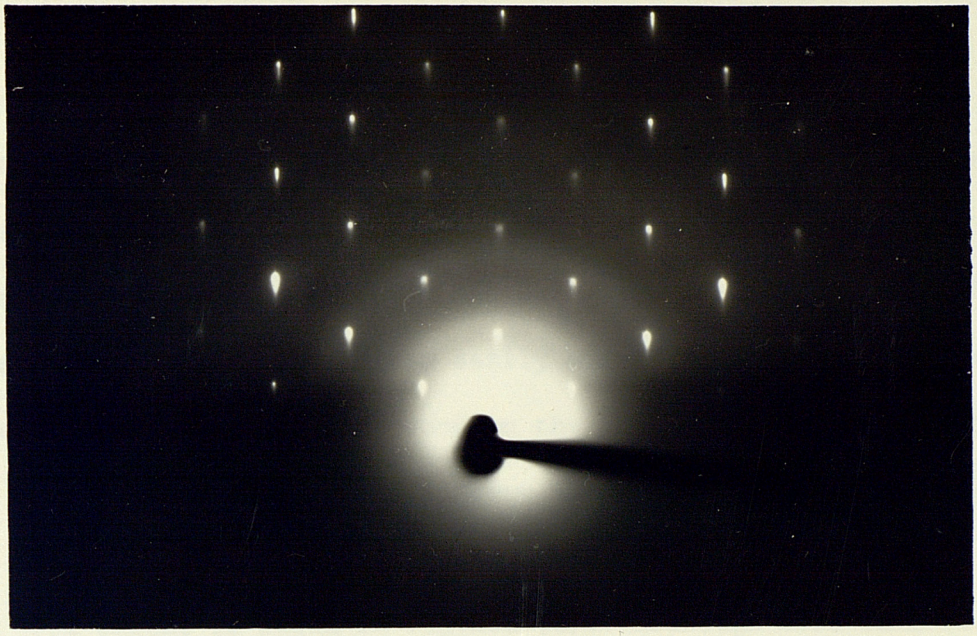

rotated, the Kikuchi lines move across the diffraction pattern, appearing to be rigidly attached to the specimen. Hence, they can be used to determine, accurately, the orientation of the specimen. However, we have not attempted to do this. It was often found that although the Kikuchi pattern was easily observed on the microscope screen, the contrast was very poor on the photographic plate. Fig.4.16(a) is an example of a diffraction pattern showing some Kikuchi lines.

A diffraction pattern of a very thin (110) epitaxial film, about 400Å thick, is shown in Fig.4.16(b). Although this is a single crystal spot pattern, a few rings are visible which do not intersect the spots. This could be due to some free Indium or Arsenic on the surface, or contamination by unknown impurities. The d-spacings of the rings correspond closely to some Arsenic reflections. It is possible that free Arsenic could have condensed on the film if the substrate temperature was reduced below 100-200°C, while the Arsenic pressure was still high.

Examination of layers which appeared to have an Indium excess, because the deposition temperature was too high (HCl test, see section 3.1.4), gave ring patterns which could only be identified as that of InAs and not free Indium. It is possible that the blobs observed under the optical microscope, (section 4.3.1) were in fact a mixture of polycrystalline InAs and free Indium, rather than just free Indium.

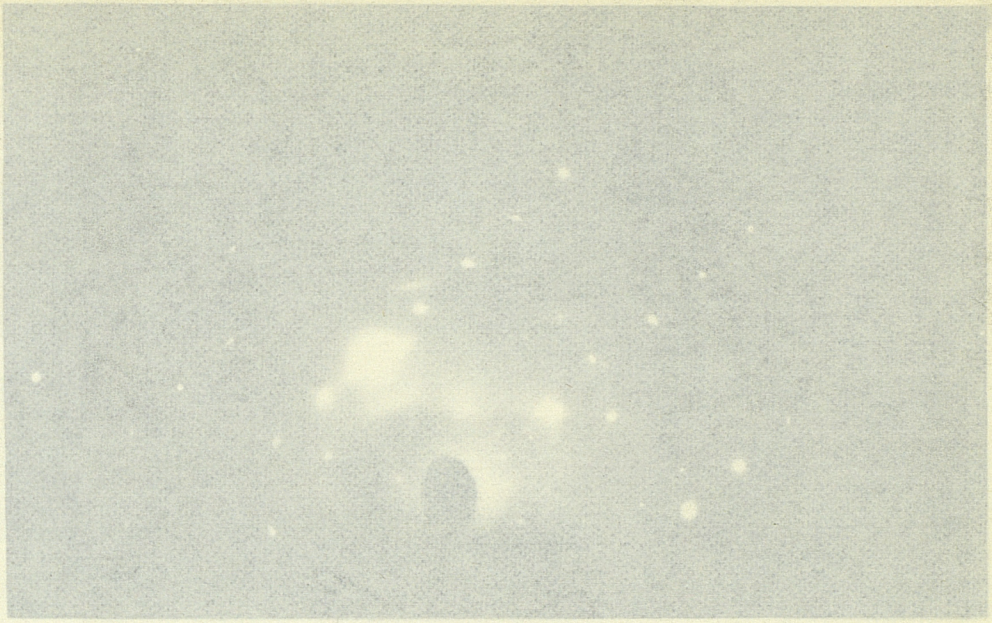

(a) Epitaxial InAs on {100} GaAs, showing some Kikuchi lines

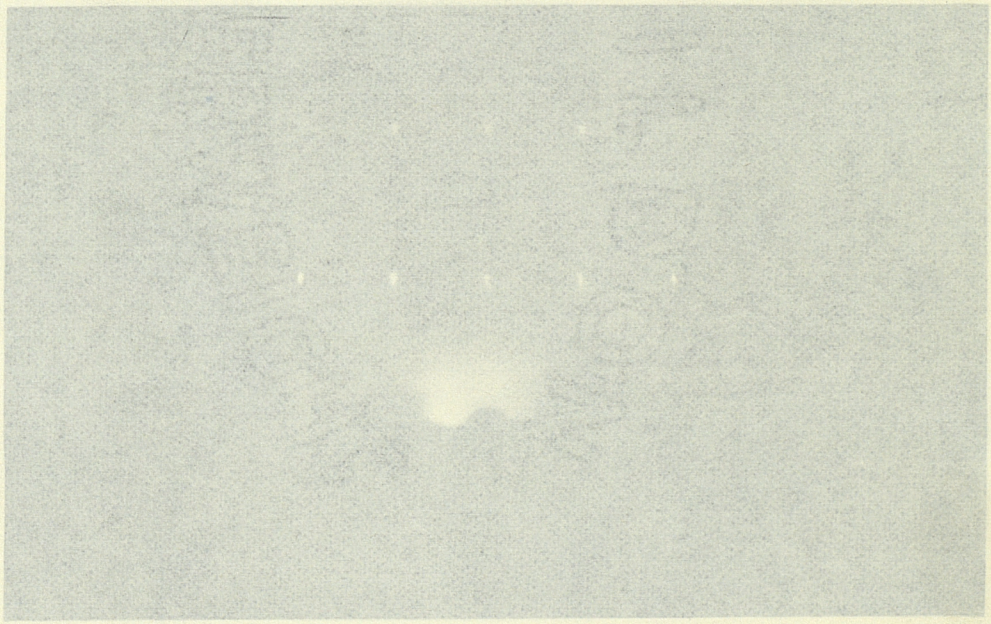

(b) A very thin InAs film (~400Å) on {110} GaAs seen at <011> . Weak rings which do not intersect the main spots can be observed.

Fig.4.16

Some comments should be made on the observed differences in substrate temperature, for the transition from twinned to untwinned epitaxy, on the various orientations. In chapter 2 it was suggested that this could be due to differences in interfacial energies as well as surface parameters of the various orientations. Another reason suggested by Holloway et. al[4.9], is due to the difference in the angles between the growth direction and the <111> twin axes. Deposition below the optimum temperature results in faceted surfaces. Generally an increase in planarity is observed with increasing deposition temperature, and the {111} facets which deviate most from planarity will disappear at the lowest temperature. Thus, from table 4.4 it can be seen that twinning should disappear in the order:

$$T_{(001)} < T_{(110)} < T_{(111)}$$

This indicates a reversal in the order of the (001) and (110) temperatures compared to our results (section 3.1.4). However, the above order has been observed by Holloway et. al[4.9] in the chemical deposition of GaAs on Germanium. If this explanation is correct, then from table 4.4., twinning about $[\bar{1}11]$ and $[1\bar{1}1]$ on (110) orientations should disappear first, whereas on (111) orientations, twinning about $[111]$ only should persist up to the transition temperature.

Growth Direction	Twin Axis			
	[111]	[$\bar{1}$11]	[$\bar{1}\bar{1}$1]	[1$\bar{1}$1]
[001]	54.7°	54.7	54.7	54.7
[110]	35.3	90	35.3	90
[111]	0	70.5	70.5	70.5

Table 4.4

Angles Between <111> Twin Axes And Growth Directions

In conclusion, it should be pointed out that an epitaxial film possessing a large density of low angle grain boundaries could still result in a good single crystal electron diffraction pattern. Therefore, techniques such as X-ray rocking curves, described earlier, and X-ray topography would be very useful in order to obtain further information on the perfection of these layers, with the advantage that thinning of the crystal is not necessary.

4.3. Optical Examination

4.3.1. Surface Features And Cleavage Sections

The crystallites of thick polycrystalline films could easily be observed under an optical microscope, at magnifications between 1000 and 3000. By measuring the approximate diameter of about thirty

crystallites in each micrograph, an average value of the crystallite size was obtained and this is plotted as a function of film thickness in Fig.4.8. These films usually have very rough surfaces because of the large grain size.

Optical examination of the epitaxial films also indicate various growth features. The micrographs to be shown are of films which have mirror smooth surfaces by visual examination, unless otherwise stated. Using a Nomarski unit with polarized light, the contrast was increased considerably.

Fig.4.17 shows some growth features observed on {100} surfaces. Using oblique incidence light it was deduced that the features in (a) were hillocks rather than pits. A micrograph of a {110} surface is shown in Fig.4.18(a). Generally these features were observed when the substrate temperature during deposition was slightly below the optimum value. Fig.4.18(b) is an example of a {111} layer, showing pits which could have been caused by thermal etching. Apparently etching is caused by residual gases, such as Oxygen, which attack the surface at high substrate temperatures. Although this is often referred to as thermal etching, it is in fact a form of chemical etching[4.11]. It should be pointed out that epitaxial layers on both {110} and {111} GaAs substrates have been deposited which are smooth and featureless, (see Fig.4.19(a)).

Films which were deposited at too high a temperature had surfaces which were visually very rough with a metallic appearance, and were suspected to be Indium rich. Fig.4.20(d) is a typical micrograph

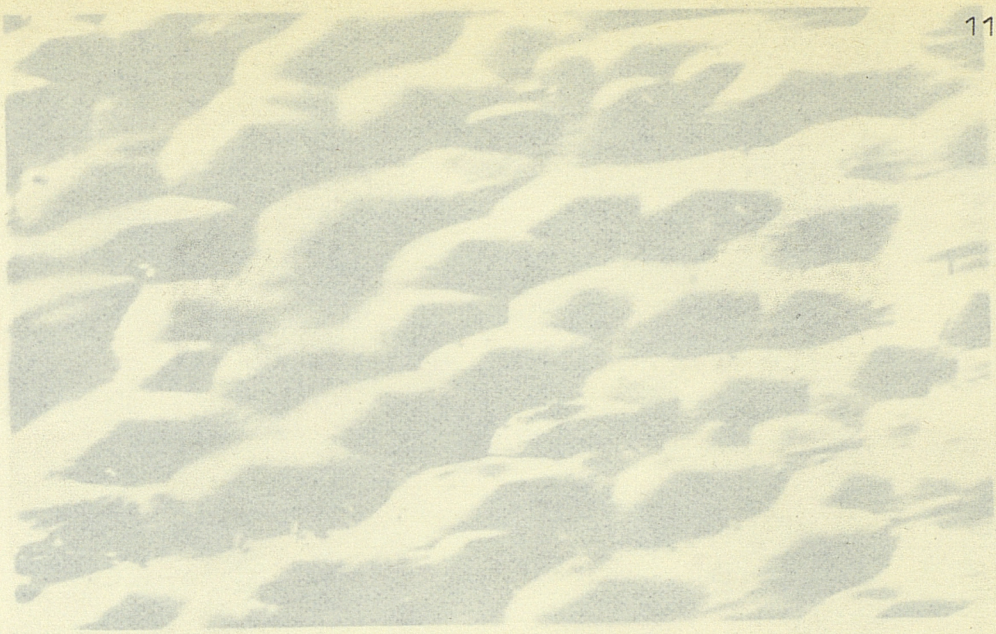

(a)

25 μm

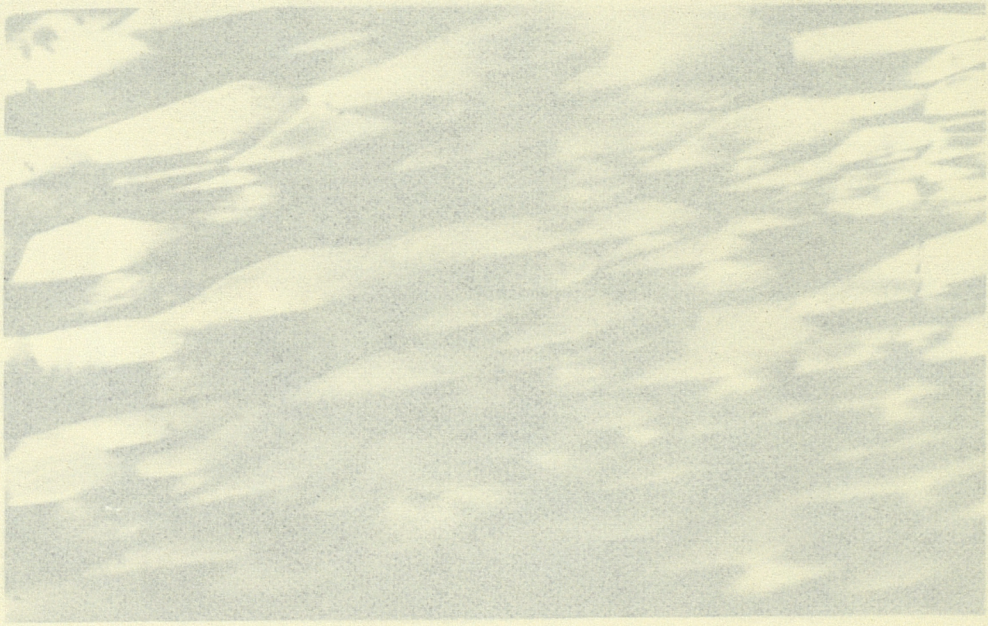

(b)

Fig.4.17
Surface growth features on epitaxial InAs, {100} orientation. 5.6 μm layer

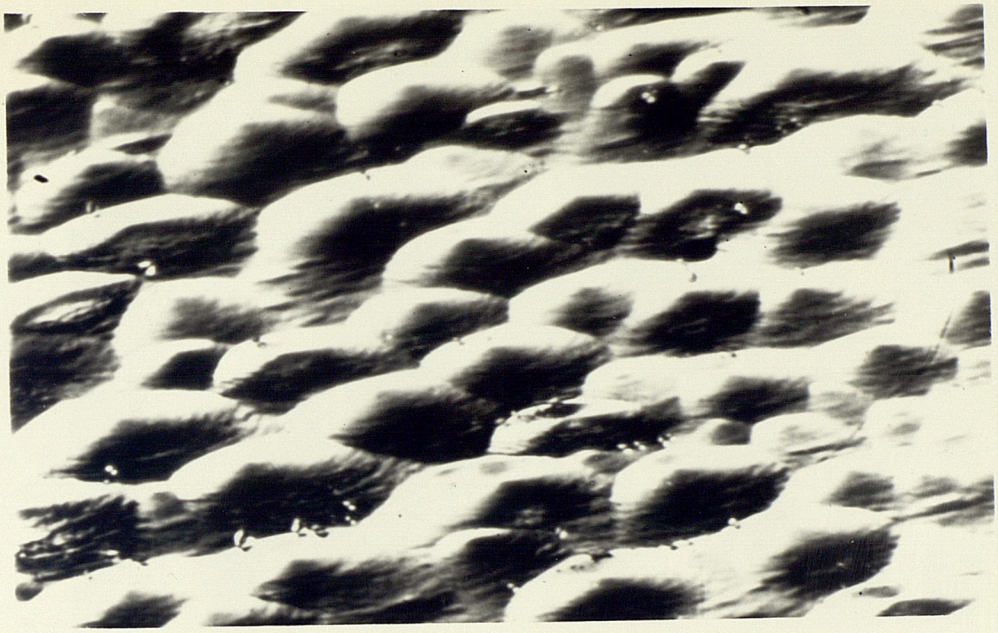

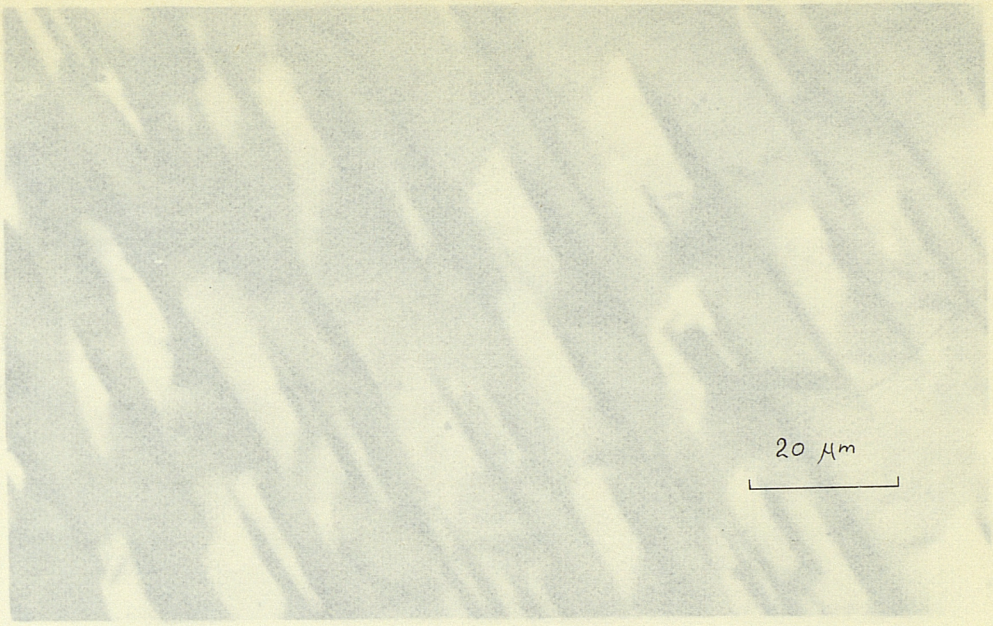

(a)

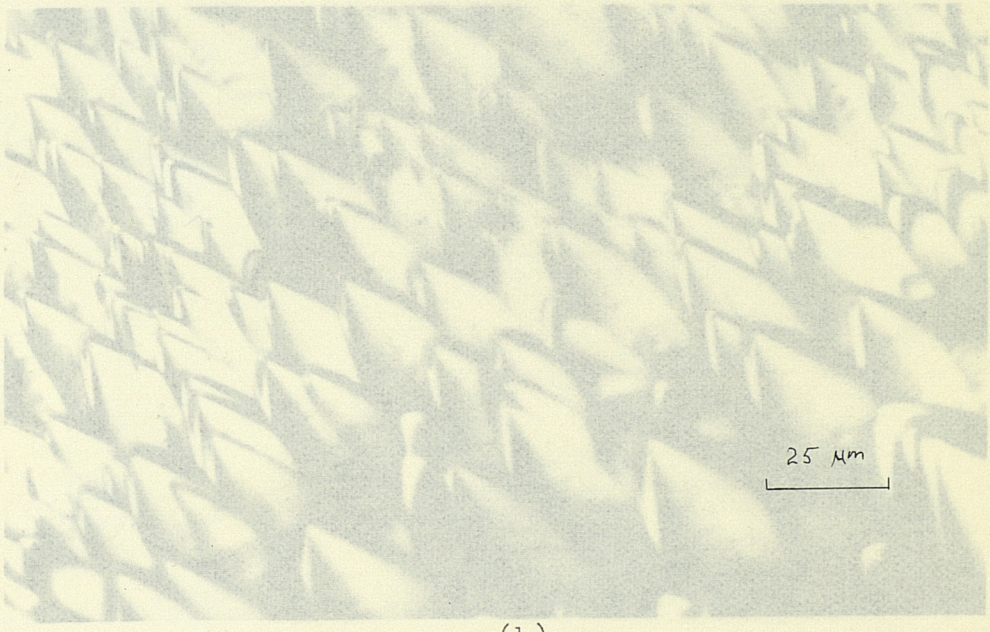

(b)

Fig.4.18
Surface features on epitaxial InAs, (a) {110} (b) {111} orientation

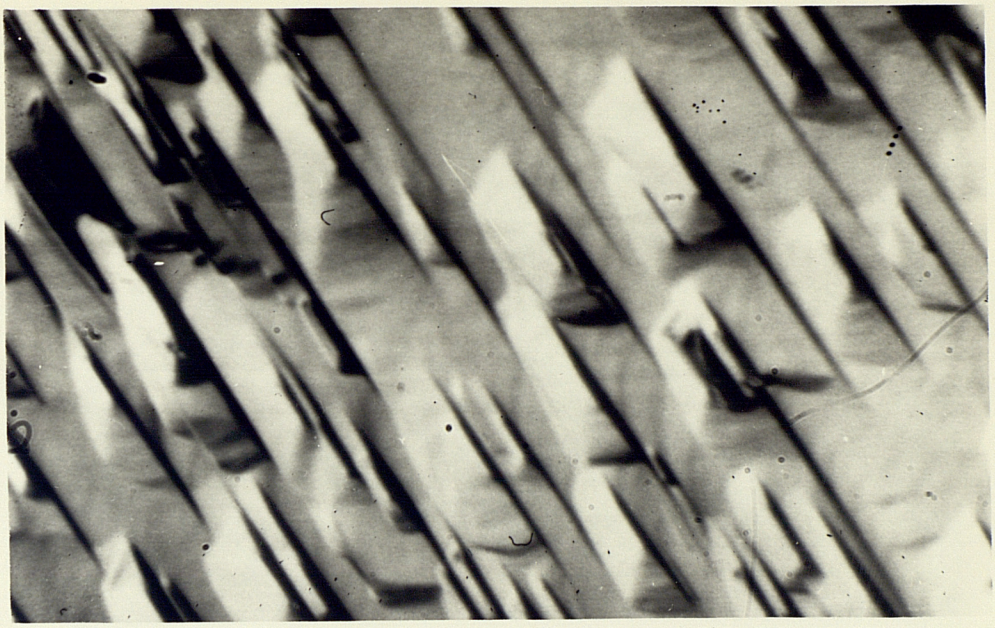

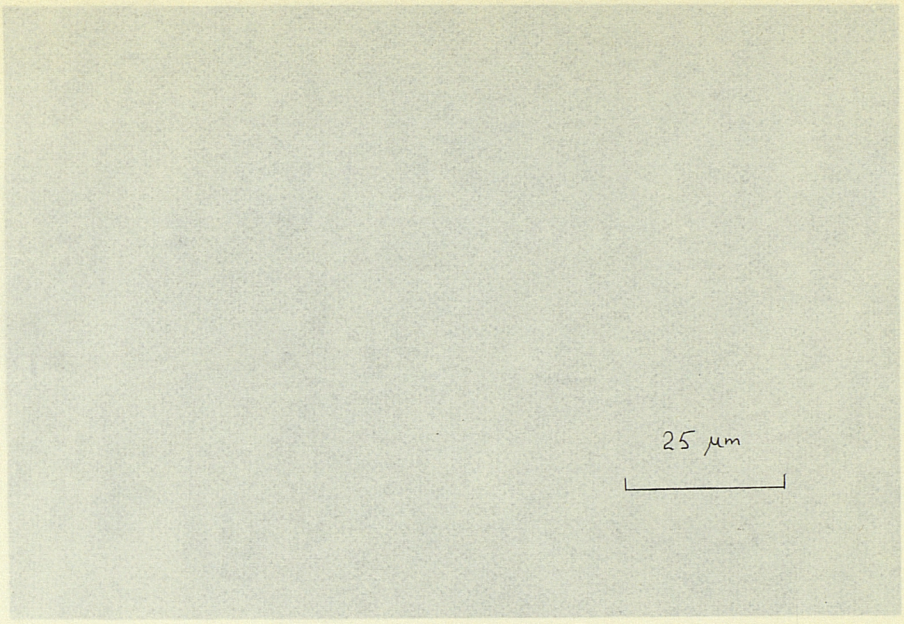

(a)

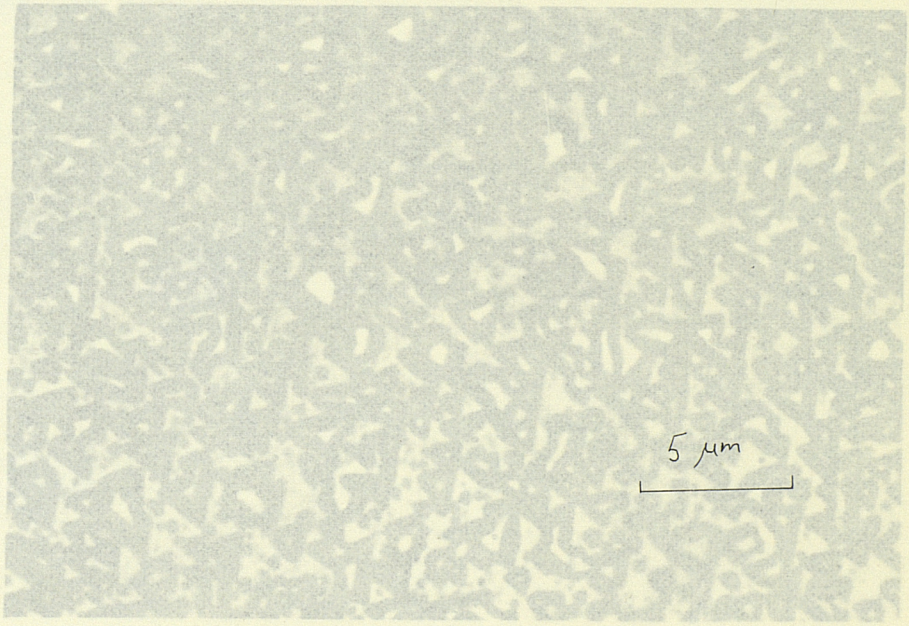

(b)

Fig.4.19

(a) Surface of an almost featureless {111} InAs film. 12 μm thick

(b) Surface of a highly twinned InAs film, {111} orientation

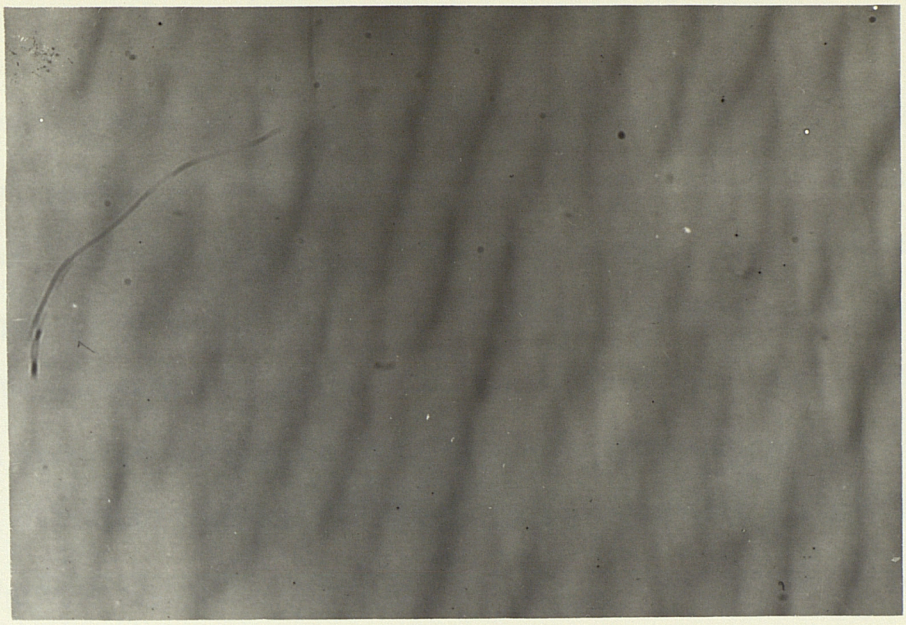

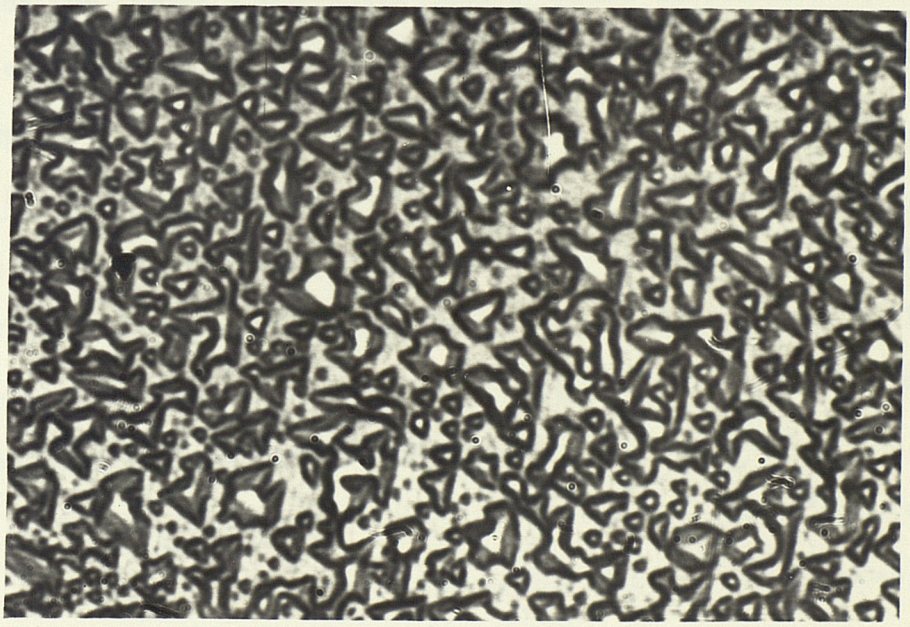

showing blobs which according to electron diffraction data, could consist of polycrystalline InAs and free Indium. Fig.4.19(b) is a surface of a highly twinned InAs film, giving a diffraction pattern of the type shown in Fig.4.10. Many of the triangular crystallites are seen to be pointing in certain directions. Such films have matt surfaces.

In order to examine the InAs/GaAs interface and also for accurate thickness measurement, cleavage sections were stained in (a) $1HNO_3:1HC\ell:1H_2O$ (20 secs. R.T.), or (b) Sodium Hypochlorite, and examined under the microscope. Fig.4.20(a) shows a cleavage section of a {111} epitaxial layer, which indicates a sharp interface. This demonstrates that the lower substrate temperatures required for epitaxy by the 'three temperature method' could result in very sharp interfaces, which is very useful in the study of heterojunctions, for example.

4.3.2. Dislocation Etch Pits

In order to obtain an estimate of the dislocation densities in the GaAs substrate and the epitaxial InAs, {111} Arsenic surfaces were chemically dislocation etched. The following etches were used to reveal dislocations in the GaAs substrate.

I	$1HF:2H_2O_2:5H_2O$	50^oC	10-15 minutes
II	$1HF(50\%):3HNO_3:4H_2O(0.25\%\ AgNO_3)$	R.T.	3-4 minutes

The first etch results in pits which tend to be circular, whereas the second gives triangular pits. Apparently the latter correspond to a 60^o edge type dislocation intersecting the surface[4.10].

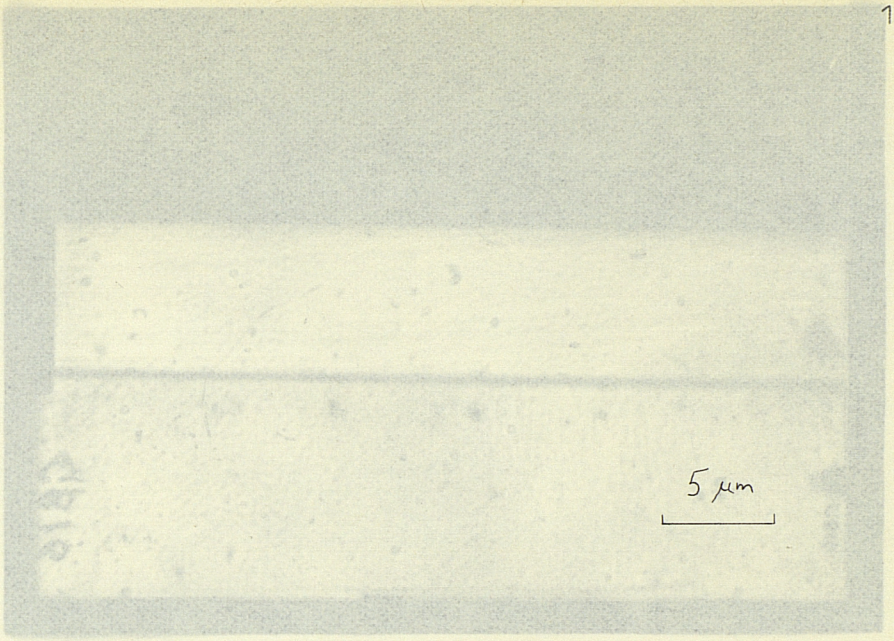

(a) Stained cleavage section of a {111} epitaxial layer

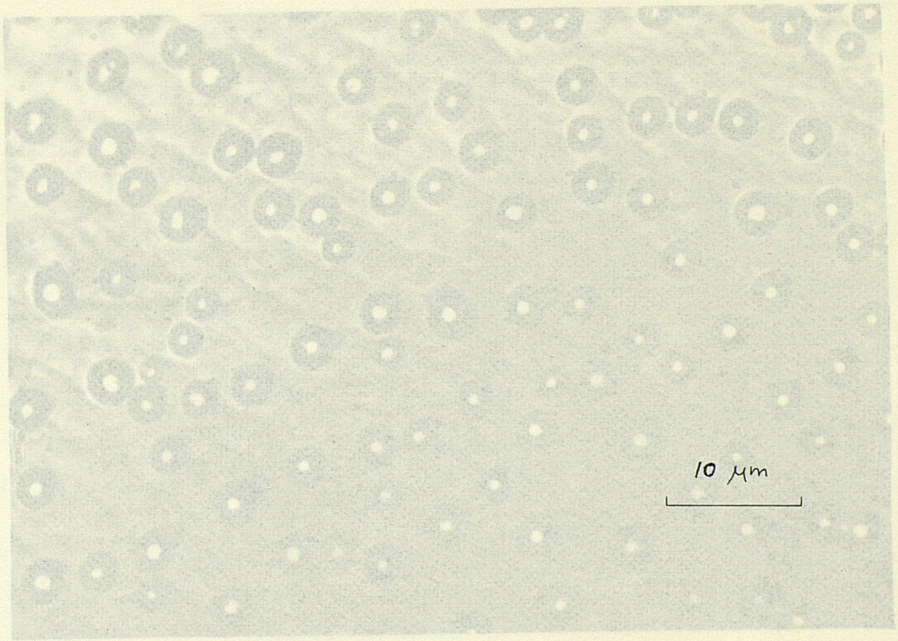

(b) Surface of an Indium rich film, {100} orientation

Fig.4.20


CBIP
CBIP

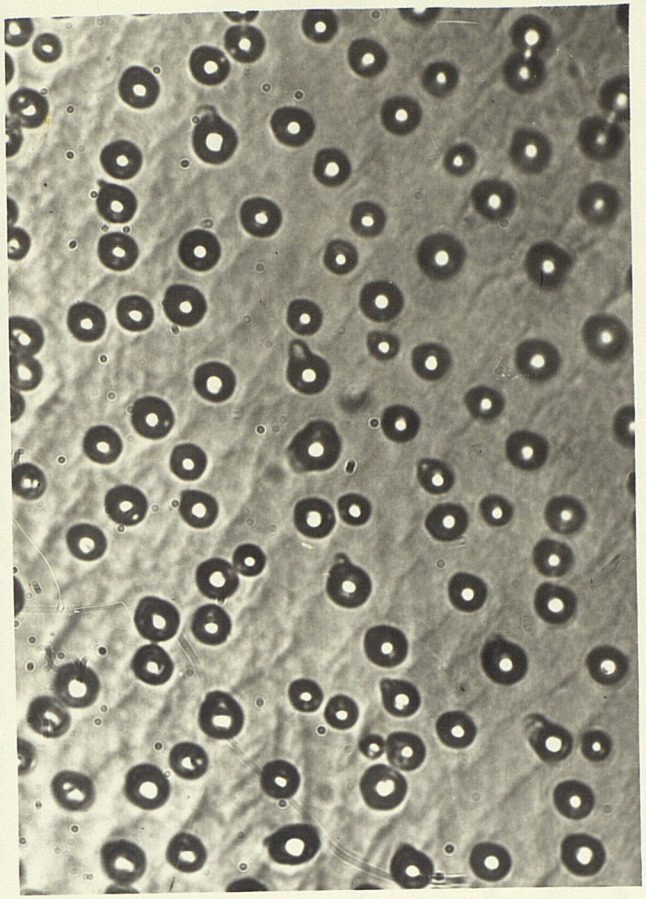

The substrates had been previously chemically polished, as discussed in section 3.1.3. Care must be taken to avoid mechanically polished surfaces since this will reveal an anomalously large number of pits along scratch lines[4.11]. Fig.4.21(a) shows typical etch pits on GaAs using etch II given above. The etch pit densities in the GaAs were of the order of 2 - 10x10^{4}cm^{-2} depending on the area of the substrate examined, but in general, they were in the region of 3 - 6x10^{4}cm^{-2}. Figures from RRE, give values of 1 - 3x10^{4}cm^{-2} near the centre of the slices, increasing to 5 - 10x10^{4}cm^{-2} towards the periphery. Apparently, this is also a function of the position of the slice along the rod crystal.

In order to reveal dislocation etch pits in the epitaxial InAs layer, the following etch was used:

III $1HNO_3:1H_2O_2$:6 parts 40% aqueous solution Tartaric acid at 50°C for approximately 10 minutes.

The advantage of this etch is that it removes very little material, which is important when etching thin films. However, the pits are not well defined, as shown in Fig.4.21(b).The above etch is probably suitable for the {111} In face. Various other etches were used, but none was found suitable. The etch pit densities were of the order of 1 - 3x10^{4}cm^{-2}, which is less than that on the GaAs substrate. A similar reduction has been observed in epitaxial GaAs on GaAs[4.12].

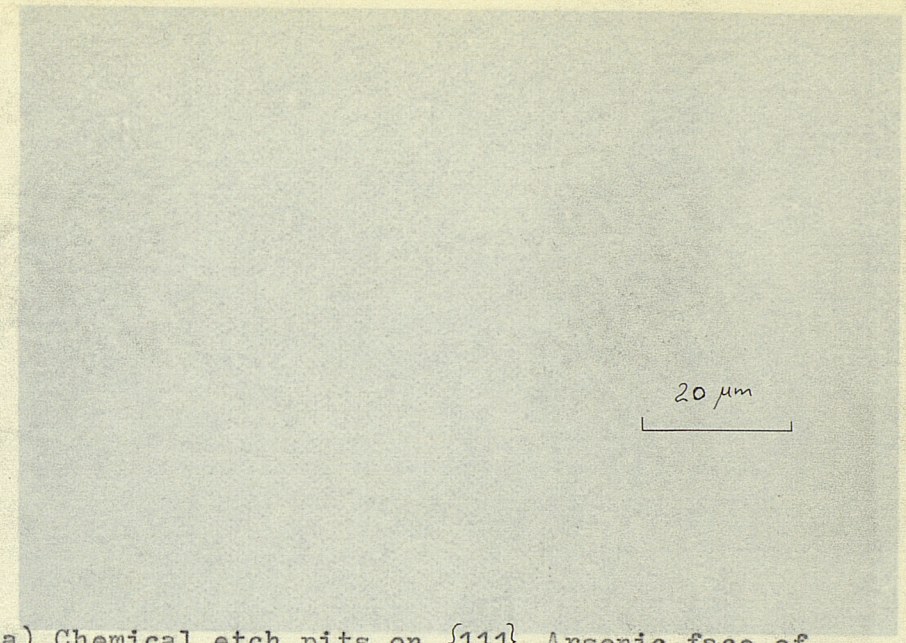

(a) Chemical etch pits on {111} Arsenic face of GaAs substrate, using etch II

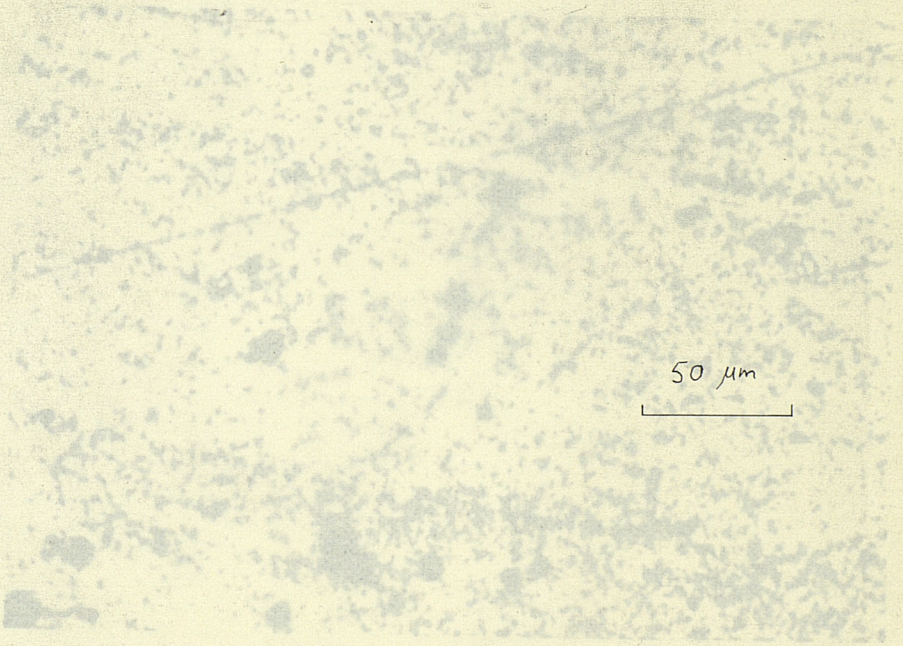

(b) Chemical etch pits on {111} Arsenic face of epitaxial InAs

Fig.4.21

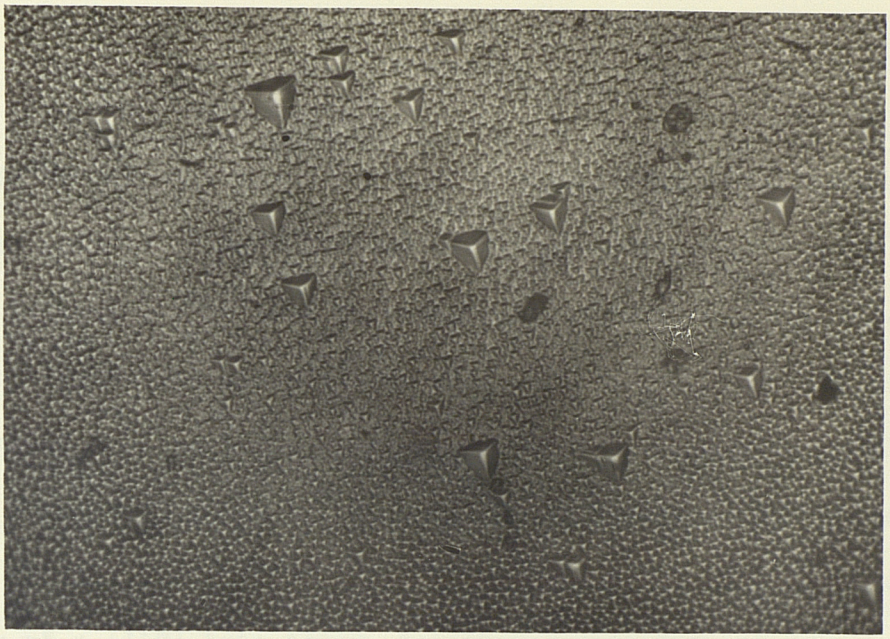

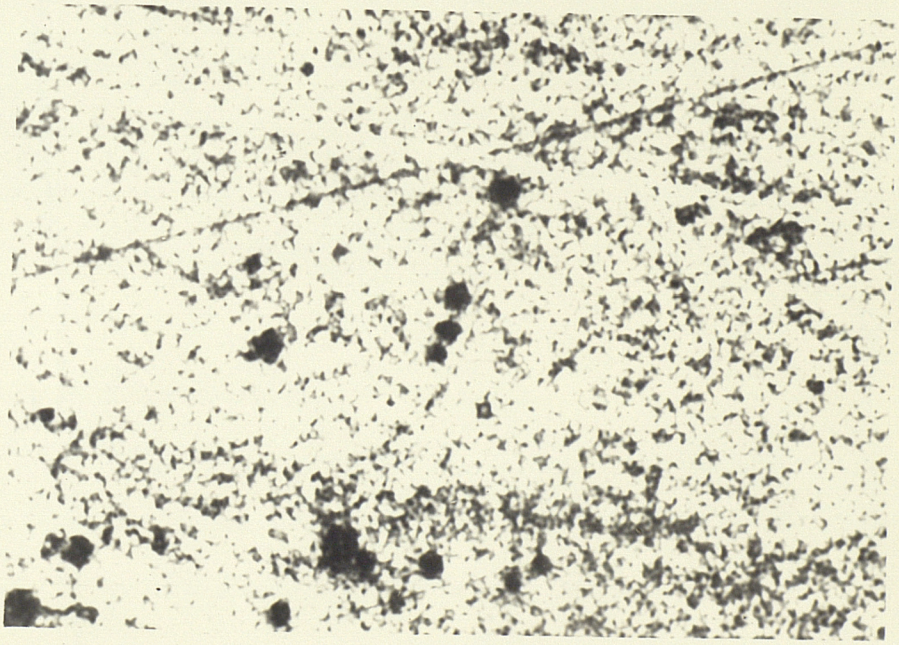

4.3.3. Infra-red Absorption

Infra-red absorption spectra of both polycrystalline and epitaxial InAs have been obtained in the 2 - 10μm wavelength range. Unfortunately, with the polycrystalline films, the corning glass substrates are absorbing in this region, and even with a compensating substrate the results are not representative of the films. However, this is not so with the epitaxial films, since the GaAs is not absorbing above 1μm. Fig.4.2.2 shows a typical absorption spectrum of a {110} InAs layer, together with a GaAs spectrum. The energy gap of the InAs layer calculated from the absorption edge is 0.357eV at 300^{o}K. The published value is 0.36eV.

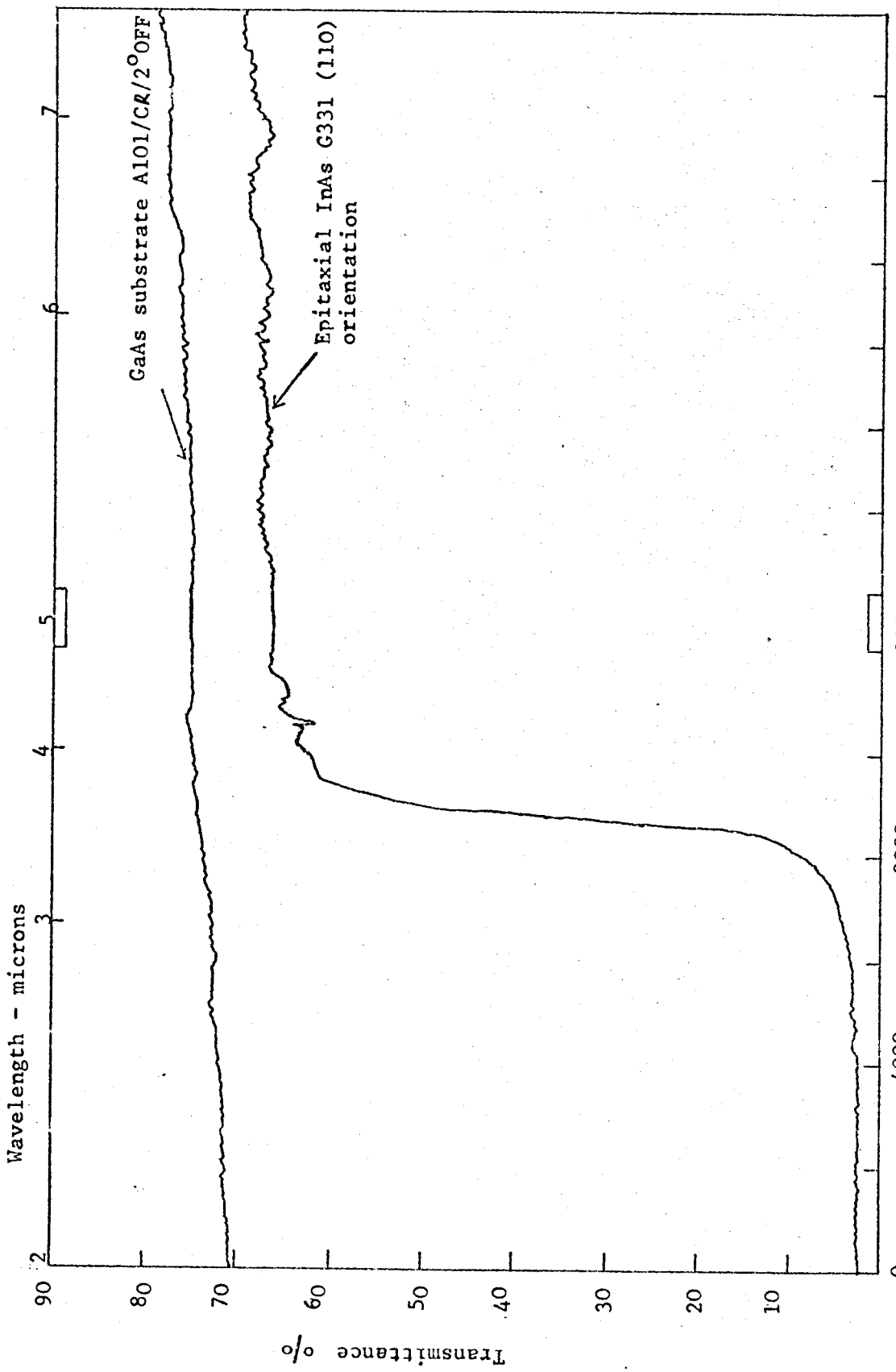

Fig.4.22

Typical Infra-Red Spectra Of Epitaxial InAs and GaAs Substrate

5. RESULTS OF ELECTRICAL MEASUREMENTS

5.1. Polycrystalline Indium Arsenide Films

5.1.1. Effect Of Annealing Temperature And Time

An investigation was carried out first on the deposition of polycrystalline films on amorphous substrates. A large number of samples were prepared under various deposition conditions. Annealing the samples was found to be one of the most important parameters to achieve good electrical properties. In order to investigate the effect of annealing, several sets of samples were deposited simultaneously at substrate temperatures below 500°C, cooled immediately and removed from the plant. The samples were then placed in the plant one at a time and annealed in an Arsenic pressure of approximately 10^{-4}torr. The effect of annealing time, at a constant annealing temperature, on one set of samples is shown in Fig.5.1. This indicates that annealing periods above ten minutes cause very little change in the film properties. The effect of annealing at a constant annealing period of about eight minutes, is illustrated in Fig.5.2. One of the samples was given a second anneal above 620°C which resulted ina loss of Arsenic and a degradation of the mobility.

Optical microscope examination of the films demonstrated clearly that annealing caused an increase in crystallite size. As discussed in section 4.2.1. the crystallite size is limited by the film thickness. Thus, the maximum mobility of the 8000Å films in Fig.5.2 is less than that in Fig.5.1, although a higher annealing temperature was used.

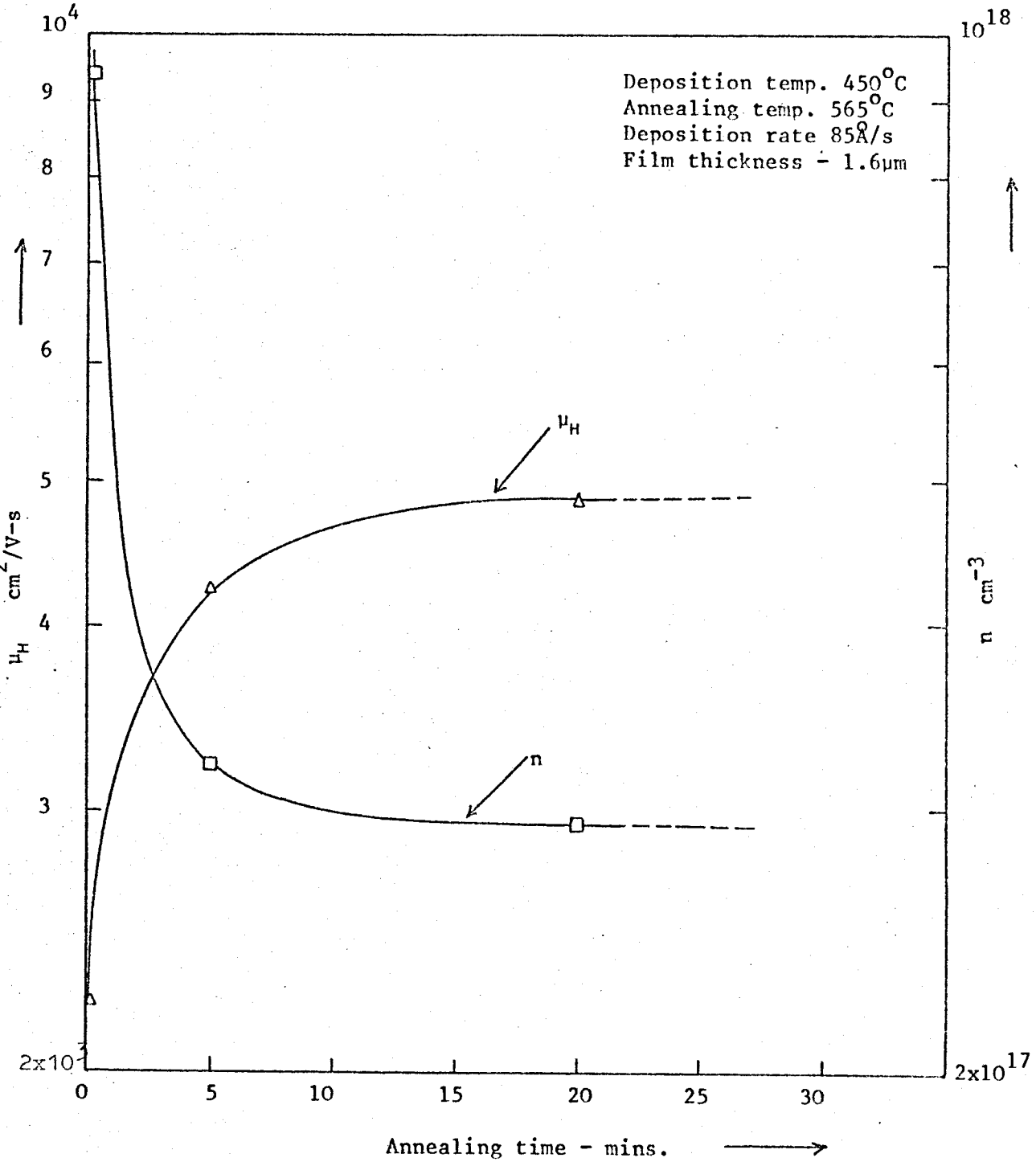

Fig.5.1

Effect Of Annealing Time On The Hall Mobility And Electron Density Of Poly-Crystalline InAs Films

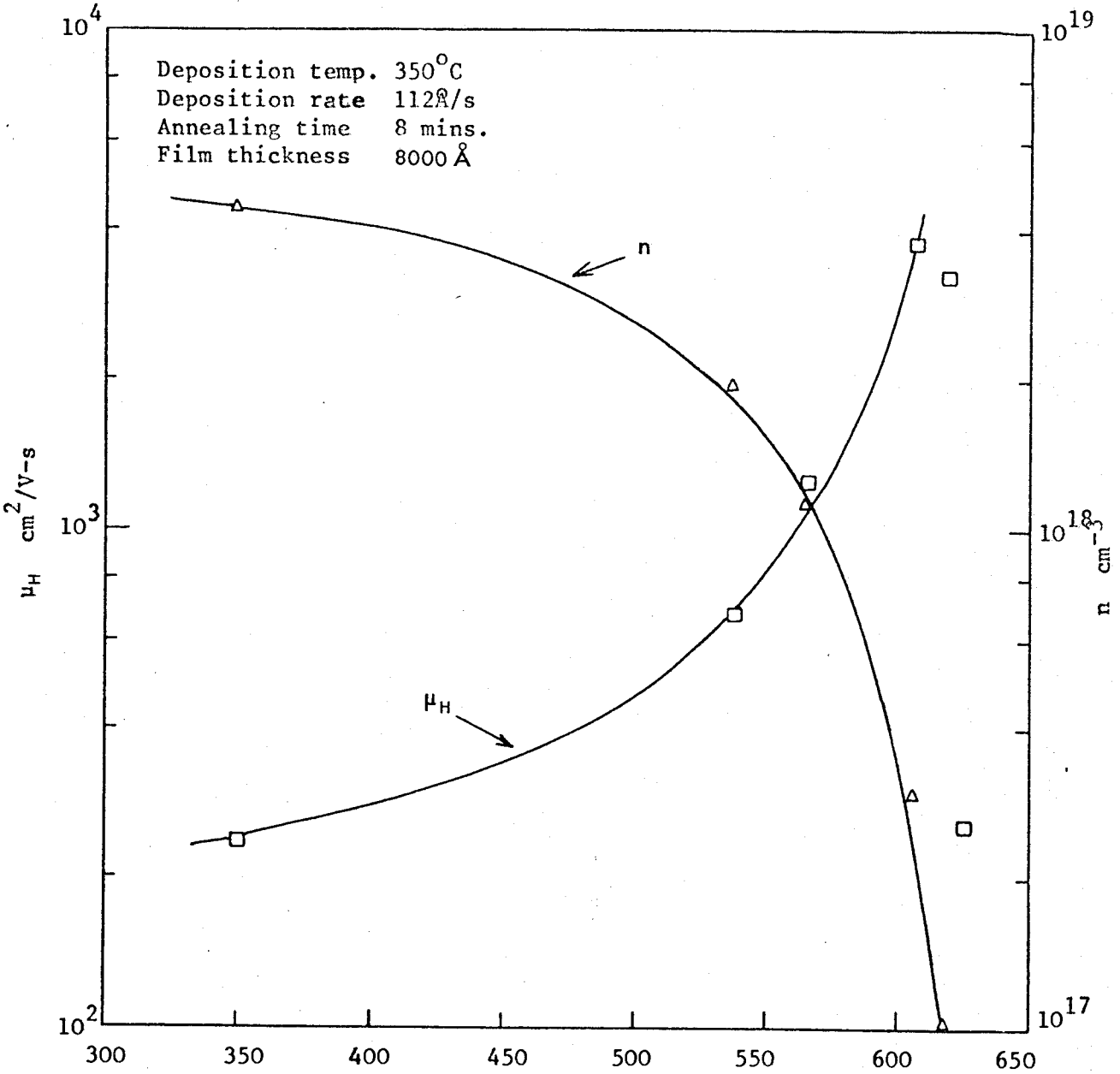

Fig.5.2

Effect Of Annealing Temperature On The Electron Mobility And Concentration Of Polycrystalline Films

5.1.2. Electron Concentration Dependence On Depostion Rate

In order to investigate the effect of the rate of condensation, several films were deposited in the range 1400 - 1800Å, under similar annealing conditions, but at different rates. The electron concentration vs. rate is shown in Fig.5.3, which indicates there is no significant effect in the range 0.4 to 270Å/sec. Johnson[5.1,5.2], using the three temperature method, has observed a linear relation between 1/n and deposition rate, but we have found no evidence to support this.

5.1.3. Effect Of Crystallite Size And Film Thickness

The variation of mobility and electron concentration with crystallite size and film thickness is shown in Figs.5.4 and 5.5. It appears that one of the main mechanisms limiting the mobility in polycrystalline films is due to grain boundaries. However, the reduction with film thickness could be due to the combined effect of grain boundary and surface scattering, since a reduction in thickness also results in smaller grains, as shown in Fig.4.8. In order to observe the effects of intercrystalline boundaries only, it would be necessary to measure the grain size of very thick films, annealed at different temperatures. However, determination of the smaller grain size would be rather difficult since such samples are too thick for transmission electron microscopy.

The reduction in electron concentration with annealing appears, again, to be connected with the increase in grain size. It is difficult to believe that this could be due to diffusion of impurities to the

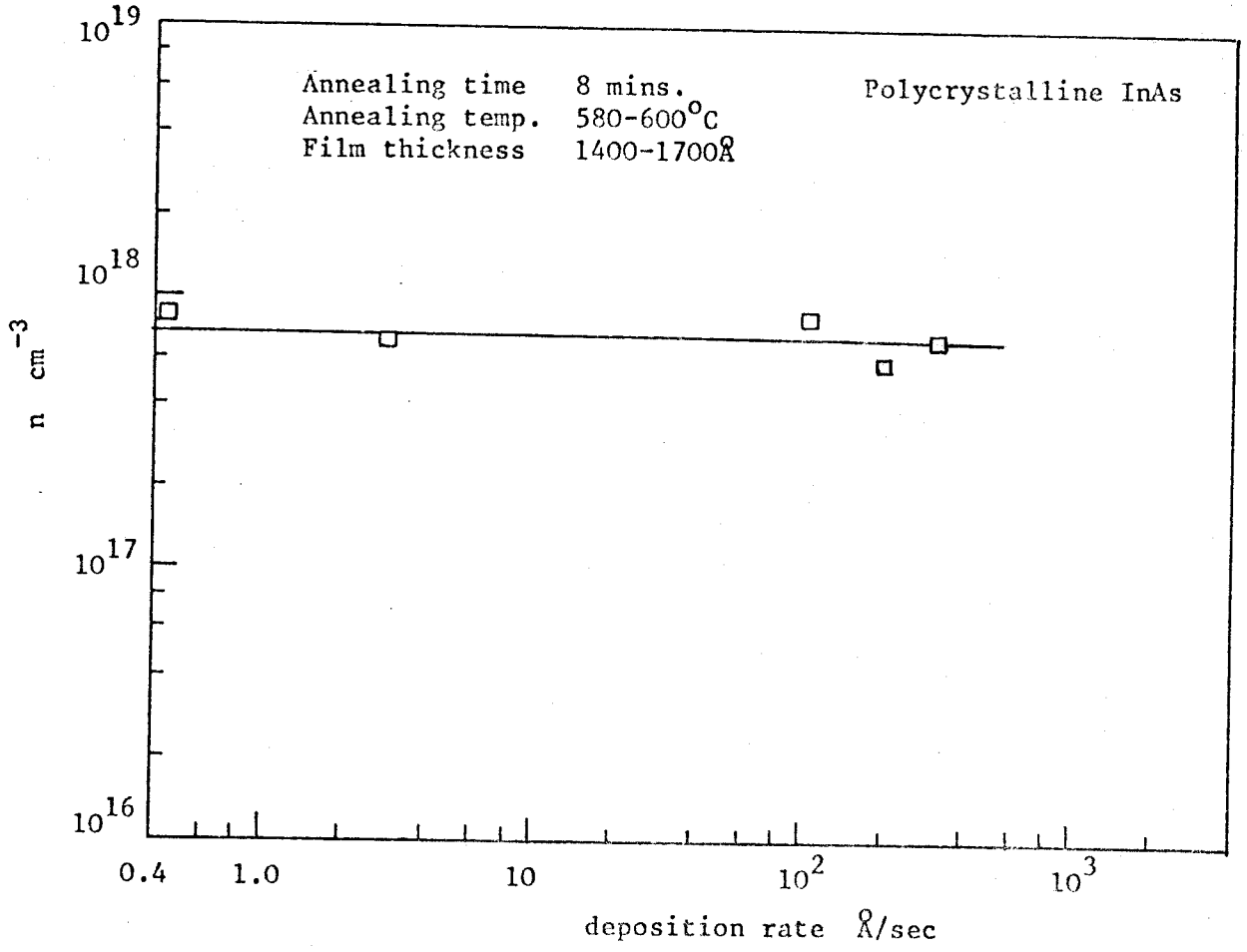

Fig.5.3

Carrier Concentration vs. Rate Of Deposition

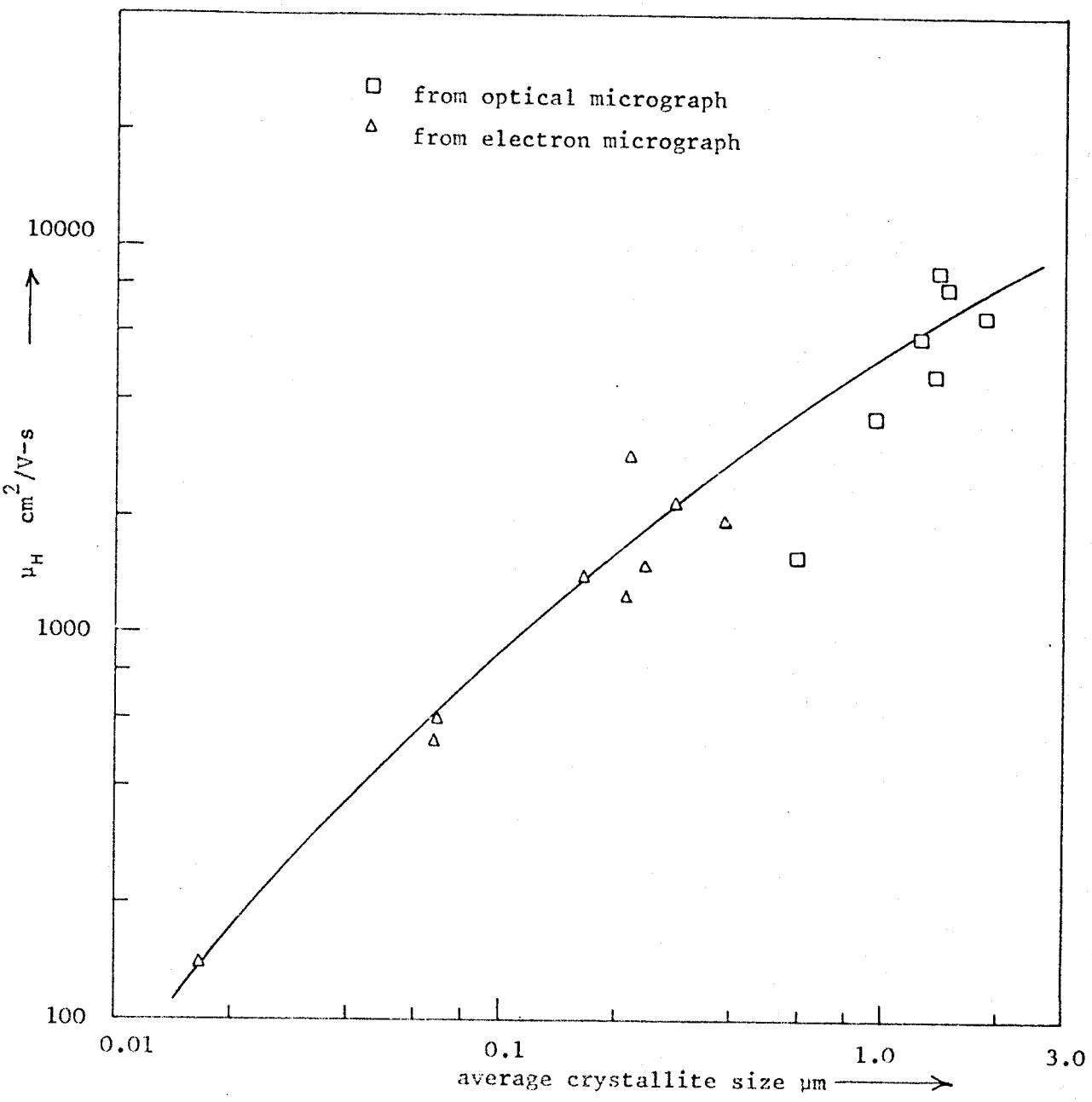

Fig.5.4

Electron Mobility Variation With Crystallite Size

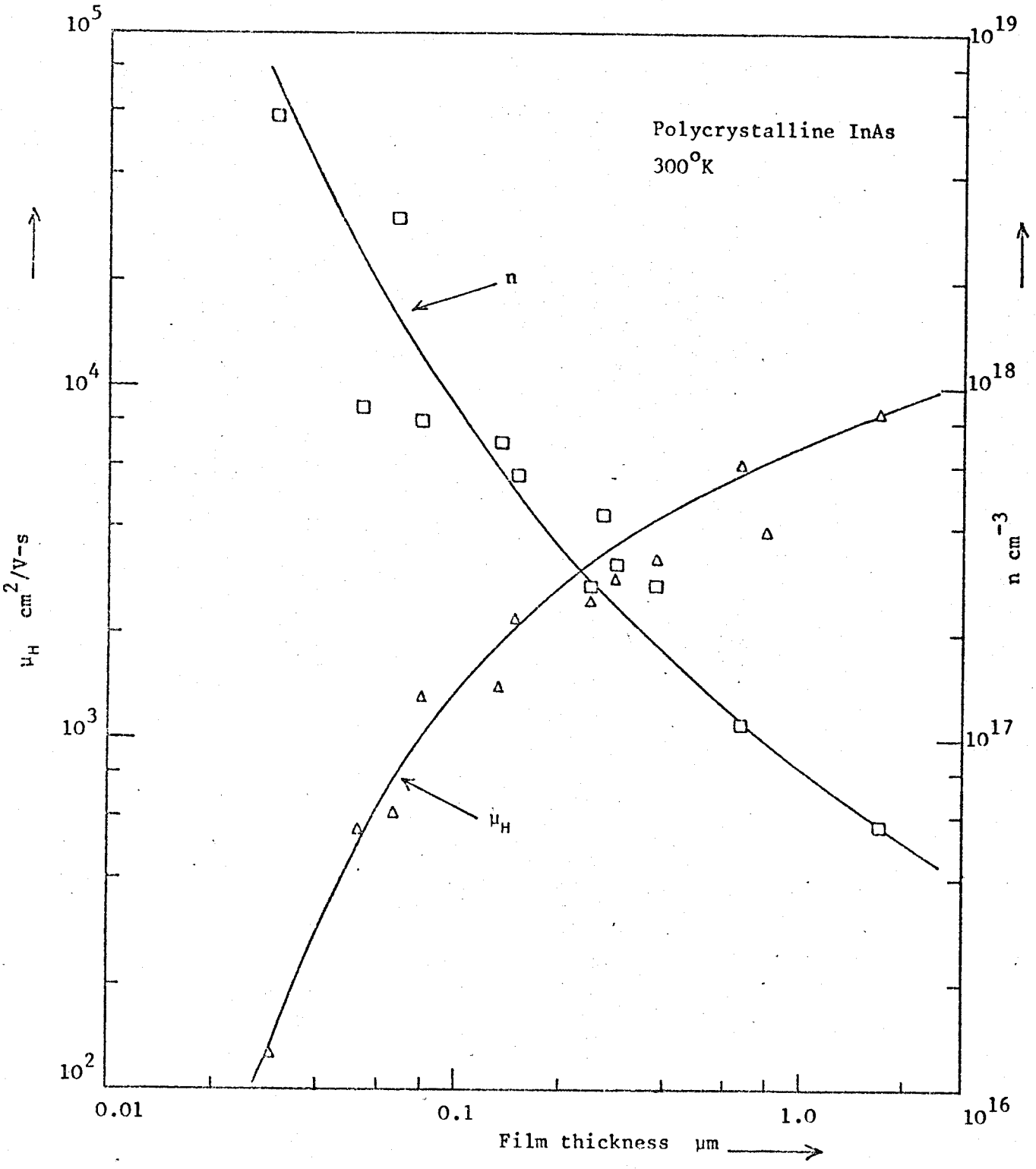

Fig.5.5

Electron mobility and concentration as a function of film thickness

surface, with subsequent re-evaporation, because the reduction is smaller in thinner films. It can be explained if we assume the grain boundaries give rise to donor type states.

Dixon and Enright[5.3,5.4] and Edmond and Hilsum[5.5] have found that heat treamment of single crystal InAs above 450°C, with a subsequent quench, increased the carrier contentration of n-type material and decreased it in p-type material. Such variations were reversed by heat treatment below 350°C. Dixon and Enright have suggested that these effects are caused by impurities which collect around dislocations, where they are electrically inactive. At temperatures above 550°C the impurities escape and may be frozen in their new position by quenching. Annealing below 350°C allows them to migrate back to the dislocation. Hilsum[5.6] has suggested that copper is the impurity. Apparently, copper is a rapidly diffusing donor in InAs, but it has a tendency to migrate to sites where it becomes electrically inactive.

It would be difficult to believe that a similar mechanism is taking place in these films. In the first instance, the carrier concentration is reduced, rather than increased, with annealing above 300°C. Secondly, the larger crystallites result in fewer grain boundaries where the donors could migrate and become inactive. Further, unlike the case of single crystal material, annealing our samples caused a considerable change in the structure of the films.

5.1.4. Mobility And Hall Coefficient Variation With Temperature

Figs. 5.6 and 5.7 show the variation of mobility and Hall coefficient with temperature for various film thicknesses. The interesting feature of all these curves is the mobility minimum just above room temperature, which has not been observed in the epitaxial films. This can be explained by the barrier model discussed in section 6.2.2.

The Hall coefficient has a normal temperature dependence, indicating that all the donors are ionized and above room temperature the material is becoming intrinsic.

5.1.5. Magnetic Field Dependence Of Hall Coefficient And Magneto-Resistance

Fig.5.8 shows the variation of the Hall coefficient with magnetic field at $300^{o}K$. The high to low field ratio of the thicker films is usually greater than 1.1, whereas the thinner films have a ratio near unity.

The transverse magneto-resistance of several polycrystalline samples is plotted in Fig.5.10, with the film surface perpendicular to the magnetic field. In order to avoid the geometrical contribution, through shorting of the Hall voltage by the current contacts, the magneto-resistance was measured at the voltage probes. Therefore, these results should represent the 'physical' magneto-resistance. The slopes of the characteristics are in the region of 1.85 at low fields, i.e. $\Delta\rho/\rho_o \propto B_z^{1.85}$. The variation of magneto-resistance with temperature is plotted in Fig.5.11.

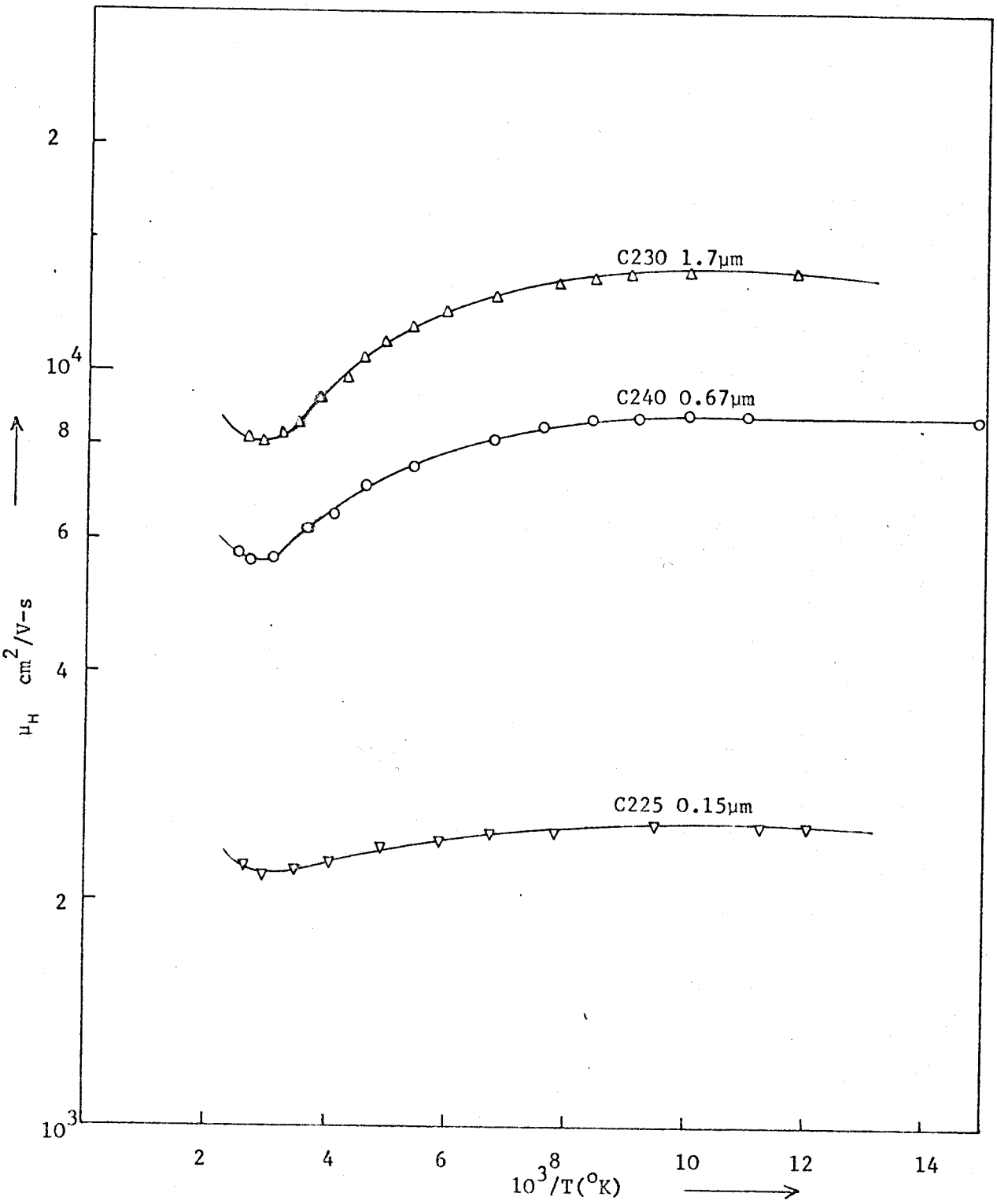

Fig.5.6

Hall Mobility As A Function Of Temperature - Polycrystalline Films

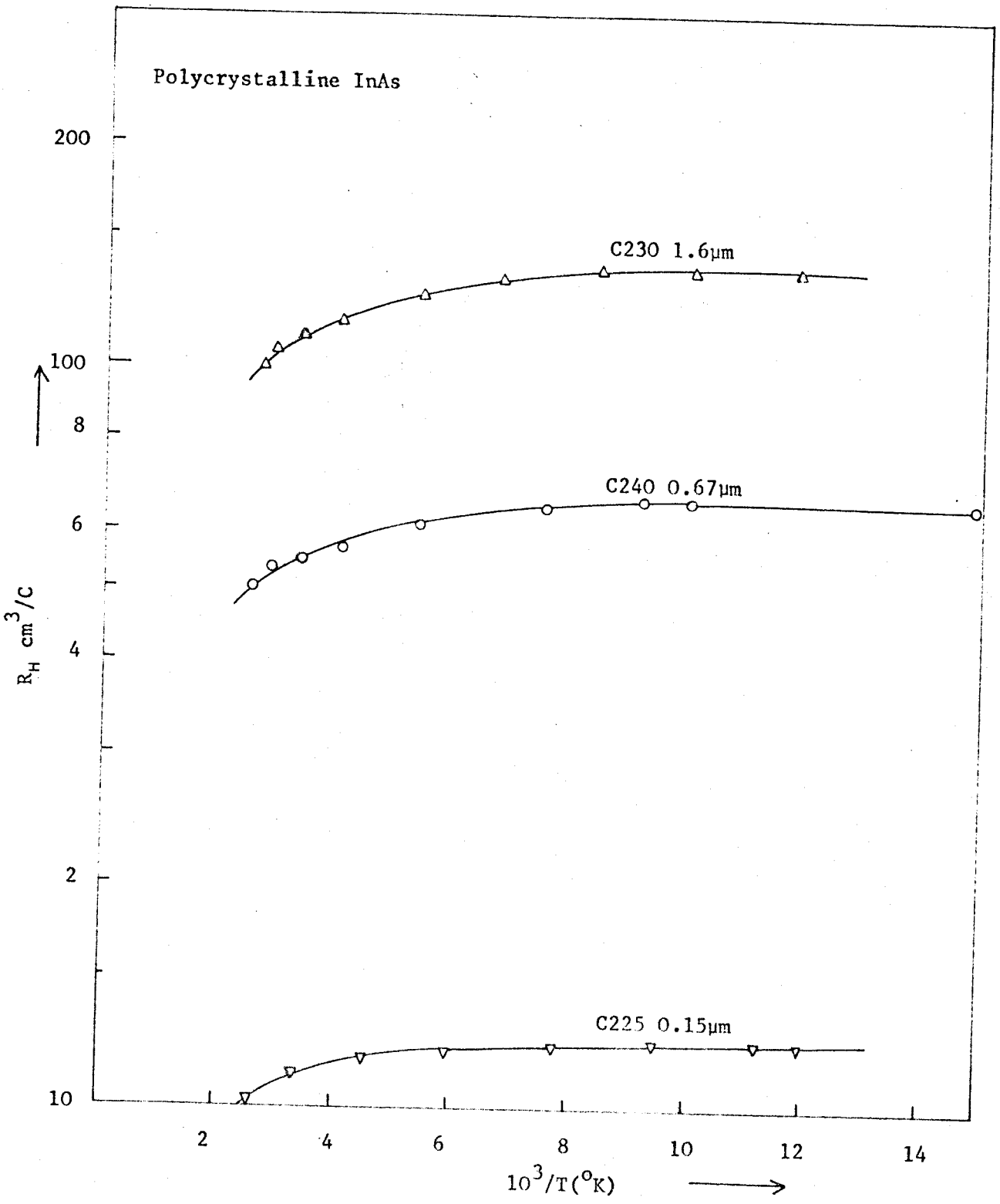

Fig.5.7

Hall Coefficient As A Function of 1/T

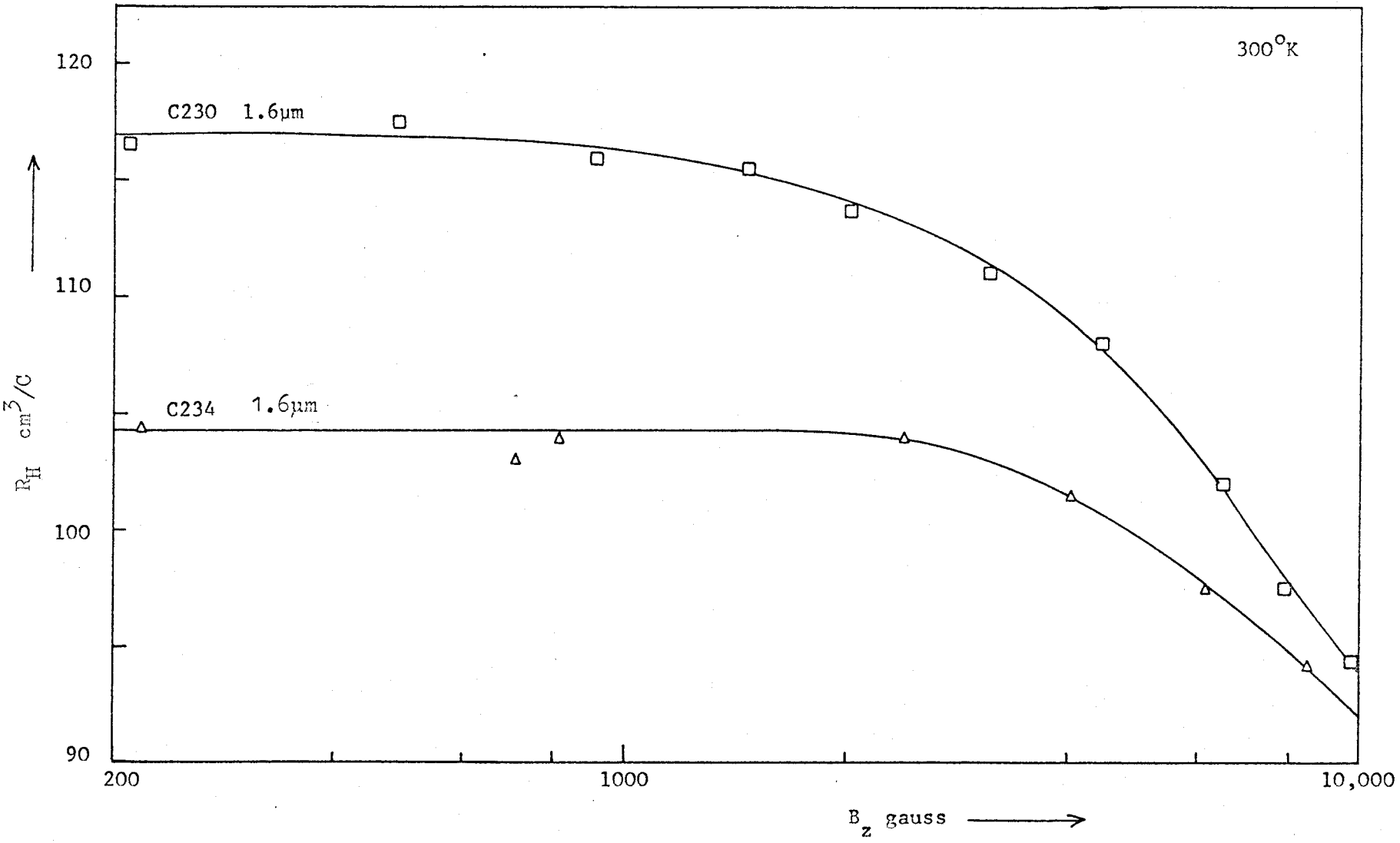

Fig.5.8.

Hall Coefficient As A Function Of Magnetic Field -

Polycrystalline InAs

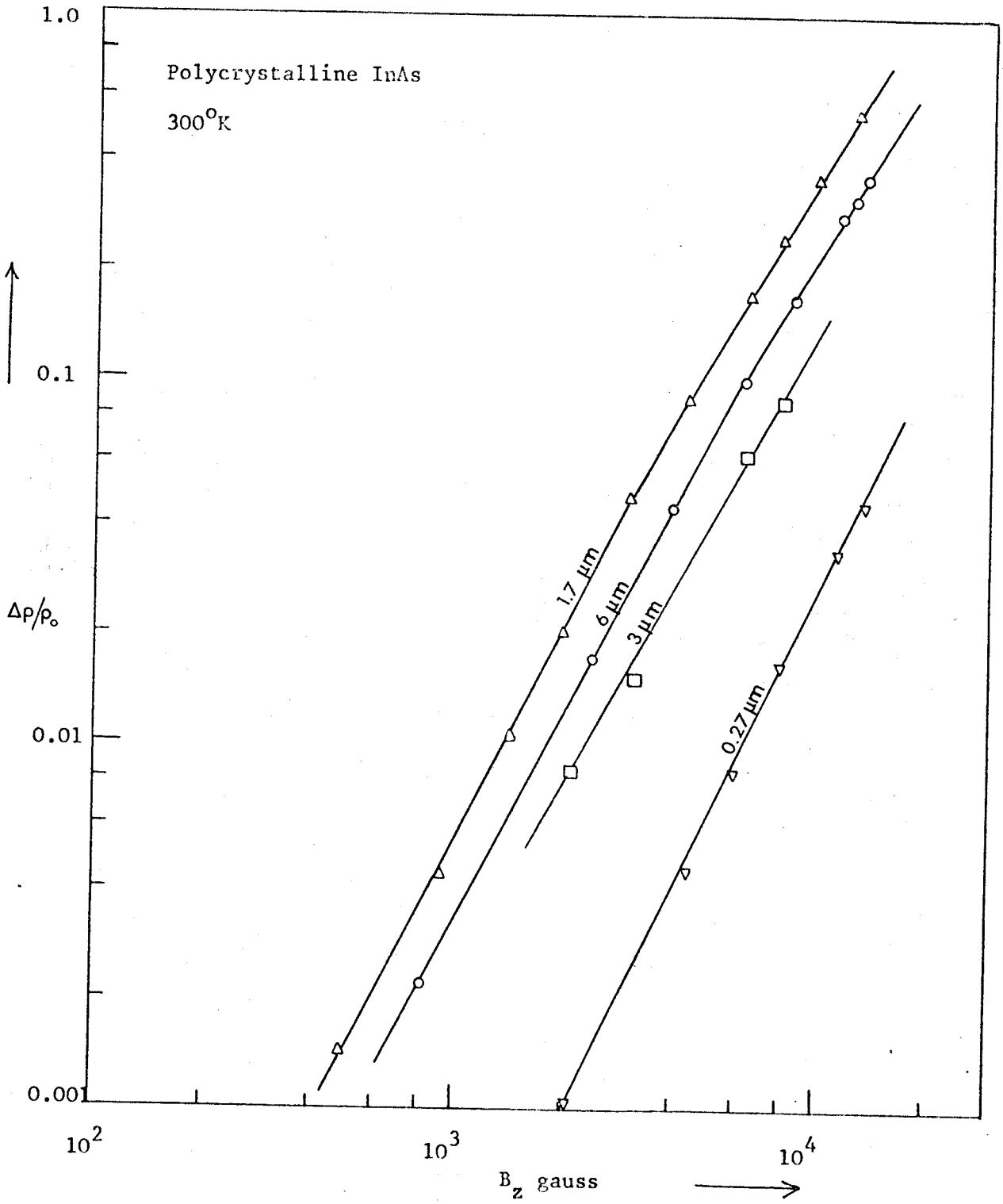

Fig.5.10

Transverse Magnetoresistance Variation With Magnetic Field

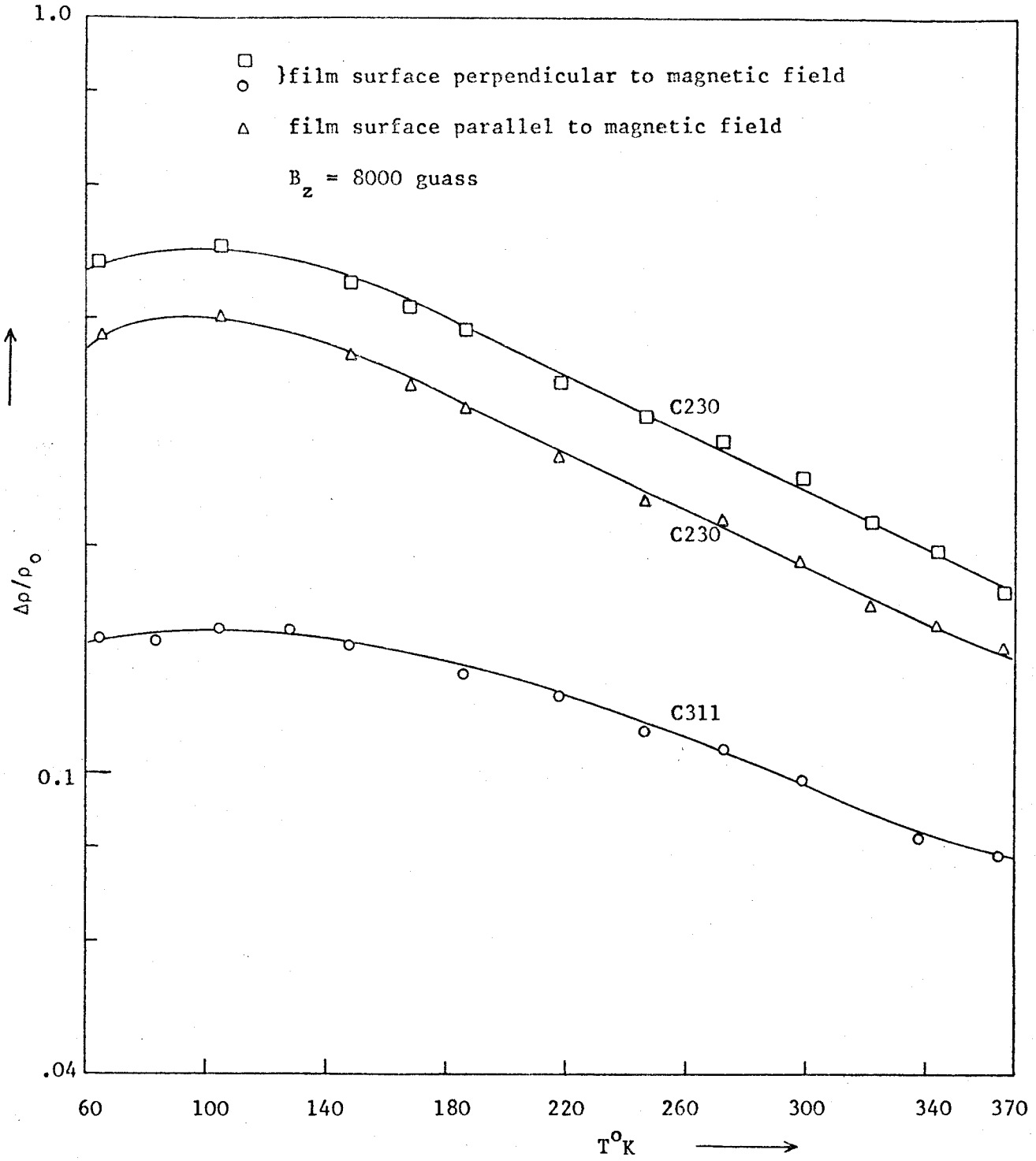

Fig.5.11

Transverse Magnetoresistance As A Function Of Temperature - Polycrystalline InAs

5.2. Epitaxial Indium Arsenide

5.2.1. Mobility And Electron Concentration As A Function Of Film Thickness

The reduction of the mobility of the epitaxial films with film thickness is plotted in Fig.5.12, together with the polycrystalline results for comparison. The highest room temperature mobilities achieved are of the order of 23,000cm^2/V-sec with films 5μm and thicker.

Fig.5.13 shows the variation of the free electron density with film thickness at 300°C. If we assume all the donors are ionized and flat bands at the surface, n then represents the net donor concentration. The higher electron concentration in the thinner films could be due to auto-doping by the substrate. Sulphur and selenium are two rapidly diffusing donors in InAs. A calculation, using the published values of the diffusion coefficients of these two donors in InAs, indicates very little auto-doping at the temperatures and times in these evaporations.

The mobility as a function of electron concentration is plotted in Fig.5.14. The results of the thick and thin films are plotted using different symbols. Also included are some of McCarthy's results for thick epitaxial layers, some of which were doped. These results indicate that the reduction in mobility with film thickness is not due to ionized donor scattering.

5.2.2. Mobility, Hall Coefficient And Conductivity Variation With Temperature

Mobility variation with reciprocal temperature is plotted in Fig.5.15 for 5 - 10μm thick layers. This shows a normal temperature

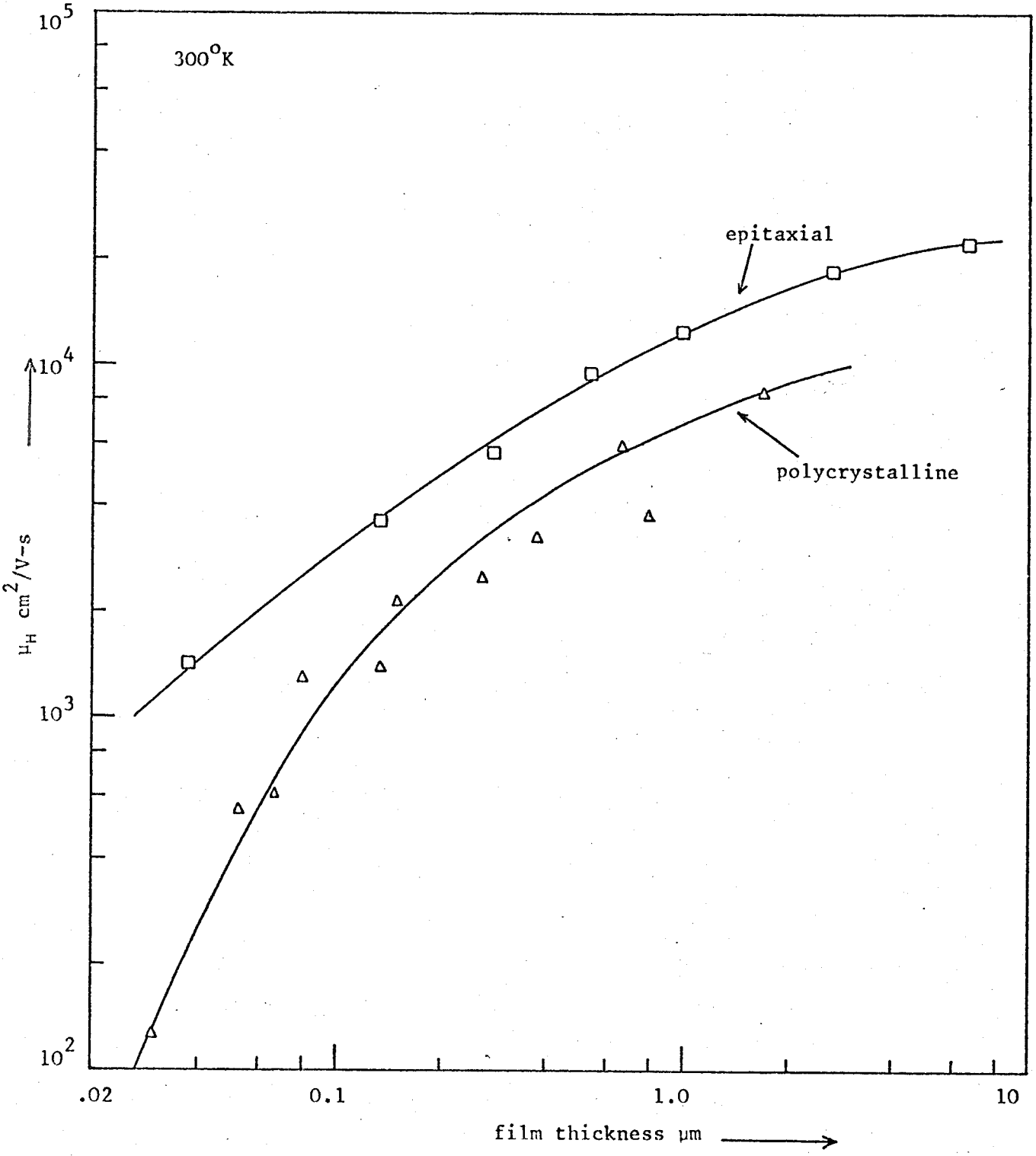

Fig.5.12

Hall Mobility Variation With Film Thickness

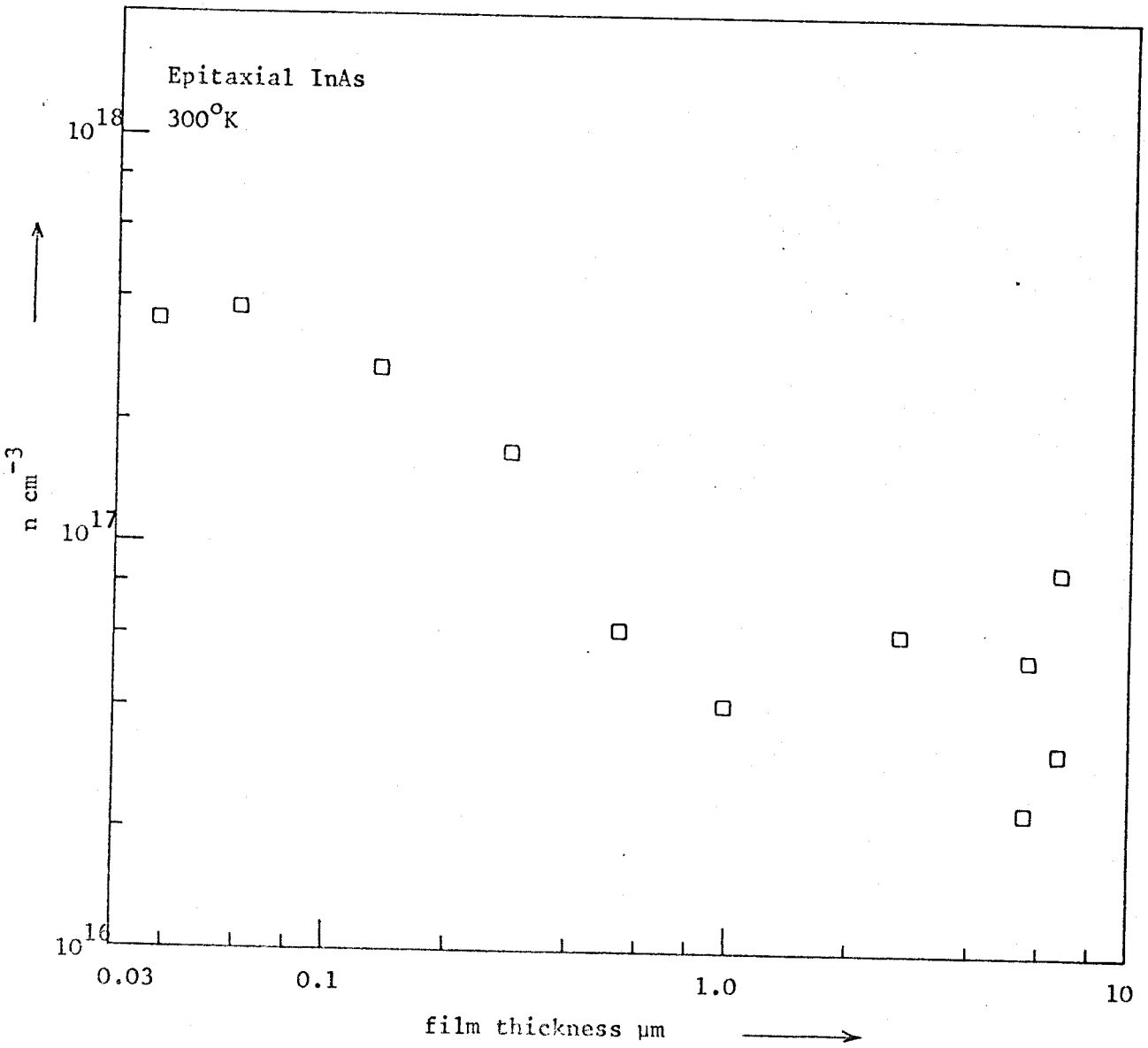

Fig.5.13

Electron Concentration As A Function Of Film Thickness

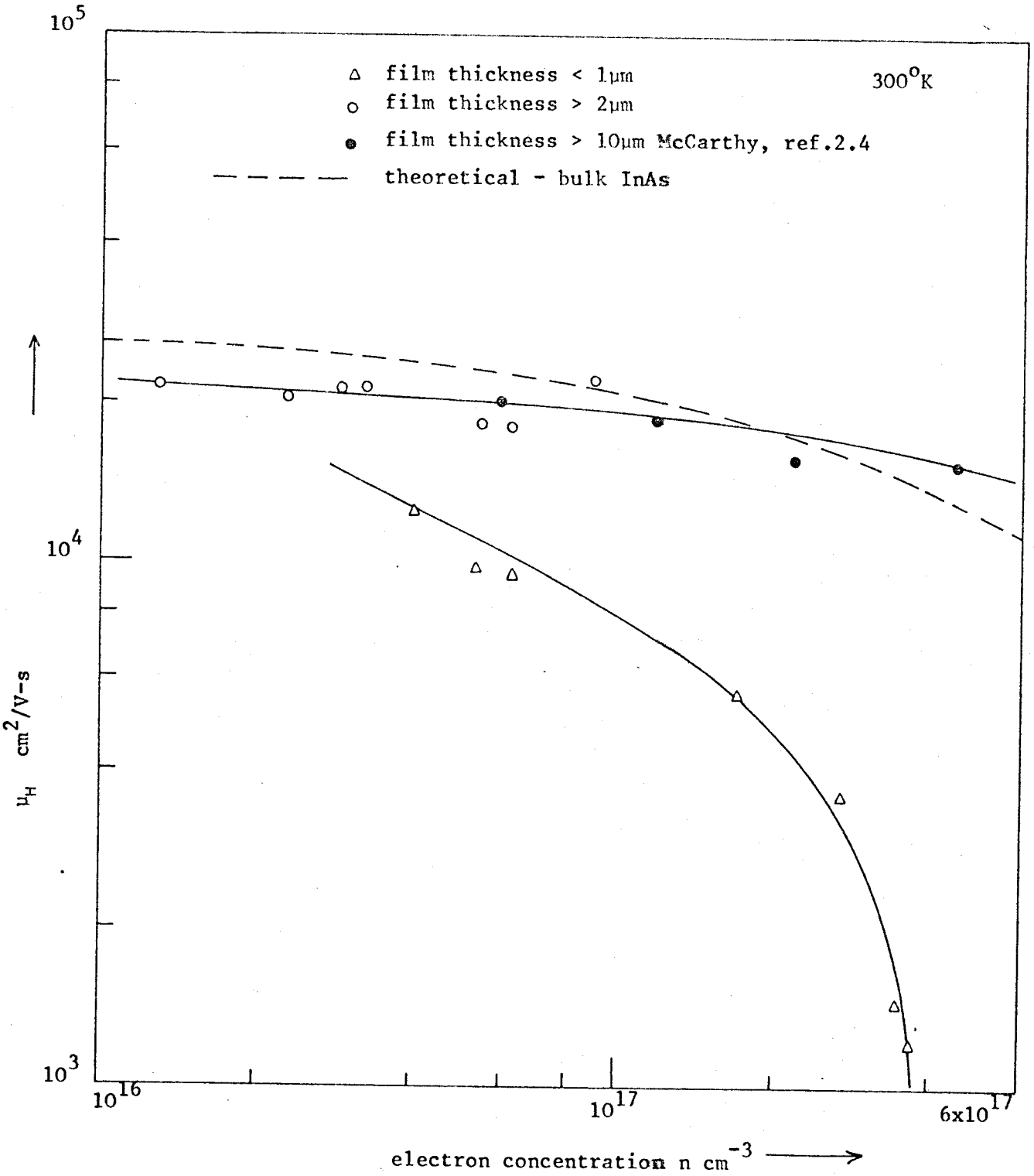

Fig.5.14

Hall mobility as a function of the electron concentration of epitaxial InAs

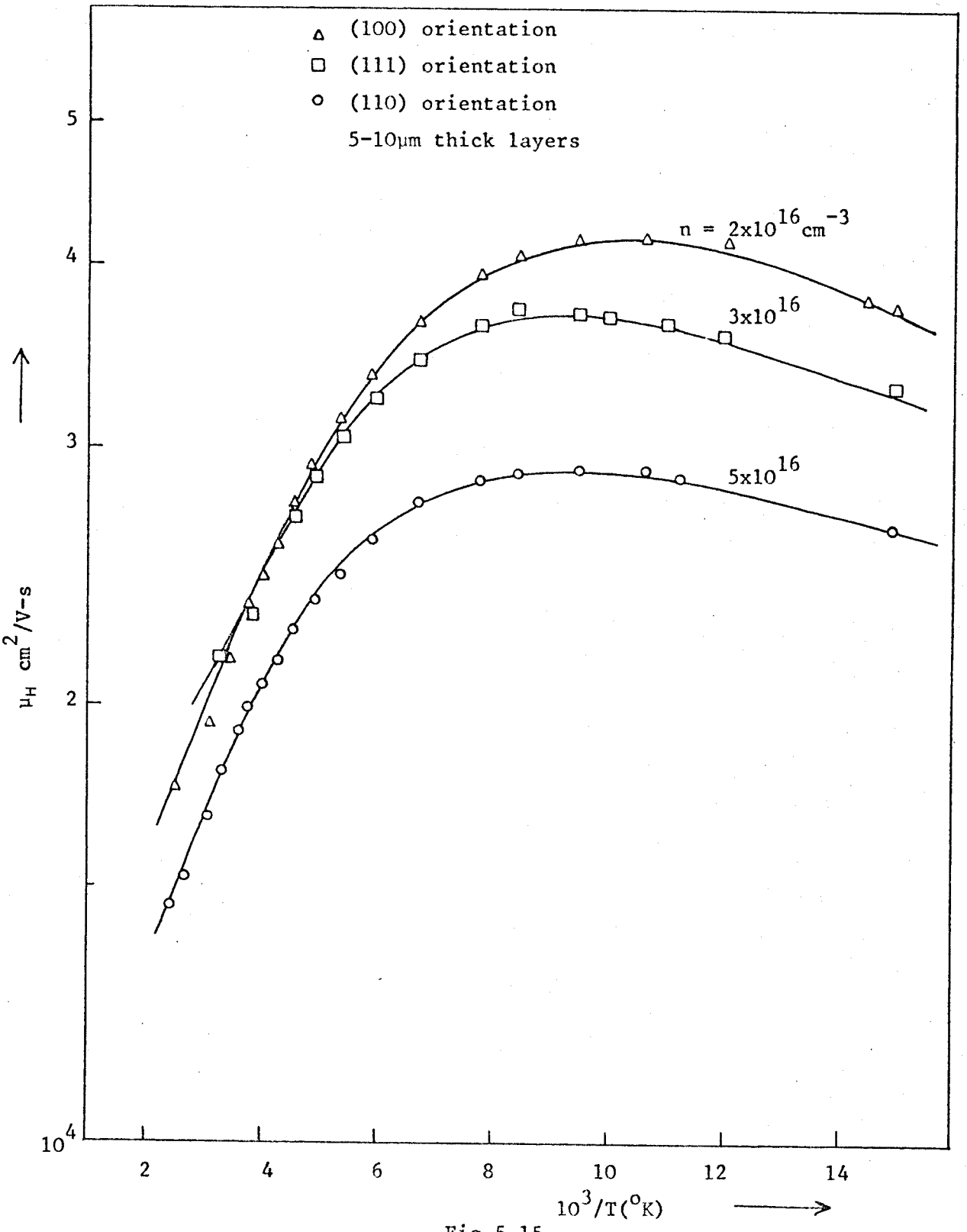

Fig.5.15

Hall Mobility As A Function Of 1/T For Thick Epitaxial Layers

dependence, with polar scattering dominating at higher temperatures and impurity scattering below 100°C.

Fig.5.16 shows the effect of film thickness on the temperature variation of the mobility, indicating a gradual reduction in the slope with a reduction in film thickness, the slope becoming negative with films below 1000Å thick. It is probably due to a change from a predominantly lattice scattering mechanism to a surface scattering mechanism. This will be considered in chapter 6.

The Hall coefficient and conductivity as a function of 1/T are plotted in Figs.5.17 and 5.18.

5.2.3. Magnetic Field Dependence Of Hall Coefficient And Magneto-Resistance

The normalised Hall coefficient for several films is plotted in Fig.5.19 and Fig.5.20. Similar to the polycrystalline samples, the thinner films have a Hall coefficient which is nearly independent of magnetic field. This will be discussed in sections 6.2.3. and 6.3.5.

Fig.5.21 shows the transverse magneto-resistance of two thick samples measured at the probes with the film surface perpendicular to the field. Fig.5.22 is the magneto-resistance measured at the current contacts, with the film surface perpendicular and parallel to the field. The variation of magneto-resistance with temperature is shown in Fig.5.23.

The linearity of Hall voltage with current is demonstrated by the results plotted in Fig.5.24, for polycrystalline and epitaxial films.

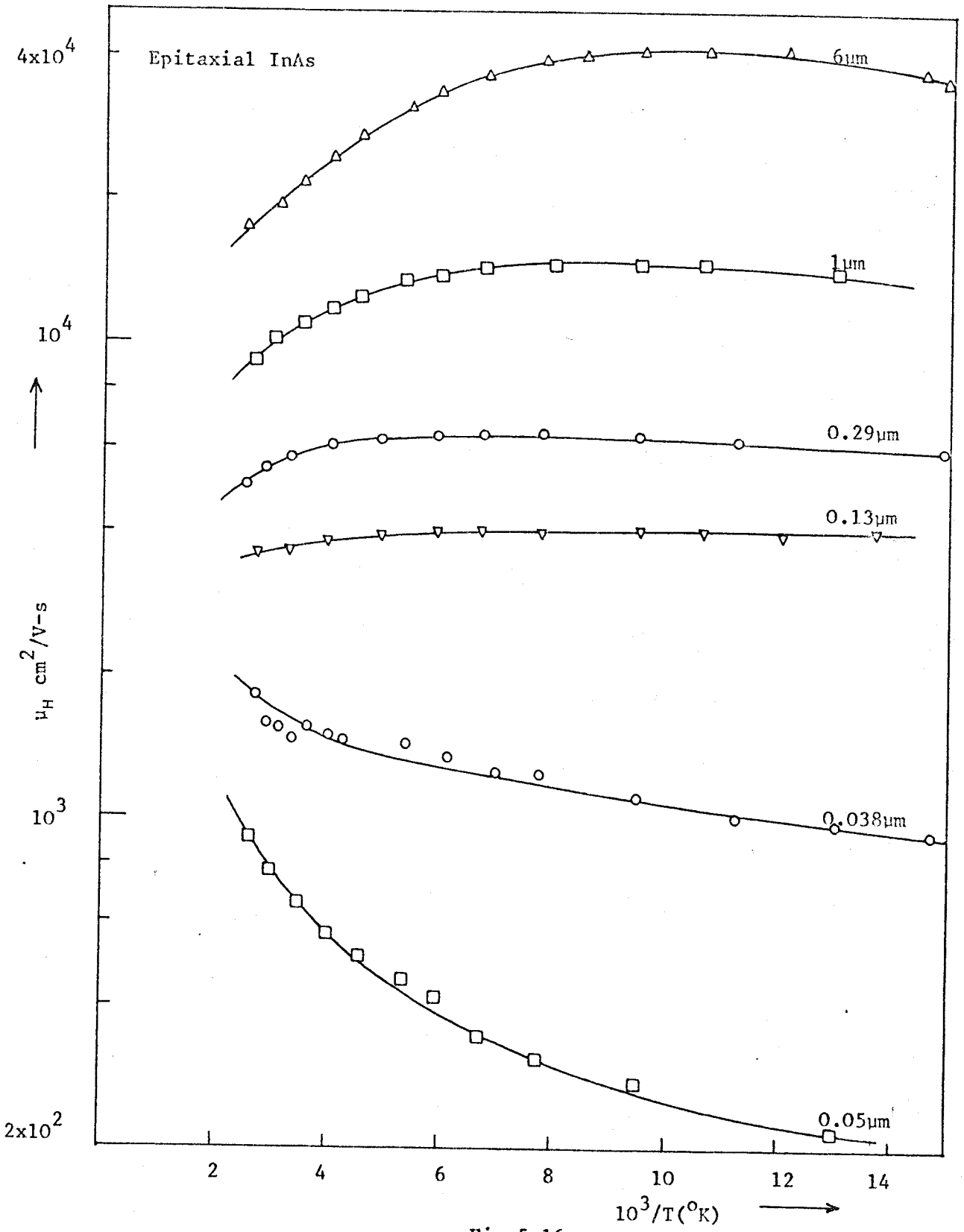

Fig.5.16

Hall Mobility Varation With Reciprocal Temperature
For Several Film Thicknesses

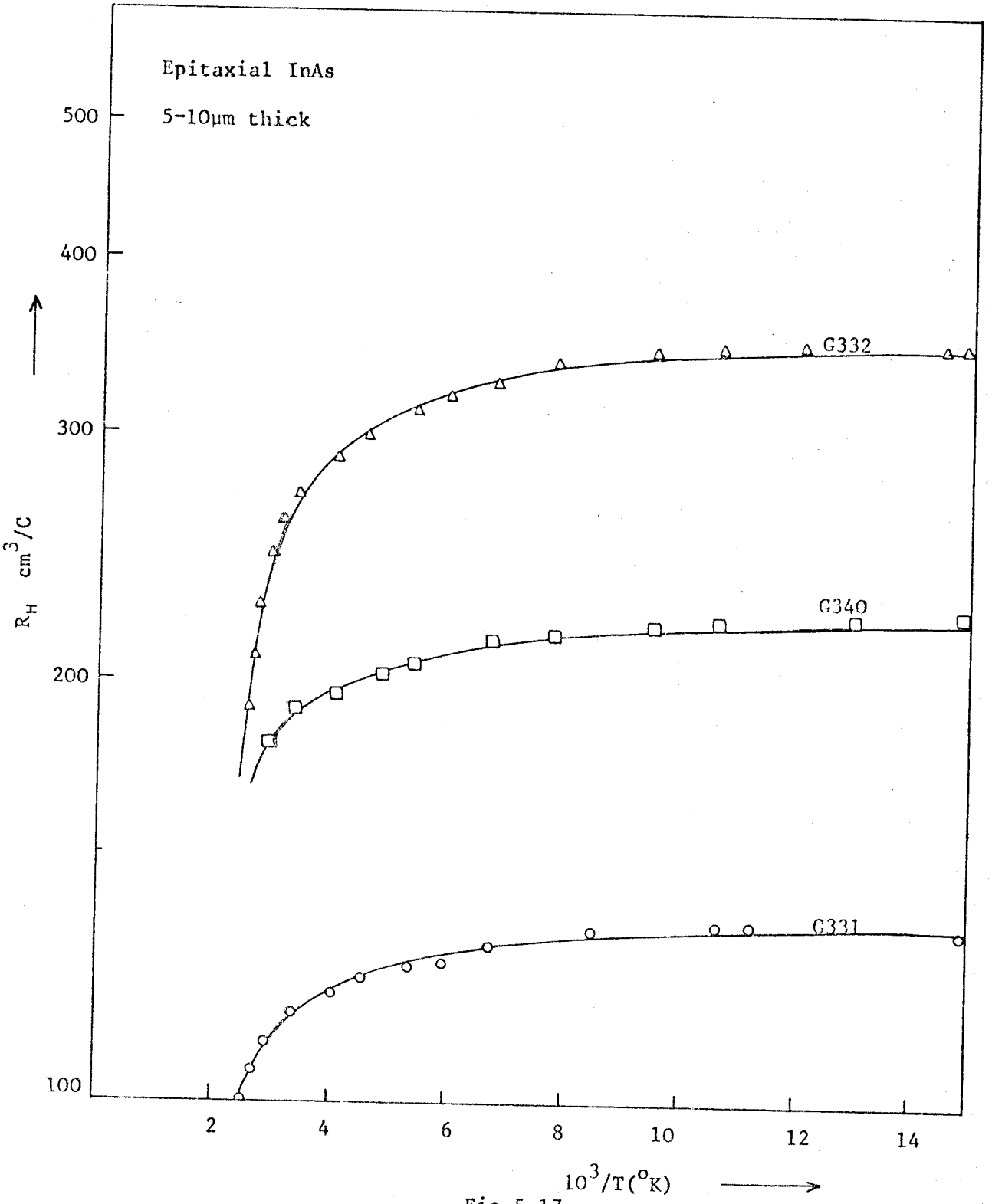

Fig.5.17

Hall Coefficient As A Function Of Reciprocal Temperature - Epitaxial Films

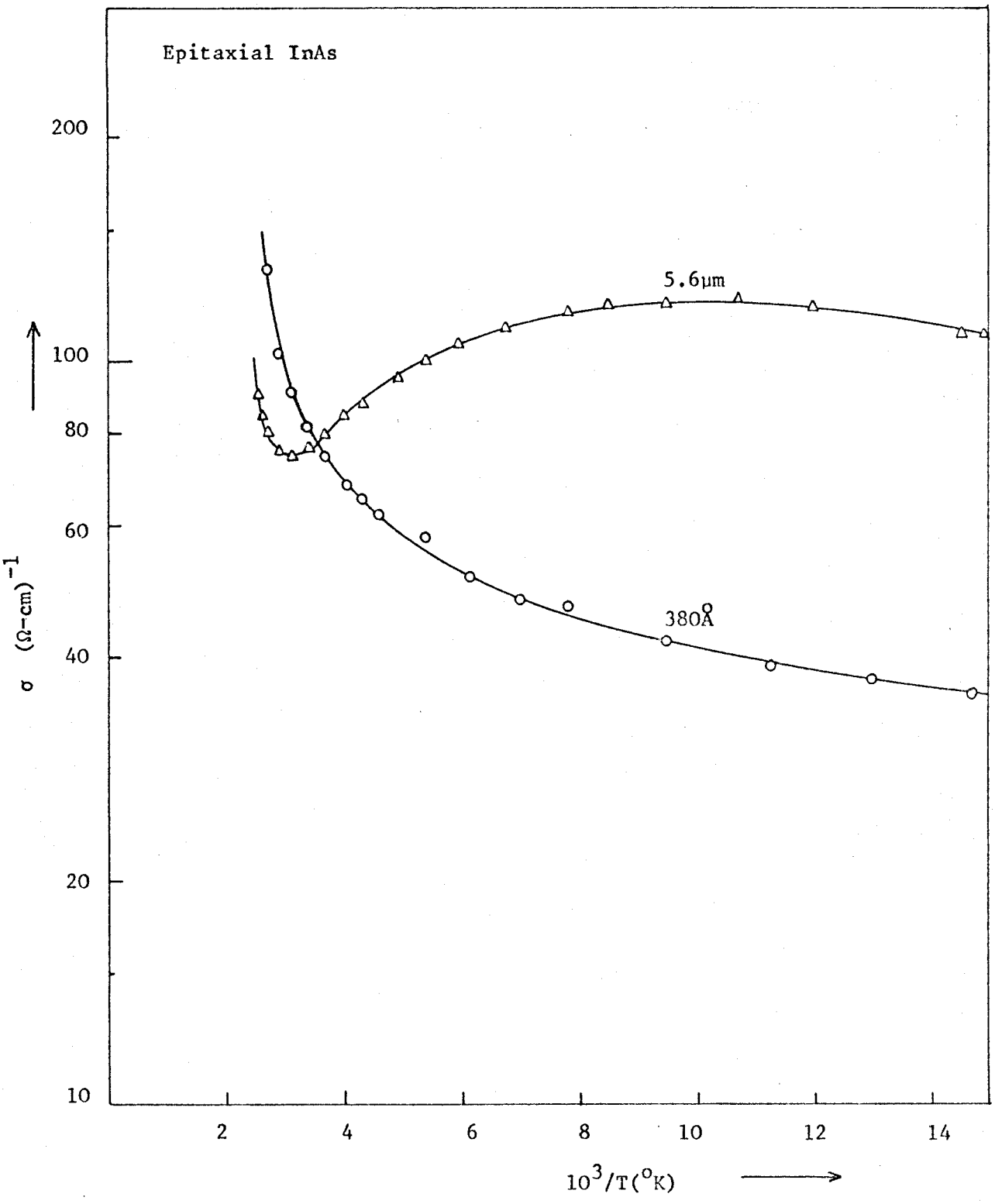

Fig.5.18

Conductivity As A Function Of Reciprocal Temperature

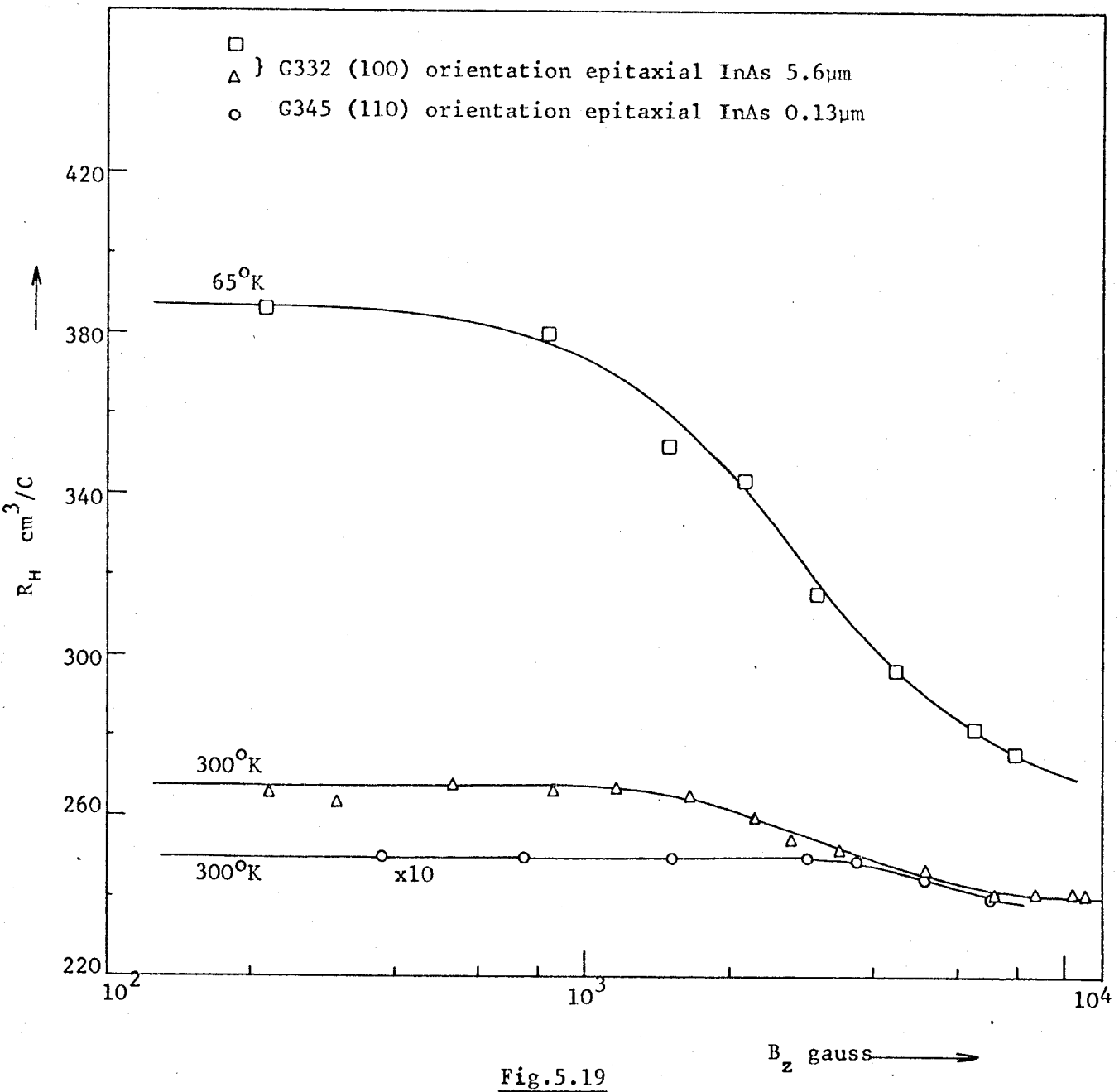

Fig.5.19

Hall Goefficient Variation With Magnetic Field
Illustrating Effect of Film Thickness.

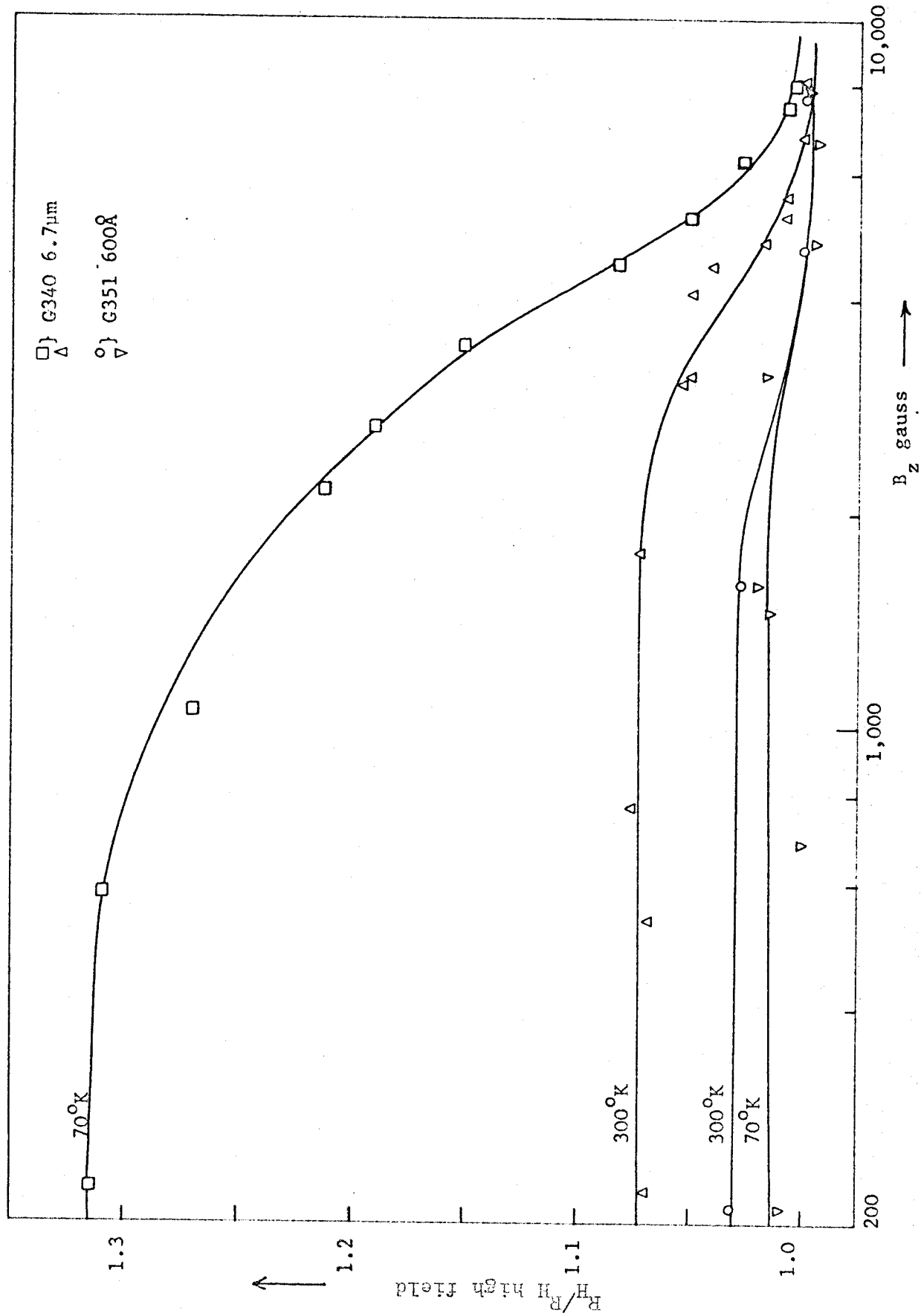

Fig.5.20.

Normalized Hall Coefficient As A Function Of Magnetic Field - Epitaxial InAs

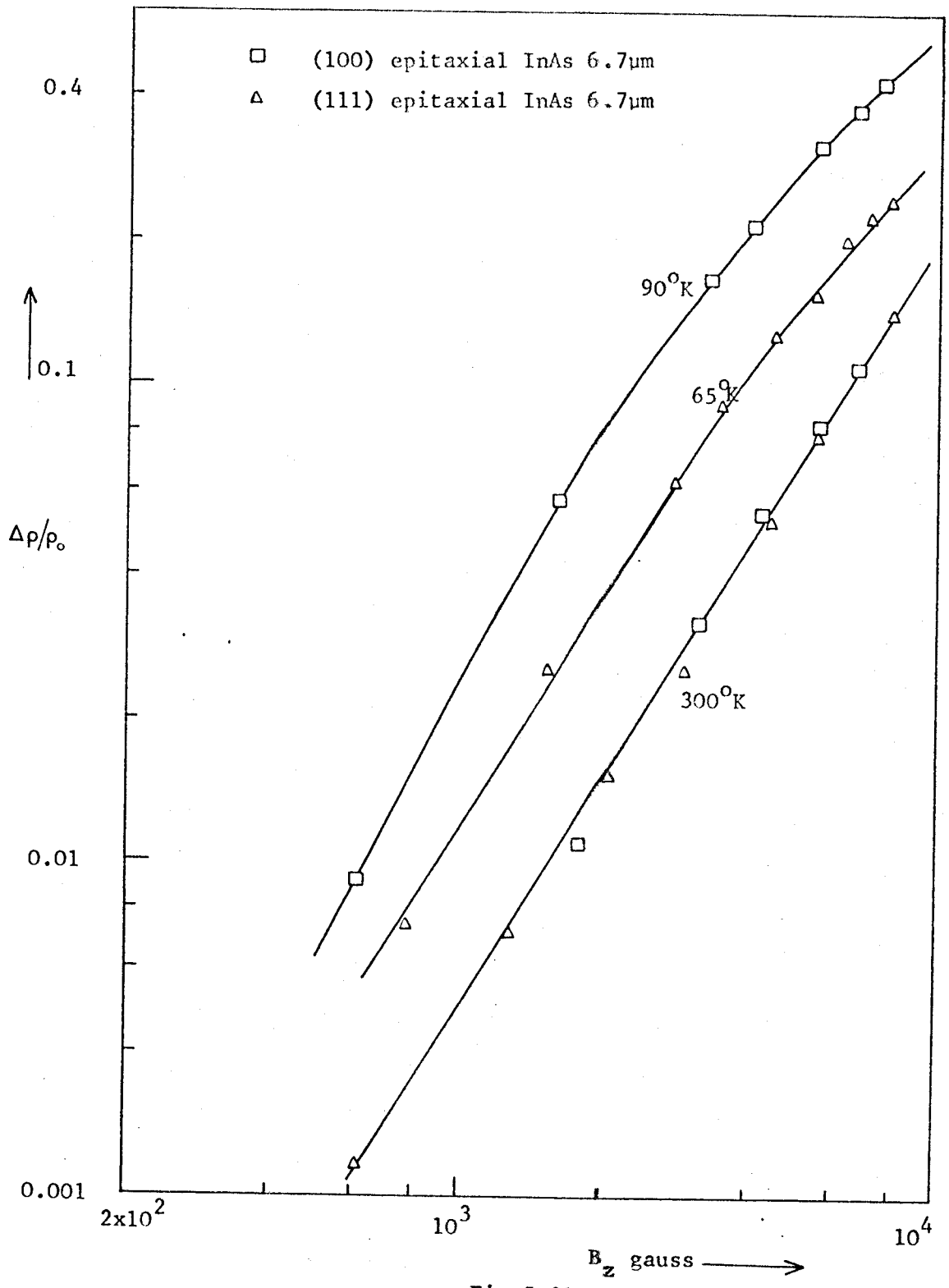

Fig.5.21

Transverse magnetoresistance - epitaxial InAs

△▽ measured at probes - film surface perpendicular to field

□ measured at current contacts - film surface perpendicular to field

o measured at current contacts film surface parallel to field

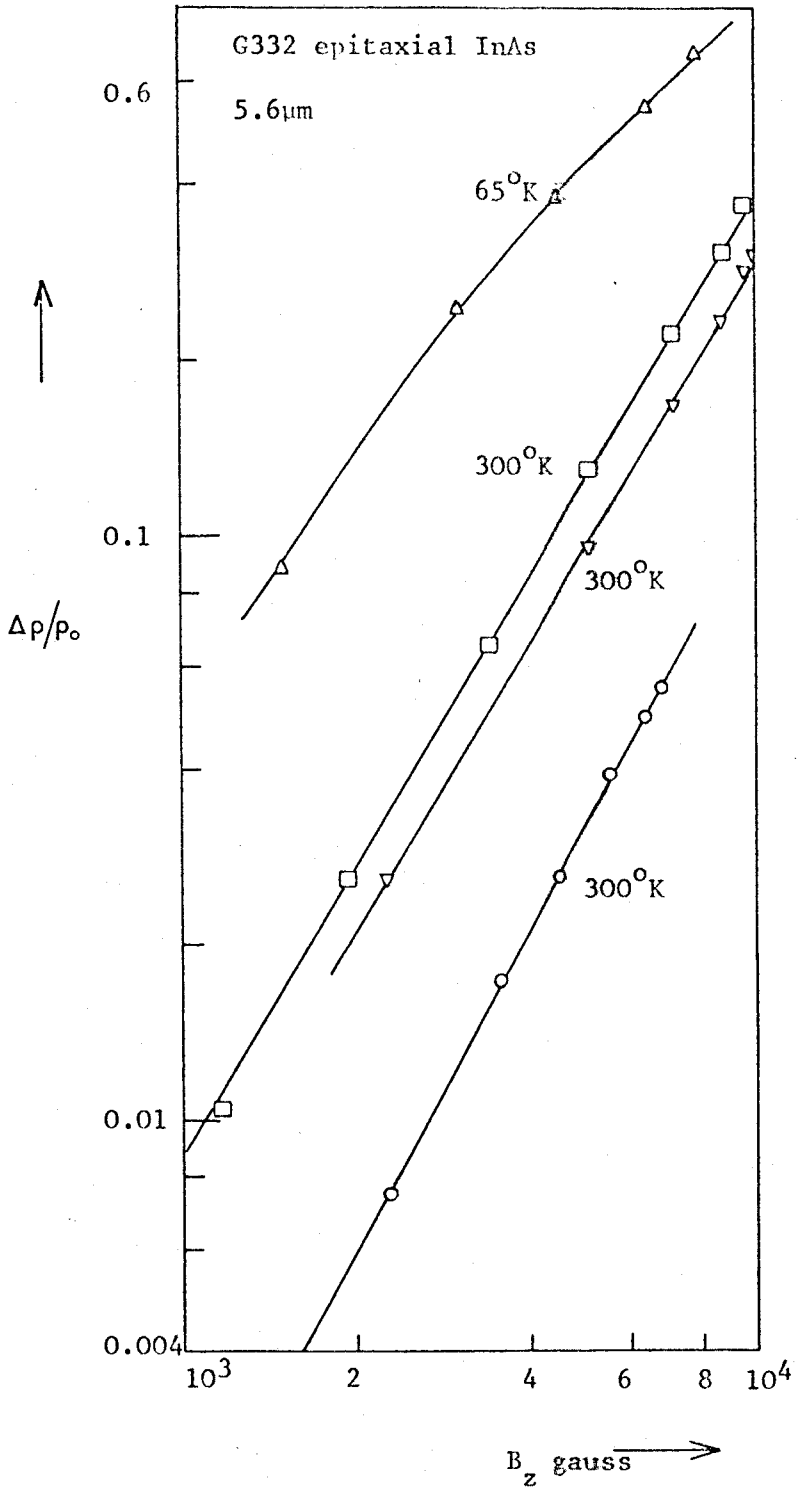

Fig.5.22

Transverse Magnetoresistance With Film
Surface Parallel And Perpendicular To Field

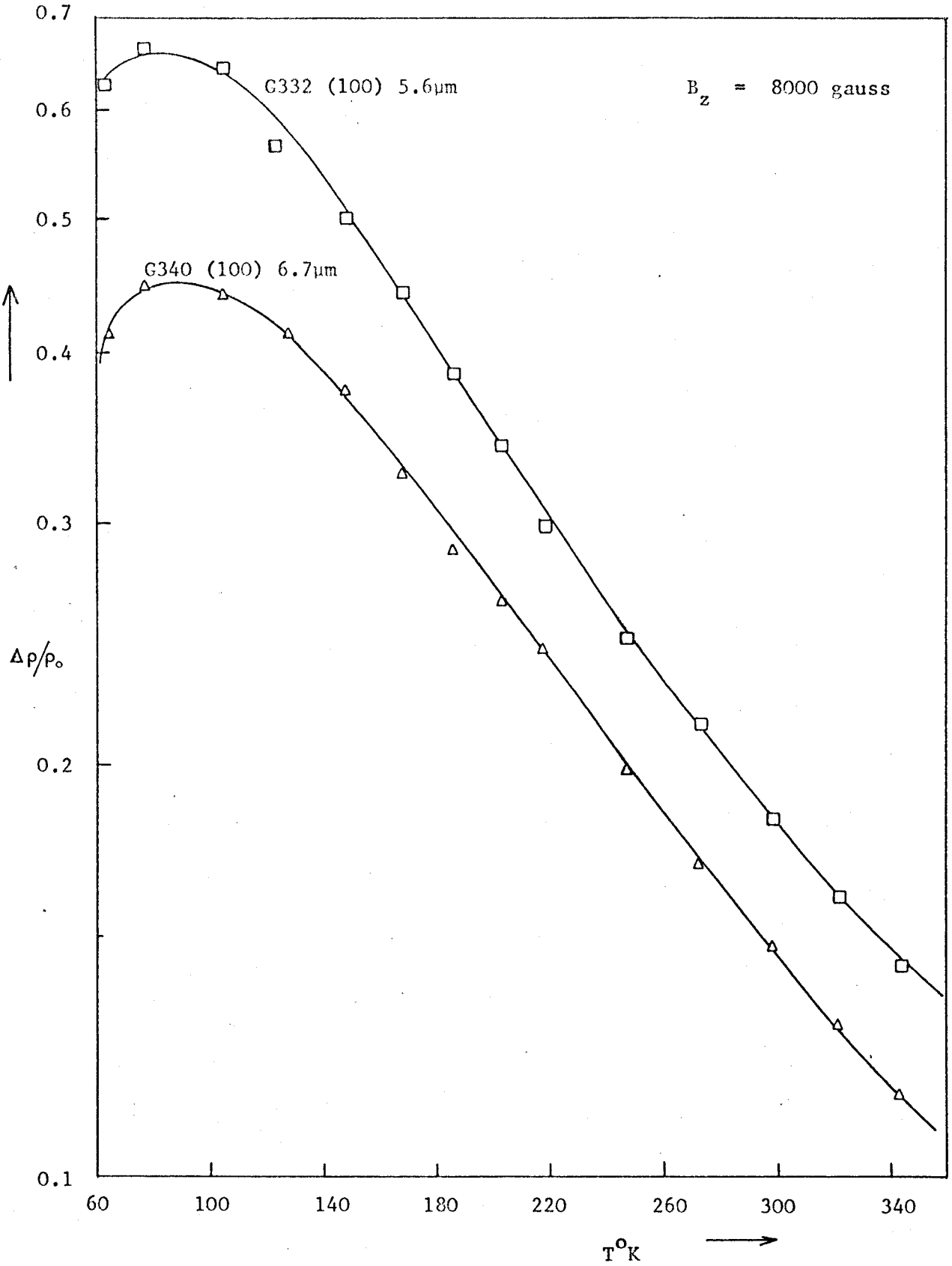

Fig.5.23

Magnetoresistance Variation With Temperature
- epitaxial InAs

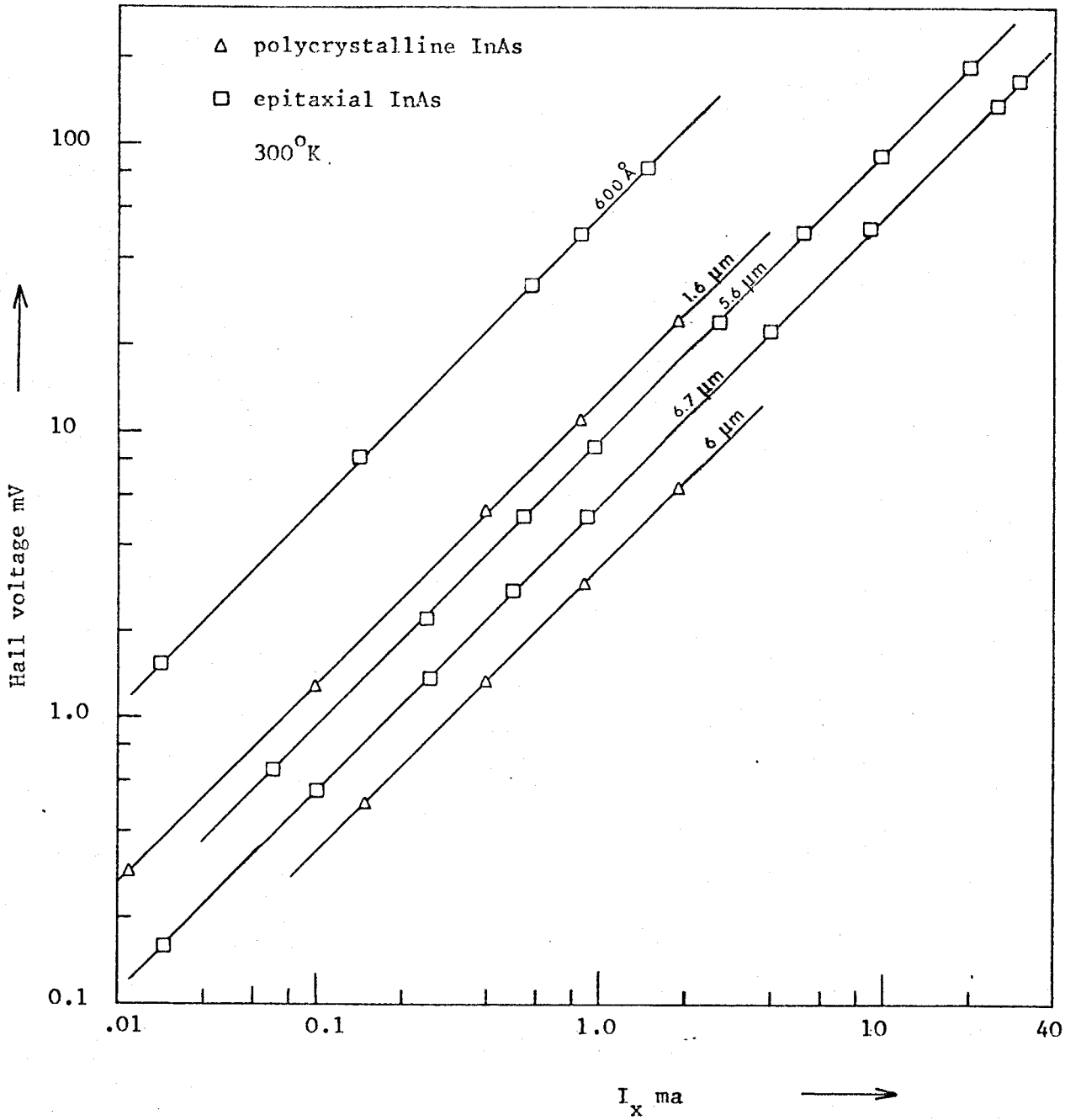

Fig.5.24

Variation Of Hall Voltage With Current In A Field Of 2000 Gauss, Illustrating Linearity

5.2.4. Comparison Of Results Using Various Deposition Methods

Table 5.1 shows typical results of epitaxial InAs deposited by various methods. To the best of our knowledge, the results of Cronin et. al[2.2], McCarthy[2.3,2.4] and Vlasov and Semiletov[2.13] are the only published work on epitaxial InAs at present.

It should be noted that Cronin et. al, and presumably McCarthy have used 6N pure source materials, which may have resulted in their lower electron densities and, therefore, higher mobilities at 77°K.

	Deposition Method	Film Thickness	μ_{H} $cm^2/V\text{-}s$ $_{300°K}$	μ_{H} $cm^2/V\text{-}s$ $_{77°K}$	Electron Density n cm^{-3}
Cronin et.al ref.2.2	Chemical vapour dep.	20μm	23,000	70,000	8.7×10^{15}
McCarthy ref.2.4	Chemical vapour dep.	>10μm	22,200	80,000	6.0×10^{15}
Vlasov and Semiletov ref.2.13	Vacuum-Flash evap.	20μm	17,600	35,600	1.6×10^{16}
Our results	Vacuum-Three temp. method	5.6μm	21,500	43,000	2.3×10^{16}
		6.7μm	22,700	32,000	9.0×10^{16}

Table 5.1

Mobility and electron concentration of epitaxial InAs

Deposited by various methods

5.3. Field Effect Measurements

5.3.1. Drain Current And Conductivity Modulation

Field effect devices have been fabricated on both polycrystalline and epitaxial InAs. However, since the conductivity modulation of the polycrystalline structures was poor, results of the epitaxial devices only will be presented.

Some characteristics are shown in Fig.5.25 of devices on one slice, which indicate very poor saturation and hysteresis. The only comments we will make here is that improvement in device characteristics should be possible with, (1) a reduction in the impurity density in the InAs films, (2) the use of a stable gate insulator, (3) a reduction in surface state densities with proper annealing procedures, (4) elimination of parasitic resistances by using a suitable metallic alloy for the source and drain contacts, and alloying them in after deposition. Examination of the 10μm and 110μm device characteristics, Figs.5.25(b) and (d), clearly shows that the latter has better saturation characteristics, presumably due to the lower percentage fraction of contact resistance to channel resistance. Drift in the drain current of these devices is probably due to the combined effects of slow surface states and mobile ions in the insulator, the InAs itself being very stable.

The drain current modulation of a 500Å InAs film for various source to drain lengths is plotted in Fig.5.26. The D.C. source-drain conductance modulation of a 110μm gap is shown in Fig.5.27. Since there was a hysteresis effect in the device characteristics, the

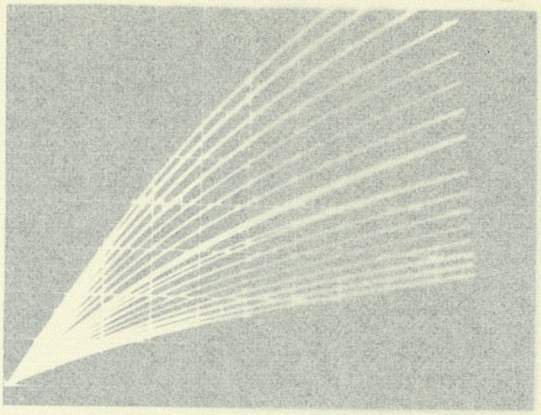

(a) 10 μm source-drain length
vert. 2ma/div
horiz 1V/div
gate ±2V/step

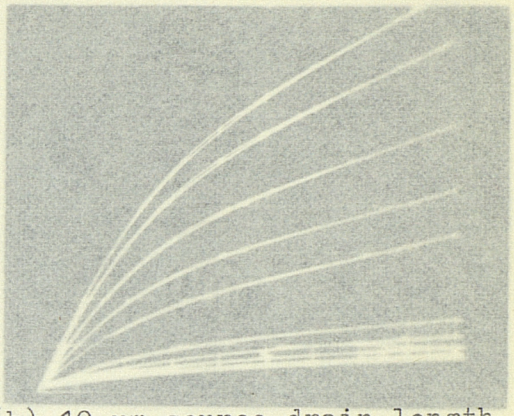

(b) 10 μm source-drain length
vert. 2ma/div
horiz. 2V/div
gate ±5V/step

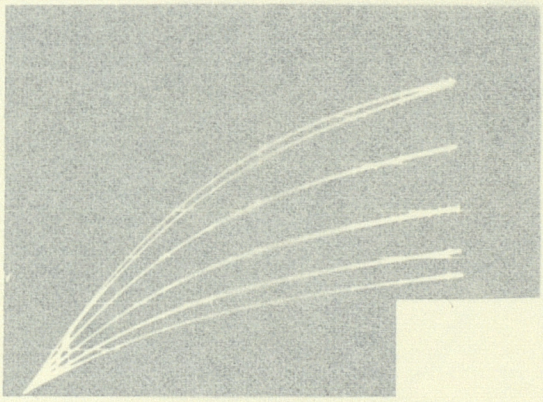

(c) 40 μm source-drain length
vert. 2ma/div
horiz. 2V/div
gate -2V/step

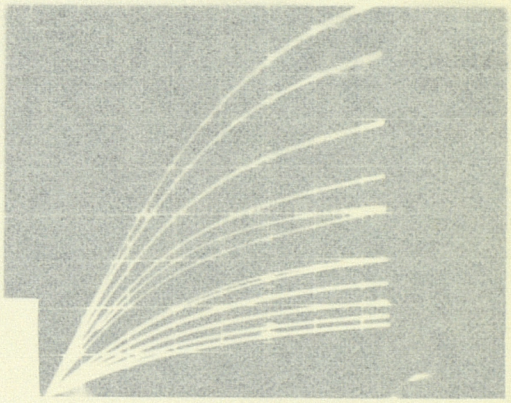

(d) 110 μm source-drain length
vert. 2ma/div
horiz. 1V/div
gate ±5V/step

Fig.5.25

Epitaxial InAs field effect device characteristics InAs-500Å, SiO-3000Å. Note the hysterisis and poor saturation. These particular characteristics were recorded one year after fabrication

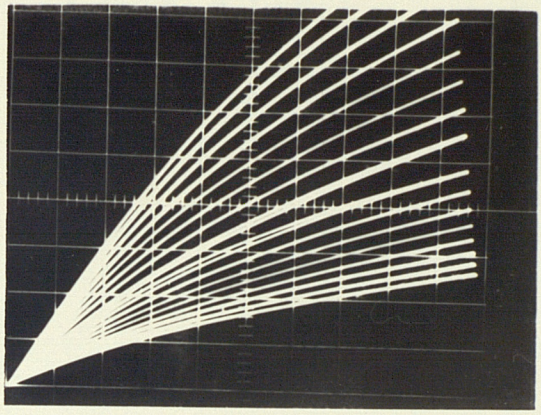

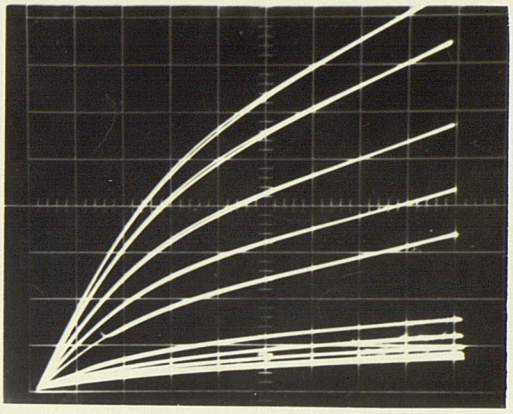

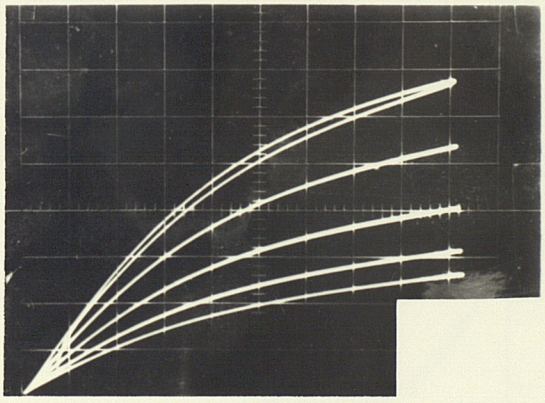

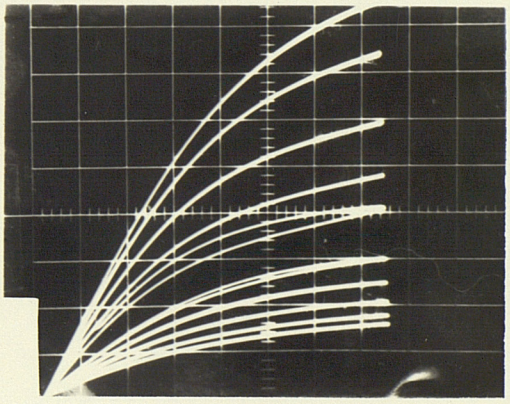

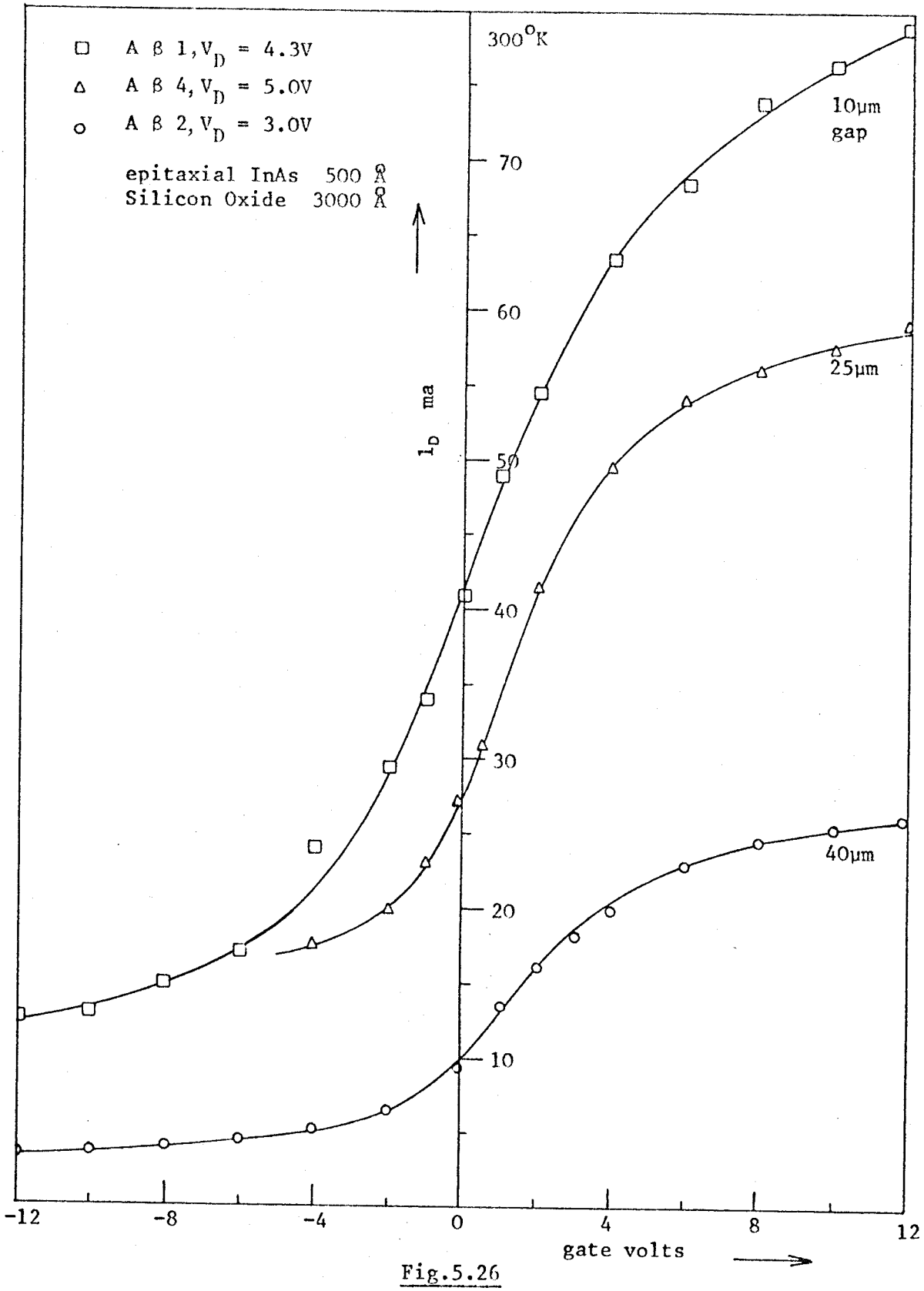

Fig.5.26

Drain Current Variation With Gate Voltage
For Several Source-Drain Gap Lengths.

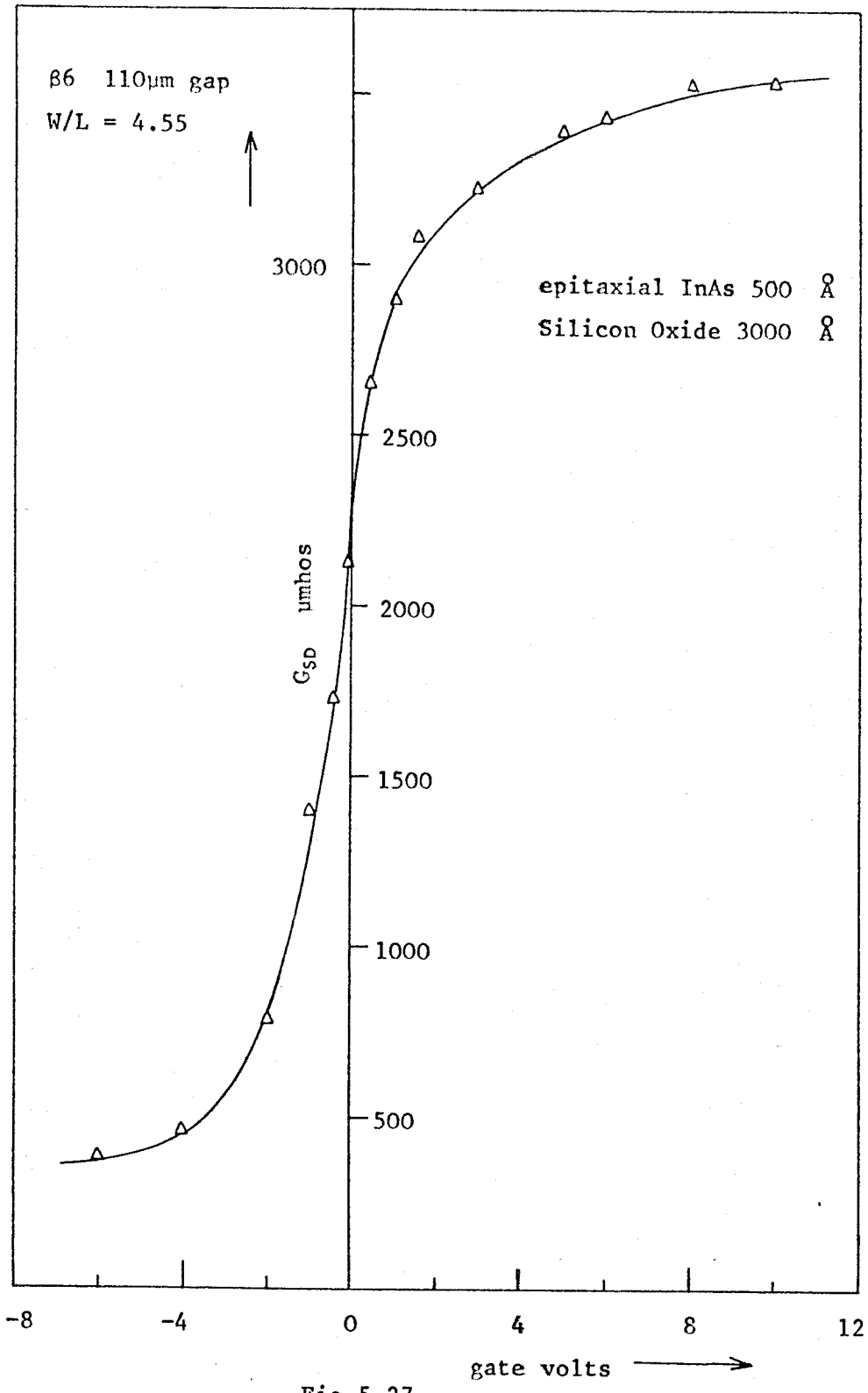

Fig.5.27

D.C. Source-Drain Conductance Variation With Gate Voltage

measurements were carried out by starting at a large negative gate voltage and varying the voltage in one direction only. These readings were taken after a short period when the current was constant, the gate circuit was monitored continuously to check that insulator breakdown was not occuring.

In order to get an estimation of the source and drain contact resistance, channel resistance at zero gate bias was plotted as a function of gap length and extrapolated to zero length. This yielded a resistance of approximately 5 ohms per contact, which is of the order of 5% of the 110μm channel resistance.

5.3.2. Electron Concentration Variation With Gate Bias

Fig.5.28 shows the variation of the free electron concentration per unit area with gate bias. This was calculated from the Hall coefficient assuming the factor r to be unity. Because of the shorting effect of the source and drain contacts a correction was made to the measured Hall voltage. The correction factor[5.7] is 6.66 for a length to width ratio of 0.22.

The saturation in the free electron density is probably due to a large number of traps just below the conduction band, which are filled as the bands are bent toward accumulation.

5.3.3. Hall Mobility And Field Effect Mobility

Fig.5.29 shows a plot the the Hall mobility of electrons in the channel as a function of electron concentration per cm^2, at two difference temperatures. By plotting the mobility as a function of n_s one avoids any effects of instability in the oxide and surface

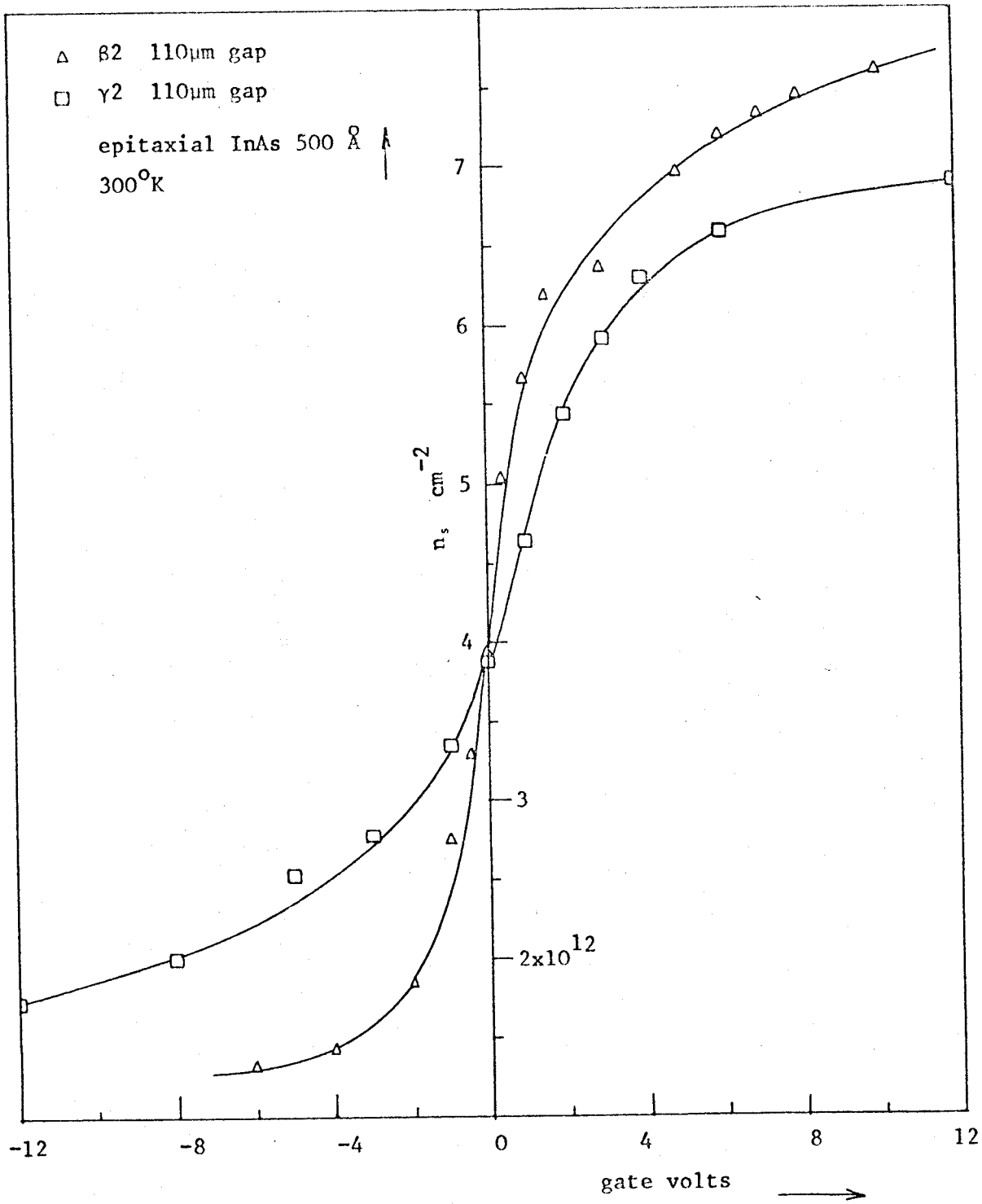

Fig.5.28

n_s variation with gate voltage measured by Hall effect

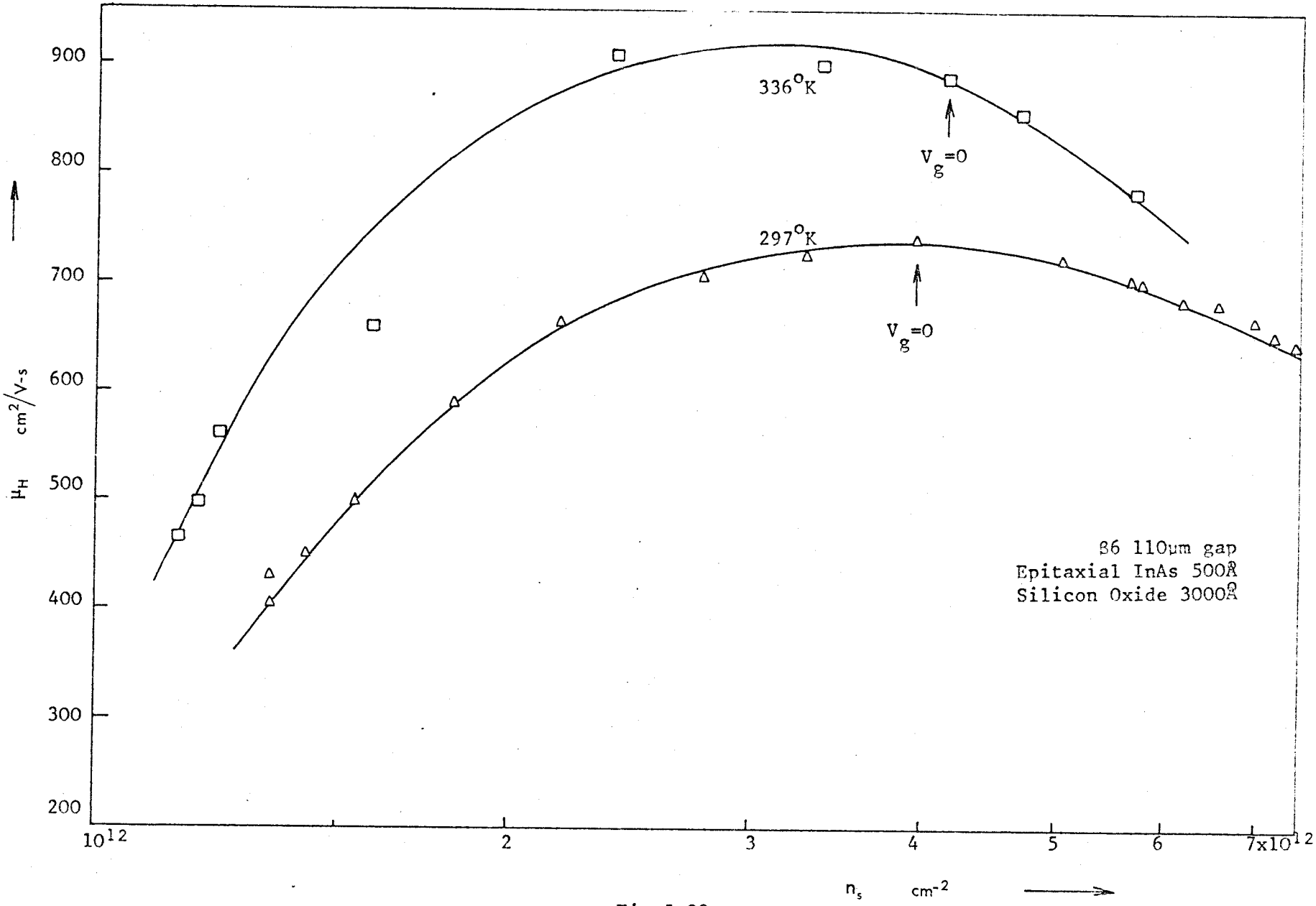

Fig.5.29.

Hall Mobility As A Function Of Surface Electron Concentration In The Field Effect Devices

states, since μ_H and n_s are intrinsic properties of the semiconductor. The fall in mobility in the accumulation region is probably due to surface scattering at the semiconductor-insulator interface. This will be considered in section 6.3.3.

The field effect mobility was calculated from the transconductance, g_m, at 1 Kc/s using the following expression[5.8]:

$$\mu_{FE} = \frac{g_m L d_{ox}}{\varepsilon_{ox}\varepsilon_o W V_{sd}} \quad cm^2/V\text{-}sec \qquad ...(5.1)$$

d_{ox} is the oxide thickness

ε_{ox} is the relative dielectric constant of the oxide. By measuring some of the plain capacitors on the same slice, a value of $\varepsilon_{ox} = 7$ was obtained.

The variation of μ_{FE} with gate bias for a 110μm device is plotted in Fig.5.30. The field effect mobility at zero gate bias is smaller than the Hall mobility by a factor of three, which gives an indication of the amount of induced charge being trapped. The fall off with positive gate voltage is also much more rapid, again confirming that the trapped charge is increasing.

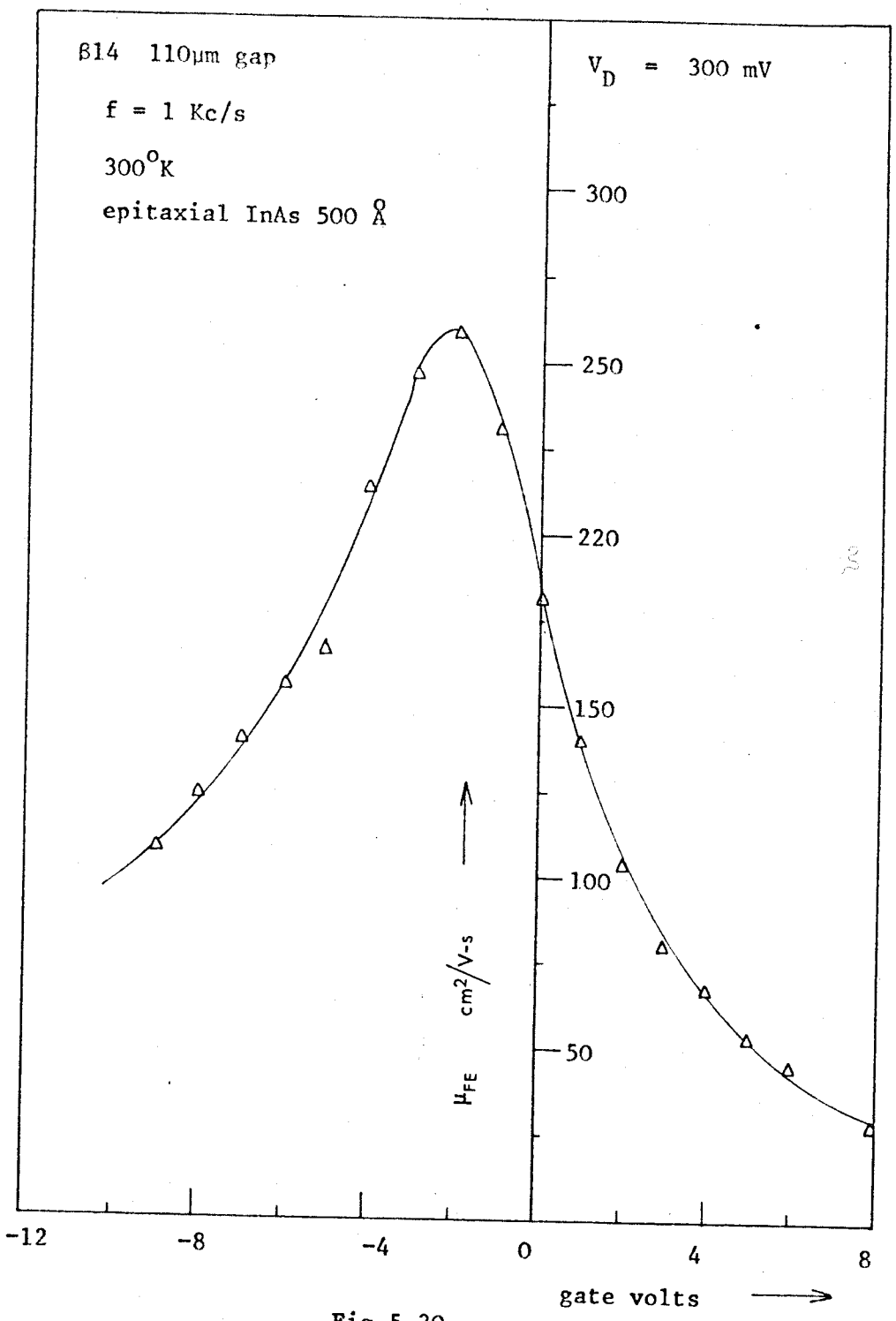

Fig.5.30

Field effect mobility as a function of gate voltage

6. TRANSPORT THEORY

6.1. Space Charge Analysis

6.1.1. Space Charge Calculations In Thin Semiconductor Films

We will consider the modulation of the electron concentration per unit surface area by an electric field perpendicular to the surface. The emphasis will be on accumulation and depletion modes of operation and the effect of film thickness. We will not consider conductance modulation here because this would require a knowledge of the variation of carrier mobility with surface potential, which will be examined later.

Most of the analyses[6.1,6.2] of charge modulation have assumed the thickness of the semiconductor to be much larger than the extrinsic Debye length, hence ensuring that even under maximum band bending, bulk conditions will be achieved sufficiently deep inside the semiconductor. This is illustrated in Fig.6.1(a) for the case of equal band bending at each surface. However, when the above condition is not satisfied, as shown in Fig.6.1(b), then the analysis is modified slightly[6.3,6.4,6.5,6.6]. We will consider the case where there are no surface states at the film substrate interface and the potential is varied only on the other surface. Non-degenerate statistics will be used and the donors and acceptors are assumed to be completely ionized.

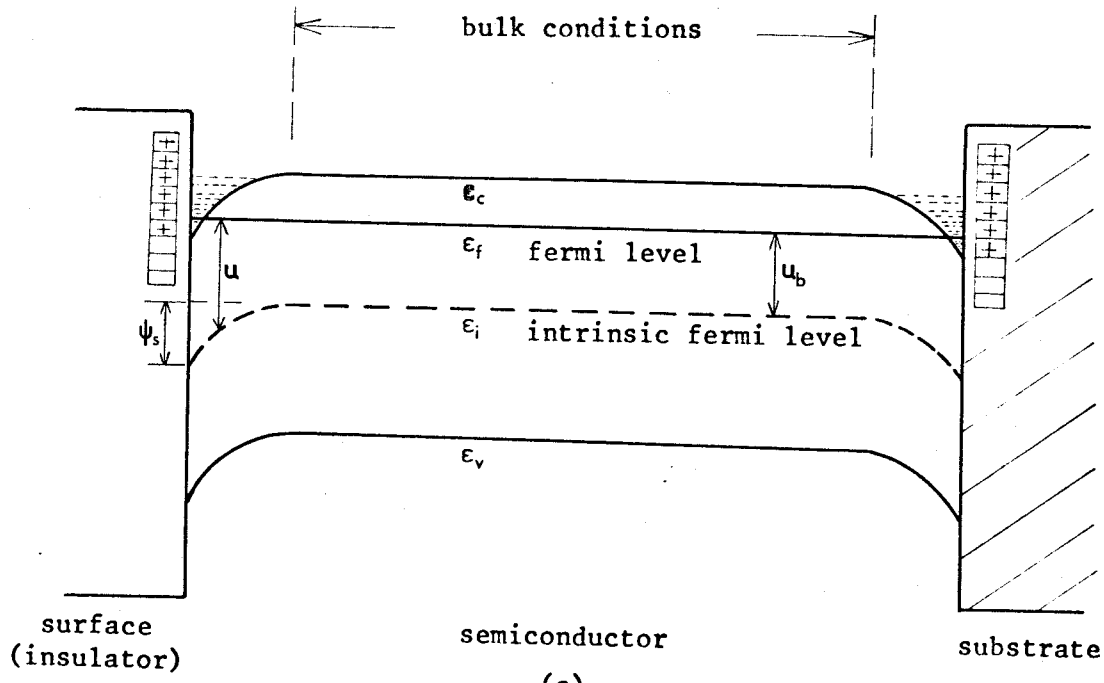

(a)

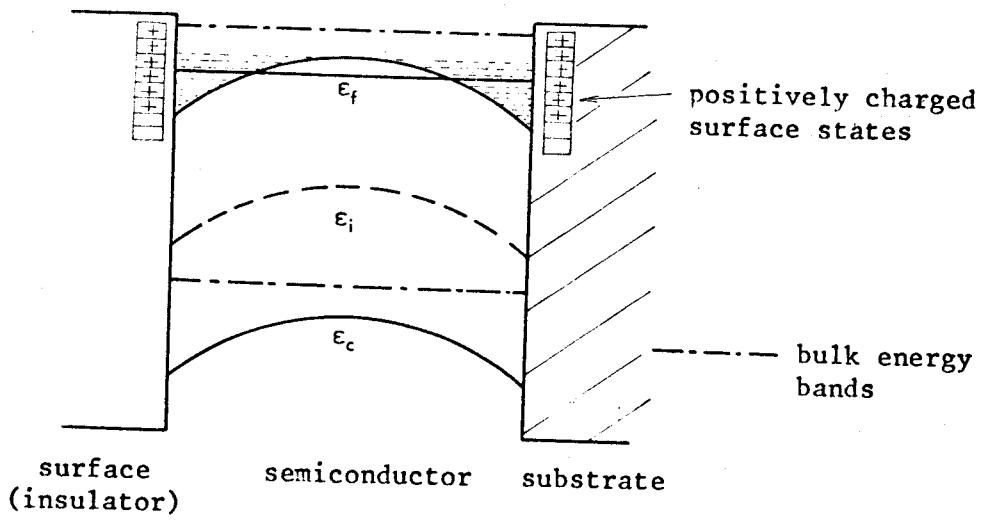

(b)

FIG.6.1

Energy Band Diagram For A Thin Film, Showing Effect Of Surface States At Both Interfaces, (a) $2d \gg L_B$, (b) $2d \leq L_B$

The net charge density at any point in the space charge layer is:

$$\rho(\psi) = -q(n-p+N_A-N_D) \qquad ...(6.1)$$

where $n = n_i \exp(u_b-\psi)$

$p = n_i \exp(-u_b+\psi)$

$N_D = n_b = n_i \exp(u_b)$

$N_A = p_b = n_i \exp(-u_b)$ ...(6.2)

ψ is the band bending in kT/q units = u_b-u

u_b is the bulk fermi potential normalized to kT/q = $(\varepsilon_F-\varepsilon_i)/kT$

Poissons equation in one dimension may then be written:

$$\frac{d^2\psi}{dz^2} = -\frac{q\rho(\psi)}{\epsilon_s\epsilon'_o kT} = \frac{-L_B^{-2}}{2}\left[(1-\exp(-\psi)) + \lambda^{-2}(\exp(\psi)-1)\right] \qquad ...(6.3)$$

where $L_B = (\epsilon_s\epsilon'_o kT/2q^2n_b)^{\frac{1}{2}}$ is the extrinsic Debye length, plotted in Fig.6.2 as a function of n_b for InAs. When $n_b = n_i$, $L_B = L_D$, the intrinsic Debye length.

$$\lambda = n_b/n_i = \exp(u_b)$$

is the normalised bulk doping density.

Integration of equation 6.3 between the limits ψ_d to ψ gives:

$$L_B\frac{d\psi}{dz} = \pm\left[(\exp(-\psi)+\psi-\psi_d-\exp(-\psi_d)+\lambda^{-2}\{\exp(\psi)-\psi+\psi_d-\exp(\psi_d)\}\right]^{\frac{1}{2}}$$

$$= \pm F(\psi, \psi_d, \lambda) \qquad ...(6.4)$$

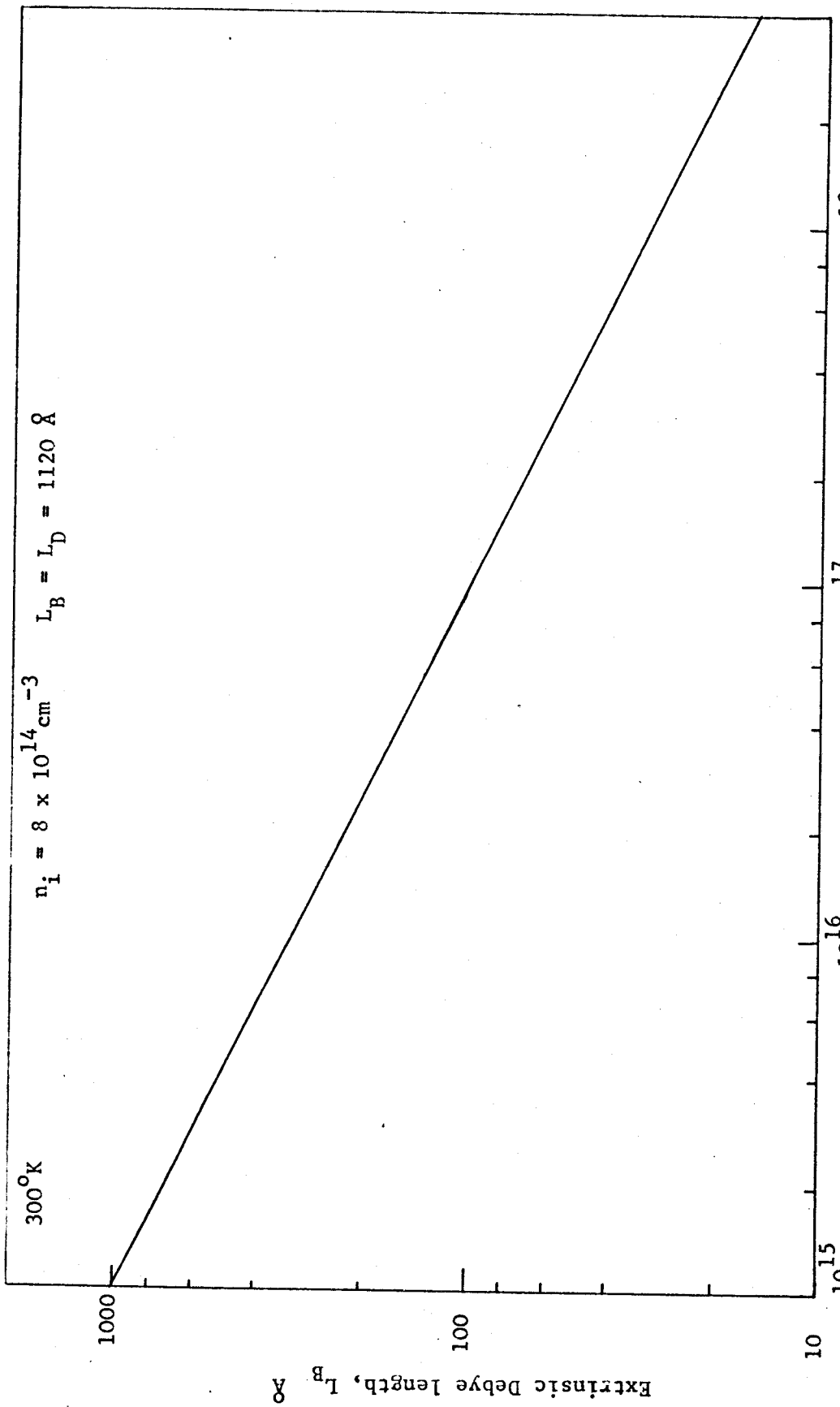

FIG.6.2

Extrinsic Debye Length As A Function Of Bulk Electron Concentration For InAs.

The positive sign is for accumulation layers, the negative sign for depletion/inversion.

When $\psi_d = 0$, i.e. thick slabs, $d >> L_B$, $\lambda^{\frac{1}{2}}F(\psi,\psi_d,\lambda)$ reduces to $F(u,u_b)$, which was originally derived by Kingston and Neustadter[6.1] and is tabulated by Frankl[6.3].

The surface electric field is given by:

$$E_z = -\frac{kT}{qL_B} F(\psi,\psi_d,\lambda) \qquad ...(6.5)$$

The excess carrier concentrations are given by:

$$\Delta n_s = \int_0^{2d} (n-n_b)dz = n_i\lambda L_B \int_{\psi_s}^{\psi_d} \frac{\exp(-\psi)-1}{F(\psi,\psi_d,\lambda)}\, d\psi \qquad ...(6.6)$$

$$\Delta p_s = n_i\lambda^{-1}L_B \int_{\psi_s}^{\psi_d} \frac{\exp(\psi)-1}{F(\psi,\psi_d,\lambda)}\, d\psi \qquad ...(6.7)$$

All these expressions reduce to those for thick slabs when $\psi_d = 0$, i.e.

$$\Delta n_s = n_i L_D G(-u_s-u_b) \qquad ...(6.8)$$

$$\Delta p_s = n_i L_D G(u_s,u_b) \qquad ...(6.9)$$

These G functions have been tabulated by Frankl[6.3] for various values of u_s and u_b.

We can obtain an expression in terms of the film thickness, 2d, from equation 6.4 as follows:

$$2d = \pm L_B \int_{\psi_d}^{\psi_s} \frac{d\psi}{F(\psi,\psi_d,\lambda)} \qquad \ldots(6.10)$$

Equation 6.10 may be used to obtain the value of ψ_d for various film thickness and band bending. However, the integrations can only be carried out numerically, unless approximations for $F(\psi,\psi_d,\lambda)$ are used, as given in the following section.

6.1.2. Effect Of Film Thickness On The Electrostatic Potential At The Substrate Interface

(a) Weak Band Bending

Consider the case of weak band curvature $|\psi_d| < |\psi_s| < 1$ expanding the exponential terms in equation 6.4 one obtains:

$$F(\psi,\psi_d,\lambda) \doteq \frac{\left\{1+\lambda^{-2}\right\}^{\frac{1}{2}}}{2} (\psi^2-\psi_d^2)^{\frac{1}{2}} \qquad \ldots(6.11)$$

Substituting this in equation 6.10 and integrating, gives:

$$\psi_d = \psi_s \operatorname{sech} 2\gamma_o d \qquad \ldots(6.12)$$

where $\gamma_o = \left[\frac{1+\lambda^{-2}}{2L_B^{\,2}}\right]^{\frac{1}{2}}$

Equation 6.12 is plotted in Fig.6.3 as a function of film thickness for various bulk doping densities.

(b) Heavy Electron Accumulation

For heavy electron accumulation, i.e. $\psi_s << \psi_d < 0$ and with $\lambda > 1$, equation 6.4 reduces to:

$$F(\psi,\psi_d,\lambda) \doteq \left[\exp(-\psi)-\exp(-\psi_d)\right]^{\frac{1}{2}} \qquad \ldots(6.13)$$

Substituting this in equation 6.10 and integrating yields:

$$\psi_d = 2\ln\left\{\frac{2d}{\pi L_B}\right\} \qquad 2d < \pi L_B \qquad \ldots(6.14)$$

This expression is plotted in Fig.6.4. Note that ψ_d appears to be independent of ψ_s under the above conditions. It can be seen that the assumption $\psi_d = 0$ is incorrect for very thin films, below approximately 1000Å, and for bulk doping densities less than $10^{16}cm^{-3}$. This is an important consideration in calculations of surface scattering mobilities, (see section 6.3.4.), in very thin film field effect structures.

The simple analysis given above is useful when the surface band bending is not too large. At high fields, quantization of the conduction band states occurs, as mentioned in chapter 1. Under these conditions it is necessary to obtain a simultaneous solution of Schroedingers and Poissons equations. Apparently, this modifies the shape of the potential well such that the electric field penetrates further into the bulk. Hence, the effects described above, of a non-zero ψ_d in very thin films, would be even more important. A further discussion of quantum effects will be given in section 6.4.1.

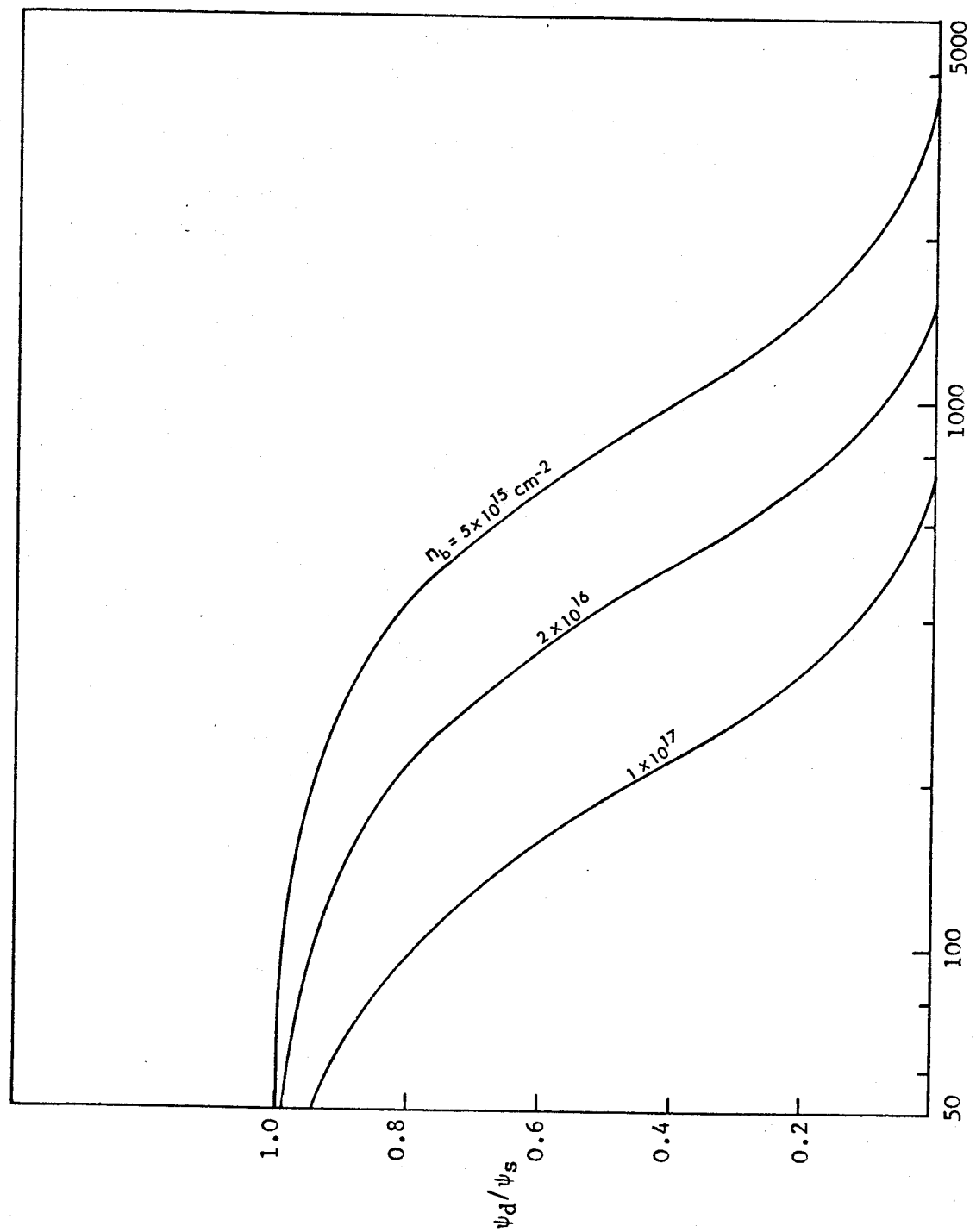

FIG.6.3

ψ_d/ψ_s As A Function Of Film Thickness - Weak Band Bending

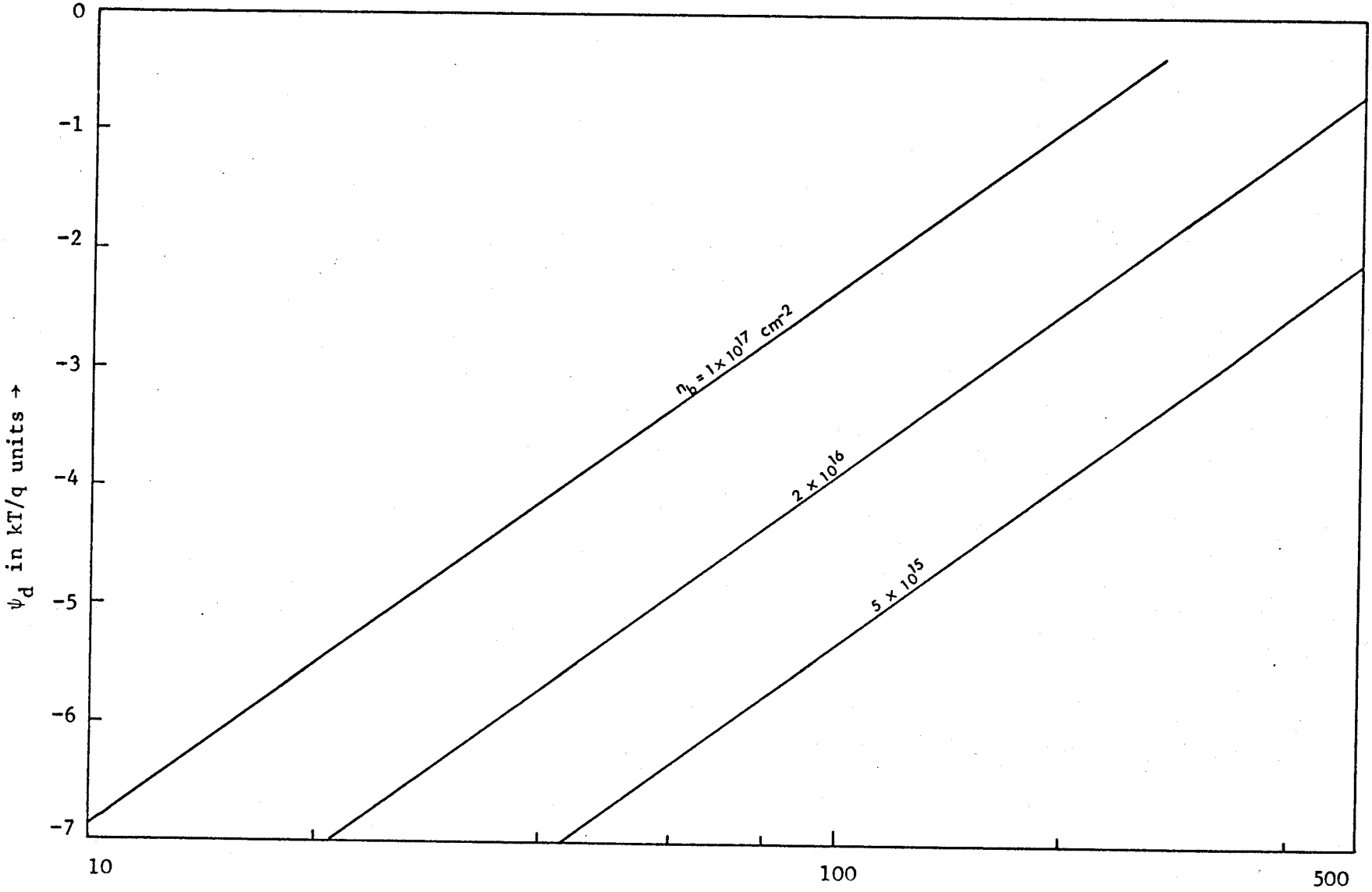

FIG.6.4

Normalized Potential ψ_d As A Function Of Film Thickness - Heavy Electron Accumulation, $\psi_s << \psi_d < 0$

6.2. Bulk Transport Phenomena In InAs

6.2.1. Scattering Mechanisms In Bulk Single Crystal InAs

The dominant scattering mechanism at room temperature in single crystals of several III - V compounds is the polar interaction of the carriers with the optical lattice vibrations[6.7,6.8]. This interaction is particularly strong in compounds because of the relative vibrations of the two unequal atoms in the unit cell of the lattice. The polar mobility is given by[6.7]:

$$\mu_o = K_p \frac{T^{\frac{1}{2}}}{m^{*3/2}} F(\theta_1/T) \left\{\exp(\theta_1/T)-1\right\} \qquad \ldots(6.15)$$

where K_p is a constant for a particular material,

$\theta_1 = \hbar\omega_1/k$ is the optical mode temperature = 340°K in InAs

ω_1 is the longitudinal fundamental optical frequency = $4.4\times10^{13}\,sec^{-1}$ in InAs

$F(\theta_1/T)$ is a slowly varying function of T, For $T < \theta_1$, $F(\theta_1/T) \propto T^{-\frac{1}{2}}$

Therefore

$$\mu_o \propto \exp(\theta_1/T) \qquad T < \theta_1 \qquad \ldots(6.16)$$

The experimental results for thick epitaxial InAs appear to follow this relationship (Fig.5.15), but at lower temperatures the effect of ionized impurities dominates.

The mobility due to ionized impurities[6.9] is given approximately, for InAs, by:

$$\mu_I = \frac{4\times10^{18}T^{3/2}}{(N_D^+ + N_A^-)} \cdot \frac{1}{\ln\left\{1+\frac{4.4\times10^8T^2}{(N_D^+ + N_A^-)^{2/3}}\right\}} \quad cm^2/V\text{-}s \qquad \ldots(6.17)$$

where $(N_D^+ + N_A^-)$ is the total ionized impurity concentration. The effect of ionized impurities is seen to cause a peak in the mobility of thick samples around 100°K. The mobility due to the combined polar and impurity scattering mechanisms given by $\mu = \mu_I\mu_o/(\mu_I+\mu_o)$, is plotted in Fig.5.14, assuming $n = N_D^+$ and $N_A^- = 0$, and using $\mu_o = 27{,}000 cm^2/V\text{-}sec$. This follows approximately the experimental curve for thick epitaxial layers.

6.2.2. Barrier Scattering In Polycrystalline Films

In polycrystalline films the inter-crystalline barriers cause a pronounced reduction in the carrier mobility even in thick samples, (see Fig.5.6). Following Petritz[6.10], Waxman et al[6.11] and Brunnschweiler[6.12] have used the barrier model shown in Fig.6.5 to derive an expression for the barrier mobility. The model consists of regions of low resistivity, the crystallites, and regions of high resistivity, the inter-crystalline boundaries. They obtained an expression of the form:

$$\mu_B = q\langle v\rangle \exp(-\phi_B/kT)/4N_1kT \qquad ...(6.18)$$

where $\langle v\rangle$ is the average thermal velocity of the carriers,

ϕ_B is the barrier height in eV, see Fig.6.5,

N_1 is the number of barriers per unit length = $1/\bar{a}$, $\bar{a}$ is the average crystallite size.

Substituting $\langle v\rangle = \{8kT/\pi m^*\}^{\frac{1}{2}}$ in equation 6.4, the barrier mobility is:

$$\mu_B = q\bar{a}\exp(-\phi_B/kT)/(2\pi m^*kT)^{\frac{1}{2}} \qquad ...(6.19)$$

The different thermal equilibrium electron concentrations in the two regions gives rise to the energy barrier given by:

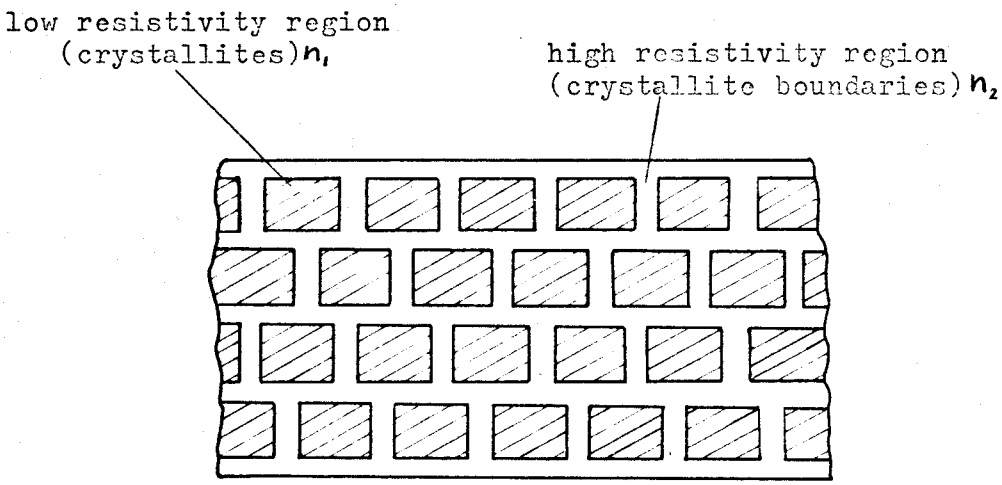

(a)

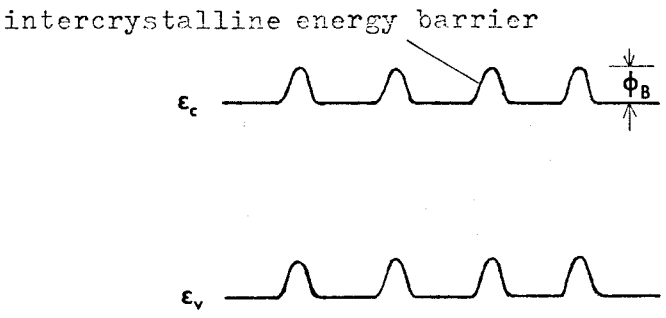

(b)

Fig.6.5

(a) Polycrystalline barrier model,

(b) energy band diagram

$$\phi_B = kT\ln(n_1/n_2) \qquad \ldots(6.20)$$

Since the electron density in these InAs films remains fairly constant below 300°K the exponential term in equation 6.19 may be assumed to be constant. Therefore $\mu_B \propto T^{-\frac{1}{2}}$, $T < 300^{\circ}K$. Equation 6.19 gives the mobility for barrier scattering only. There will also be a contribution due to polar and/or impurity scattering within the crystallite, and surface scattering. Since all, except the barrier mechanism should be present in the epitaxial films, we can obtain μ_B, approximately, from the experimental results by subtracting the reciprocal mobility of an epitaxial film of similar thickness and impurity concentration. This is shown in Fig.6.6, plotted as a function of $T^{-\frac{1}{2}}$, giving a straight line relationship over a limited temperature range.

Above room temperature the material is approaching the intrinsic range, hence n_1 and n_2 will begin to increase. For a given increase in the two regions, the ratio n_1/n_2 will decrease, thus decreasing ϕ_B/kT. If this increase is sufficiently large, the mobility will tend to increase, according to equation 6.19. In fact this is what has been observed in the polycrystalline films (see Fig.5.6), but not in the epitaxial films.

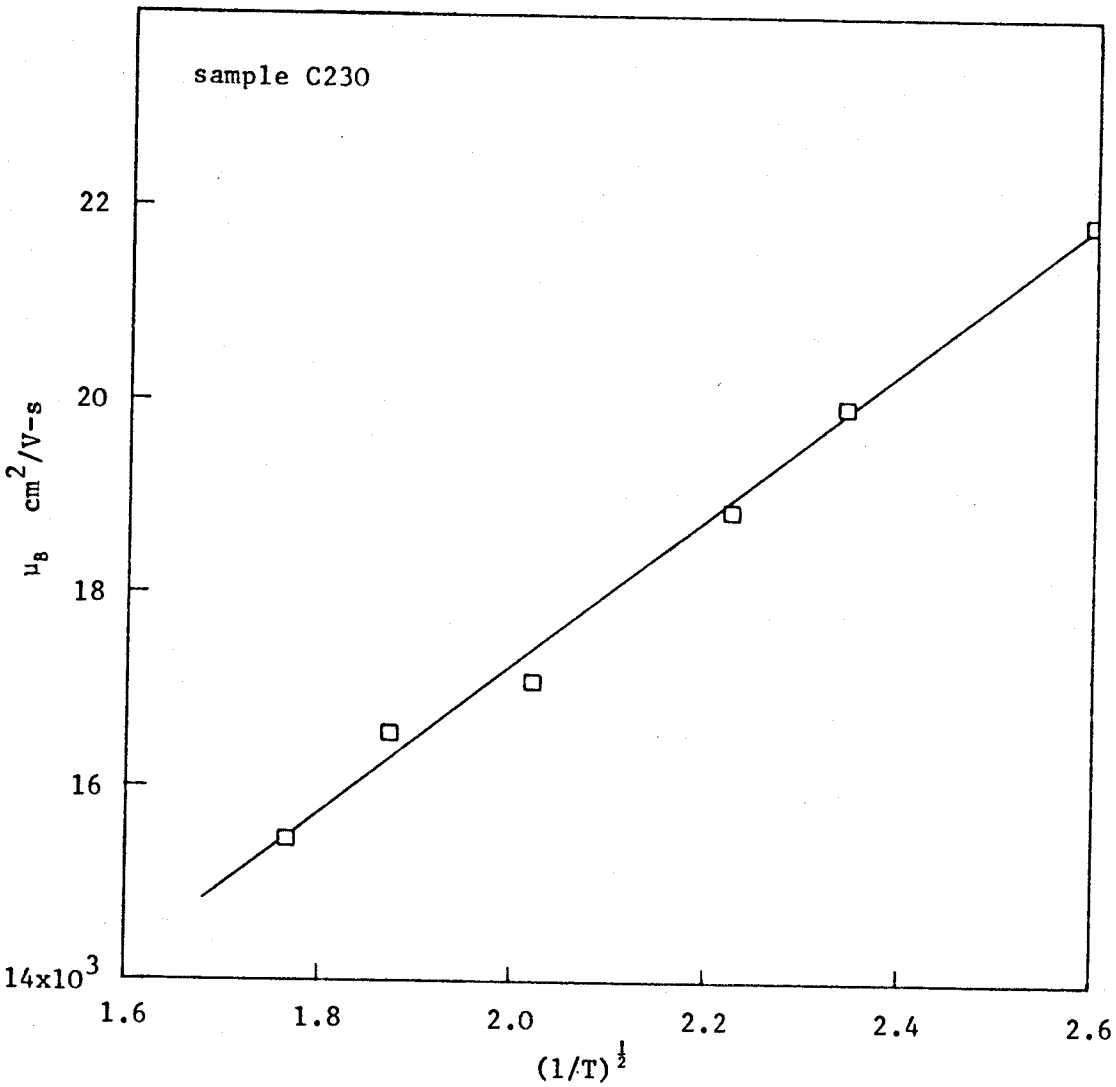

FIG.6.6

Intercrystalline Barrier Mobility
As A Function Of $T^{-\frac{1}{2}}$

6.2.3. Energy Dependence Of Relaxation Time And Hall Coefficient Factor

Most mechanisms which scatter electrons or holes can be described by a relaxation time which is energy dependent, i.e.,

$$\tau \propto \varepsilon^{\alpha} \qquad \ldots(6.21)$$

where ε is the carrier energy and α is a constant for a particular scattering mechanism. This energy dependence gives rise to the Hall coefficient factor, given in equation 6.22.

Assuming spherical constant energy surfaces (parabolic bands), the bulk transport coefficients of a semiconductor are obtained by solving Boltzmanns equation with the appropriate electric and magnetic field terms, (see Putley[6.37] for example). Generally, the assumption of parabolic bands is difficult to justify. However, the conduction band of InAs is, apparently, parabolic near the minimum[6.8] which is at (000) in the ε-k diagram. It only begins to deviate from parabolicity at higher energies, the curvature decreasing, thus increasing the effective mass of the electrons. If we assume the electrons are confined near the bottom of the conduction band, then the assumption of spherical constant energy surfaces is a good approximation. The analysis[6.37] then yields for the Hall coefficient in the limit of weak magnetic fields ($\mu B_z \ll 1$):

$$R_H = -\frac{3\pi^{\frac{1}{2}}}{4} \cdot \frac{\Gamma(2\alpha+5/2)}{\Gamma^2(\alpha+5/2)} \cdot \frac{1}{ne} = -\frac{r}{ne} \qquad \ldots(6.22)$$

where the gamma functions can easily be evaluated for integer or fractional values (for integer values $\Gamma(m+1) = m!$). The Hall coefficient factor, r, is equal to the ratio of Hall mobility to conductivity mobility. For impurity scattering, $\alpha = 3/2$, and $r = 315\pi/512 = 1.93$. If $\alpha = 0$, i.e. all the carriers have the same velocity, $r = 1$.

In the limit of very strong magnetic fields ($\mu B_z >> 1$) r approaches unity for all the scattering mechanisms. Thus, the ratio of the Hall coefficient in weak and strong magnetic fields should provide further information about the type of scattering mechanisms occuring. Unfortunately, often several mechanisms can contribute to the relaxation time at any particular temperature, which complicates matters.

The results in Fig.5.19 of R_H vs. B_z for a thick epitaxial InAs layer at various temperatures, indicate that ionized impurity scattering is beginning to dominate the mobility at 70°K, although $r < 1.93$. This is, presumably, due to the contribution of polar scattering. The energy dependence of polar scattering is not well understood. According to Hilsum and Rose-Innes[6.13] α is zero, yet they give a value of r between 1.0 and 1.14 for this mechanisms. However, Putley[6.37] gives $\alpha = \frac{1}{2}$, which results in $r = 1.105$. This is much closer to the value we obtain at room temperature in the thick epitaxial films.

There are two interesting results to be considered. The ratio, r, measured in thick polycrystalline films appears to be of the order of

1.1 to 1.3 (see Figs. 5.8 and 5.9), which is larger than the value obtained for the thick epitaxial layers. Equation 6.18 indicates that barrier scattering has an energy dependence $\varepsilon^{\frac{1}{2}}$, which gives r = 1.105. Although this is at the lower limit of the experimental values, it does give further support to the barrier model.

The other interesting point is the ratio, r, measured on very thin epitaxial films, which have a value near unity at room and liquid nitrogen temperatures. This would seem to discount that impurities are responsible for the mobility reduction in thin films. In section 6.3.5. we will consider theoretically the effect of film thickness on the Hall coefficient factor.

Equation 6.22 does not take into account the effect of impurity density on the factor r. Beer[6.14,6.15] has shown that large donor concentrations will tend to reduce the value of r, but the analysis becomes rather complicated, so we will not consider these effects. However, qualitatively this can be explained by the fact that at large degeneracy only carriers with the fermi velocity will contribute significantly to conduction, thus approaching the single velocity case of $\alpha = 0$, $r = 1$.

6.2.4. Physical Magneto-Resistance Due To An Energy Dependent Relaxation Time

If we accept the assumption of parabolic bands, as discussed in section 6.2.3., then the 'physical' magnetoconductance in weak

magnetic fields is given by the Boltzmann equation analysis as follows[6.37]:

$$\frac{\Delta\sigma}{\sigma_o} = \mu_H^2 B_z^2 \cdot \frac{\Gamma(\alpha+5/2)\Gamma(3\alpha+5/2)}{\Gamma^2(2\alpha+5/2)} = \mu_H^2 B_z^2 M \qquad \ldots(6.23)$$

This is also approximately equal to the magneto-resistance ratio $\Delta\rho/\rho_o$ if $\mu_H^2 B_z^2 \ll 1$, i.e. in weak fields.

Assuming $\alpha = \frac{1}{2}$, then M = 0.085. From the slope of $\Delta\rho/\rho_o$ vs. B_z^2 plotted in Fig.5.21 for an epitaxial sample, the mobility calculated from equation 6.23 is 19,800 cm^2/V-sec at 300°K. This compares favourably with the Hall effect value of 21,300 cm^2/V-sec.

At lower temperatures the magneto-resistance increases considerably not only because the mobility increases but also due to the increase in the energy dependence of the relaxation time.

The polycrystalline films usually have a larger magneto-resistance than the epitaxial films at room temperature, which could be connected with the higher α they appear to have. However, it appears that inhomogenieties can increase the magneto-resistance, as discussed by Weiss[6.16]. Thus, a calculation of the mobility on the basis of equation 6.23 would give an incorrect value.

A better method to obtain an estimate of the mobility from magneto-resistance would be to use a corbino disc. This would give the geometrical magneto-resistance, because of the complete shorting of the Hall voltage by the current contacts, and would not require a knowledge of the index α to calculate the mobility.

6.3. Boltzmann Surface Transport Theory

6.3.1. Introduction

Some of the earliest work on surface scattering in thin metal films was carried out by Fuchs[6.17], who obtained a solution of Boltzmanns equation for both, diffuse scattering and partially specular reflection at the surface. Later, Sondheimer[6.18] extended the analysis to the galvanomagnetic properties of thin metal films. Schrieffer[6.19] was the first to examine the effect of the surface on the mobility of the carriers in the surface space charge layers in semiconductors. In order to simplify the analysis he assumed a linear potential in the space charge layer and a truncated linear potential. The linear potential appears to be a reasonable assumption in strong inversion or accumulation regions. Later, Greene et. al[6.20] carried out an analysis, within Schrieffers basic framework, but with the exact field at the surface.

All these analyses have been based on a solution of Boltzmanns equation, with the following assumptions:

1. Simple parabolic band structure (spherical constant energy surfaces), hence a constant scalar effective mass m*,
2. A constant, energy independent, bulk relaxation time,
3. Non-degenerate statistics, classical electron gas.

Ham and Mattis[6.21] and Pierrett and Sah[6.22] have extended the theory to cover ellipsoidal energy surfaces. However, the latter results indicate a very small difference with the spherical constant energy surface case.

6.3.2. Surface Scattering In Thin Semiconductor Films With Flat Bands - Solution Of Boltzmanns Equation With Partially Specular Surfaces

Boltzmanns equation may be written, using the relaxation time approximation, as follows[6.23]:

$$v.\nabla f + a.\nabla_v f = -\frac{(f-f_o)}{\tau_b} \qquad \ldots(6.24)$$

where $f(x,y,z,v_x,v_y,v_z)$ is the distribution function of the carriers, f_o the equilibrium distribution function, v the velocity and a the acceleration of the carriers. τ_b is the bulk relaxation time.

The right hand side of equation 6.24 is an approximation for the rate at which equilibrium is restored by scattering and is valid[6.23] for small deviations of f from its equilibrium value, f_o.

We assume a homogeneous film with its surface parallel to the x-y plane, and a small uniform measuring field, E_x, is applied in the x-direction. The equilibrium distribution function assuming non-degenerate statistics is given by[6.23]:

$$f_o = \frac{n_h}{2}\left\{\frac{h^2}{2\pi m^* kT}\right\}^{3/2} \exp\left\{-\frac{m^* v^2}{2kT}\right\} \qquad \ldots(6.25)$$

The acceleration of the carriers in the x-direction is qE_x/m^*. The distribution function is independent of the x and y co-ordinates, and if we assume flat bands, $E_z = 0$. Then equation 6.24 reduces to:

$$v_z \frac{\partial f_1}{\partial z} + \frac{f_1}{\tau_b} - \frac{qE_x v_x f_o}{kT} = 0 \qquad \ldots(6.26)$$

where $f_1 = f - f_o$ is a small perturbing function. Second order terms in the small quantities E_x and f_1 have been ignored.

The general solution of equation 6.26 is of the form[6.24,6.25]:

$$f_1 = f_{11}\left\{1+g(v)\exp(-z/v_z\tau_b)\right\} \qquad ...(6.27)$$

where $$f_{11} = qE_x v_x \tau_b f_o/kT \qquad ...(6.28)$$

is the deviation of the equilibrium distribution in the bulk with the applied field E_x.

$g(v)$ is a function which is evaluated with the boundary conditions applied to equation 6.27.

We assume partially specular reflection at each of the two surfaces of the film, represented by the Fuchs reflectivity parameters γ and ω, the latter applying to the film-substrate interface at $z = 2d$. These two parameters represent the fraction of carriers specularly reflected by each of the two surfaces and can take values between zero and unity. Thus the boundary conditions are:

$$f_1^+(z = 0) = \gamma f_1^-(z = 0) \qquad ...(6.29)$$

$$f_1^-(z = 2d) = \omega f_1^+(z = 2d) \qquad ...(6.30)$$

In appendix B the boundary conditions are applied to equation 6.27 to give the following solutions for f_1:

$$f_1^+ = f_{11}\left\{1-\frac{\left[1-\gamma+\gamma(1-\omega)\exp(-2d/v_z\tau_b)\right]}{1-\gamma\omega\exp(-4d/v_z\tau_b)}\exp(-z/v_z\tau_b)\right\}$$

$$v_z \geq 0 \qquad \ldots(6.31)$$

$$f_1^- = f_{11}\left\{1-\frac{\left[1-\omega+\omega(1-\gamma)\exp(2d/v_z\tau_b)\right]}{1-\gamma\omega\exp(4d/v_z\tau_b)}\cdot\exp\left(\frac{2d-z}{v_z\tau_b}\right)\right\}$$

$$v_z \leq 0 \qquad \ldots(6.32)$$

The current through the sample is then given by[6.26]:

$$I_{nx} = -q\int_0^{2d}\iiint_{v_x,v_y,v_z=-\infty}^{\infty} N(v)v_x f_1 dz dv_x dv_y dv_z \qquad \ldots(6.33)$$

$N(v) = 2(m^*/h)^3$ is the density of states in velocity space. The integration over v_z must be performed with f_1^- (equation 6.32) from $-\infty$ to 0, and with f_1^+ (equation 6.31) from 0 to ∞. I_{nx} is the current per unit width of the film, the current per unit cross-sectional area is $I_{nx}/2d$. Thus, the flat band film mobility is:

$$\mu_F = I_{nx}/(2qdn_bE_x) \qquad \ldots(6.34)$$

The integration of equation 6.33 is performed in appendix C, from which the ratio of film to bulk mobility is given by:

$$\mu_F/\mu_b = \left\{1-\frac{(2-\gamma-\omega)}{2\beta}\Gamma_1(\beta)+\frac{(1-\gamma-\omega+\gamma\omega)}{\beta}\Gamma_2(\beta)+\frac{(\gamma+\omega-2\gamma\omega)}{2\beta}\Gamma_3(\beta)\right\}$$

$$\ldots(6.35)$$

where $\beta = d/\lambda_h$ and

$$\lambda_n = \tau_b (kT/2\pi m^*)^{\frac{1}{2}} \qquad \ldots(6.36)$$

λ_n is similar to the mean free path in the bulk but is a factor of about five smaller.

The integrals in equation 6.35 are as follows:

$$\Gamma_1(\beta) = \int_0^\infty \frac{\exp(-\nu)d\nu}{1-\gamma\omega\exp\{-2\beta/(\pi\nu)^{\frac{1}{2}}\}} \qquad \ldots(6.37)$$

where $\nu = m^* v_z^2/2kT$ is the energy of the carriers due to the z motion, normalized to kT.

$$\Gamma_2(\beta) = \int_0^\infty \frac{\exp\{-\nu-\beta/(\pi\nu)^{\frac{1}{2}}\}d\nu}{1-\gamma\omega\exp\{-2\beta/(\pi\nu)^{\frac{1}{2}}\}} \qquad \ldots(6.38)$$

$$\Gamma_3(\beta) = \int_0^\infty \frac{\exp\{-\nu-2\beta/(\pi\nu)^{\frac{1}{2}}\}d\nu}{1-\gamma\omega\exp\{-2\beta/(\pi\nu)^{\frac{1}{2}}\}} \qquad \ldots(6.39)$$

These integrals can be evaluated numerically only. For the case of complete diffuse scattering at both surfaces, $\gamma=\omega=0$, the last term in equation 6.35 vanishes, $\Gamma_1(\beta) = 1$ and $\Gamma_2(\beta)$ is given by:

$$\Gamma_2(\beta) = \int_0^\infty \exp\{-\nu-\beta/(\pi\nu)^{\frac{1}{2}}\}\, d\nu \qquad \ldots(6.40)$$

The expression for μ_F/μ_b then reduces to that given by Many et. al[6.26]. The integral in equation 6.40 has been evaluated by Flietner[6.27], which we have used to calculate μ_F/μ_b for various values of ω with $\gamma = 0$,

(i.e. diffuse scattering at the surface z = 0). We have also assumed $\Gamma_3(\beta)$ is approximately equal to the integral in equation 6.40. The results are plotted in Fig. 6.8 as a function of β. Also shown in Fig.6.8 are the experimental results of Fig.5.12 for epitaxial InAs, assuming m* = 0.03m, which is a value for the effective mass of electrons in InAs quoted in the literature[6.8]. The bulk mobility is assumed to be 23,000 cm^2/V-sec, the value obtained in the thick samples, thus λ_n = 610Å. The experimental curve appears to follow the general shape of the theoretical curve for $\gamma = \omega = 0$, but is shifted to the right by a constant factor. A better fit is obtained with λ_n = 2300Å, i.e. m* = 0.309m, a value very much larger than that quoted by various workers.

So far we have assumed that the bands are flat right upto the surface, which is probably not the case. The higher electron concentration measured in the thinner films, (see Fig.5.13) could be due to (i) auto-doping by the substrate, (ii) the bands bending towards accumulation caused by surface charge. If we assume the latter is the case, then one would expect a further reduction in the mobility, if the surfaces are diffuse (or partially specular), since a larger proportion of the carriers are confined near the surface. This could then explain the discrepancy in Fig.6.8. In section 6.3.4. expressions will be derived for the film mobility with band bending, which occurs either through surface states or an external applied field.

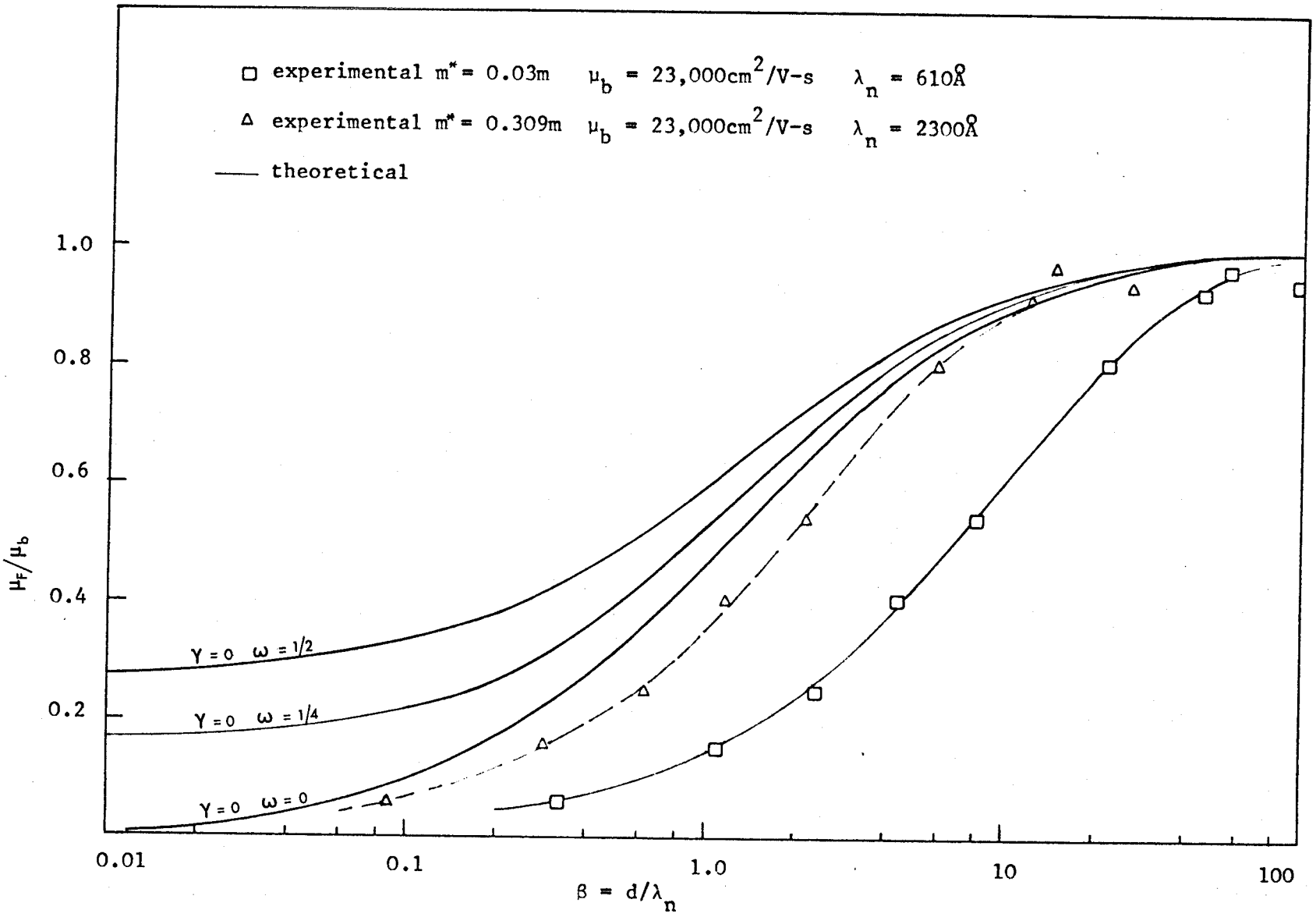

FIG.6.8

Normalized Flat Band Surface Scattering Mobility As A Function Of β, The Normalized Film Thickness.

In the above analysis we have assumed that the Fuchs reflectivity parameters, γ and ω, can take on values between zero and unity, depending on the type of surface, but are independent of the angle of incidence at the surface, and the wavelength of the electrons. Parrott[6.62] has suggested that, in analogy with the scattering of light from diffuse surfaces, the reflectivity parameter should be large for grazing angles of incidence and long wavelengths, and small for near normal incidence and short wavelengths. Greene[6.63] has analysed this problem and introduced another parameter, the kinetic specularity probability, which is also angle dependent, and apparently quite distinct from the Fuchs parameter. Greene and O'Donnell[6.64] have applied this analysis to the particular case of scattering by surface charges and have shown both parameters to be strongly dependent on the angle of the incident k vectors, with about 10^{12} scatterers/cm^2. Another important consideration is that with a non-spherical energy surface, even specular reflection can result in decrease in mobility. Since the effective mass is anisotropic, in general the velocity parallel to the surface will be changed, although the momentum is preserved. Friedman and Koenig[6.49] and Price[6.65] have used this to explain the reduction in conductivity of thin Bismuth crystals at liquid helium temperatures. They found that the conductivity tends to a finite value as the thickness is reduced below a certain limit, and concluded from this that the surfaces are specular.

From the discussion above it appears that several modifications are necessary to the theory presented earlier. Also an energy dependent relaxation time should be included. The theory would then become extremely complicated and comparison with experimental results would be difficult, since a knowledge of various parameters would be required.

6.3.3. Temperature Dependence Of Surface Scattering Mobility

The surface scattering mobility will be a function of temperature through the variation of λ_n temperature. If we substitute $\tau_b = m^*\mu_b/q$ in equation 6.36, we have:

$$\lambda_n = \mu_b\left\{\frac{m^*kT}{2\pi q^2}\right\}^{\frac{1}{2}} \qquad \ldots(6.41)$$

With a decrease in temperature μ_b increases, but this increase is a function of the ionized impurity concentration. If N_D^+ is about $2 \times 10^{16} cm^{-3}$ then, μ_b increases by approximately 2, between 300^oK and 100^oK, i.e. with a decrease in temperature by a factor of 3. This results in an increase in λ_n of $2/\sqrt{3} \sim 1.15$. Thus, the mobility increases with a decrease in temperature, even for film thicknesses below 1000Å. Also, the increase is much greater when compared with the experimental results, (Fig.5.16) for films above this thickness.

As explained earlier, it is difficult to believe that the reduction in mobility with decreasing temperature of the very thin films is due to impurities within the bulk of the film. The measured electron concentration of films below 1000Å was less than $4 \times 10^{17} cm^{-3}$, and if we assume that this is equal to the ionized impurity concentration the electron mobility in the temperature range down to $70^{o}K$ should be well above 10,000 $cm^2/V\text{-}sec$. In fact, the results of Harman et. al[6.28] and Schroeder[6.29] indicate mobilities above 7,000 $cm^2/V\text{-}sec$ at donor concentrations of $10^{19} cm^{-3}$ in bulk InAs. Alternatively the mobility could be limited by neutral impurities[6.30], which has a temperature independent scattering mechanism, but neither would this explain the fall in mobility with temperature. Zemel[6.38] indicates that as the film thickness is reduced, the mobility should show a slower increase than in the bulk, with a decrease in temperature, but does not give any quantitative results.

A mechanism that appears likely to explain the temperature dependence of the very thin films is that due to charged centres at the surface of the film, as put forward recently by Kawaji and Kawaguchi[6.31] and Stern and Howard[6.32], to explain the electron mobility variation in inversion layers in silicon and InAs at very low temperatures. This, and the quantum size effect, will be considered later.

6.3.4. Surface Scattering In Thin Films With Band Bending And Diffuse Surfaces

In this section we obtain a solution to Boltzmanns equation with band bending at the surface, following the method of Greene et. al[6.20] but with modifications to the boundary conditions.

Similar to equation 6.26 Boltzmanns equation, 6.24, can be written for the case when $E_z \neq 0$, as follows:

$$v_z \frac{\partial f_1}{\partial z} + \frac{qE_z}{m^*} \frac{\partial f_1}{\partial v_z} + \frac{f_1}{\tau_b} + \frac{qE_x v_x f_o}{kT} = 0 \qquad \ldots(6.42)$$

where the second order terms in E_x and f_1 have again been ignored.

The equilibrium distribution function with band bending ψ, is given by:

$$f_o(v,z) = \frac{n_b}{2}\left\{\frac{h^2}{2\pi m^* kT}\right\}^{3/2} \exp(-m^* v^2/(2kT) - \psi) \qquad \ldots(6.43)$$

By a change in variable from (v_z,z) to (v_z,ν), where ν is the carrier 'energy' in the z-direction, now given by:

$$\nu = m^* v_z^2/(2kT) + \psi \qquad \ldots(6.44)$$

equation 6.42 can be written:

$$\frac{qE_z}{m^*} \cdot \frac{\partial f_1}{\partial v_z} + \frac{f_1}{\tau_b} - \frac{qv_x E_x}{kT} f_o(v_x,v_y,\nu) = 0 \qquad \ldots(6.45)$$

E_z is a function of ψ given by equation 6.5, if $2d \leqslant L_B$.

The general solution of equation 6.45 is:

$$f_1 = f_{11}\left\{1+H(v)\exp^{-K(v_z,v_{zs})}\right\} \qquad \ldots(6.46)$$

f_{11} is given by equation 6.28 and $K(v_z,v_{zs})$ by:

$$K(v_z,v_{zs}) = m^*/q \int_{v_{zs}}^{v_z} \frac{dv'_z}{\tau_b E_z} \qquad \nu \text{ constant} \quad ...(6.47)$$

H(v) is a function which must be determined from the boundary conditions.

Originally, Schrieffer[6.19] used only one boundary condition: that of diffuse scattering at one of the surfaces. However, this does not specify f_1 everywhere, and so Greene et. al[6.20] used a second boundary condition. They assumed that carriers moving toward the surface from deep within the bulk, in thick slabs, have the bulk distribution f_{11}. They also considered a partially specular surface, with $2d \lesssim L_B$. However, in both cases it was assumed that the sample was symmetrical about its midplane. This is appropriate when interpreting results where, for example, gas cycles are used to vary the surface potential at both surfaces of a single crystal slab. With thin hetero-epitaxial films we must include the boundary condition at the film-substrate interface, where there is no independent control of the surface potential. The results of section 6.3.2. indicate that both surfaces of the epitaxial films are diffuse scatters (or may have a small amount of specularity). We will, therefore, use the following boundary conditions:

at $z = 0$ $\qquad f_1(v_{zs}) = 0 \qquad ...(6.48)$

at $z = 2d$ film-substrate interface $\qquad f_1(v_{zd}) = 0 \qquad ...(6.49)$

i.e. both surfaces will be assumed to be diffuse.

Substituting these conditions in equation 6.46 we obtain the following solution for f_1 (appendix D):

$$f_1 = f_{11}\{1-\delta\} \qquad \ldots(6.50)$$

where δ is given with reference to Fig.6.9 of the (v_z,ν) plane. The parabolas in Fig.6.9 are loci of equation 6.44. δ is specified in the shaded regions as follows (see Appendix D)

$\psi_s \geq 0$ Depletion Regime, Fig.6.9(a)

$$\delta = \exp\{-K(v_z-v_{zs})-K(v_{zd},v_{zs})\} \quad \psi_d \leq \nu \leq \psi_s \qquad \ldots(6.51.a)$$

$$\delta = \exp -K(v_z,v_{zs}) \quad v_z \geq 0 \qquad \ldots(6.51.b)$$

$$\delta = \exp\{-K(v_z,-v_{zs})-K(v_{zd},v_{zs})\} \quad v_z \leq 0 \qquad \ldots(6.51.c)$$

$\Big\}\ \psi_s \leq \nu \leq \infty$

$\psi_s \leq 0$ Accumulation Regime, Fig.6.9(b)

$$\delta = \exp -K(v_z,v_{zs}) \quad \psi_s \leq \nu \leq \psi_d \qquad \ldots(6.51.d)$$

$$\delta = \exp -K(v_z,v_{zs}) \quad v_z \geq 0 \qquad \ldots(6.51.e)$$

$$\delta = \exp\{-K(v_z,-v_{zs})-K(v_{zd},v_{zs})\} \quad v_z \leq 0 \qquad \ldots(6.51.f)$$

$\Big\}\ \psi_d \leq \nu \leq \infty$

The bounded electrons ($\nu \leq \psi_s$) in depletion layers will be specularly reflected by the potential barrier and therefore their last encounter will have been at the surface z = 2d. Therefore their

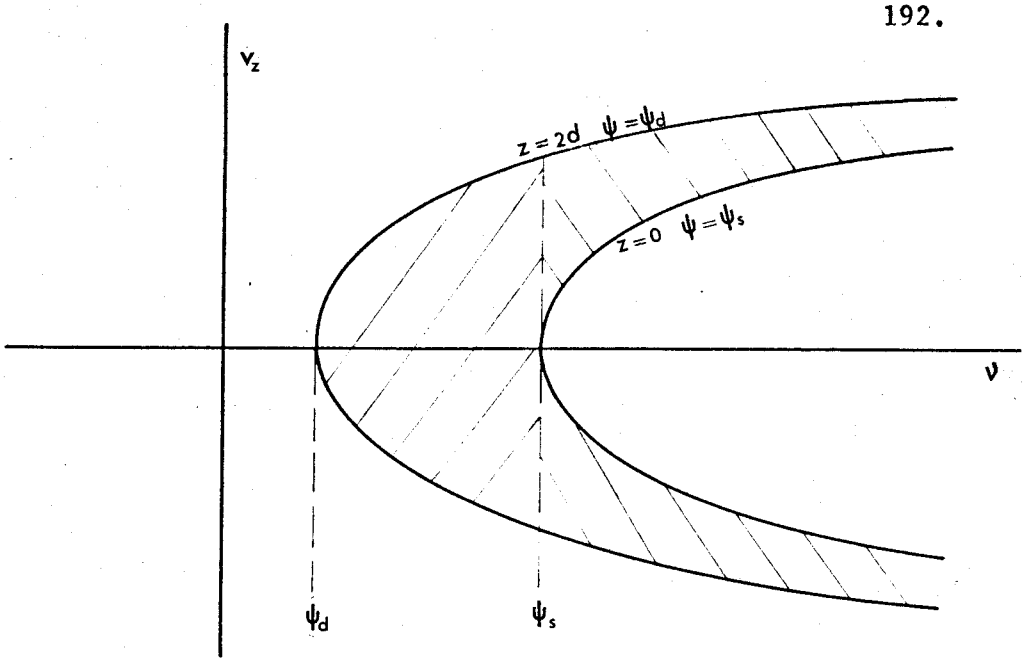

(a) $\psi_s \geqslant 0$ depletion regime

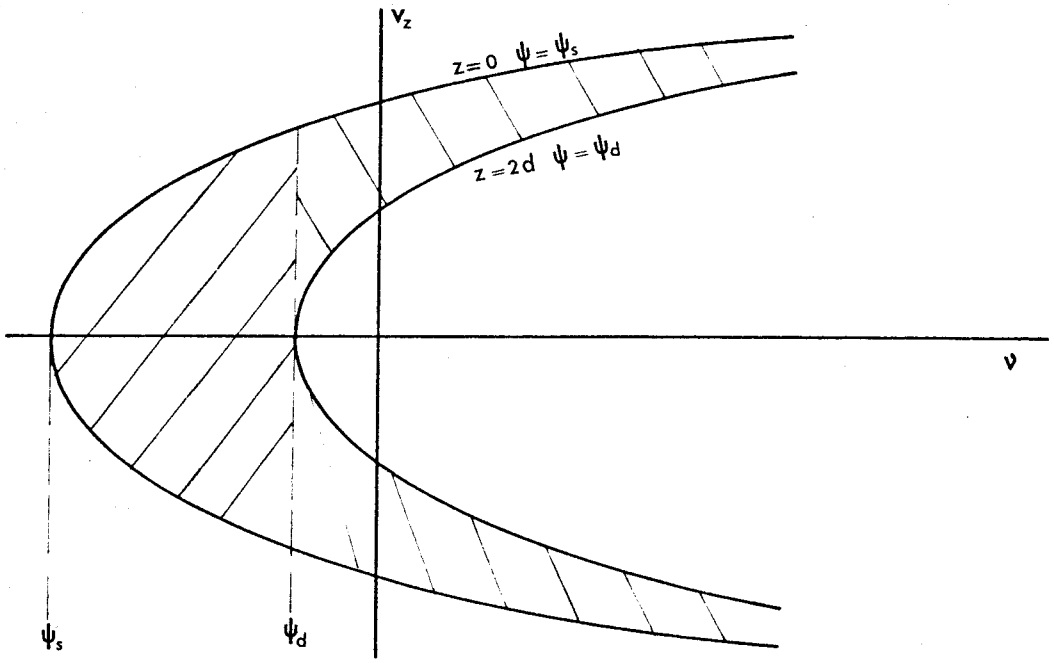

(b) $\psi_s \leqslant 0$ accumulation regime

Fig.6.9

Domains of solution of Boltzmanns Equation in the v-v_z plane, with surface band bending

distribution function, with δ of equation 6.51(a) is characteristic of the surface $z = 2d$, and the integration must be carried out over the shaded region from ψ_d to ψ_s and $-v_{zd}$ to v_{zd}.

Similarly, in the accumulation regime the bounded electrons, with z-velocity greater or less than zero, will have last encountered the surface $z = 0$. Therefore, their distribution function is given by equation 6.51(d), and the integration must be carried out from ψ_s to ψ_d and $-v_{zs}$ to v_{zs}.

The current per unit width flowing through the film can now be obtained by substituting for f_1 from equations 6.51 in equation 6.33 and integrating over the appropriate limits. This is performed in appendix E.

The effective mobility, μ_s, with band bending is then given by:

$$\mu_s = \frac{I_{nx}}{E_x} \cdot \frac{1}{2qn_b d(1+\Delta n_s/2dn_b)} \qquad \ldots(6.52)$$

where (Δn_s+2dn_b) is the total number of carriers per unit surface area, consisting of the flat band and the excess carrier contributions. Usually, the surface mobility is defined as the surface excess conductance per excess carrier charge in the space charge layer. Theoretically, this is obtained by subtracting the flat band current from the total current I_{nx}. Experimentally, in accumulation and depletion layers the surface mobility is extracted from the measurements using a model proposed by Petritz[6.33]. This method is essential when thick slabs ($2d >> L_B$) are used, where the bulk contribution to the total current may

be much larger than the surface contribution. However, with thin epitaxial layers, it is more appropriate to include the contribution of all the carriers, as in equation 6.52, because even at flat bands the surface has a large influence on the mobility of the carriers.

Substituting the expression for I_{nx} of equation E.11 (appendix E), in equation 6.52, the effective film mobility is given as follows:

$\psi_s \geq 0$ Depletion Regime:

$$\mu_s/\mu_b = \frac{1}{(1+\Delta n_s/2dn_b)} \cdot \left\{ 1+ \frac{\Delta n_s}{2dn_b} - \frac{\lambda_n}{2d} \left\{ \exp-\psi_s + \exp-\psi_d \right\} \right.$$

$$+ \frac{\lambda_n}{2d} \int_{\psi_d}^{\psi_s} \exp\left\{-\nu+K(-v_{zs},v_{zd})+K(v_{zs},v_{zd})\right\} d\nu$$

$$\left. + \frac{\lambda_n}{d} \int_{\psi_s}^{\infty} \exp\left\{-\nu+K(v_{zs}, v_{zd})\right\} d\nu \right\} \quad \ldots(6.53)$$

Δn_s is given by equation 6.6 and

$$K(v_{zs},v_{zd}) = \frac{1}{2\sqrt{\pi}\eta} \int_{\psi_d}^{\psi_s} \frac{d\psi}{(\nu-\psi)^{\frac{1}{2}} F(\psi,\psi_d,\lambda)}$$

ν constant ...(6.54)

after substituting for E_z from equation 6.5 in equation 6.47.

$$\eta = \lambda_n/L_B = \mu_b \left\{ \frac{m^* n_b}{\pi \varepsilon_s \varepsilon'_o} \right\}^{\frac{1}{2}} \quad \ldots(6.55)$$

$\psi_s \lesssim 0$ Accumulation Regime:

$$\mu_s/\mu_b = \frac{1}{\left\{1+\frac{\Delta n_s}{2dn_b}\right\}}\left\{1+\frac{\Delta n_s}{2dn_b}-\frac{\lambda_n}{2d}\{\exp-\psi_s+\exp-\psi_d\}\right.$$

$$+\frac{\lambda_n}{2d}\int_{\psi_s}^{\psi_d}\exp\{-\nu+2K(v_{zs},0)\}\,d\nu$$

$$\left.+\frac{\lambda_n}{d}\int_{\psi_d}^{\infty}\exp\{-\nu+K(v_{zs},v_{zd})\}\,d\nu\right\} \quad ...(6.56)$$

$$K(v_{zs},0) = \frac{1}{2\sqrt{\pi\eta}}\int_{\nu}^{\psi_s}\frac{d\psi}{(\nu-\psi)^{\frac{1}{2}}F(\psi,\psi_d,\lambda)} \quad ...(6.57)$$

At flat bands $\psi_s \to \psi_d \to 0$ and it can be shown that $K(v_{zs},v_{zd}) \to -d/\lambda_n(\pi\nu)^{-\frac{1}{2}}$ (see appendix E). Equations 6.53 and 6.56 then reduce to:

$$\mu_s/\mu_b = 1-\frac{\lambda_n}{d}+\frac{\lambda_n}{d}\int_0^{\infty}\exp\{-\nu-d/\lambda_n(\pi\nu)^{-\frac{1}{2}}\}\,d\nu \quad ...(6.58)$$

which is the same as the flat band result, equation 6.35, with $\gamma = \omega = 0$.

Similar to the flat band case, expressions can be dervied for partially specular surfaces, with the parameters γ and ω. However, the expressions become rather cumbersome.

The integrals in equations 6.53 and 6.56 can be evaluated only numerially, if the exact potentials are used, i.e. E_z from equation 6.5 This would require integrating K numerically, between the appropriate limits, for constant values of ν and then summing the exponential terms

for each value of ν between the appropriate limits. Unfortunately, owing to a lack of time we have not attempted to write a computer program to do this.

Expressions for μ_s/μ_b vs. n_s or ψ_s can then be plotted with film thickness as running parameter, and also for various values of η. In order to compare the experimental results with the theoretical expressions of equations 6.53 and 6.56 we would need to use a value for the effective mass and therefore λ_n which would give a good fit at flat bands, as discussed in section 6.3.2. For a particular semiconductor material, η is a function of the doping density and μ_b. (NOTE: m* is also slightly dependent on N_D). Goldstein et. al[6.34,6.26] have obtained approximations for the excess carrier mobility in thick slabs and computed these for various values of η. For large values of η their results show a very large dip, or cusp, as the flat band condition is approached. In fact, for a sufficiently large η the surface mobility becomes negative. Greene[6.35] has considered this cuspidal surface mobility and has shown that, theoretically, there is a definite discontinuity at the flat band point. This has been attributed to the contribution of the unbounded carriers. Since a high η can be obtained with a high mobility semiconductor, Davis[6.36] conducted field effect emperiments on InSb surfaces at 79°K, where η was about 2, but did not observe a cusp. η has a value of about 1.25 at room temperature in InAs, assuming $m^* = 0.03m$ and $n = 2 \times 10^{16} cm^{-3}$.

Although we have measured the effective mobility of all the carriers, if there is a cusp in the mobility of the excess carriers this should have been observed, but was not. It is difficult to predict the behaviour of the mobility in equations 6.53 and 6.56 without numerically computing the expressions. The theory of Greene et. al[6.20] predicts a monotonic decrease in the mobility with increasing accumulation, and tends to the bulk value in depletion. However, as explained earlier, they assumed the carriers moving towards the surface have a velocity characteristic of the bulk, which is equivalent to saying that the carriers have been specularly reflected in the bulk. Under these boundary conditions one would expect that the mobility would tend to the bulk value in depletion, since the carriers are confined away from the diffuse surface. However, with the boundary conditions we have used- diffuse scattering at both interfaces - the expressions above should result in a mobility reduction as the channel is depleted, since in this regime the carriers can still be diffusely scattered at the film -substrate interface and are confined in an increasingly narrower channel. This could then explain the mobility reduction in depletion which we have observed, as shown in Fig.5.29.

Most of the work on surface mobility measurements has been carried out on Germanium and Silicon. Since 1962 the majority of these measurements have been on Silicon inversion layers, using the MOS system, where it has been found that the mobility falls off rapidly as threshold is approached, and this cannot be explained by the Boltzmann

theory. Recently, Reddi[6.66] has measured the majority carrier field effect and effective mobilities in accumulation and depletion layers, in thin (2-5μm) epitaxial silicon films on an opposite conductivity type Silicon substrate, using the MOS system. His results show that the mobility tends to the bulk value in depletion, unlike our results. There could be two reasons for this; first, the films he has used were much thicker than ours, and so in depletion most of the carriers are confined to the bulk. Second, since it is a homo-epitaxial system, it seems reasonable to assume that the film-substrate interface is specular.

There is a possibility that the fall in mobility we have measured in the depletion regime could be due to an error in interpreting the Hall measurements. In calculating the mobility we have assumed a one carrier system. However, Stern and Howard[6.32] and Fang and Fowler[6.56] suggest that as the carriers in a surface space charge layer are depleted, screening of attractive coulomb centres at the surface is reduced, which results in bound states. If these bound states overlap they can contribute to the conduction, but with a lower mobility than the free electrons. Assuming a Hall coefficient factor of unity for both bands, the Hall coefficient for a two carrier system is[6.37]:

$$R_H = \frac{1}{qn_m} = \frac{(b^2 n_1 + n_2)}{q(bn_1 + n_2)^2}$$

where $b = \mu_1/\mu_2$ is the ratio of the mobility of the free electrons to the bound electrons, of concentration n_1 and n_2, respectively. n_m is the measured electron concentration.

Since $\sigma = q\mu_2(bn_1+n_2)$, the measured Hall mobility is:

$$\mu_H = R_H \cdot \sigma = \frac{(b^2 n_1 + n_2)\mu_2}{(bn_1 + n_2)}$$

Thus, as the fraction n_1/n_2 is reduced, the measured mobility reduces from μ_1 to μ_2. If a two band system does exist, n_m should go through a minimum as the fraction of free electrons is varied. Although our measurements do not show a minimum in the range of gate voltages used, (see Fig.5.28) the electron concentration is certainly decreasing very slowly in this region. However, the bound state model is only important at low temperatures, Stern and Howard[6.32] suggest that it will not play a significant role in InAs, even at these temperatures, because the bound state band will merge with the conduction band, presumably due to the very small effective mass.

Further, it is not believed that the hole contribution is significant in this region because of the large mobility ratio. This, of course, assumes that the hole mobility is also significantly reduced by surface scattering.

6.3.5. Galvanomagnetic Surface Transport

In sections 6.3.2. and 6.3.4., the solutions to Boltzmanns equation have been obtained assuming zero magnetic field. In order to interpret Hall measurements on thin films and space charge layers it is necessary to include the effect of the magnetic field on the acceleration of the carriers, i.e., instead of qE/m* we must substitute q(E+vxB)/m* in equation 6.24. Zemel[6.39] and Amith[6.40] have attempted this problem for the case of a truncated linear potential at the surface, and the latter also considered the limiting case of flat bands in thin films. They assumed diffuse surfaces and, of course, all the simplifying assumptions considered earlier. Two expressions result; one for the current, I_{nx}, and the other for the Hall current, I_y. The latter is set to zero, to conform with the measurement conditions, and this gives an expression connecting E_x and E_y. The final result, for the case of a thin film with flat bands, in the limit of weak magnetic fields, is[6.26]:

$$R_H = - r_s(\beta) \cdot 1/(qn) \qquad \ldots(6.59)$$

where

$$r_s(\beta) = \frac{\left\{1-2/\beta+(2/\beta)\Gamma_2(\beta)+\Gamma_4(\beta)\right\}}{\left\{1-1/\beta+(1/\beta)\Gamma_2(\beta)\right\}^2} \qquad \ldots(6.60)$$

$$\beta = d/\lambda_n$$

$r_s(\beta)$ is analagous to the Hall coefficient factor r in equation 6.22, for bulk scattering mechanisms. $\Gamma_2(\beta)$ is given by equation 6.40, and

$\Gamma_4(\beta)$ by:

$$\Gamma_4(\beta) = \int_0^\infty (\pi\nu)^{-\frac{1}{2}} \exp\left\{-\nu - \beta/(\pi\nu)^{\frac{1}{2}}\right\} d\nu \quad \ldots(6.61)$$

Amith[6.40] has evaluated this expression and the results are presented in Fig.6.10. The interesting feature is that for $d/\lambda_n < 1$, r_s increases above unity and can achieve very large values in very thin films. Since our thinnest films are of the order of λ_n = (610Å, assuming m* = 0.03m), or greater, this should result in an r_s of unity, which is what we have observed. (In the limit of high magnetic fields, $r_s \to 1$, according to Amith's calculations). However, the assumption of an energy independent relaxation time would, in any case, give a value of unity in thick samples, (see equation 6.22). Further, if we assume a λ_n of 2300Å, in order to fit the mobility data, this would, theoretically, give an r_s of about 2.5 for a 400Å film.

The analysis also yields a finite magnetoresistance in very thin films ($d/\lambda_n < 1$), although in the bulk the magnetoresistance would be zero. This seems reasonable, since the velocity of carriers near the surface is reduced, and the Hall field only compensates the Lorentz force for the average velocity. In order to observe this magnetoresistance, it would be necessary to deposit films much less than λ_n thick. However, below a certain thickness the films would be discontinuous, in which case the Boltzmann theory would not be applicable.

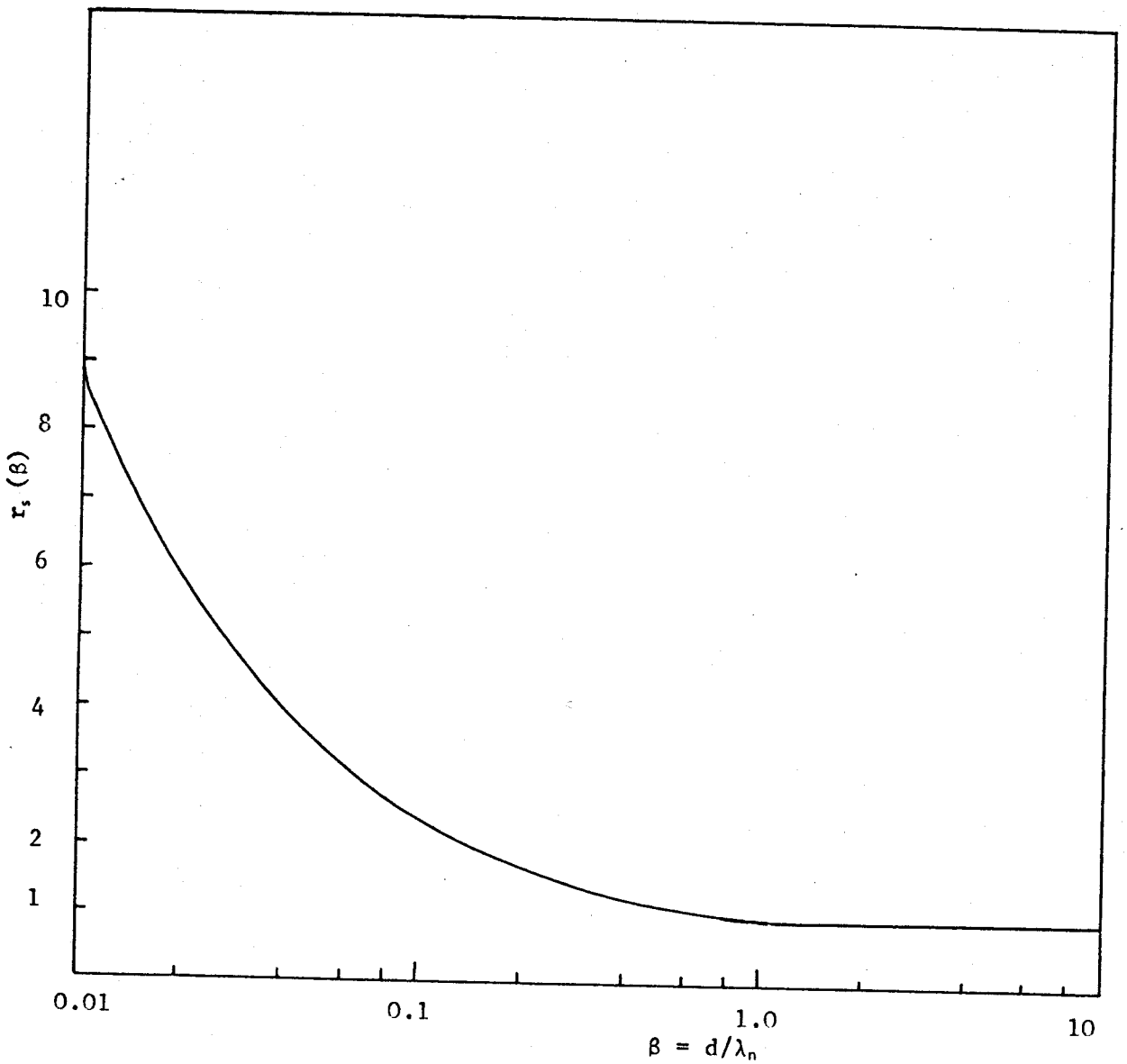

FIG.6.10

Surface Scattering Hall Coefficient Factor As A Function Of β, the Normalized Film Thickness (After Amith, ref.6.40)

6.4. Quantization Of Conduction Band Energy Levels

6.4.1. Quantum Size Effect

In chapter 1 it was briefly mentioned that in a thin film, of thickness comparable to the electron wavelength, λ_e (in InAs $\lambda_e \sim 400\text{Å}$ at $300^\circ K$), the electron energy is quantized, due to quantization of the electron wavevector perpendicular to the surface. In the case of a thin film with flat bands, the simple solution of Schrödinger's equation for a square well potential with infinitely high walls[6.41], is a good approximation. The electron energy may then be written:

$$\varepsilon = \frac{\hbar^2}{2m^*}(k_x^2 + k_y^2) + \varepsilon_N \qquad \ldots(6.62)$$

where the energy eigen-values are:

$$\varepsilon_N = \frac{\pi^2\hbar^2N^2}{8m^*d^2} \qquad \ldots(6.63)$$

$$N = 1, 2, 3 \ldots$$

The separation of any two levels, N and N+1, (see Fig.1.2), is then given by:

$$\Delta\varepsilon_{N,N+1} = \frac{\pi^2\hbar^2(2N+1)}{8m^*d^2} \qquad \ldots(6.64)$$

The separation of the two lowest sub-bands $\Delta\varepsilon_{1,2}$ is plotted as a function of film thickness in Fig.6.11. If this separation is greater than the electron energy, i.e., greater than about $3/2kT$, most of the electrons will be confined to the ground level, (N = 1), resulting in a two dimensional electron gas in k-space. From Fig.6.11 it can be seen that at temperatures below $300^\circ K$ the above condition

will be satisfied if the film thickness is less than 400Å. Since a change in K_z will not be possible if $\Delta\varepsilon_{1,2}$ is sufficiently large, this can affect considerably the interaction of electrons and phonons and, hence, the mobility. Zemel[6.38] has indicated that as the temperature is reduced the number of electrons and phonons capable of interacting decreases exponentially, and therefore one should observe a rapid increase in mobility. In fact, if diffuse surface scattering is absent, which is what may be expected in a quantized band[6.42], then the mobility could be even higher than in the bulk. This is contrary to our experimental results. However, scattering by surface charges could then dominate the mobility as discussed in section 6.5.

We have assumed above that the quantized sub-bands are of single energy levels. However, due to electron scattering there is a broadening of these sub-bands, which according to the uncertainty principle, is of the order of $\hbar/\tau$, where τ is the electron scattering relaxation time. Hence, quantization would only be expected to affect the electron transport if the energy separation $\Delta\varepsilon_{1,2}$ is greater than $\hbar/\tau$. Substituting $\tau = m^*\mu/q$, and using equation 6.64, this would require the following condition to be satisfied:

$$\mu > \frac{8qd^2}{\pi^2\hbar(2N+1)} \qquad \ldots(6.65)$$

This is plotted in Fig.6.11, for the lower limit of μ, and with $N = 1$, as a function of d. Thus, it appears that this condition could also be satisfied by the epitaxial InAs films below 400Å thick.

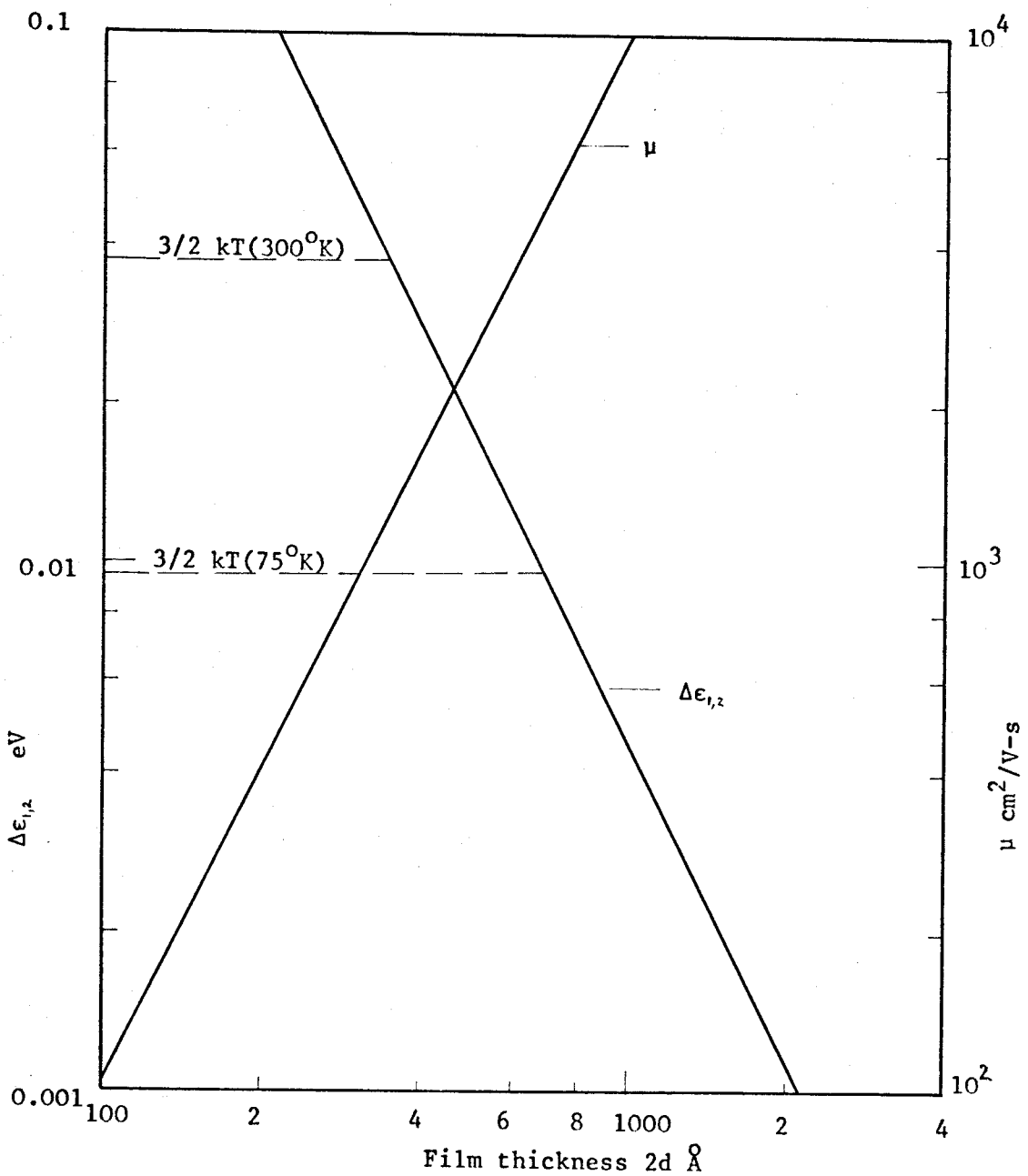

FIG.6.11

$\Delta\epsilon_{1,2}$ as a function of film thickness due to quantization in a thin film. Also shown is the lower limit of the mobility in equation 6.65.

Tavger[6.45] has considered the quantum size effect on electron transport in thin films by a Boltzmann equation method, in which he has derived an expression for the electron mobility in a two dimensional gas, presumably assuming that surface scattering is absent. The results indicate a mobility which is directly proportional to film thickness and has a temperature dependence which is very similar to the bulk scattering mechanism occuring. Berchtold and Huber[6.46] have used Tavger's theory to explain the increase in mobility with temperature in thin polycrystalline InSb films, where they have assumed ionized impurity scattering in the bulk, which, in any case, would give such a temperature dependence. However, it appears doubtful that quantization does occur in such a disordered structure. (In very thin polycrystalline InAs films, we have not observed the anomalous temperature dependence of mobility which occurs in the epitaxial films).

Ogrin et. al[6.47] have observed oscillations in the mobility and Hall coefficient with film thickness, in epitaxial Bismuth films on mica, which they attribute to the quantum size effect. The various film thicknesses were obtained by depositing the films simultaneously, thus avoiding any spreads due to varying deposition conditions. Similarly, Kommik and Bukhshtab[6.48] have observed small conductivity oscillations with thickness in polycrystalline Bismuth films, which they too attribute to quantization. Friedman and Köenig[6.49] have studied Bismuth single crystals which were thinned, and concluded that the surfaces are specular, thus favouring observation of the quantum size effect.

6.4.2. Quantization In Surface Space Charge Layers

If the surface band bending is sufficiently large, so that the distance from the surface corresponding to a change in potential of about kT/q, is of the order of the electron wavelength, then again the electron motion perpendicular to the surface will be quantized, and the conduction band will be split into sub-bands. It was Schrieffer[6.50] who originally suggested that this could affect the mobility in surface space charge layers, but as discussed earlier, he indicated that collision broadening could mask these effects. Greene[6.51] has indicated that quantization would cause an increase in the width of the space charge layer for a given surface potential, due to a decrease in the screening charge near the surface. This would result in a higher mobility than predicted classically. He has shown that surface fields approximately in excess of $6\times10^{3}(T/300)^{3/2}(m^*/m)V/cm$ would cause an appreciable deviation from the classical result.

In order to calculate the energy eigen-values, it is necessary to obtain self consistent solutions of Poisson's equation and Schrödinger's equation for the surface space charge layer. This has been done by Handler and Eisenhour[6.52], who studied Germanium surfaces, and more recently by Stern and Howard[6.32] for n-type inversion layers in Silicon. However, an approximate solution can be obtained by using a linear potenital, as shown in Fig.6.12(a), in Schrödinger's equation.

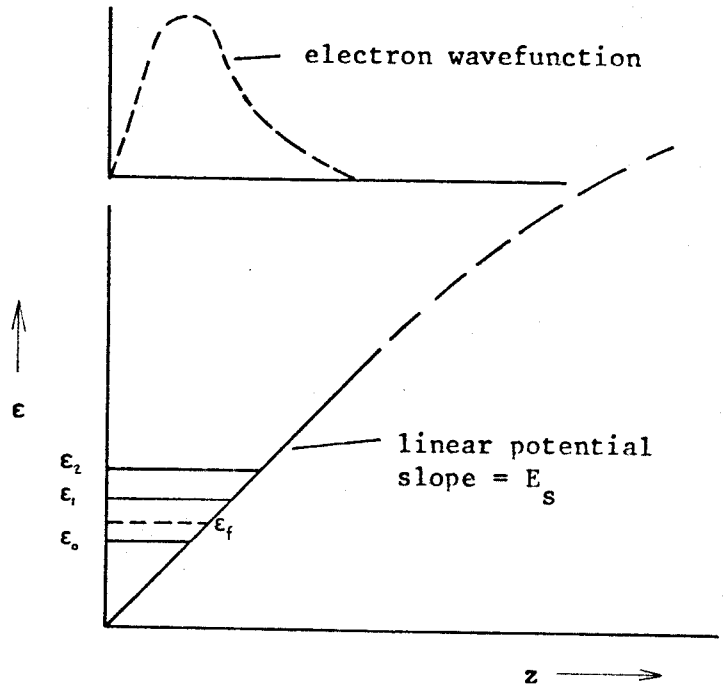

(a)

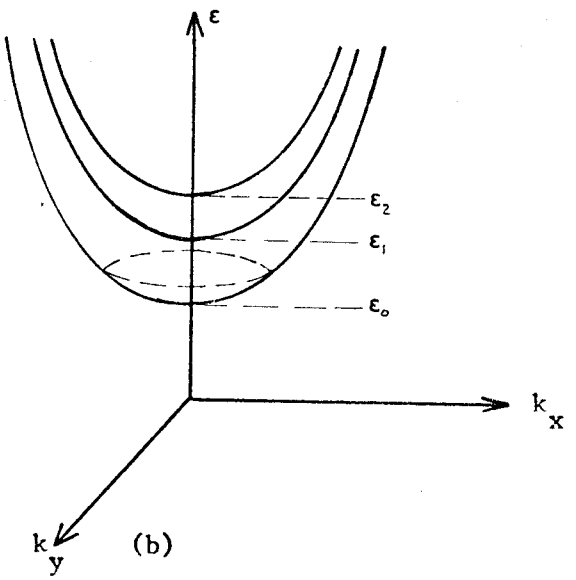

(b)

FIG.6.12

(a) Quantized energy levels in a linear potential well

(b) ε-k diagram of a quantized band

The electron wavefunction that results[6.53] can be expressed as the sum of two Bessel functions of order 1/3, the Airy functions, and the energy eigen-values are given by[6.53,6.54,6.55,6.44]:

$$\varepsilon_N = \frac{1}{2}\left\{\frac{3\pi q E_s \hbar}{m^{*\frac{1}{2}}}\right\}^{2/3}(N+3/4)^{2/3} \qquad \ldots(6.66)$$

$$N = 0, 1, 2, 3 \ldots$$

Shown in Fig.6.12(a) are the three lowest sub-bands and the electron wavefunction (the dotted curve), which tends to zero at the surface and within the bulk. (These are, in fact, the boundary conditions).

Fig.6.12(b) shows the ε-k diagram for a quantized band, where the energy continium in k_x, k_y space is given by the first term in equation 6.62 and the separation of the parabolas is given by equation 6.66.

If we ignore the fixed acceptor charge in strong accumulation layers, by Gauss' law E_s is:

$$E_s \approx \frac{q\Delta n_s}{\varepsilon'_o \varepsilon_s} \qquad \ldots(6.67)$$

Substituting this in equation 6.66, we obtain, in the case of InAs:

$$\varepsilon_N = 1.78\times10^{-9}\Delta n_s^{2/3}(N+3/4)^{2/3}\ \text{eV} \qquad \ldots(6.68)$$

The separation, $\Delta\varepsilon_{0,1}$, of the ground level and the first excited level is plotted in Fig.6.13 as a function of Δn_s. Also, shown is the electric field at the semiconductor surface, (since we have assumed a linear potential, and therefore a constant field within the space charge layer, this field is equal to the slope of the linear

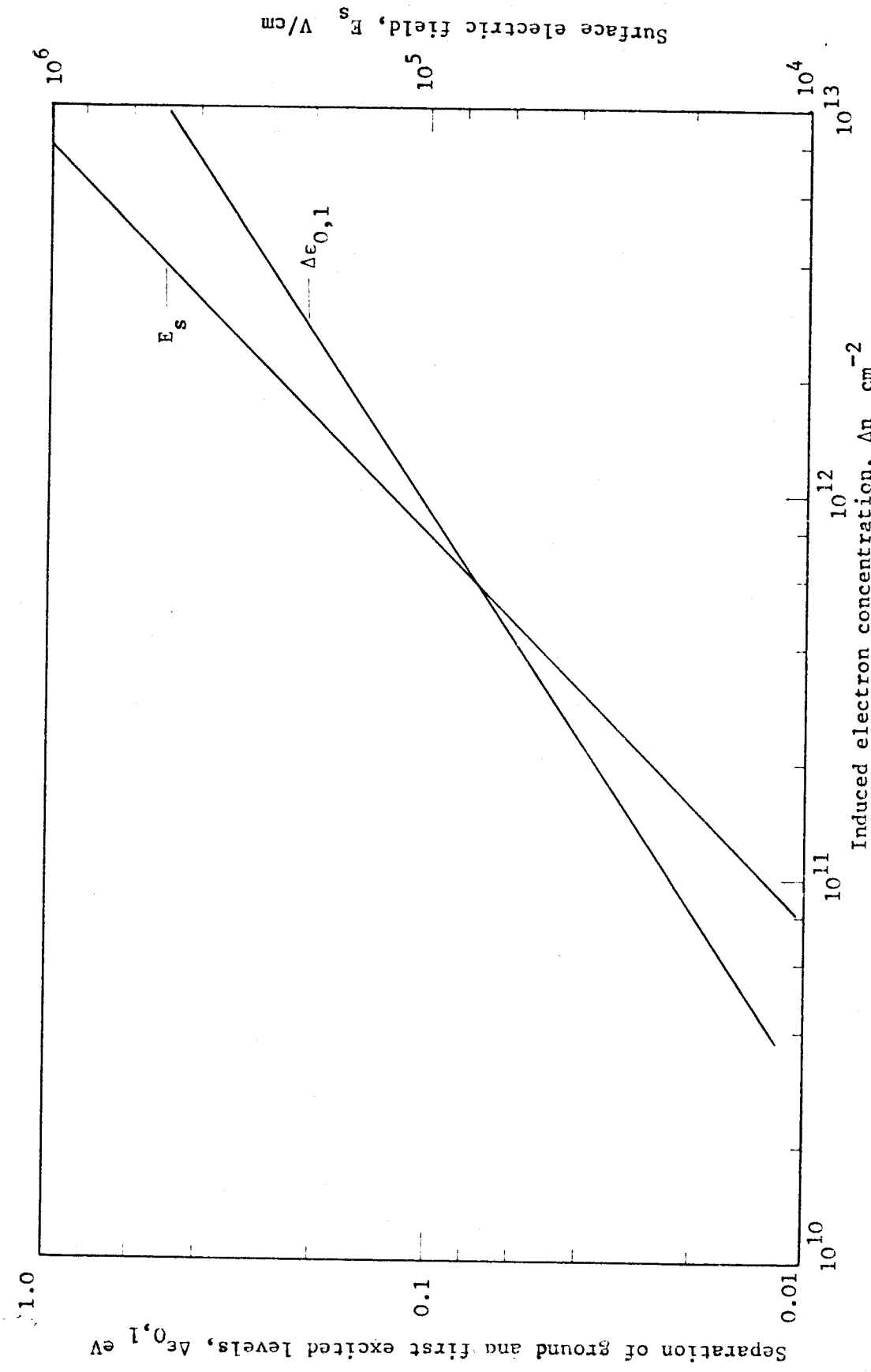

FIG.6.13

Quantization In Surface Space Charge Layers. Separation Of The Ground And First Excited Levels As A Function Of The Induced Electron Concentration, For A Linear Potential. Also Shown Is The Surface Electric Field.

potential). It can be seen that even under a moderate induced charge, the splitting of the sub-bands can be greater than the thermal energy of the electrons, resulting again in a two-dimensional gas. At low fields only the ground level will be occupied, at higher fields the next sub-band will begin to be populated. Generally, with a maximum induced charge of about $10^{13}cm^{-2}$, only the first two or three sub-bands will be populated. Another result of quantization is that energy states below ε_o in the potential well, will be eliminated (see Fig.6.12(a)). Also, since the electron wavefunction tends to zero as the surface is approached, the electrons will be confined away from the surface, thus reducing any diffuse surface scattering which occurs. This may explain the fairly high mobilities observed in strong inversion layers in Silicon[6.56,6.57].

As a result of quantization the density of states of a two-dimensional electron gas is independent of energy ($= 8\pi m^*/\hbar^2$), whereas in the three dimensional case it is proportional to $\varepsilon^{\frac{1}{2}}$. Thus, in the magneto-oscillatory conductance experiments of Fowler et. al[6.43] on Silicon MOS structures, the two-dimensional electron transport was confirmed since the period of the conductance peaks with gate voltage was constant, because the density of states in each Landau level is constant, while in a three-dimensional gas each successive Landau level would have an increasing density of states[6.44]. These experiments were carried out in very high magnetic fields and at liquid Helium temperatures. Also, the conductance oscillations were only observed with

low source-drain voltages, of the order of tens of mV. Presumably, higher voltages result in a decrease in the relaxation time, and therefore, broadening of the quantized levels. These experiments could be usefully applied to InAs, and other III - V compound semiconductor field effect structures, where quantization should be even more pronounced because of the very small electron effective mass, and may permit observation of conductance oscillations at higher temperatures. Further, unlike the multivalley system in Silicon, most of the III - V compounds have a conduction band which is symmetrical about the centre of the Brillouin zone, thus making the interpretation of measurements less complicated. Such experiments have an important bearing on electron transport at semiconductor surfaces, and in particular, can provide a value for the effective mass of electrons near the surface.

Kawaji et. al[6.58] have measured electron mobilities in InSb inversion layers in strong magnetic fields and at low temperatures. Their results indicate a reduction in mobility with an increase in $\hbar\omega_c/kT$, the ratio of the Landau level splitting to the thermal energy ($\omega_c = qB/m^*$ is the cyclotron frequency). However, they do not mention the observation of conductance oscillations with gate voltage. Similarly, Kawaji and Gatos[6.59] measured very small changes in the conductance of inversion layers in InAs, in very strong magnetic fields, but did not observe any oscillations. Presumably, this is because the amount of charge they could induce was very small. There appears to be a very limited amount of experimental work done on surface transport in III - V compounds so far.

At present there does not appear to be a theory on surface scattering which assumes a quantized band, and which can explain the experimental results. However, Stern and Howard[6.32] have developed a theory for scattering by surface charges, which is based on a quantum model, but it is limited to low temperatures and surface fields, so that only the ground state is occupied, which they refer to as the electric quantum limit. Duke[6.60], and Alferieff and Duke[6.61] have also developed a theory in the electric quantum limit, for scattering by surface irregularities and by impurities, All these theories are rather complicated, and as yet they do not explain the experimental results completely.

6.5. Scattering By Surface Charges

In section 6.3.3. we indicated that the Boltzmann surface transport theory is not capable of explaining the increase in electron mobility with temperature observed with films in the region of 500Å or less. The experimental results suggest that the density of ionized donors is not sufficiently high to cause such a large mobility reduction. Further, if the dominant scattering mechanism was due to ionized impurities within the film, the mobility should have remained constant as the surface potential was varied, but as shown in Fig.5.29, the mobility did vary considerably. However, a high density of charged surface states could affect considerably the carrier mobility, through the coulomb interaction, in films of the order of a few hundred angstroms thick, and in surface space charge layers. Kawaji and Kawaguchi[6.31] considered this problem for the case of an n-type inversion layer , in order to explain their measurements on InAs at very low temperatures. They assumed a two dimensional electron gas due to surface quantization. A consequence of this is that, since the momentum perpendicular to the surface must be conserved, one would expect that diffuse surface scattering does not occur, particularly at low temperatures. Therefore, the dominant scattering mechanism is assumed to be due to coulomb interaction with the charged surface states. Below we attempt a simple derivation for the mobility due to this mechanism.

Following Kawaji and Kawaguchi[6.31], the differential 'cross-section' for scattering in two dimensions, similar to the three dimensional case[6.41], is given by:

$$\sigma(\theta) = \frac{Zq^2}{8\pi\varepsilon_s\varepsilon'_o m^* v^2} \cdot \frac{1}{\sin^2\theta/2} \qquad \ldots(6.61)$$

where Zq is the charge of the surface state, and v is the velocity of the carriers, which is unchanged by the scattering, since we assume it is elastic. $\sigma(\theta)$ has dimensions of metres.

The scattering angle, θ, is given by:

$$\tan\theta/2 = \frac{Zq^2}{4\pi\varepsilon_s\varepsilon'_o m^* v^2 a_o} \qquad \ldots(6.62)$$

where a_o is the impact parameter.

$\sigma(\theta)d\Omega$ is the differential area of the incident particles which are scattered through θ, into the solid angle $d\Omega$. Similar to the Conwell-Weisskopf[6.9] impurity scattering theory, the number of collisions per unit time = $N_{ss}v\sigma(\theta)d\Omega$, where N_{ss} is the density of charged surface states/unit area. The equivalent number of velocity destroying collisions per unit time is:

$$dn_{ss} = d(1/\tau_{ss}(v)) = N_{ss}v\sigma(\theta)(1-\cos\theta)d\Omega \qquad \ldots(6.63)$$

where τ_{ss} is the relaxation time due to scattering by charged surface states.

The total relaxation time is obtained by integrating equation 6.63 over θ, with limits from 0 to θ_z, where θ_z is given by equation 6.62 for a carrier at a distance z from the surface.

Thus, since $d\Omega = 2\pi\sin\theta d\theta$, we have:

$$1/\tau_{ss}(v) = \frac{N_{ss}Zq^2}{2\varepsilon_s\varepsilon'_o m^*v}\int_o^{\theta_z}\sin\theta d\theta$$

$$= \frac{N_{ss}Zq^2}{2\varepsilon_s\varepsilon'_o m^*v}(1-\cos\theta_z) \qquad ...(6.64)$$

Substituting for θ_z from equation 6.62, gives:

$$\tau_{ss}(v) = \frac{\varepsilon_s\varepsilon'_o m^*v}{N_{ss}Zq^2}\left\{1 + \left\{\frac{4\pi\varepsilon_s\varepsilon'_o m^*v^2 z}{Zq^2}\right\}^2\right\} \qquad ...(6.65)$$

We need to average this over v, as follows:

$$\langle\tau_{ss}\rangle = \frac{\langle v^2\tau_{ss}(v)\rangle}{\langle v^2\rangle} = \frac{\int_o^\infty v^4\tau_{ss}(v)\exp(\frac{-m^*v^2}{2kT})dv}{\int_o^\infty v^4\exp(\frac{-m^*v^2}{2kT})dv} \qquad ...(6.66)$$

Performing this integration and averaging over half the film thickness- assuming the film is symmetrical about its midplane - and remembering $\mu = q\tau/m^*$, we obtain finally:

$$\mu_{ss} = \frac{8\varepsilon'_o\varepsilon_s}{3N_{ss}Zq}\left\{\frac{2kT}{\pi m^*}\right\}^{\frac{1}{2}}\left\{1 + \frac{(16\pi kT\varepsilon_o\varepsilon_s d)^2}{Zq^2}\right\} \qquad ...(6.67)$$

This epxression indicates that the mobility tends to a finite value as d tends to zero, and is inversely proportional to the density of charged surface states. Further, the temperature dependence is of the form $T^{\frac{1}{2}}(1+AT^2)$.

Substituting the appropriate constants for InAs in equation 6.67 we have:

$$\mu_{ss} = \frac{4\times10^{13}T^{\frac{1}{2}}}{N_{ss}} (1+1.13\times10^{9}d^{2}T^{2}) \text{ cm}^2/\text{V-sec} \quad \ldots(6.68)$$

where N_{ss} is in cm^{-2} and d in cm.

Assuming a rather high density of charged surface states, $10^{14}cm^{-2}$, Fig.6.14, shows the variation of μ_{ss} with temperature for several film thicknesses, and the experimental results for a 500Å film. The latter shows a smaller increase with temperature than the theoretical result. If we assume that quantization is important at the lower temperatures, then as the temperature increases it would tend to be smeared out and diffuse surface scattering should increase, thus reducing the slope of the measured mobility vs. temperature.

The assumption of such a high surface state density is difficult to believe. However, in chapter 2 we calculated the density of dangling bonds at a GaAs/InAs interface to be in the region of $10^{14}cm^{-2}$, which could give rise to a high density of charge at the film-substrate interface. Also, a difference in the surface state density could explain why the mobility of the 500Å film in Fig.5.16 is lower than that of the 380Å film. In the field effect structures the surface state density at the semiconductor-insulator interface was estimated to be in the region of $1\text{-}5\times10^{12}cm^{-2}$.

Obviously the above derivation is rather crude and it should not be pushed too far, but it does indicate the correct dependence on the various parameters, particularly the temperature dependence. We have averaged τ_{ss} over energy assuming a three dimensional gas, whereas,

if quantization is important at low temperatures this should be done for a two dimensional gas.

In conclusion, it appears that more experimental results are required of very thin films (less than 300Å) and of the field effect structures fabricated with various film thicknesses. The temperature dependence of the Hall mobility in strong accumulation and depletion layers should provide further information on the possible scattering mechanisms that are operative.

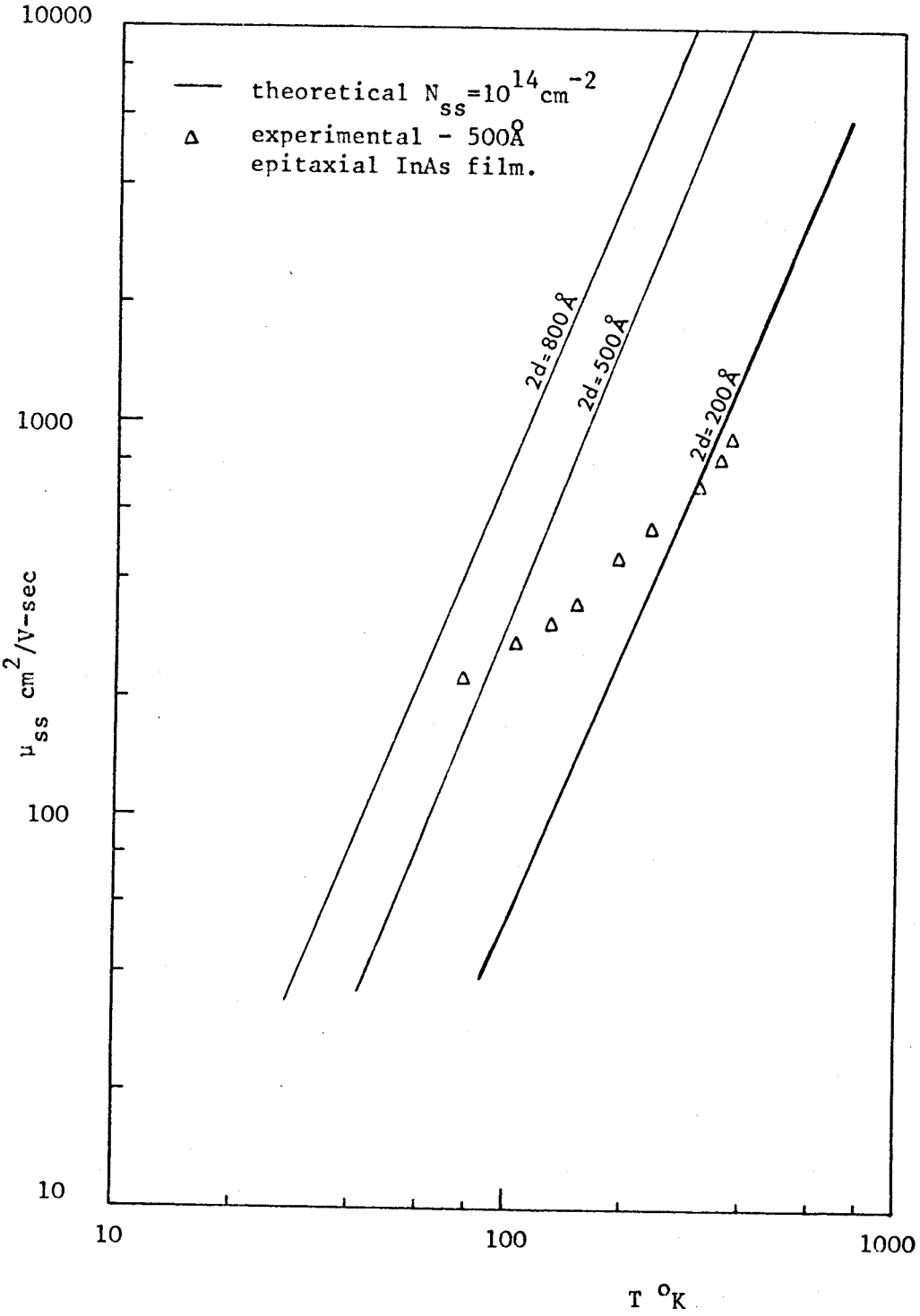

Fig.6.14

Electron mobility in a very thin film due to scattering by charged surface states, as a function of temperature

7. CONCLUSION AND SUGGESTIONS FOR FUTURE WORK

We have demonstrated that the 'three temperature' vacuum evaporation method is suitable for depositing good quality epitaxial InAs on semi-insulating GaAs. Although it has been found that the polycrystalline films are not suitable for field effect transistor applications, because of the surface roughness and higher electron concentration, they are well suited to various Hall effect applications.

Reproducibility of the epitaxial films is good since post-deposition annealing does not appear to change the electrical properties, whereas with polycrystalline films it does. Except for a small reduction in the electron concentration, of the order of 10-20% in the first week after deposition, the stability of the electrical properties is very good. Mobilities upto 23,000 cm^2/V-sec indicate that the epitaxial films are comparable to melt grown InAs. The use of 6N pure source materials may result in a reduction of the ionized impurity concentration to the $10^{15} cm^{-3}$ region.

Further studies on the effect of deposition rate need to be carried out. According to the heterogeneous nucleation theory as applied to epitaxy, it appears that lower substrate temperatures could be used with lower deposition rates. Since this should reduce further any auto-doping that is occuring, it would help towards a better understanding of the very thin films. Higher deposition rates may be desirable when depositing thick films, and this again may be possible using higher substrate temperatures.

Although we have obtained good epitaxial films with a fixed Indium rate and Arsenic pressures between $5x10^{-5}$ and $2x10^{-4}$torr, the In/As ratio could, perhaps, affect the concentration of defects. Shaw et.al[7.1] using an HCl transport method, have observed a variation in electrical properties of epitaxial GaAs, with different Ga/As ratios, and have suggested that it could be due to (i) a strong dependence of the vapour-solid segregation co-efficient of impurities on vapour composition, (ii) the formation of physical imperfections, e.g. vacancies, interstitials, whose concentrations are functions of vapour composition. Hence, further work on the effects of In/As ratio is desirable.

We have deposited good epitaxial layers on {100}, {110}, and {111} As faces of GaAs. It would be interesting to extend this to the {111} Ga face. Apparently, due to orientation dependent contamination, epitaxy of GaAs on the {111} Ga face is more perfect than that on the Arsenic face. The deposition of doped layers, particularly p-type InAs, with a resevoir source would be very useful. Attempts to deposit p-type InAs layers by chemical transport have been unsuccessful.[7.2]

Preliminary attempts to deposit epitaxial InAs on Silicon in our laboratory, indicate that this is quite feasible. The deposition of other III - V compounds and psuedo-binary alloys, using this multisource method, would be interesting. Recently Fawcett et.al[7.3] have suggested that alloys of the form $(In_xGa_{1-x})As$ and $In(As_xP_{1-x})$ may prove to be useful for microwave devices, such as Schottky barrier field effect tansistors[7.4,7.5], because of the

predicted high saturation velocities in such materials. Since the Schottky barrier F.E.T. requires a thin semiconductor film[7.6], of the order of a fraction of a micron, the deposition method we have employed could be useful for such application.

Regarding the field effect transistors, it appears that films with lower impurity concentration are required to improve their saturation characteristics. This would also permit using thicker films, of the order of a few thousand angstroms, having higher mobilities. Stability of device characteristics may be achieved by using a different gate insulator, such as an RF sputtered SiO_2/Si_3N_4 sandwich, used by Neugebauer et.al[7.7] or Al_2O_3 by plasma anodization used by Zaininger and Waxman[7.8]. These insulators are, apparently, very stable and can be deposited at temperatures below 300°C.

It should be pointed out that, with the fabrication procedures we have employed, resistor networks using the thin semiconductor film, and capacitors, can be incorporated in integrated form without any further processing steps. Also, since the technology is simple and the temperatures employed are reasonably low, high yields should be possible.

Measurements of the Hall mobility variation with gate voltage in the field effect structures demonstrates that the mobility is reduced with high gate fields. These measurements should be extended

to different film thicknesses and to the temperature dependence. Numerical computation of the theoretical expressions given in chapter 6 is required, in order to explain these results. However, quantization of the energy levels must be seriously examined, and could invalidate the classical Boltzmann equation theory.

APPENDIX A Derivation Of The Free Energy Of Formation Of A Critical Nucleus

Gibbs free energy of formation of a given cluster composed of i^* atoms can be expressed as follows:

$$\Delta G = V.\Delta G_v + \sum_s \sigma_s A_s \qquad \ldots(A.1)$$

ΔG_v is the Gibbs free energy change per unit volume associated with the transformation of the absorbed atoms to the crystalline embryo and V is the volume of the embryo. $\sum_s \sigma_s A_s$ is the summation of the product of the surface areas, of the various interfaces created (or destroyed) by the formation of the embryo, and the interfacial free energy per unit area associated with each area.

From the hemispherical cap model in Fig.A.1 we can write:

$$\Delta G = \underbrace{\frac{4}{3}\pi r^3 f_1(\theta)\Delta G_v}_{\text{volume of cap}} + \underbrace{4\pi r^2 f_2(\theta)\sigma_{c-v}}_{\text{surface area of cap}} + \underbrace{\pi r^2 \sin^2\theta \{\sigma_{c-s} - \sigma_{s-v}\}}_{\text{surface area of substrate destroyed}} \qquad \ldots(A.2)$$

where θ is the contact angle

$$f_1(\theta) = \left\{\frac{2-3\cos\theta+\cos^3\theta}{4}\right\} \qquad \ldots(A.3)$$

$$f_2(\theta) = \frac{(1-\cos\theta)}{2} \qquad \ldots(A.4)$$

σ_{c-v} is the condensate-vapour interfacial energy

σ_{c-s} is the condensate-substrate interfacial energy

σ_{s-v} is the substrate-vapour interfacial energy.

It can be shown that:

$$\sigma_{s-v} - \sigma_{c-s} = \sigma_{c-v}\cos\theta \qquad \ldots(A.5)$$

Substituting equation A.5 in A.2 and differentiating w.r.t. r and equating to zero, we obtain the radius of the critical nucleus, r^*

$$r^* = -\frac{2\sigma_{c-v}}{\Delta G_v} \qquad \ldots(A.6)$$

and substituting equation A.6 in A.2 we have for the free energy of formation of the critical nucleus:

$$\Delta G^* = \frac{16\pi\sigma_{c-v}^3}{3\Delta G_v^2} f_1(\theta) \qquad \ldots(A.7)$$

Equations A.2 and A.3 are plotted in Fig.A.2 and A.3.

If the equilibrium contact angle θ is zero, i.e. if there is complete "wetting" of the substrate by the condensate, ΔG^* is zero and nucleation is most rapid. However, if $\theta = 180^o$, there is no "wetting" at all and the substrate has negligible potency as a nucleation catalyst.

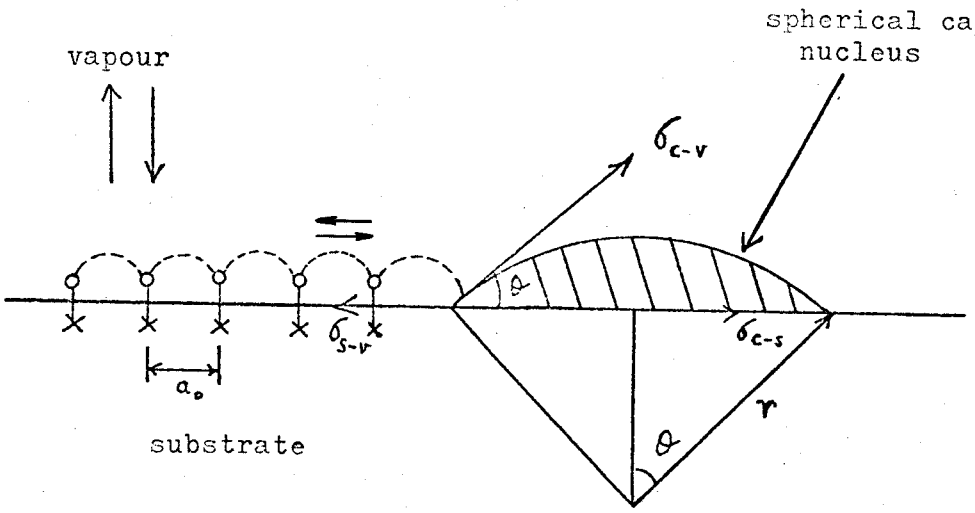

Fig.A.1
Hemispherical cap model for heterogeneous nucleation

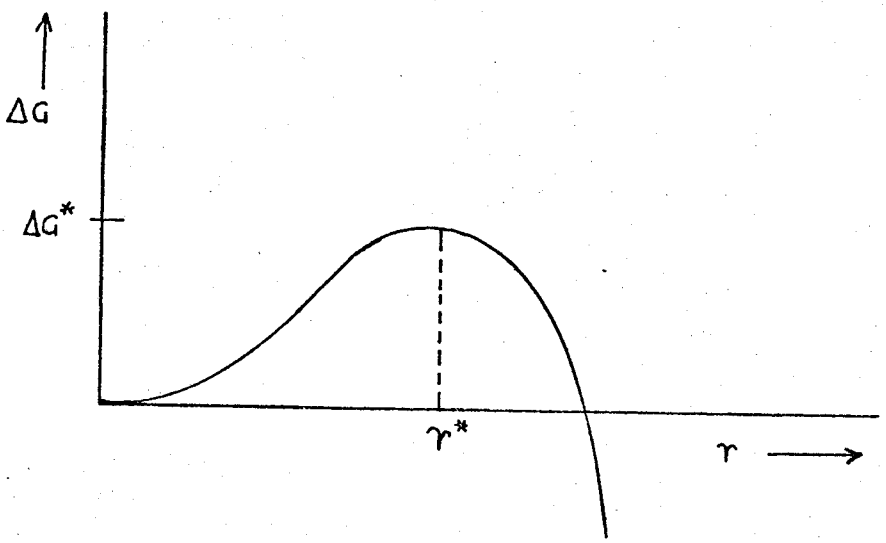

Fig.A.2
Free energy of formation of a critical nucleus
as a function of its radius

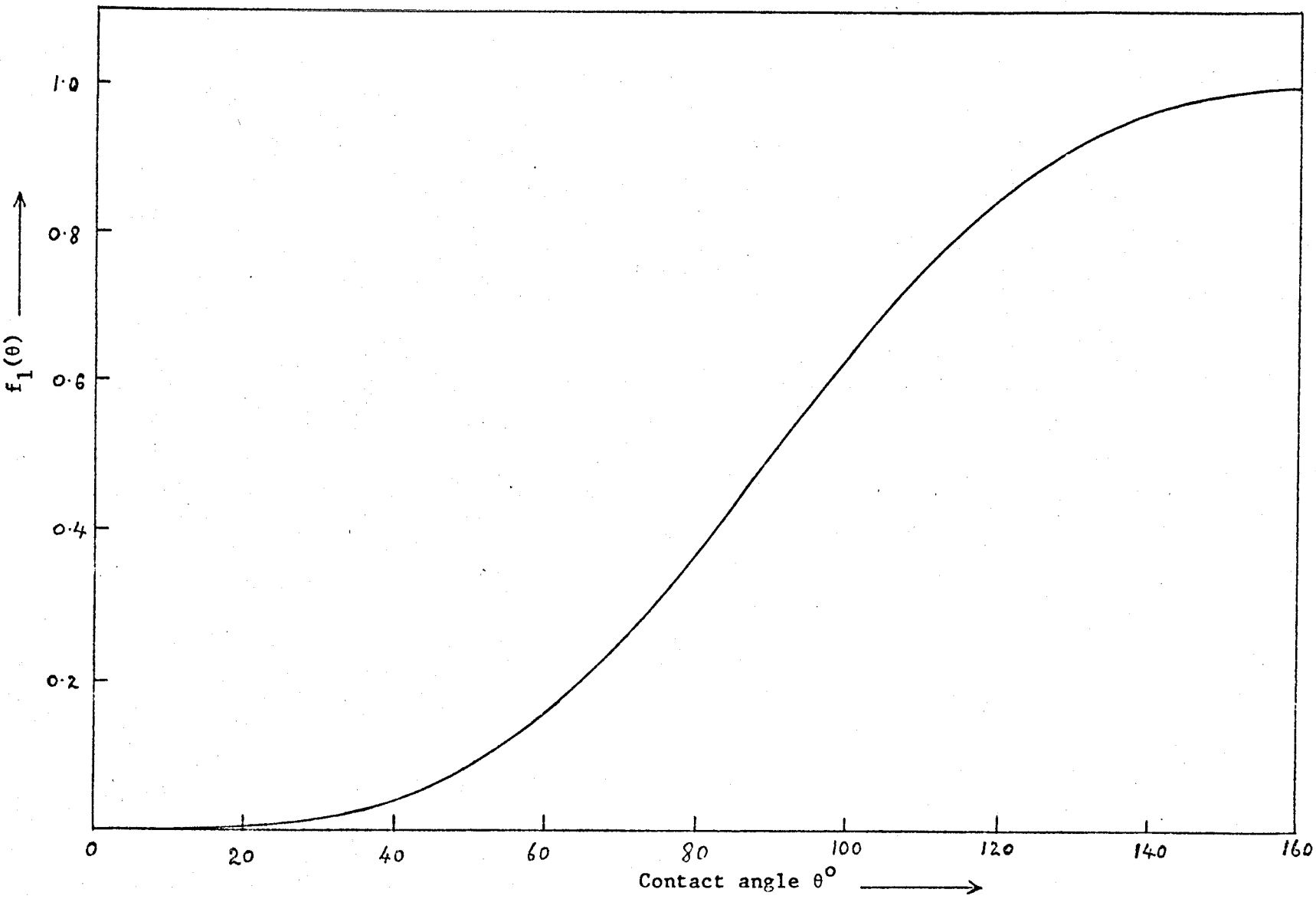

Fig.A.3

$f_1(\theta)$ as A Function Of The Nucleus Contact Angle

APPENDIX B

Flat Band Solution Of Boltzmanns Equation With Boundary Conditions

Substituting the boundary conditions at z = 0 and 2d, equations 6.29 and 6.30, in the general solution, equation 6.27, we have:

$$f_{11}\left\{1+g^{+}(v)\right\} = \gamma f_{11}\left\{1+g^{-}(v)\exp(-2d/v_z\tau_b)\right\} \qquad \ldots(B.1)$$

$$f_{11}\left\{1+g^{-}(v)\right\} = \omega f_{11}\left\{1+g^{+}(v)\exp(-2d/v_z\tau_b)\right\} \qquad \ldots(B.2)$$

Substituting $g^{+}(v)$ from B.1 in B.2 we have:

$$g^{-}(v) = \omega-1+\omega\left\{\gamma-1+\gamma g^{-}(v)\exp(-2d/v_z\tau_b)\right\}\exp(-2d/v_z\tau_b) \qquad \ldots(B.3)$$

re-arranging, we have:

$$g^{-}(v) = -\frac{1-\omega+\omega(1-\gamma)\exp(-2d/v_z\tau_b)}{1-\gamma\omega\exp(-4d/v_z\tau_b)} \qquad \ldots(B.4)$$

Similarly $g^{+}(v)$ is:

$$g^{+}(v) = -\frac{1-\gamma+\gamma(1-\omega)\exp(-2d/v_z\tau_b)}{1-\gamma\omega\exp(-4d/v_z\tau_b)} \qquad \ldots(B.5)$$

Substituting B.4 and B.5 in equation 6.27 will give the expressions for f_1 in equation 6.31. It must be remembered that in f_1^{-} all the terms with v_z must change sign because v_z is negative for carriers moving away from the surface z = 2d.

APPENDIX C

Integration Of Flat Band Current I_{nx}

Integration of Equation 6.33 is performed with f_1^+ of equation 6.31 with limits of v_z from 0 to ∞. The other half of the integration from $-\infty$ to 0 is identical, but with γ and ω interchanged.

Substituting f_1^+ from equation 6.31 and f_{11} and f_o from equations 6.28 and 6.25 in equation 6.33, the v_x and v_y integrals are:

$$\int_{-\infty}^{\infty} v_x^2 \exp(-m^* v_x^2/2kT)\,dv_x = (\pi/4a^3)^{\frac{1}{2}} \qquad \ldots(C.1)$$

$$a = m^*/2kT$$

$$\int_{-\infty}^{\infty} \exp(-m^* v_y^2/2kT)\,dv_y = (\pi/a)^{\frac{1}{2}} \qquad \ldots(C.2)$$

The product of these two integrals = $2\pi k^2 T^2/m^{*2}$

Integrating over z from 0 to 2d gives:

$$I_o = \left\{ 2d + v_z\tau_b \left\{ \frac{(1-\gamma)+\gamma(1-\omega)\exp(-2d/v_z\tau_b)}{1-\omega\gamma\exp(-4d/v_z\tau_b)} \right\} \left\{ \exp(-2d/v_z\tau_b)-1 \right\} \right\}$$

$$= \left\{ 2d + v_z\tau_b \left\{ \frac{(\gamma-1)+(1-2\gamma+\omega\gamma)\exp(-2d/v_z\tau_b)+\gamma(1-\omega)\exp(-4d/v_z\tau_b)}{1-\omega\gamma\exp(-4d/v_z\tau_b)} \right\} \right\}$$

$$\ldots(C.3)$$

Integrating over v_z from 0 to ∞ gives for the first term in eqn.C.3:

$$2d\int_0^\infty \exp(-m^*v_z^{\,2}/2kT)dv_z \;=\; d(\pi/a)^{\frac{1}{2}} \qquad \ldots(C.4)$$

By a change of variable from v_z to $\nu = m^*v_z^{\,2}/2kT$, the other integrals are:

$$-(1-\gamma)\frac{\tau_b kT}{m^*}\int_0^\infty \frac{\exp-\nu\,d\nu}{1-\omega\gamma\exp(-2d/\lambda_n(\pi\nu)^{-\frac{1}{2}})} \;=\; -\frac{(1-\gamma)kT\tau_b}{m^*}\cdot\Gamma_1(\lambda_n/d)$$

$$\text{where}\quad \lambda_n = \tau_b(kT/2\pi m^*)^{\frac{1}{2}} \qquad \ldots(C.5)$$

$$(1-2\gamma+\omega\gamma)\frac{kT\tau_b}{m^*}\int_0^\infty \frac{\exp(-\nu-d/\lambda_n(\pi\nu)^{-\frac{1}{2}})d\nu}{1-\omega\gamma\exp(-2d/\lambda_n(\pi\nu)^{-\frac{1}{2}})} \;=\; (1-2\gamma+\omega\gamma)\frac{kT\tau_b}{m^*}\Gamma_2(\lambda_n/d) \qquad \ldots(C.6)$$

$$\gamma(1-\omega)\frac{kT\tau_b}{m^*}\int_0^\infty \frac{\exp(-\nu-2d/\lambda_n(\pi\nu)^{-\frac{1}{2}})d\nu}{1-\omega\gamma\exp(-2d/\lambda_n(\pi\nu)^{-\frac{1}{2}})} \;=\; \gamma(1-\omega)\frac{kT\tau_b}{m^*}\Gamma_3(\lambda_n/d) \qquad \ldots(C.7)$$

Using the results of equations C.1, C.2, and C.4 to C.7, the current I_{nx} for $v_z > 0$, is:

$$\underset{(v_z>0)}{I_{nx}} = n_b/2(h/2\pi m^*kT)^{3/2}2(m^*/h)^3\,\frac{q^2E_x\tau_b}{kT}\,\frac{2\pi k^2T^2}{m^{*2}}\cdot$$
$$\left\{d\left(\frac{2\pi kT}{m^*}\right)^{\frac{1}{2}} - (1-\gamma)\frac{kT\tau_b}{m^*}\Gamma_1(\lambda_n/d) + (1-2\gamma+\omega\gamma)\frac{kT\tau_b}{m^*}\Gamma_2(\lambda_n/d)\right.$$
$$\left. + \gamma(1-\omega)\frac{kT\tau_b}{m^*}\Gamma_3(\lambda_n/d)\right\} \qquad \ldots(C.8)$$

Substituting λ_n we have:

$$I_{\substack{nx \\ (v_z>0)}} = 2q\frac{2n_b E_x \tau_b d}{m^*}\left\{\tfrac{1}{2} - \frac{(1-\gamma)}{2\beta}\Gamma_1(\beta) + \frac{(1-2\gamma+\omega\gamma)}{2\beta}\Gamma_2(\beta) + \gamma\frac{(1-\omega)}{2\beta}\Gamma_3(\beta)\right\} \quad \ldots(C.9)$$

where $\beta = d/\lambda_n$

The current for $v_z < 0$, is identical to C.9, but with γ and ω interchanged. This must be added to C.9 to obtain the total current.

APPENDIX D

Boltzmanns Equation Solution With Boundary Conditions-Band Bending

Substituting the boundary condition at $z = 0$, equation 6.48, in equation 6.46, we have:

$$0 = f_{11}\left\{1+H^{+}(v)\exp(-K(v_{zs},v_{zs}))\right\}$$

Now $K(v_{zs},v_{zs}) = 0$, therefore, $H^{+}(v) = -1$ and the solution for $v_z \geq 0$ is:

$$f_1^{+} = f_{11}\left\{1-\exp(-K(v_z,v_{zs}))\right\} \qquad v_z \geq 0 \qquad \ldots(D.1)$$

Similarly, substituting equation 6.49 in equation 6.46, we have:

$$0 = f_{11}\left\{1+H^{-}(v)\exp-K(-v_{zd},-v_{zs})\right\}$$

and the solution for $v_z \leq 0$ is:

$$f_1^{-} = f_{11}\left\{1-\exp(-K(v_z,-v_{zs})+K(v_{zs},v_{zd}))\right\} \qquad \ldots(D.2)$$

APPENDIX E

Integration Of I_{nx} With Surface Band Bending

Substituting for f_1, f_{11} and f_o from equations 6.50, 6.28 and 6.43 in equation 6.33 and remembering that the v_x and v_y integrals are identical to equations C.1 and C.2 in appendix C, we have:

$$I_{nx} = qn_b\mu_b\left(\frac{m^*}{2\pi kT}\right)^{\frac{1}{2}} E_x \int_o^{2d} dz \int_{-\infty}^{\infty} e^{-\nu}(1-\delta)dv_z$$

$$= q\mu_b \left(\frac{m^*}{2\pi kT}\right)^{\frac{1}{2}} E_x(n_b I_3 - n_b I_4) \qquad \ldots(E.1)$$

$$n_b I_3 = \int_o^{2d} n_b dz \int_{-\infty}^{\infty} \exp(-mv_z^2/2kT-\psi)dv_z = \left(\frac{2\pi kT}{m^*}\right)^{\frac{1}{2}} n_b \int_o^{2d} \exp(-\psi)dz \qquad \ldots(E.2)$$

Now

$$\Delta n_s = \int_o^{2d} (n-n_b)dz = n_b \int_o^{2d} e^{-\psi}dz - 2dn_b \qquad \ldots(E.3)$$

Therefore

$$n_b I_3 = (2\pi kT/m^*)^{\frac{1}{2}}(\Delta n_s + 2dn_b) \qquad \ldots(E.4)$$

Now since $E_z = -\frac{kT}{q}\frac{\partial \psi}{\partial z}$, from equation 6.44 we have:

$$\partial z = -\frac{kT}{qE_z}\,\partial \nu \qquad \ldots(E.5)$$

and from equation 6.47

$$\frac{\partial K}{\partial v_z} = m^*/q\tau_b E_z \qquad \ldots(E.6)$$

Therefore

$$\partial z = -\frac{kT\tau_b}{m^*}\,\frac{\partial K}{\partial v_z}\,\partial \nu \qquad \ldots(E.7)$$

Using equation E.7, I_4 can be written:

$$I_4 = \frac{kT\tau_b}{m^*} \int_{-\infty}^{\infty} \exp -\nu \, d\nu \int_{v_{z_1}}^{v_{z_2}} \delta \frac{\partial K}{\partial v_z} \partial v_z \qquad \ldots(E.8)$$

The integration of I_4 must be carried out separately for depletion and accumulation, using δ from equation 6.51.

Depletion Regime $\psi_s \gtrless 0$

The integration of I_4 , with δ from equation 6.51(a) is:

$$I_{4_A} = \frac{kT\tau_b}{m^*} \int_{\psi_d}^{\psi_s} \exp -\nu \, d\nu \int_{-v_{zd}}^{v_{zd}} \exp \left\{-K(v_z - v_{zs}) - K(v_{zd}, v_{zs})\right\} \frac{\partial K}{\partial v_z} \cdot \partial v_z$$

$$= \frac{kT\tau_b}{m^*} \int_{\psi_d}^{\psi_s} e^{-\nu} d\nu \left\{1 - \exp\left(-K(v_{zd} - v_{zs}) - K(v_{zd}, v_{zs})\right)\right\}$$

$$= -\frac{kT\tau_b}{m^*} \left\{(e^{-\psi_s} - e^{-\psi_d}) + \int_{\psi_d}^{\psi_s} \exp\left(-\nu - K(v_{zd} - v_{zs}) - K(v_{zd}, v_{zs})\right) d\nu\right\}$$

$$\ldots(E.9)$$

The integration of I_4 with δ from equation 6.51(b) and (c) is:

$$I_{4_B} = \frac{kT\tau_b}{m^*} \int_{\psi_s}^{\infty} e^{-\nu} d\nu \left\{ \int_{v_{zs}}^{v_{zd}} \exp\left(-K(v_z, v_{zs})\right) \frac{\partial K}{\partial v_z} \partial v_z \right.$$

$$\left. + \int_{-v_{zd}}^{-v_{zs}} \exp\left(-K(v_z - v_{zs}) - K(v_{zd}, v_{zs})\right) \frac{\partial K}{\partial v_z} \cdot \partial v_z \right\}$$

Note: $K(v_{zd}, v_{zs}) = -K(v_{zs}, v_{zd})$

$$= \frac{2kT\tau_b}{m^*} \int_{\psi_s}^{\infty} e^{-\nu} \left\{1-\exp K(v_{zs},v_{zd})\right\} d\nu$$

$$= \frac{2kT\tau_b}{m^*} \left\{ e^{-\psi_s} - \int_{\psi_s}^{\infty} \exp\left(-\nu+K(v_{zs},v_{zd})\right) d\nu \right\} \qquad \ldots(E.10)$$

Substituting I_3, I_{4_A} and I_{4_B} from equations E.4, E.9 and E.10 in equation E.1, we have for the total current:

$$I_{nx} = q\mu_b E_x \left\{ 2dn_b + \Delta n_s - \lambda_n n_b (e^{-\psi_d} + e^{-\psi_s}) + \lambda_n n_b \int_{\psi_d}^{\psi_s} \exp\Big(-\nu + K(-v_{zs},v_{zd}) + K(v_{zs},v_{zd})\Big)\, d\nu + 2\lambda_n n_b \int_{\psi_s}^{\infty} \exp\left(-\nu+K(v_{zs},v_{zd})\right)\, d\nu \right\} \qquad \ldots(E.11)$$

We can express $K(v_{zs},v_{zd})$ in terms of the field function $F(\psi,\psi_d,\lambda)$ by substituting for E_z from equation 6.5 in equation 6.47. By differentiating equation 6.44 with ν constant, we can obtain a change of variable from dv_z to $d\psi$, i.e.:

$$dv_z = -\frac{kT}{m^* v_z} d\psi = -\left\{\frac{kT}{2m^*(\nu-\psi)}\right\}^{\frac{1}{2}} d\psi \qquad \ldots(E.12)$$

since $v_z = \left\{\frac{2kT}{m^*}(\nu-\psi)\right\}^{\frac{1}{2}}$ from equation 6.44.

Therefore,

$$K(v_{zs},v_{zd}) = \frac{L_B}{2\sqrt{\pi}\lambda_n} \int_{\psi_d}^{\psi_s} \frac{d\psi}{(\nu-\psi)^{\frac{1}{2}} F(\psi,\psi_d,\lambda)} \qquad \ldots(E.13)$$

Under flat band conditions, ($\psi_s \to 0$), it can be shown that $K(v_{zs},v_{zd}) \to -d/\lambda_n(\pi\nu)^{-\frac{1}{2}}$, as follows:

$$K(v_{zs},v_{zd}) = -\int_{v_{zs}}^{v_{zd}} \frac{m^*dv_z}{q\tau_b E_z} = -\int_o^{2d} \frac{dz}{\tau_b v_z} \qquad \ldots(E.14)$$

since

$$\frac{q\tau_b E_z}{m^*} = \mu_b E_z = v_z \qquad \ldots(E.15)$$

and $dv_z = dz/\tau_b$, and the limits of integration are:

$z = 0 \qquad v_z = v_{zs}$

$z = 2d \qquad v_z = v_{zd}$

Therefore,

$$K(v_{zs},v_{zd}) = -\int_o^{2d} \frac{(v_z - v_z + v_{zB})}{\tau_b v_z v_{zB}} dz = -\int_o^{2d} \frac{dz}{\tau_b v_{zB}} + \int_o^{2d} \frac{(v_z - v_{zB})}{\tau_b v_z v_{zB}} dz \qquad \ldots(E.16)$$

now under flat band conditions $v_z \to v_{zB}$, hence the second term $\to 0$, and:

$$K(v_{zs},v_{zd}) \to -2d/\tau_b v_{zB} = -d/\lambda_n(\pi\nu)^{-\frac{1}{2}} \qquad \ldots(E.17)$$

since

$\nu = m^*v_{zB}^2/2kT$ when $\psi = 0$

Appendix F

A summary of some relevant properties of Indium Arsenide:

Crystal structure	sphalerite (zinc-blende)
Band structure	see Fig.1.1
Lattice constant	6.05838 ± 0.00005Å
Density	5.66 gms/cc
Thermal expansion coefficeint	$6.67 \times 10^{-6}/^{o}C$
Melting point	$943^{o}C$
Dielectric constant	14.5
Index of refraction	3.42
Energy gap	$0.44 - 2.8 \times 10^{-4} T(^{o}K)$ eV
Electron effective mass	0.025m
Light hole mass	0.026m
Heavy hole mass	0.41m
Intrinsic carrier concentration ($300^{o}K$)	$8 \times 10^{14} cm^{-3}$
Electron concentration of the purest melt grown InAs produced	$1\text{-}2 \times 10^{16} cm^{-3}$
Electron mobility of single crystal melt grown material ($300^{o}K$)	23,000 - 30,000 $cm^2/V\text{-}sec$
Hole mobility ($300^{o}K$)	450 $cm^2/V\text{-}sec$

Appendix G.1

Timetable of Work Progress

January 1967	Project begun.
January-June 1967	Reading literature. Setting up deposition Apparatus, film monitors, etc.
July 1967-June 1968	Investigation into deposition of stoichiometric compounds on glass substrates. Effect of vapour pressure, substrate temperature, etc., on film composition. Electrical evaluation of polycrystalline films deposited. Structural investigations. Field effect device fabrication using polycrystalline films.
July 1968-July 1969	Deposition of epitaxial films on single crystal substrates. Electrical evaluation and electron diffraction studies. Epitaxial field effect device fabrication and measurements. Theoretical studies.
August 1969-December 1969	Writing thesis.

Appendix G.2

Cleaning Of Glass substrates

According to Holland[3.3] vapour degreasing in iso-propyl alcohol produces a higher standard of surface cleanliness than can be achieved with either detergents or ultrasonic cleaning. He indicates, however, that vapour degreasing is not effective in removing gross contamination, and, therefore, ultrasonic cleaning should also be employed.

The glass we have used is Corning 7059 and the manufacturers suggsst[3.4] that the cleaning of this material be kept to a minimum. Their experience indicates that vapour degreasing tends to leave deposits or residues, while acid cleaning methods leach the glass surfaces Presumably, vapour degreasing would be useful when the substrate surfaces are contaminated with oil or grease. Since we have had no problems with poor adhesion of the deposited films, it may be concluded that the cleaning procedures we have employed, (see section 3.1.3) are sufficient.

Appendix G.3

Deposition of Silicon Oxide

The electrical properties of evaporated silicon oxide depend on the deposition conditions, to a large extent. Holland[3.5] has indicated that low deposition rates (less that 5 Å/sec) result in a low loss angle and a low dielectric constant. This is aided by a high oxygen pressure during evaporation, of the order of 10^{-4}torr. Presumably, the combination of a low deposition rate and a high oxygen pressure result in a deposited film which approaches silicon dioxide in composition. However, since a high dielectric constant was required in our case in order to achieve good field effect modulation, we have used high deposition rates and low pressures (5×10^{-6}torr), which result in the monoxide being deposited. These conditions also give rise to a high loss angle, but this was not considered to be important.

References

3.3 L. Holland, The Properties of glass surfaces, Chapman and Hall, London, (1964), p.308.

3.4 Leaflet on Corning 7059 glass substrates, Corning Electronics, Division of Corning Glass Works, New York.

3.5 L. Holland, Thin film microelectronics, Chapman and Hall, London, (1965), p.24 and 155.

REFERENCES

CHAPTER 1

1.1. Welker, H., Z.Naturforsch, 7a, 744, (1952).

1.2. Hilsum, C., in "Semiconductors and Semimetals", R.K. Willardson and A.C. Beer, (Editors), Vol. 1, Physics of III - V compounds, p.3, Academic Press, N.Y., (1966).

1.3. Madelung, O., Physics of III - V compounds, p.69, J.Wiley, N.Y., (1964).

1.4. Weimer, P.K., Proc.IRE, 50, 1462, (1962).

1.5. DeGraff, H.C., Solid State Electronics, 10, 51, (1967).

1.6. Brody, T.P., and Kunig, H., Appl.Phys.Lett., 9, 259, (1966)

1.7. Kunig, H., Solid State Electronics, 11, 335, (1968).

1.8. Brody, T.P., Private Communication, (1968).

1.9. Page, D.J., Solid State Electronics, 11, 87, (1968).

1.10. Günther, K.G., in "Compound Semiconductors", Vol. 1, Preparation and Properties of III - V compounds, p.311 , R.K. Willardson and H.L. Goering, (Editors), Reinhold Publ.Co., (1962).

1.11. Günther, K.G., in "The Use Of Thin Films In Physical Investigations", J.C. Anderson, (Editor), Academic Press, N.Y. (1966).

1.12. Godinho, N., and Brunnschweiler, A., Solid State Electronics, in print, (1969).

1.13. Weiss, H., Structure and Applications of Galvanomagnetic Devices, Pergammon Press, Oxford, (1969).

1.14. Chopra, K.L., and Bobb, L.C., in "Single Cyrstal Films", p.373, M.H. Francombe and H. Sato, (Editors), Pergammon Press, Oxford, (1964).

1.15. Campbell, D.S., Reference 1.11, p.299.

1.16. Blatt, F.J., Solid State Physics, Vol. 4, p.199, Academic Press, N.Y., (1957).

1.17. Fowler, A.B., Fang, F.F., Howard, W.E., and Stiles, P.J., Phys.Rev.Lett., 16, 901, (1966).

1.18. Murphy, N.St.J., Lecture given at Southampton University, (1969).

CHAPTER 2

2.1. Paparoditis, C. "Compound Semiconductors", Vol.1, Preparation Of III - V Compounds, p.326, R.K. Willardson and H.L. Goering, (Editors), Reinhold Publ.Co., N.Y., (1962).

2.2. Cronin, G.R., Conrad, R.W. and Borrello, S.R., J.Electrochem.Soc., 113, 1336, (1966).

2.3. McCarthy, J.P., Solid State Comm. 5, 5, (1967).

2.4. McCarthy, J.P., Solid State Electronics, 10, 649, (1967).

2.5. Robinson, P.H., R.C.A. Rev., 24, 574, (1963).

2.6. Nelson, H., R.C.A. Rev., 24, 603, (1963).

2.7. Brown, M.A.C.S., and Porteaus, P., Solid State Electronics, 10, 76, (1967).

2.8. Bolger, D.E., Franks, J., Gordon, J. and Whitaker, J., Proc. Intl. Symposium on GaAs, Reading, U.K., paper No.3, (1966).

2.9. Harris, L. and Siegel, M., J. Appl. Phys., 19, 739, (1948).

2.10. Richards, J.L., Hart, P.B. and Gallone, L.M., J. Appl. Phys., 34, 3418, (1963).

2.11. Richards, J.L. "The Use Of Thin Films In Physical Investigations", J.C. Anderson (Editor), Academic Press, London and N.Y., p. (1966).

2.12. Juhasz, C. and Anderson, J.C., Proc. Conf. on Thin Films, Imperial College, London, paper No.25, (1966).

2.13. Vlasov, V.A. and Semiletov, S.A., Kristallografia, 13, 683, (1968).

2.14. GÜnther, K.G., Naturforsch, Z., 13a, 1081, (1958).

2.15. Günther, K.G., Naturwissenschaften, 45, 415, (1958).

2.16. Günther, K.G., and Freller, H., Z. Naturforsh., 16a, 279, (1961).

2.17. GÜnther, K.G., Ref.2.11., p.213.

2.18. Günther, K.G., Ref.2.1., p.313.

2.19. Hönig, E., R.C.A. Rev., 18, 195, (1957).

2.20. Goldfinger, P., and Jeunehomme,, M., Adv. in Mass Sepectroscopy, Pergamon, London, p.254, (1959).

2.21. Renner, T., Solid State Electronics, 1, 39, (1960).

2.22. Itoh, T., Hasegawa, S., and Kaminaka, N., J. Appl. Phys., 39, 5310, (1968).

2.23. Marais, M., Menoret, M., and Perigaud, A., Le'Onde Electrique, XLIV, 1005, (1964).

2.24. Johnson, J.E., J. Appl. Phys., 37, 2188, (1966).

2.25. De Klerk, J., and Kelly, E.F., Rev. Sci. Instrum., 36, 506, (1965).

2.26. Davey, J.E., and Pankey, T., J. Appl. Phys., 39, 1941, (1968).

2.27. Steinberg, R.F., and Scruggs, D.M., J. Appl. Phys., 37, 4586, (1966).

2.28 Bassett, G.A., Menter, J.W., and Pashley, D.W., "Structure And Properties Of Thin Films", C.A. Neugebauer, J.B. Newkirk, and D.A. Vermilyea, (Editors), Wiley, N.Y., (1959).

2.29. Pashley, D.W., Advances in Physics, 14, 327, (1965).

2.30. Hirth, J.P., and Pound, G.M., "Condensation And Evaporation", Progress in Material Science, Vol.II. MacMillian, N.Y., (1963).

2.31. Walton, D., J. Chem. Phys. 37, 2182, (1962).

2.32. Rhodin, T.N., Ref.2.11, p.187, (1966).

2.33. Russell, K.C., Lothe, J., and Pound, G.M., "Condensation And Evaporation Of Solids", Gordon and Breach, N.Y., p.503, (1964).

2.34. Holloman, J.H., and Turnbull, D., Progress in Metal Physics, Vol.4, B. Chalmers, (Editor), Pergamon Press, Oxford, (1953).

2.35. Stirland, D.J., Ref.2.11, p.163, (1966).

2.36. Chakraverty, B K., and Pound, G.M., Ref.2.33, p.553, (1964).

2.37. Pashley, D.W., Stowell, M.J., Jacobs, M.H., and Law, T.J., Phil. Mag., 10, 127, (1964).

2.38. Jacobs, M.H., Pashley, D.W., and Stowell, M.J., Phil. Mag., 13, 129, (1966).

2.39. Stowell, M.J., Ref.2.11, p.131, (1966).

2.40. Howson, R.P., Brit. J. Appl. Phys. (J. Phys. D), Series 2, Vol.1, 15, (1968).

2.41. Harris, J.S., and Snyder, W.L., Solid State Electronics, 12, 337, (1969).

2.42. Kenty, J.L., and Hirth, J.P., Surface Science, 15, 403, (1969).

2.43. Straumauis, M.E., and Kim, C.D., Acta Cryst., 19, 256, (1965).

2.44. Holt, D.B., J. Mat. Science, 1, 280, (1966).

2.45. Holloway, H., Phil. Mag., 11, 263, (1965).

2.46. Van Der Merwe, J.H., "Single Crystal Films", M.H. Francombe, and H. Sato, (Editors), Pergamon Press, Oxford, p.139, (1964).

2.47. Holt, D.B., J. Phys. Chem. Solids, 27, 1053, (1966).

2.48. Oldham, W.G., and Milnes, A.G., Solid State Electronics, 7, 153, (1964).

2.49. Kuntze, R., Chambers, A., and Prutton, M., Thin Solid Films, 4, 47, (1969).

2.50. Moazed, K.L., Ref.2.11, p.203, (1966).

2.51. Mathews, J.W., and Grunbaum, E., Phil. Mag., 11, 12233, (1965).

2.52. Abraham, M.S., Weisberg, L.R., Buiocchi, C.J., and Blanc, J., J. Mat. Sci., 4, 223, (1969).

CHAPTER 3

3.1. Reisman, A., and Rohr, R., J.Electrochem.Soc., 111, 1425, (1964).

3.2. Horsful, P., M.Sc. Dissertation, Southampton University, (1968).

CHAPTER 4

4.1. Holloway, H., "The Use of Thin Films in Physical Investigations", J.C. Anderson, (Editor), p.111, Academic Press, London, (1966).

4.2. Bobb, L.C., Holloway, H., Maxwell, K.H., and Zimmerman, E., J.Phys.Chem.Solids, 27, 1679, (1966).

4.3. Cullity, B.D., Elements of X-ray Diffraction, Addison Wesley Publishing Company, Massachusetts, (1956).

4.4. Giesecke, G., Semiconductors and Semimetals, Vol.2, Physics Of III - V Compounds, R.K. Willardson and A.C. Beer, (Editors), Academic Press, (1966).

4.5. Johnson, J.E., J.Appl.Phys., 37, 3188, (1966).

4.6. Hirsch, P.B., Howie, A., Nicholson, R.B., Pashley, D.W., and Whelan, M.J., Electron Microscopy of Thin Crystals, Butterworths, London, (1965).

4.7. Thomas, G., Transmission Electron Microscopy of Metals, J. Wiley and Sons, New York, (1962).

4.8. Holloway, H., J.Phys.Chem.Solids, 29, 1977, (1968).

4.9. Holloway, H., Wollmann, K., and Joseph, A.S., Phil.Mag., 11, 263, (1965).

4.10. Abrahams, M.S., and Ekstrom, L.K., in "Properties of Elemental and Compound Semiconductors", H.C. Gatos, (Editor), p.225, Interscience, New York, (1960).

4.11. Faust, J.W., in "Compound Semiconductors", Vol.I, Preparation of III - V Compounds, p.445, R.K. Willardson and H.L. Goering, Reinhold Publishing Corporation, New York, (1962).

4.12. Williams, F.V., Proc.Intl.Symposium GaAs, Reading, IPPS Conference Series No.3, paper 5, p.27, (1966).

4.13. See reference 4.4.

4.14. Pashley, D.W., and Stowell, M.J., Phil.Mag., 8, 1605, (1963).

4.15. Holt, D.B., J.Mat.Sci., 4, 935, (1969).

CHAPTER 5

5.1. Johnson, J.E., IEEE Trans. Electron Devices, ED-13, 678, (1966).

5.2. Johnson, J.E., Private Communication, (1967).

5.3. Dixon, J., and Enright, E., J.Appl.Phys., 30, 753, (1959).

5.4. Dixon, J., and Enright, E., J.Appl.Phys., 30, 1462, (1959).

5.5. Edmond, J.T., and Hilsum, C., J.Appl.Phys., 31, 1300, (1960).

5.6. Hiluum, C., Proc.Phys.Soc., (London), A73, 685, (1959).

5.7. Lark Horovitz, K., and Johnson, V.A., "Methods of Experimental Physics", Vol. 6., Academic Press, N.Y., (1959).

5.8. Weimer, P.K., "Field Effect Transistors", J.T. Wallmark and H. Johnson, (Editors), Prentice Hall, N.J., (1966).

CHAPTER 6

6.1. Kingston, R.H., and Neustadter, S.F., J.Appl.Phys., 26, 718, (1955).

6.2. Garrett, C.G.B., and Brattain, W.H., Phys.Rev., 99, 376, (1955).

6.3. Frankl, D.R., Electrical Properties of Semiconductor Surfaces, p.42, Pergamon Press, Oxford, (1967).

6.4. Sebenne, C., and Balkanski, M., Surface Sciences, 1, 42, (1964).

6.5. Gasanov, L.S., Soviet Physics-Semiconductors, 1, 673, (1967).

6.6. Gasanov, L.S., Radio Enginng. and Electronic Physics, 12, 1425, (1967).

6.7. Ehrenreich, H., J.Phys.Chem.Solids, 120, 1951, (1960).

6.8. Madelung, O., Physics of III-V Compounds, J.Wiley, N.Y., (1964).

6.9. Conwell, E., and Weisskopf, V.F., Phys.Rev., 77, 388, (1950).

6.10. Petritz, R.L., Phys.Rev., 104, 1508, (1956).

6.11. Waxman, A., Henrich, V.E., Shallcross, F.V., Borkan, H., and Weimer, P.K., J.Appl.Phys., 36, 168, (1965).

6.12. Brunnschweiler, A., Ph.D. Thesis, University of Manchester, (1967).

6.13. Hilsum, C., and Rose-Innes, A.C., Semiconducting III-V Compounds, Pergamon Press, Oxford, (1960).

6.14. Beer, A.C., Solid State Physics, Suppl. 4., Galvanomagnetic Effects In Semiconductors, Academic Press, (1963).

6.15. Beer, A.C., Solid State Electronics, 9, 339, (1966).

6.16. Weiss, H., in "Semiconductors and Semimetals," Vol. 1, Physics Of III-V Compounds, R.K. Willardson and A.C. Beer, (Editors), Academic Press, N.Y., (1966).

6.17. Fuchs, K., Proc.Camb.Phil.Soc., 34, 100, (1938).

6.18. Sondheimer, E.H., Adv.Phys., Vol. 1, p.1, N.F. Mott (Editor), (1952).

6.19. Schrieffer, J.R., Phys.Rev., 97, 641, (1955).

6.20. Greene, R.F., Frankl, D.R., and Zemel, J.N., Phys.Rev., 118, 967, (1960).

6.21. Ham, F.S., and Mattis, D.C., IBM J.Res. and Dev., 4, 143, (1960).

6.22. Sah, C.T., and Pierret, R.F., Solid State Electronics, 11, 279, (1968).

6.23. McKelvey, J.P., Solid State and Semiconductor Physics, p.182, Harper and Row, N.Y., (1966).

6.24. Lucas, M.S.P., J.Appl.Phys., 36, 1632, (1965).

6.25. Campbell, D.S., in "The use of thin films in Physical Investigations", J.C. Anderson, (Editor), p.299, Academic Press, London, (1966).

6.26. Many, A., Goldstein, B., and Grover, N.B., Semiconductor Surfaces, p.313, North-Holland Publ.Co., Amsterdam, (1965).

6.27. Flietner, H., Phys.Status Solidi, 1, 483, (1961).

6.28. Harman, T.C., Goering, H.L., and Beer , A.C., Phys.Rev., 104, 1562, (1956).

6.29. Schroeder, J.B., in "Compound Semiconductors", Vol.1, Preparation Of III-V Compounds, p.222, Reinhold, N.Y., (1962).

6.30. Erginsoy, C., Phys.Rev., 79, 1013, (1950).

6.31. Kawaji, S., and Kawaguschi, Y., J.Phys.Sci.Japan., Suppl. 21, 336, (1966).

6.32. Stern, F., and Howard, W.E., Phys.Rev., 163, 816, (1967).

6.33. Petritz, R.L., Phys.Rev., 110, 1255, (1958).

6.34. Goldstein, Y., Grover, M.B., Many, A., and Greene, R.F., J.Appl.Phys., 32, 2540, (1961).

6.35. Greene, R.F., Phys.Rev., 131, 592, (1963).

6.36. Davis, J.L., Surface Science, 2, 33, (1964).

6.37. Putley, E.H., The Hall Effect And Semiconductor Physics, Dover Publ., N.Y., (1968).

6.38. Zemel, J.N., ref.6.25, p.329, (1966).

6.39. Zemel, J.N., Phys.Rev., 112, 762, (1958).

6.40. Amith, A., J.Phys.Chem.Solids, 14, 271, (1960).

6.41. Schiff, L.I., Quantum Mechanics, p.37, McGraw-Hill Book Co.Inc., (1955).

6.42. Murphy, N.St.J., Surface Science, 2, 86, (1964).

6.43. Fowler, A.B., Fang, F.F., Howard, W.E., and Stiles, P.J., J.Phys.Soc. Japan, 21, 331, (1966).

6.44. Zemel, J.N., and Kaplit, M., Surface Science, 13, 17, (1969).

6.45. Tavger, B., Phys.Stat.Sol., 22, 31, (1967).

6.46. Berchtold, K., and Huber, D., Phys.Stat.Sol., 33, 425, (1969).

6.47. Ogrin, Yu.F., Lutskii, V.N., and Elinson, M.I., Soviet Phys. J.Exp.Theor.Phys., (JETP) Lett., 3, 71, (1966).

6.48. Komnik, Yu.F., and Bukhshtab, E.I., Soviet Phys. - JETP, 27, 34, (1968).

6.49. Friedman, A.N., and Koenig, S.H., IBM J.Res. and Dev., 4, 158, (1960).

6.50. Schrieffer, J.R., in "Semiconductor Surface Physics", p.70, K.H. Kingston, (Editor), University of Pennsylvania Press, Philadelphia, (1957).

6.51. Greene, R.F., Surface Science, 2, 101, (1964).

6.52. Handler, P., and Eisenhour, S.E., Surface Science, 2, 64, (1964).

6.53. Flügge, S., and Marschall, H., Rechenmethoden Der Quanten Theorie, Vol.1, p.70, Springer-Verlag, Berlin, (1952).

6.54. Kobayashi, A., Oda, Z., Kawaji, S., Arata, H., and Sugiyama, K., J.Phys.Chem.Solids, 14, 37, (1960).

6.55. Komatsubara, K.F., Kamioka, H., and Katayama, Y., J.Appl.Phys., 40, 2940, (1969).

6.56. Fang, F.F., and Fowler, A.B., Phys.Rev., 169, 619, (1968).

6.57. Murphy, N.St.J., Berz, F., and Flinn, I., Solid State Electronics, 12, 775, (1969).

6.58. Kawaji, S., Huff, H., and Gatos, H.C., Surface Science, 3, 234, (1965).

6.59. Kawaji, S., and Gatos, H.C., Surface Science, 7, 215, (1967).

6.60. Duke, C.B., Phys.Rev., 168, 816, (1968).

6.61. Alferieff, M.E., and Duke, C.B., Phys.Rev., 168, 832, (1968).

6.62. Parrott, J.E., Proc.Phys.Soc., 85, 1143, (1965).

6.63. Greene, R.F., Phys.Rev., 141, 687, (1966).

6.64. Greene, R.F., and O'Donnell, R.W., Phys.Rev., 147, 599, (1966).

6.65. Price, P.J., IBM J.Res.Dev., 4, 152, (1960).

6.66. Reddi, V.G.K., IEEE Trans.Electron Devices, ED-15, 151, (1968).

CHAPTER 7

7.1. Shaw, D.W., Conrad, R.W., Mehal, E.W., and Wilson, O.W., Proc.1st.Intl.Symposium GaAs, Reading, paper 2, p.10, IPPS Conf. Series 3, (1966).

7.2. McCarthy, J.P., Solid State Electron. 10, 649, (1967).

7.3. Fawcett, W., Hilsum, C., and Rees, H.D., Electron.Lett., 5, 313, (1969).

7.4. Hower, P.L., Hooper, W.W., Tremere, D.A., Lehrer, W., and Bittman, C.A., Proc.2nd.Intl.Symposium GaAs, paper 29, p.187, IPPS Conf. Series 7, (1968).

7.5. Turner, J.A., and Wilson, B.L.H., Proc.2nd.Intl.Symposium GaAs, Dallas, Texas, paper 30, p.195, IPPS Conf. Series 7, (1968).

7.6. Statz, H., and Munch, W.V., Solid State Electron., 12, 111, (1969).

7.7. Neugebauer, C.A., Miller, D.C., and Hall, J.W., General Electric Research and Development Centre, N.Y., Report, No. 67-C-454, (1967).

7.8. Zaininger, K.H., and Waxman, A.S., IEEE Trans.Electron Devices, ED-16, 333, (1969).